Determination of the electronic and structural configuration of coordination compounds by synchrotron-radiation techniques

Determination of the electronic and structural configuration of coordination compounds by synchrotron-radiation techniques

Claudio Garino,[a,b] Elisa Borfecchia,[a,b,c] Roberto Gobetto,[a,b] Jeroen A. van Bokhoven,[d,e] and Carlo Lamberti*[a,c,f,g]

[a] Department of Chemistry, University of Turin, Via P. Giuria 7, 10125 Torino, Italy
[b] NIS Centre of Excellence, University of Turin, Italy
[c] INSTM reference center at University of Turin, Italy
[d] ETH Zurich, Institute for Chemical and Bioengineering, HCI E127 8093 Zurich, Switzerland
[e] Laboratory for Catalysis and Sustainable Chemistry (LSK) Swiss Light Source, Paul Scherrer Instituteaul Scherrer Institute, Villigen, Switzerland
[f] CrisDI center of crystallography, University of Turin, Italy
[g] Southern Federal University, Zorge street 5, 344090 Rostov-on-Don, Russia

Keywords: Homogeneous catalysis; Heterogeneous catalysis; Photoactive coordination compounds; Synchrotron; Structural determination; Electronic structure; X-ray scattering techniques; X-ray spectroscopies.

Table of contents

Abstract
In this review we provide an overview on the potentialities of synchrotron radiation techniques in the understanding of the structural and electronic properties of coordination compounds. Besides the largely employed multi-wavelength anomalous dispersion (MAD) and X-ray absorption spectroscopy (XAS), in both near (XANES) and post (EXAFS) edge regions, we also discuss the contribution arising from more specialized techniques that however started to become more widely used in the last years, such as the total scattering approach in the XRPD data analysis and the X-ray emission spectroscopy (XES). Comparison with the commonly used laboratory techniques (XRD, UV-Vis, luminescence, NMR, EPR) is used to underline the plus value of synchrotron radiation techniques when applied to already well characterized samples. The fundamental role of DFT calculations in interpreting both diffraction and spectroscopic data to understand structural and electronic properties of coordination complexes is highlighted in several examples. A perspective summary is reported at the end of the manuscript.

1 Introduction
The aim of the present review is to provide to colleagues working in the field of synthesis [1-10], grafting [11-20], encapsulation [21-23], functionalization [8, 24, 25] of coordination compounds, the basic concepts of synchrotron radiation techniques and their potentialities in understanding the structural and electronic properties of such systems. Comparison with the commonly used laboratory techniques (XRD, UV-Vis, luminescence, NMR, EPR) is used to underline the plus value of synchrotron radiation techniques applied to already well characterized samples. The fundamental role of DFT calculations in interpreting diffraction and spectroscopic data [26-39] to understand structural and electronic properties of coordination complexes is highlighted in several examples reported in this review.
It is a matter of fact that the progressively increased availability of synchrotron light sources made possible, starting from the late seventies, to perform experiments requiring a high X-ray flux in a continuous interval of energies (or wavelengths) [40-45]. Among them, X-ray absorption spectroscopy (XAS, also known as X-ray absorption fine-structure, XAFS) [46-49] in both near (XANES) [50-53] and post (EXAFS) [54-56] edge regions, has become in the last four decades a powerful characterization technique in catalysis [57-76], coordination chemistry [65, 77-83], electrochemistry [84, 85], solid state physics and chemistry [86-91], physics and chemistry of liquids [92-94], nanomaterials [59, 90, 91], materials science [84, 86, 95-97], high pressure physics [87], earth science [98, 99], archaeometry [100-102], cultural heritage [102], biology [103-111] agronomy [112], and medicine [113, 114].
More recently, X-ray emission spectroscopy (XES) [115-127], in both resonant and non-resonant conditions, has significantly increased the information on the electronic structure of metal centres accessible to X-ray based spectroscopies. In addition, X-ray magnetic circular dichroism (XMCD) is a powerful synchrotron technique to understand the magnetic properties of open shell transition metal complexes [128-135].
Coming to scattering techniques, it is evident that multi-wavelength anomalous dispersion (MAD) [136-141] has taken great advantage from the development of third generation synchrotron radiation facilities [142]. The same holds for total scattering studies [143-146], requiring high photon fluxes at very short wavelength values.
The peculiarities of third generation synchrotrons and of free electron lasers (FELs) make time [147-153] and space [154-156] resolved experiments possible at different scales which lower limits are progressively improved year after year.
This review is structured in five main sections and one appendix. The present introduction is followed by Section 2, that reports a comparative overview on the available methods for structural characterization in coordination chemistry, in terms of advantages/disadvantages and type of the accessible structural information, with an emphasis on X-ray based techniques. In particular, we will devote a special attention to synchrotron-based approaches, clarifying the unique contribution of third generation synchrotron sources in the structural determination of coordination compounds. Structural characterization methods are classified into scattering techniques, X-ray absorption techniques and magnetic resonance techniques. Section 3 is devoted to a description of the main spectroscopies that provide insights into the electronic structure. When needed, in both Sections 2 and 3, the description of the discussed techniques is supported by examples relevant in coordination chemistry. Section 4, organized into three main subsections, reports an overview of applications pertinent to the fields of homogeneous catalysis, heterogeneous catalysis and photoactive coordination compounds. Finally, perspectives and conclusions are reported in Section 5. Along Sections 1-5 we decided to limit as much as possible the use of mathematical equations in order to make the text more fluent and to allow the reader to focus on the scientific issues rather than on the mathematical formalism that describes the interaction of X-rays with matter. To partially overcome this lack, a brief summary of the most relevant concepts and related equations is reported at the end of the text in the form of a short appendix (Section 6).

2 Structural characterization of coordination compounds
Scheme 1 reports a general-purpose classification of the several methods currently available in the coordination chemist's toolbox for structural characterization. The principal techniques include elastic scattering/ diffraction methods (mainly using X-rays or neutron as probes), X-ray absorption spectroscopy (primarily EXAFS, but as we will

discuss in Section 2.5 also XANES) and magnetic resonance spectroscopies (basically NMR and EPR). The latter techniques are exclusively laboratory-based methods, whereas the use of third generation synchrotron sources is sorely needed to perform XAS experiments. With respect to XRD, the technique is widely applied using laboratory setup, but the use of synchrotron sources is advantageous in several cases, and often opens novel perspectives for the XRD applicability.

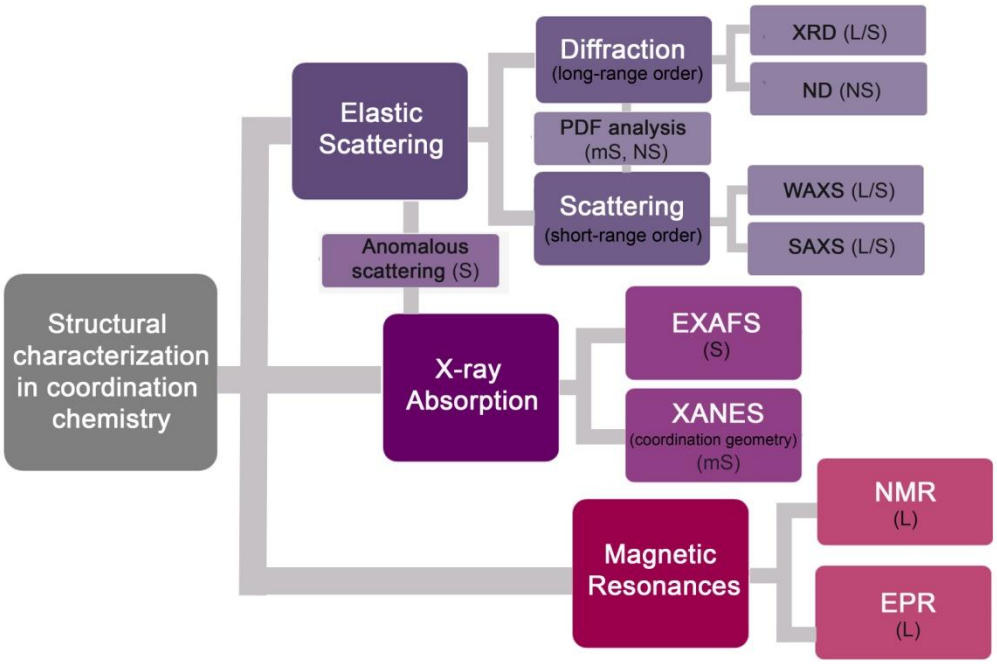

Scheme 1. General classification of the principal methods currently available for structural characterization of coordination compounds. For each technique, the following abbreviations indicate where it is (preferentially) performed: L = lab-scale setups; S = synchrotron sources (mS = mainly synchrotron sources, for cases where most of the studies are performed at synchrotrons but also lab-based applications have been demonstrated); NS: neutron sources.

In the present Section we propose a comparative overview focused on X-ray methods, in terms of advantages/disadvantages and type of the available structural information, with an emphasis on X-ray based characterization. In particular, we will devote special attention to synchrotron-based approaches, clarifying the unique contribution of third generation synchrotron sources in the structural determination of coordination compounds.

2.1 Structural determination by elastic scattering: probe and interactions

Most of the methods indicated in Scheme 1 definitely rely on an elastic scattering interaction between a suitable probe beam and the investigated sample. Here, the key ingredients for the structural determination are the interference between the wavefronts diffused by the atoms of the system of interest, and the possibility to relate *via* Fourier transform (FT) operation the interference pattern to the spatial arrangement of the scatterers, bridging the reciprocal space of exchanged momentum (q-space, where q is directly related to the scattering angle θ, $q = 4\pi \sin\theta/\lambda$) to the real space of distances (r-space). In the case of crystalline (long-range ordered) materials, characterized by a periodic arrangement of atoms inside the crystal lattice (crystallography), the elastic scattering process is commonly referred to as diffraction, and the scattered intensity is characterized by sharp, well-defined Bragg peaks [157-160]. In the case of X-rays, the elastic scattering geometry is represented in Scheme 6 and a brief mathematical description of the process is reported in the appendix (Section 6.2). The diffusion/interference mechanism is enabled by selecting the probe wavelength (or De Broglie wavelength λ_D, for particle probes) to match the order of magnitude of the structural parameters to elucidate. Hence, to achieve atomic-level structural sensitivity, the best suited probes are hard X-rays photons (X-ray diffraction, XRD), neutrons (neutron diffraction, ND) or electrons with λ_D in the Å range. Although the first diffraction experiments performed with electrons were carried out with $\lambda_D \sim 1$ Å [161-163], actually electrons diffraction experiments are carried out on transmission electron microscopes that work with a much shorter λ_D in order to partially increase the intrinsically short penetration depth of the probe [164, 165]: for instance, in a TEM instrument working at 300 keV, $\lambda_D = 0.0197$ Å.

Although a common basic scheme and substantially equivalent mathematics can be adopted to describe X-ray, neutron and electron elastic scattering, the details of the interaction with matter are strictly probe-dependent. As a consequence, each of these probes shows attractive peculiarities, and a remarkable complementary is observed in some of the accessible structural features. In particular, X-rays are mainly scattered by electrons, thus providing information on the spatial distribution of the electron density in matter. Conversely, neutrons are primarily scattered

by atomic nuclei, which have a size of few fm and behave as point-scatterers. As a consequence, X-rays provide information on the electron density localized around the atomic nuclei, whereas neutrons provide information directly on nuclear density. Here, a good example is the discrepancy between the refined O–H (or C–H) distances commonly observed comparing XRD and ND experiments. In particular, ND provides the more reliable inter-nuclear distances, while the analysis of XRD data yields remarkably shorter distances, due to the preferential localization of the electron cloud next to the more electronegative O or C atom (see *e.g.* ref. [166] for the sucrose case).

In addition, neutrons possess a magnetic moment, and are consequently subjected to magnetic coherent scattering interaction with any other magnetic moment in matter (mainly spin and orbital moments resulting from unpaired valence electrons). This kind of interaction allows the determination of the magnetic structure in coordination complexes and materials, using polarized neutron beams. A detailed discussion of the underlying physics and related applications is beyond the scope of the present work and can be found in the specialized literature, see e.g. refs [167-171].

The nuclear scattering interaction is characterized by lower cross-sections with respect to X-ray scattering from electron clouds. Conversely, the direct charge-charge Coulomb interaction of electrons in matter yields scattering cross-sections of several orders of magnitude higher with respect to the X-rays case (~10^6 barns for electrons at 200 keV, λ_D = 0.025 Å, to be compared with 1–10 barns for X-rays with λ = 1.5 Å [172]), making electrons an ideal surface-sensitive probe.

The reduced mean free path of electrons in matter (indicatively from several Å to a few nm [173]), despite its unique potential for the most challenging surface-science applications [174-176], severely limits the application of electron scattering techniques to coordination chemistry problems. Indeed, excluding gas-phase studies of simple compounds with sufficient volatility [177-180], bulk sensitivity is preferred for the most common solid-state and solution-phase applications of metal complexes. Furthermore, more extended supramolecular architectures as coordination polymers and MOFs are critically sensitive to electron-beam damaging, which hampers their characterization using electron diffraction methods, *e.g.* at TEM instruments, without using very advanced setups [181-183]. Consequently, only a limited number of examples can be found in the recent literature, see *e.g.* refs [183-188]. It is however worth anticipating that the XAS signal in the EXAFS region (Section 2.5) intimately relies on an electron elastic scattering interaction: as it will be discussed below, the limited photoelectron mean free path ensures an element-selective structural sensitivity, which is a crucial advantage of the technique.

2.2 X-ray and Neutron diffraction: relevance and complementarity

X-ray diffraction (XRD) is by far the most common method for structural determination, as well as the most explored within the coordination chemistry community. For a detailed discussion of XRD theory and experimental aspects we refer the reader to the broad specialized literature (see *e.g.* refs [158-160, 189-194] and the brief mathematical description reported in the appendix, Section 6.2.1), here we provide an overview on the technique features, and advantages/disadvantages in comparison with ND.

Single crystal XRD is nowadays a mature and widespread technique and, although the use of synchrotron radiation is advantageous under several aspects (Section 2.3), high-quality chemical crystallography is routinely performed using laboratory diffractometers. XRD allows one to determine unit cell geometry and space group, to locate the atoms in the "asymmetric unit", and to obtain the anisotropic displacement parameters, which principally describes the atomic vibrations along the three spatial directions but can also be influenced by structural disorder and crystalline imperfections [191]. This information allows a full reconstruction of the intra- and inter-molecular geometry, being a major driving force in *de novo* structural determination of coordination compounds of increasing complexity: a look to the most recent statistics (January 2013) released by the Cambridge Structural Database [195, 196] reveals that more than half of the total deposited structures (~ 54 %) contain transition metal atoms [197].

The standard uncertainty on the structural parameters derived from XRD refinement depends, in relation with the structural complexity of the analysed system, on the precision and accuracy of the collected data, on the quality of the structural model employed as starting point for the refinement and, critically, by the quality of the measured single crystal sample. Depending on the specific coordination compound investigated, the crystallization process can yield unsatisfactory results (poor crystallinity, multiple or twinned specimens, significant structural disorder, reduced dimensions), and in some unfortunate cases it is totally unsuccessful. In these conditions X-ray powder diffraction (XRPD) [194, 198, 199] can play a key-role. After the introduction of efficient refinement strategies based on matching observed and calculated XRD patterns (Rietveld refinement [200-203]) and the remarkable advances in the development of *ab initio* phasing strategies [204] this method has turned from the "ugly duckling" of crystallography into a well-established alternative to single-crystal XRD to tackle structural determination [205, 206]. Nevertheless, the collapse of a 3D single-crystal diffraction pattern into a 1D powder pattern unavoidably sets a limit on the size (number of atoms in the asymmetric unit) and structural complexity of systems that can be refined *via* XRPD [207-210]. As it will be discussed in more details in Section 2.3, the use of X-rays from synchrotrons allows a great extension of the XRPD applicability with respect to laboratory setups, as demonstrated by the rapidly growing number of successful application of synchrotron-XRPD to large-unit cell coordination compounds such as MOFs [211, 212].

Despite its powerful and extensive use, also X-ray crystallography has its own Achilles' heel. Firstly, the X-rays scattering factors (or atomic form factors) $f(q)$ steeply decrease as the scattering wavenumber (or, equivalently, the scattering angle) increases (see Figure 1a). This behaviour directly derives from the interaction with the atomic electron clouds which are spatially extended in a region of comparable dimension with respect to the adopted X-ray beam wavelength. As a consequence, the phase differences between the waves scattered by different unit volumes of electron density increase at higher q-values, enhancing the destructive interference phenomena, which strike down the form factors (a detailed discussion can be found *e.g.* in ref. [213], whereas the key mathematical passages are reported in the appendix, Section 6.2). And, unfortunately, the high-q data are the most crucial to improve the resolution in structural determination by diffraction measurements. Indeed, the effective resolution achievable from a specific XRD dataset is inversely proportional to the maximum angle where a Bragg peak can be significantly detected. In particular, the geometry of a coordination compound is considered reliably solved when a resolution significantly lower than interatomic bond distances is achieved (a typical value of 0.8 Å is commonly demanded). The space resolution (d_{min}) of the electron density reconstructed from a diffraction experiment is given by $d_{min} = \lambda/[2 \sin(\theta_{max})]$, being θ_{max} the highest angle where a Bragg peak has been observed in that data collection [213] (see also the appendix, Section 6.2.1).

Moreover, as it clearly emerges from the curves reported in Figure 1a, $f(q)$ values for X-rays are strongly dependent on the atomic number Z of the atoms involved in the scattering process, being equal to Ze^- for the perfect in-phase scattering condition at $q = 0$ Å^{-1}. This implies (*i*) scarce sensitivity to light atoms (especially H, but also *e.g.* C, N and O) in particular in proximity of strongly scattering metal centres, which is a ubiquitous case in coordination chemistry and (*ii*) difficult discrimination between almost iso-electronic elements.

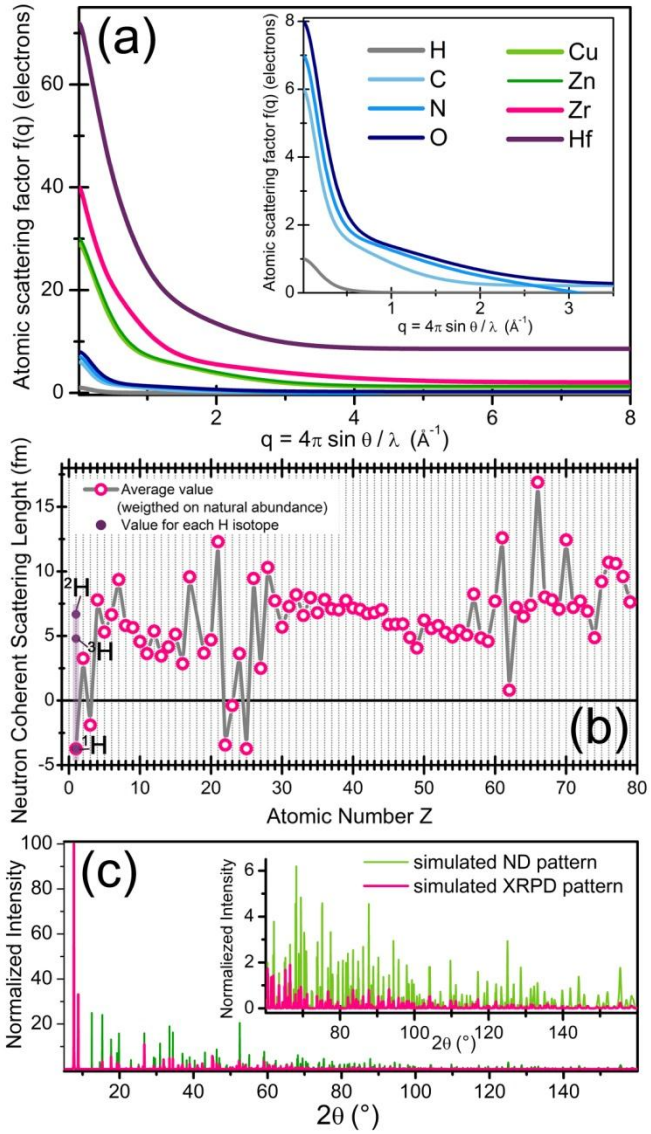

Figure 1. (a) X-ray scattering factors $f(q)$ for a selection of elements commonly found in coordination compounds, including light atoms often present in ligands (H, C, N, and O, see also magnified detail in the inset), and transition metals acting as coordination centres (Cu, Zn, Zr, and Hf). (b) Neutron coherent scattering lengths as a function of the atomic number Z, for $1 < Z < 80$, averaged on the different isotopes, weighting by their natural abundance. For H, the values for each isotope are also reported as full violet circles. The figure reports values from the tables by Sears [214]; the same data can be also found at the NIST web site

(http://www.ncnr.nist.gov/resources/n-lengths/). (c) Simulated XRPD and ND patterns for UiO-66 MOF (Section 2.5.1) in its desolvated form (λ = 1.954 Å); the insets reports a magnification of the high-*q* region, evidencing the damping of XRPD intensities with respect to the ND ones, by courtesy of A. Piovano (ILL, Grenoble F). Adapted from ref. [213]. Unpublished Figure.

All these difficulties are solved point by point by neutron diffraction (ND). Full description of ND principles and experimental setups is far beyond the scope of the present work and can be found elsewhere, see *e.g.* refs [215-222]. In brief, thermal neutrons employed in diffraction studies see atomic nuclei as point-like objects, showing *q*-independent nuclear coherent scattering lengths b_c. Hence ND is inherently superior to XRD in the collection of high-quality data in the high-*q* region. Actually, the amplitude of the high 2θ reflections is still dumped in ND experiment because of the thermal motion of the electron clouds, that drag along the atomic nuclei. Thus, they behave no more as point-scatterers [213]. Data collection at liquid He temperature significantly reduces this drawback. As an example, in Figure 1c the simulated XRPD and ND patterns for the desolvated UiO-66 MOF are reported, evidencing the damping of XRPD intensities with respect to the ND ones in the high-*q* region. In addition, the coherent nuclear scattering lengths are fully determined by the nature of the scattering nuclide. The values are thus *Z*-independent, swinging across the periodic table (see Figure 1b), and for several elements pronounced variations are observed for in correspondence of different isotopes. This greatly facilitates the location of light elements also in contexts where heavy atoms are presents, and the discrimination between elements with similar atomic numbers (e.g. O and N or Mn and Fe). The resounding case of $WPMe_3H_2Cl_2$ [223], where ND contributed in tracking down the tendency to refine to a false minimum XRD data from complexes that crystallize in a polar space group, together with several similar examples in coordination chemistry, are concisely review *e.g.* in ref. [219].
However, these remarkable advantages of ND with respect to the X-ray based crystallography are balanced by a series of drawbacks. ND experiments are exclusively performed at large scale facilities (neutron reactors or spallation sources), with high running costs and users' accessibility even more restricted than at synchrotron sources. Furthermore, either the high incoherent scattering cross sections b_i of some isotopes (primarily ^{1}H, with b_c = –3.74 fm and b_i = 25.27 fm), or their large neutron capture cross-sections (*e.g.* ^{10}B, ^{113}Cd, or ^{155}Gd) severely limits the investigation of some systems. Samples prepared with isotopic substitutions (*e.g.* MOFs with deuterated ligands [224], being b_c = 6.67 fm and b_i = 4.04 fm for ^{2}H, see also Figure 1b, violet full circles) can be used in these cases to increase the quality of the ND data, although further complicating the sample preparation procedure. It is however worth noting that employing the latest generation of high-flux neutron powder diffractometers, operating under optimized collection geometries, the structural determination of H-containing materials without any isotropic replacement is nowadays becoming more common [225]. The final and likely the worst complication, especially from the point of view of the chemical synthesis, is the huge amount of sample required for ND studies: single crystals volumes of several mm^3 and up to grams of powder. In conclusion, X-ray and neutron diffraction are complementary, and their combination offer unique opportunities for the structural characterization of crystalline coordination compounds [226].
Finally, it is worth to remark how diffraction-based techniques are inherently not-element selective methods: the XRD or ND signal derives from the contributions of all the atoms included in the probed volume, weighted by their X-ray atomic form factors or neutron coherent scattering cross-sections. In the XRD case, this limitation can be elegantly bypassed moving to the synchrotron. Indeed, synchrotron sources uniquely allow the energy adjustment of the incident X-ray beam, enabling detailed analysis of the scattering process in proximity of selected absorption edges. Hence, exploiting the resonant (or anomalous) diffraction process, element-specific structural sensitivity can be obtained [138, 227-231]. The relevance of these methods in chemical crystallography will be discussed in more detail in Section 2.7.

2.3 Synchrotron chemical crystallography

Notwithstanding the remarkable progresses done recently by laboratory instruments (see e.g. [232-238]), in conventional chemical crystallography, the use of X-rays from synchrotrons is advantageous with respect to laboratory sources due to two key factors: (*i*) the high flux and brilliance and (*ii*) the energy tunability. As it will be discussed hereinafter, these capabilities have been primarily employed to enable or facilitate conventional XRD analysis on challenging systems (small crystals or/and large unit cell compounds) and to successfully characterize *via* XRPD compounds which structural complexity hampered the refinement from laboratory data.
Furthermore, these unique features have also allowed advanced XRD-based characterization with previously unexplored strategies; two of these specialized methods, *i.e.* charge density analysis and the resonant diffraction will be briefly introduced in the following Sections.
Let us first discuss the impact of the high flux and brilliance from synchrotrons on XRD and XRPD techniques. In general, the use of high intensity X-ray sources is among the most important developments which interested the field throughout the last two decades. In conjunction with the boom in computational power and the widespread introduction of area detectors and efficient systems for low-temperature collection, the enhancement in the intensity of the incoming X-ray beam allowed a remarkable extension of the applicability of single-crystal XRD and XRPD analysis. With respect to lab-scale setups, the introduction of rotating-anode and micro-focusing [239] X-ray tubes

ensured an increase of about 1–2 orders of magnitude in intensity [240]. Conversely, with third generation synchrotrons the X-ray flux was boosted of several orders of magnitude.

The enormous gain in flux is accompanied by the naturally high collimation of the synchrotron emission, due to its relativistic nature. In particular, undulators in third generation storage rings take to the highest level not only flux (measured in photons s^{-1}), but also brilliance (measured in photons s^{-1} mm^{-2} $mrad^{-2}$, thus considering also the spatial and angular radiation distribution) with their emission concentrated is in a narrow cone of half-aperture $1/[\gamma(nN)^{1/2}]$ both in the horizontal and vertical direction, where $\gamma = 1/(1-\beta)^{1/2}$ being β is the Lorentz factor for the oscillating electrons, n in the harmonic order and N the number of the magnet poles [43, 241-244]. For indication, brilliance values in the order of 10^{21}–10^{22} photons s^{-1} mm^{-2} $mrad^{-2}$ 0.1% $bandwidth^{-1}$ are obtained using undulator insertion devices, whereas that displayed by laboratory tubes range from 10^{9} photons s^{-1} mm^{-2} $mrad^{-2}$ 0.1% $bandwidth^{-1}$ (for stationary anode tubes) up to 10^{12} photons s^{-1} mm^{-2} $mrad^{-2}$ 0.1% $bandwidth^{-1}$ (for a rotating anode with micro-focusing) [45].

As reviewed in details in the perspective article by Clegg [240], these properties perfectly meet the increasing demand coming from some of the growing areas of coordination chemistry, including microporous materials and supramolecular assemblies. With respect to single crystal XRD, it is interesting to note how diffraction intensities obtained at a given incident X-ray wavelength are (approximately) proportional to $I_0 \cdot \lambda^3 \cdot [V_{crystal}/V_{cell}^2] \cdot \Sigma_i f_i^{\,2}$, where I_0 and λ are the incident X-ray intensity and wavelength, $V_{crystal}$ and V_{cell} the volume of the probed crystal and of the crystallographic unit cell, respectively, and $\Sigma_i f_i^{\,2}$ is the sum of the squared X-rays form factors extended to all the atoms in the unit cell. Then, reduced crystal dimensions and/or large unit cell cause weak diffraction spots, complicating the XRD analysis. Unfortunately, the research areas mentioned before are affected by both the criticalities. Coordination polymers, MOFs and many other fascinating supramolecular architectures are inherently large-unit-cell systems, often including disordered portions (crystallization solvent molecules, guest species [245], template molecules for cavities, …). Moreover, these coordination compounds are often difficult to crystallize in specimens of suitable size to be analysed with conventional laboratory diffractometers. As evident from the previously reported expression, the I_0 values attainable at synchrotrons balance reduced values of $V_{crystal}$ and/or the increased values of V_{cell}. At synchrotrons, high-quality patterns can be obtained also from micrometric crystals, in particular when their unit cells contain high-Z atoms enhancing the scattering intensity thorough the $\Sigma_i f_i^{\,2}$ term.

As anticipated, synchrotron radiation offers also specific advantages for XRPD analysis, such as the high 2θ resolution [246-254], allowing to reduce overlap problems and to tackle high-complexity compounds which are difficult or impossible to crystallize with sufficiently large $V_{crystal}$ to allow single crystal data collection. With the outstanding X-ray fluxes available at synchrotrons, a much more accurate wavelength selection can be afforded maintaining optimal acquisition statistics: wavelength resolution $\Delta\lambda/\lambda$ better than 2×10^{-4} is routinely employed. Such a spectral resolution for the incident X-ray probe drastically reduces the monotonous increase observed in the XRPD peak widths with 2θ. Furthermore, the high degree of collimation of synchrotron radiation, remarkably higher than the most performing lab-scale setups, results in a substantial reduction of the low-2θ angular spread, commonly affecting laboratory XRPD patterns due to inaccurate focusing geometry at low diffraction angles. The combination of these two effects allows to greatly improve the angular resolution of the XRPD data. In addition, the high-incident flux ensures a better counting statistics and thus a better S/N ratio. The interested reader can find a technical discussion on this topics *e.g.* in the International Tables for Crystallography [255], and references therein.

A major limitation of laboratory-scale diffractometers is the discrete character of the probe wavelength, which can be selected among a few possibilities, depending on the anode of the X-ray tube. The most used X-ray emission lines are Cu-K_α (λ = 1.54184 Å) and Mo-K_α (λ = 0.71073 Å), but Cr, Fe and Ag targets are also commercially available. Conversely, working with synchrotron radiation, the incident wavelength can be easily selected from a wide continuous spectral output, although with differences in the correspondent flux related to the features of the source and of the beamline monochromator and optics.

This possibility has been a breakthrough in macromolecular crystallography for multi-wavelength anomalous dispersion (MAD) phasing and it is exploited in chemical crystallography for advanced anomalous (or resonant) experiments, aiming to make XRD an element-selective or even oxidation state-selective technique. We will discuss this kind of specialized methods in Section 2.7, whereas here we will summarize the advantages related to the energy tunability with respect to conventional XRD or XRPD applications. Depending on the nature of the probed structure, specific benefits can be achieved using longer or shorter wavelengths for the incident X-ray beam, as discussed in details *e.g.* in ref. [240]. In brief, samples with large unit cells generally give more intensity and a better angular resolution in their diffraction patterns when probed with longer-wavelength X-rays. Conversely, the use of a shorter wavelength helps to reduce absorption and extinction effects, which induce systematic errors in the collected patterns. Furthermore, when shorter-wavelengths X-rays are employed, the diffraction pattern is compressed in a smaller angular spread, allowing to increase the number of overlapped reflections in the angular resolution of the instrument.

Oppositely to what is deliberately searched in anomalous experiments, the tunable wavelength enables to avoid the absorption edges of the elements included in the sample, thus reducing background fluorescence to improve the

peaks/background ratio in the diffraction patterns. This problem commonly affects laboratory diffraction patters collected with Cu-K_α radiation (~ 8027.84 eV) on Fe-rich samples (due to location of Fe K-edge at ~ 7112 eV). Using a synchrotron setup, the energy of the incident X-ray beam can be finely tuned just before the Fe K-edge, thus avoiding to excite X-ray fluorescence from Fe atoms. An equivalent strategy was for instance employed by Marra *et al.* [256] to collect high-quality XRPD patters on dehydrated Na-Rb-Y zeolite. Here, the use of synchrotron radiation (beamline BM16 at the ESRF) for XRD allowed the optimization of the incident X-ray wavelength, adjusted at 0.84973(1) Å, just longer than that of the Rb K-edge (~ 0.816 Å). The remarkable data quality achieved with synchrotron XRPD allowed the localization of 2.9(6) Na^+ cations very close to 22.4(6) Rb^+ in the site SII of the faujasite framework, which would has likely escaped detection from the refinement of conventional laboratory data.

2.3.1 X-ray charge density analysis: from geometry to valence electron density

In conventional X-ray crystallography the target is the determination of the basic geometrical structure, under the assumption of element-specific spherical X-ray form factors. In this sense, diffraction is a purely structural technique, and has to be complemented by other methods if additional information on the electronic structure of the probed compound is required (see Section 3). However, a sophisticate analysis of high-resolution diffraction data can provide information on the valence electron density distribution, including both bonding and not bonding contributions (*e.g.* lone pairs). Such a method, commonly referred to as charge density analysis, yields detailed insights in the nature of chemical bonding, beyond the elucidation of the basic atomic connectivity. A detailed discussion of the principles and methodologies of experimental charge density analysis and of the related theoretical modelling strategies can be found in the broad specialized literature [245, 257-264]. Nonetheless, due to the increasing contribution of the method to the field of coordination chemistry, a brief discussion is deserved, with an emphasis on the advantages of synchrotron data collection.

Qualitative information is firstly obtained by considering the so-called electron-density deformation maps, obtained calculating the difference between the experimental density and the model charge density calculated from a superimposition of spherical atoms, both determined by Fourier summation. A more sophisticated quantitative analysis consists in the fitting of experimental structure factors with core functions and an atom-centred expansion of multipolar (spherical harmonic) valence-density functions [265, 266]. In this approach, thermal effects are separately accounted by independent terms. From the fitting, it is possible to extract and plot the *deformation* density and also the *static* total model density, commonly employed in topological analysis to provide detailed information on chemical bonding.

It is evident that a much larger number of parameters is needed to reliably model the valence electron density with respect to standard XRD refinements. In addition, particular attention has to be put in the deconvolution between valence contributions and non-spherical distributions of the thermal displacements for the atoms involved. On the experimental ground, to meet these requirements very low-temperature collection is mandatory and high-quality diffraction patters have to be collected up to q-values significantly higher than for conventional structural refinement, to enhance as far as possible the R-space resolution of the dataset, see Section 2.2.

It is worth noting how high-Z metal centres, ubiquitously present in coordination chemistry, are intriguing but challenging targets for charge density analysis. Indeed, when high-Z atoms are involved, much more precise data have to be obtained. Indeed, for heavy atoms, the relative weight of the valence contribution to the total scattered intensity is significantly reduced with respect to that coming from core electrons. This experimental complication runs parallel to difficulties in theoretical modelling [261, 263], for instance due to the closely spaced energy levels in open-shell transition metal complexes, requiring a multi-configurational approach in the computation of the electronic structure. In addition, as evidenced by Macchi and Sironi [267] for a series of binuclear and polynuclear transition metal carbonyls complexes, metal–metal bonding and metal–ligand bonding in these systems are hardly interpreted by the sole one-electron density, and computation of two-electron density in conjunction with specific topological indicators is also required.

On these bases, it can be easily envisaged how synchrotron data collection is particularly advantageous for charge density analysis applications on coordination compounds [240]. The method has been initially conceived and it is still applied using laboratory data. However, even using the shorter-wavelength sources (*e.g.* Mo-K_α or Ag-K_α) to compress the pattern, the sampled q-range is still limited and collection is very time consuming. With laboratory setups, the acquisition of a suitable dataset for the most demanding high-Z compounds can require up to several weeks, due to the limited incident flux and the damping of XRD signal in the high-q region. Short-wavelength and high-intensity X-ray beams from synchrotrons, coupled with efficient area detectors, can greatly speed up the measurements, and improve the data quality, reducing systematic errors from absorption and extinction effects. The use of synchrotron setups fostered the application of this advanced approach to several metal complexes, even containing very heavy atoms, such as Th [268]. Charge density analysis for instance employed to investigate agostic interaction in metallocenes [269] or chemical bonding of dioxygen metal complexes [270].

More complex molecular architectures, including polynuclear metal clusters and coordination polymers have been also investigated by charge density analysis of synchrotron XRD data; a thorough literature review focusing on

synchrotron applications up to 2005 has been provided by Coppens *et al.* [259]. As an example, Figure 2 reports some recent findings on Co-based coordination compounds of increasing structural complexity. Overgaard *et al.* for instance thoroughly investigated the alkyne-bridged dicobalt complex $Co_2(CO)_6(HC{\equiv}CC_6H_{10}OH)$ [271], which is an excellent test cases for experimental electron density modelling due to its peculiar bounding properties (see Figure 2a). In addition, topological analysis of static deformation density maps obtained from multipole modelling of 16 K synchrotron XRD data on the $Co_3(C_8H_4O_4)_4(C_4H_{12}N)_2(C_5H_{11}NO)_3$ coordination polymer (see Figure 2b) contributed to clarify its magnetic properties [272]. In particular, no direct metal–metal interaction was observed, thus suggesting that the magnetic ordering in this latter compound is most likely due to super-exchange phenomena. All the metal–ligand bonds showed a closed-shell type, except the Co1–O1 and the Co–O11 bonds, which displayed evident covalent contributions, which could play a key-role as mediators of the magnetic ordering.

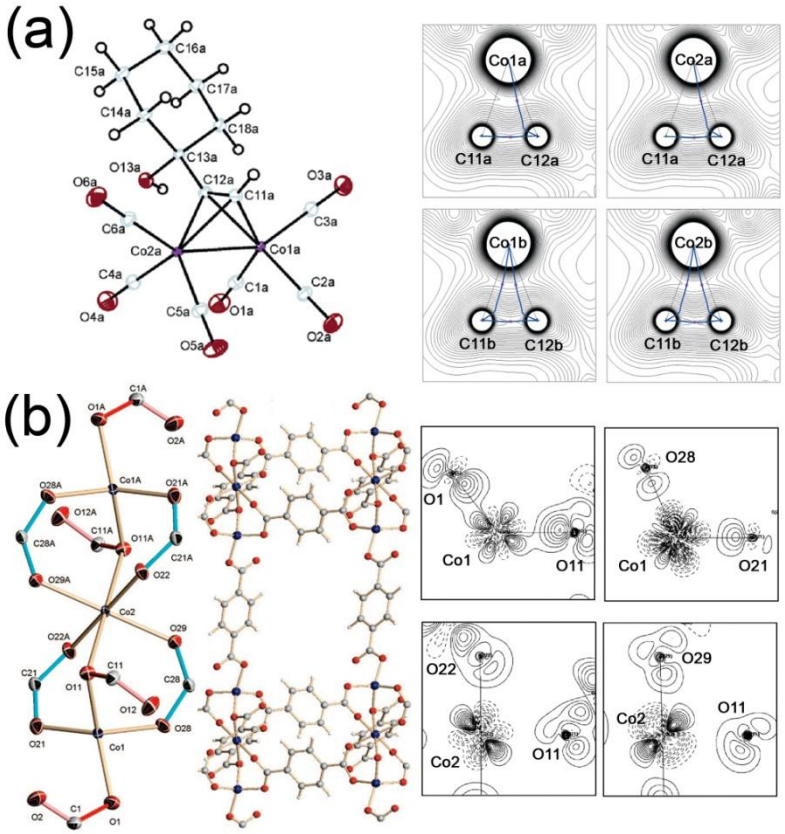

Figure 2. Examples of recent findings on metal bonding in Co-based coordination compounds of increasing structural complexity from charge density analysis of synchrotron XRD data. (a) Charge density analysis of an alkyne-bridged dicobalt complex, namely $Co_2(CO)_6(HC{\equiv}CC_6H_{10}OH)$ [271]. Left panel: structure of the complex based on the synchrotron XRD data. The thermal ellipsoids for non-hydrogen atoms are shown at the 90% probability level. Right panel: charge density in the four Co–C–C planes of the complex, obtained from 15 K synchrotron XRD data. The contour intervals are 0.1 e^- $Å^{-3}$. Adapted with permission from ref. [271]. Copyright (2008) American Chemical Society. (b) Charge density analysis of the $Co_3(C_8H_4O_4)_4(C_4H_{12}N)_2(C_5H_{11}NO)_3$ coordination polymer. Left panel: coordination of three Co atoms in the chain and resulting structure of the coordination polymer viewed along the *b*-axis of the unit cell. The thermal ellipsoids are drawn at a 90% level, and the solvent molecules have been omitted for clarity. Right panel: static deformation density maps of in four planes containing the Co centres, obtained from multipole modelling of 16 K synchrotron X-ray diffraction. The contour interval is 0.1 e^- $Å^{-3}$, with solid contours being positive and dashed contours negative. Adapted with permission from ref. [272]. Copyright (2008) American Chemical Society.

2.3.2 Time-resolved diffraction studies with synchrotron beams

For all classes of samples measurable by laboratory instruments, the much higher photon flux available at synchrotron radiation sources and the availability of new position-sensitive area detectors (with small pixel size, high area and fast read-out/erasing dead-times) permit a considerable expansion of the related research areas, making time-resolved diffraction studies possible, with a potential time resolution on the ms timescale in conventional (not pump-and-probe) schemes. This allows moderately slowly-evolving chemical reactions [64, 273-286], solid state phase transitions [247, 287], *in situ* crystallization, re-crystallization processes [288-291], dynamics in biological systems [292] etc..., to be investigated with high accuracy XRPD. Some of the experimental setups employed for these studies were conceived for the simultaneous XRPD/XAS (Sections 2.5) data collection [274, 275, 277-279, 281-283, 293]. This combination allows the investigation of both the long and the short range order and the determination of the metal oxidation state by XANES analysis (Section 3.2.1), that escape detection in standard diffraction experiments.

Single crystal time-resolved studies require a different approach because the sample rotations needed to measure the Bragg reflections in all directions of the reciprocal space with a monochromatic beam would be excessively time consuming. In such cases, time resolution on the ms timescale can be achieved using the polychromatic Laue method [157, 294, 295], that is ideal for synchrotron radiation sources [220, 296] and can be applied with neutrons as well [220]. Typical applications of time-resolved Laue diffraction include photo-activated protein dynamics [297], conformational change in biological macromolecules [141, 220, 296, 298, 299] and determination of minority intermediate structures [296].

An alternative method using the intense white X-ray beam available at synchrotron sources is the energy-dispersive X-ray diffraction (EDXRD) [300-304]. EDXRD works at fixed scattering angle; the *d*-spacings of the diggerent Bragg reflections are determined by measuring the energy (and thus the wavelength) of the diffracted photons with an energy-resolved solid state detector, similar to those used to collect EXAFS data in fluorescence mode (see Section 2.5). The great advantage of the method is the high time resolution, that depends on the readout of the detector (typically in the ms range) allowing phase transitions to be investigated [300, 301, 305-307]. The EDXRD technique finds also interesting applications in the field of high-pressure experiments [302, 308, 309], because the q-interval available using standard "angle-dispersive" XRD setups is limited by the small 2θ opening available using diamond anvil cells. Conversely, the main drawback of the technique is a poor resolution in the *d*-spacing determination because the $\Delta E/E$ of the solid state detectors is not comparable with the $\Delta\theta/\theta$ available in the standard "angle-dispersive" XRD setups.

2.4 Beyond crystallography: accessing short-range order in structural determination

Conventional XRD is tailored to investigate crystalline structures, exhibiting long range order *i.e.* translational periodicity. Relatively small deviations from the perfect periodic arrangement of atoms in the crystal lattice can still be processed within the theoretical system of conventional crystallography, by enlarged Debye Waller factors or partial occupation of lattice sites. However, there is a number of high-impact fields which routinely deal with totally or partially disordered (or better, short-range-only ordered) systems [144, 310]. In many cases, the unperiodical and local structural features are exactly the characteristics which make the system appealing towards technological applications.

Typically, coordination chemistry occurs in the solution-phase, involving *e.g.* homogeneous catalysis, bio-inorganic and medical applications. The structural parameters are influenced to different extents by the solvent-solute interplay [311] (employed solvent, solution concentration, presence of counter ions, …) and in several cases they significantly deviate from the solid-state case. Furthermore, a detailed speciation and structural investigation of ions and complexes in solution is fundamental to clarify their stability and reactivity, gaining a predictive knowledge for novel synthetic routes and applications [312].

Heterogeneous catalysis is another challenging field for structural determination, due to the necessity of isolated catalytic metal sites or nanoclusters well dispersed on high-surface area supports, to enhance the catalytic performances [76, 286, 313-315]. Although highly-crystalline microporous materials such as zeolites [256, 285, 316-318], zeotypes [284, 318] and coordination polymers [318-323] have been developed, where the active sites are incorporated in a well ordered framework, by far most of the heterogeneous catalysts are intractable using traditional crystallographic tools [324].

In addition, more and more complex macromolecular architectures [77, 325-332], possibly self-assembling [333-339], are being synthesized, with a progressive fading of the borders between coordination chemistry and materials science. These systems demand a deep update of our portfolio of structural techniques to appreciate the hierarchic organization of the structural levels, bridging the atomic to the mesoscopic scale.

Finally, the last decade has witnessed a sort of paradigm shift in structural analysis, making things more lively, although more complicated: "chemistry in action" is definitely the present state of the art in characterization. Words such as *time-resolved*, *in situ*, *operando* [340] are year after year proliferating in the literature. The direct structural tracking of slow, fast and ultrafast chemical and photochemical reactions, working catalysts, growth/synthesis processes or phase transitions, triggered by a fine control of external inputs (*e.g.* temperature, pressure, photoexcitation, reagents fluxes, electric and magnetic fields), is far beyond the conventional lab-based crystallography. Here, the boost in brilliance ensured using X-rays from third generation synchrotrons and the versatility of the related setups really made the difference [76, 286, 314, 341].

Obtaining detailed structural information also on short-range and partially ordered systems is today a key-target. In the following Sections we will mention the principal methods to access this kind of information, focusing on the X-ray based strategies more suitable for the investigation of coordination compounds, including XAS spectroscopy (principally EXAFS) and X-ray scattering (XRS) techniques (see Sections 2.5 and 2.6, respectively). We will highlight the key-role of synchrotron sources to fulfil this task, in comparison with laboratory-based strategy, when applicable. Finally, some strategies for *in situ* time-resolved characterization of coordination compounds will be discussed. Here, we will focus on the methods in which the source is employed a continuous fashion (time resolution

down to the ms scale), whereas a detailed discussion of synchrotron ultrafast characterization using pump and probe scheme can be found elsewhere (see *e.g.* refs [148-150, 153, 342-345]).

2.5 EXAFS: a good reason to apply for beamtime

The most obvious association between synchrotrons and structural characterization in coordination chemistry comes certainly from XAS technique, in particular in the EXAFS region. Since the pioneering works of Sayers, Lytle and Stern in the 70s [46, 47, 49], the technique progressively became a well-established alternative/complement to XRD, in particular for those cases where a local and element-selective structural probe is required, primarily amorphous solids, solution phase, liquids, catalytic and biochemical systems [346]. The necessity of a continuously tunable X-ray source with a very high incident flux to resolve the fine structure in the X-ray absorption spectrum makes EXAFS a synchrotron-only method. It is worth noting that for most EXAFS studies, hard X-rays are employed, indicatively from 2 keV onwards. This spectral region includes the K-edges (ejection of a 1s core electron) for elements up to the second row of the transition elements, and the L-edges (ejection of a 2s or 2p core electron) for the lanthanides and beyond, for which K-edge EXAFS collection would be unpractical (see Figure 3a for some examples).

EXAFS analysis is currently the key-method to elucidate the local structure around the metal centres in solution [27, 92, 93, 312, 347-357]. Analogously, the elemental selectivity of the technique is a remarkable advantage whenever one is interested in the closer coordination environment of dispersed catalytically- [65, 76, 358, 359] or biologically-active [78, 107-109, 111, 360-367] sites. In general, EXAFS is a turning point for any system which in its as-synthesized state or upon specific treatments shows site-specific short-range order, escaping structural determination *via* XRD.

In the framework of this overview on the available methods for structural determination, we will introduce the technique principles, with an emphasis on the attainable structural information of interest for a coordination chemist. For the physics that is beneath, and for a detailed discussion on theoretical background, experimental setups, acquisition and analysis strategies we refer to the several dedicated textbooks [368-372], book chapters [213, 371, 373-378] and recent literature reviews [54-56, 76, 78, 90] on the topic. A brief description of the most relevant concepts and related equations is reported in the appendix (Section 6).

The technique consists in the collection and analysis of the X-ray absorption coefficient $\mu(E)$ as a function of the energy E of the incident X-ray photons, probing the region immediately after an absorption edge (at energy E_0) of one of the elements contained in the sample, the "absorber" atom, typically up to 1000 eV after the edge. Here, if the absorber is surrounded by neighbours atoms, the spectrum is characterized by subtle oscillations, modulating the monotonically decreasing atomic-like background $\mu_0(E)$ (see Figure 3d).

Oversimplifying a sophisticate piece of quantum mechanics, the photoelectron, once it has been extracted from a core level of the absorber, diffuses as a spherical wave, which is back-scattered by the surrounding shells of neighbour atoms. In this picture, the fine structure in the $\mu(E)$ profile originates from the interference between the different back-scattered wavefronts: the phenomenon can be substantially assimilated to the electron diffraction case. The EXAFS oscillations can be thus related to a specific spatial arrangement of the atoms in the local environment of the absorber, using the FT operation to bridge the photoelectron wavevector space (k-space, where k is directly proportional to the square root of the photoelectron kinetic energy, $k = (1/\hbar)\ [2m_e(E - E_0)]^{1/2}$) to the r-space. The use of the keyword "local" is fully justified primarily by the short free-mean path of the photoelectron in matter and, in addition, by the damping effect of the core-hole lifetime: EXAFS sensitivity is limited in the most ordered cases to a sphere of 5−10 Å radius from the absorber [89, 379-387]. However, when the technique is applied to more disordered systems, it can result just in the determination of the first coordination shell [388-395].

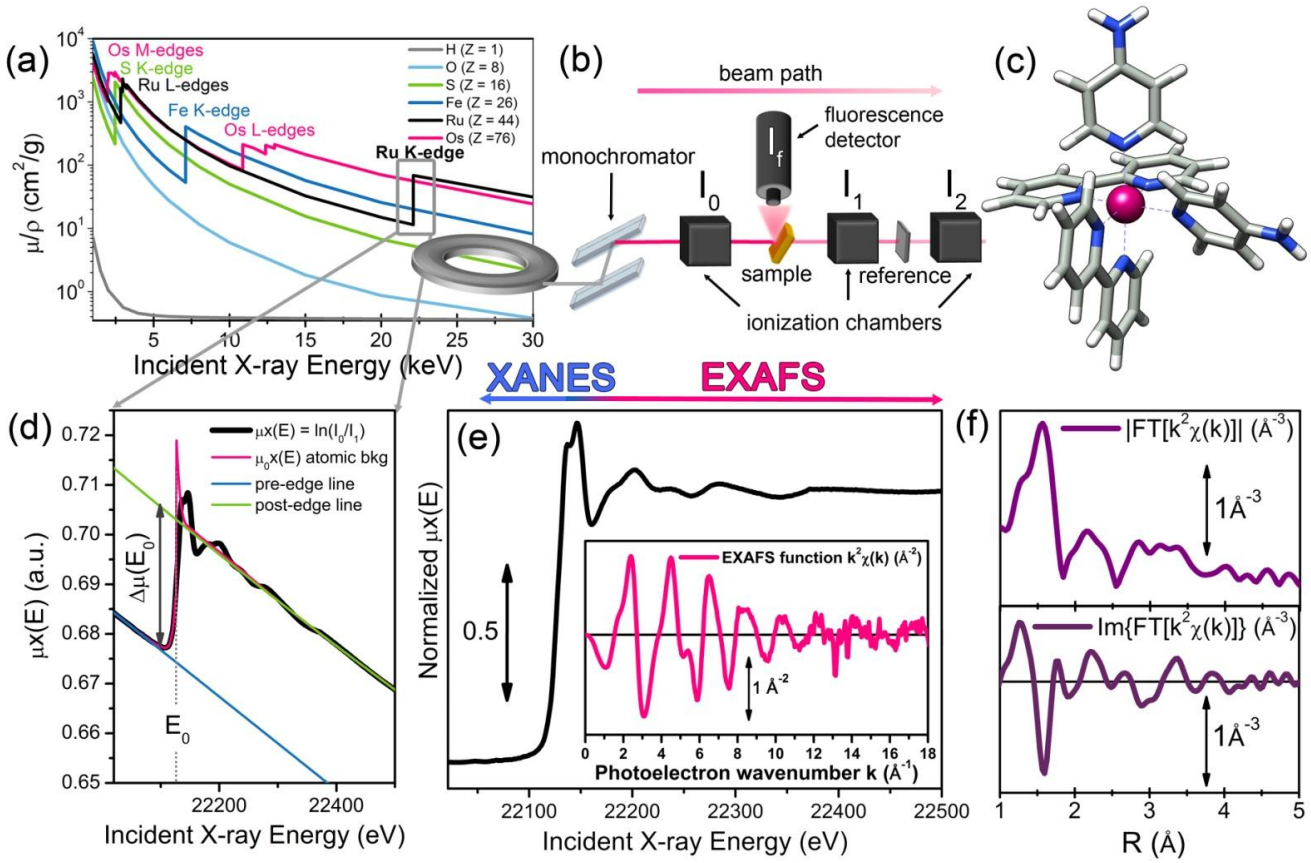

Figure 3. (a) X-ray absorption coefficient $\mu(E)/\rho$ (where ρ is the sample density) as a function of the incident X-ray energy E, in the 1–30 keV range, for a selection of elements commonly found in coordination compounds ($\mu(E)/\rho$ can be approximately expressed as: $\mu(E)/\rho \sim Z^4/AE^3$, where Z the atomic number and A the atomic mass of the element of interest). In particular, $\mu(E)/\rho$ is reported for three "light" atoms, *i.e.* H (Z = 1), O (Z = 8), and S (Z = 16) and three metals belonging to the 1st, 2nd and 3rd row of the transition metal series, *i.e.* Fe (Z = 26), Ru (Z = 44), and Os (Z = 76). The X-ray absorption edges encountered in the reported range are indicated for each element. Data obtained from NIST: http://physics.nist.gov/PhysRefData/XrayMassCoef/tab3.html. Note the logarithmic scale of the ordinate axis. (b) Schematic representation of a typical experimental setup for XAS measurements: I_0, I_1, and I_2 are ionization chambers, I_f indicates a fluorescence detector. (c) Molecular model of the complex $[Ru(bpy)_2(AP)_2]^{2+}$ (bpy = 2-2′-bipyridyne; AP = 4-amminopyridine). Atom colour code: Ru, pink; N, blue; C, grey; H, white. (d) Ru K-edge XAS spectrum (black thick line) for the $[Ru(bpy)_2(AP)_2]^{2+}$ complex shown in part (c), in water solution (10 mM concentration), collected in transmission mode at the BM29 beamline of the European Synchrotron Radiation Facility (ESRF, Grenoble, France) [396]. In the Figure are also reported: pre-edge (blue) and post-edge (green) lines (obtained by fitting the experimental data with two polynomial functions in suitable pre- and post-edge energy intervals) required to estimate the edge-jump $\Delta\mu(E_0)$ for normalization of the raw spectrum; atomic-like background $\mu_0(E)$ (pink solid line), employed in the extraction of the EXAFS oscillations, see part (e). (e) Normalized XAS signal for $[Ru(bpy)_2(AP)_2]^{2+}$ obtained from the raw data reported in part (d). The inset shows the extracted k^2-weighted $k^2\chi(k)$ EXAFS function obtained by subtracting the absorption signal expected for an isolated atom, labelled as $\mu_0(E)$ in part (d), and converting the E-values in k-values using the expression $k = (1/\hbar)\,[2m_e(E - E_0)]^{1/2}$. (f) R-space EXAFS spectra obtained by calculating the FT of the $k^2\chi(k)$ spectrum reported in the inset of part (e) in the 2–16 Å^{-1} k-range; both modulus (top part) and imaginary part (bottom part) of the FT are reported. Unpublished Figure, reporting data published in ref. [396].

On the experimental ground, a schematic representation of the basic setup for XAS measurements is reported in Figure 3b. As discussed in more details elsewhere [76, 89-91], the most common detection schemes include transmission and fluorescence modes, although other alternative exists *e.g.* electron yield and optically-detected modes (see Scheme 6 in the appendix and Section 6.1 for a representation of these different products of the X-rays/matter interaction). All these detection schemes, in their standard implementation, involve a point-by-point building of the XAS spectrum, repeating the following steps until all the required energy points have been probed: (*i*) a specific energy E is selected using a monochromator from the white spectrum extracted *e.g.* from a bending magnet; (*ii*) the X-ray absorption coefficient of the sample is measured at energy E; (*iii*) the energy is moved to the subsequent value $E + \Delta E$.

In transmission mode, the absorption coefficient at fixed energy E is obtained by measuring the intensity of the X-ray beam before the sample (I_0) and that transmitted after the sample (I_1), typically using two ionization chambers filled with a gas mixture tailored to the energy range of interest. Once I_0 and I_1 have been determined, $\mu x(E)$, where x is the sample thickness, can be simply derived from the Lambert Beer law, being $\mu x(E) = -\ln(I_1(E)/I_0(E)) = \ln(I_0(E)/I_1(E))$.

Usually, a reference sample (*e.g.* a metal foil of the same element selected as the absorber in the XAS experiment) is positioned after the I_1 ionization chamber, followed by a third ionization chamber along the beam path (labelled as I_2 in Figure 3b). In such a way it is possible to simultaneously acquire the XAS spectra for both the sample and the reference (using the I_1 and I_2 outputs) and employ the latter for an accurate energy calibration of the sample spectrum [76, 397].

Although the transmission mode is the most direct and accurate way to collect a XAS spectrum, it is not applicable in several cases, due for instance to an excessive dilution, or, conversely, to the necessity of measuring a thick or supported specimen. Here, fluorescence detection often represents a practical alternative. Working in fluorescence yield, the incident intensity is still detected by using the I_0 ionization chamber, whereas a multi-element semiconductor detector (I_f in Figure 3b) is employed to collect the X-ray fluorescence photons emitted as a secondary effect of photoelectrical absorption, when the core hole is filled by one electron from the outer levels. Assuming a linear response of the fluorescence detector, $\mu x(E)$ is proportional to the ratio $I_f(E)/I_0(E)$, from which the sample absorption coefficient is evaluated.

Figure 3d reports as an example the Ru K-edge XAS spectrum in transmission mode for the $[Ru(bpy)_2(AP)_2]^{2+}$ complex, where AP = 4-amminopyridine (the complex structure is shown in Figure 3c), measured in water solution (10 mM concentration) at the BM29 beamline of the European Synchrotron Radiation Facility (ESRF, Grenoble, France) [396]. XAS spectra are routinely normalized to the edge jump $\Delta\mu(E_0)$ (indicated in Figure 3d), to obtain data which are independent from specific experimental conditions such as sample thickness, absorber concentration, or detector/amplifiers settings (see Figure 3d). Normalized spectra can thus be easily compared to other data, regardless of the measurement conditions, or to theoretical simulations.

The analysis of the EXAFS spectra is performed primarily in *k*-space, after "extraction" of the oscillatory part of $\mu(E)$ by subtraction of the atomic-like background $\mu_0(E)$ from the normalized XAS spectrum, resulting in the determination of the EXAFS function $\chi(E)$. The latter is then simply converted in $\chi(k)$ using the above-mentioned relation $k = (1/\hbar)[2m_e(E - E_0)]^{1/2}$ (see the inset of Figure 3e). Hence, the $\chi(k)$ function can be related *via* FT to a specific spatial arrangement of atomic neighbours in the local environment of the absorber, bridging *k*-space to *r*-space, where the different coordination shells are more easily visualized, *e.g.* as maxima in the modulus of the FT (see Figure 3f).

Let us now focus our attention on the extraction of structural parameters from the EXAFS analysis. With this respect, a useful parametrization of $\chi(k)$ is provided by the so-called the EXAFS equation [46-49], which models the EXAFS function as a sum of sinusoidal waves where phases and amplitudes depend on the type of atoms and on their distribution around the absorber, and related to a series of valuable structural parameters (see Section 6 6.3). In brief, the fitting of the EXAFS spectra on the basis of a guess model structure allows, for each shell of neighbours included in the analysis, an accurate refinement of some parameters of key importance in structural coordination chemistry: (*i*) coordination number and kind of atomic neighbours; (*ii*) average bond distances, with typical uncertainty in the order of few hundredths of Å, slightly higher, but still competitive with XRD analysis (note however, than when particular experimental conditions are available, using the differential approach to analyze the data, the relative variation of the first shell distance can be determined with an accuracy as good as one fm, *i.e.* 10^2 times more sensitive than that normally available [398, 399]); (*iii*) Debye-Waller (DW) factors accounting for thermal vibrations along the absorber atom – neighbour atom bond and static structural disorder. Having access to these pieces of information, with limitations remarkably less severe than for diffraction experiments on the sample features (solutions, powders, …) and dilution (a 5% *wt* of the absorber species can be indicatively assumed as the lower limit for satisfactory EXAFS quality in transmission mode, but concentration as low as a fraction of % can be measured in fluorescence mode), is definitely an excellent reason to apply for beamtime at synchrotron facilities, despite their limited accessibility. It is worth anticipating that the same spectrum contains, although in a different energy range (the XANES region, indicatively from few tens of eV before up to a hundred eV after the edge, see Figure 3e in this Section, and following Sections 3.1 and 3.2.1), also specific information on the absorber electronic structure, allowing combined structural/electronic determination in the same measure.

Despite these appealing capabilities, also EXAFS has some weak spots. Similarly to the X-ray elastic scattering, the photoelectron back-scattering process occurs mainly *via* interaction with the surrounding electron clouds (see *e.g.* refs [400, 401] for a detailed discussion on the photoelectron back-scattering amplitudes and phase shifts as a function of the atomic number of the back-scattering atom). Therefore, EXAFS suffers of similar limitations as XRD in the location of light elements and in the discrimination of almost iso-electronic atomic neighbours. As in XRD experiments, the resolution in structural determination by EXAFS and the quality achievable in the data fitting procedure depend on the extension of the sampled *k*-space. Unfortunately, the EXAFS oscillations are progressively damped as *k* increases, due to the thermal effects modelled by DW factors, causing an intrinsic reduction of the S/N ratio. With this respect, ramping up of the acquisition time as *k* increases and k^n-weighting (typically $n = 2$ or 3) to enhance the S/N ratio of the oscillatory structure in the high *k*-region are commonly applied in the EXAFS data collection and analysis.

In addition, the standard EXAFS equation [46, 47, 49] relies on the single-scattering (SS) approximation, *i.e.* only two-body scattering paths (absorber − shell of equivalent neighbours) are considered. This implies a 1D structural determination (bond distances, but not bond angles), carrying out the same level of information of radial PDF functions $g(r)$, but in an element-selective way, *i.e.* including only the atomic pairs which contains the absorber species (Section 2.6). However, the photoelectron can be involved also in many-body multiple-scattering (MS) processes, which contribution to the total EXAFS signal decreases as either the photoelectron energy or the number of "legs" increases. The full MS regime hence dominates the energy region just after the edge, on the borderline between the XANES region and the low-*k* portion of the EXAFS spectrum (sometimes referred to as XAFS). Interestingly, MS amplitudes are strongly influenced by the angles formed by the involved atoms. For instance, for three-body paths, the higher contributions are observed in correspondence of collinear configurations, and rapidly fall down as the angle between the absorber and the two scatterers decrease below 140° [363]. Hence, high-quality EXAFS spectra, extracted paying special attention to the low-*k* signal, can be fitted including also MS contributions to obtain additional information on bond angles and, in some fortunate cases, to refine the full 3D structure of the first few coordination shells [363, 376, 402-404]. Nevertheless, the SS-approach remains very useful for a preliminary screening of possible alternative models, before a more sophisticated MS analysis, or in cases where the complexity in the coordination geometry is excessive to aim at 3D structural reconstruction. It is worth noting how the impressive developments in quantitative simulation of XANES region currently allow to fully exploit its enhanced angular sensitivity [53, 405-409]. In this sense, also XANES, which is conventionally pictured as an electronic spectroscopy, can be regarded as a "structural" method: although more theoretically- and computationally-demanding with respect to EXAFS, XANES modelling can provide highly accurate 3D determination of the absorber coordination geometry.

It is worth to note that EXAFS-like signals are also detected using other techniques, including for instance total scattering analysed using the pair distribution function (PDF) approach (Section 2.6). Alternatively, EXAFS-like spectra can be obtained using modern transmission electron microscopes (TEM) equipped with an electron energy-loss spectrometer [410-415], with a technique usually referred to as extended energy-loss fine structure (EXELFS). Although this method allows to achieve the nm-spatial resolution typical of TEM instruments (2−3 order of magnitude better that what can be obtained with X-ray microscopies [90, 156, 416, 417], the necessity of working in ultra-high vacuum conditions and with sample thickness of few tens of nanometers limits its application to coordination chemistry.

2.5.1 EXAFS and XRD: exploring structural features at short and long range scales

In this Section we will add some considerations on the interplay between EXAFS and XRD/XRS methods, proposing a case-study dealing with MOFs characterization. In particular, the global/local nature of the information obtained by XRD and EXAFS is well exemplified by the structural characterization of UiO-66 MOF in its as-synthesized and desolvated forms, recently achieved by combining the two techniques.

This MOF and its iso-structural analogues, UiO-67 and UiO-68, have attracted great research attention due to their exceptional stability at high temperature/pressure and in presence of different acid and basic solvents [418, 419], properties that make UiO-66-68 among the most promising materials for practical applications. The parent UiO-66 compound has been obtained connecting $Zr_6O_4(OH)_4$ inorganic cornerstones with 1,4-benzene-dicarboxylate (BDC) linker units. The inorganic cornerstones of the as synthesized material are perfect octahedra (see Figure 4a, left models), with 6 equivalent Zr at their vertexes, 12 equivalent Zr–Zr_1 sides (R_{M1} bond distance) and 3 equivalent and Zr–Zr_2 diagonals (R_{M2} bond distance). In the resulting framework, each Zr-octahedron is 12-fold connected to adjacent octahedra, thus ensuring an enhanced stability with respect to other MOFs (Figure 4b). During desolvation, each cornerstone of the UiO-66 MOF evolves from $Zr_6(OH)_4O_4$ to Zr_6O_6 [419] with the release of two H_2O molecules (see Figure 4a, right models), as also observed for other iso-structural compounds of the UiO-66-68 family [420-422].

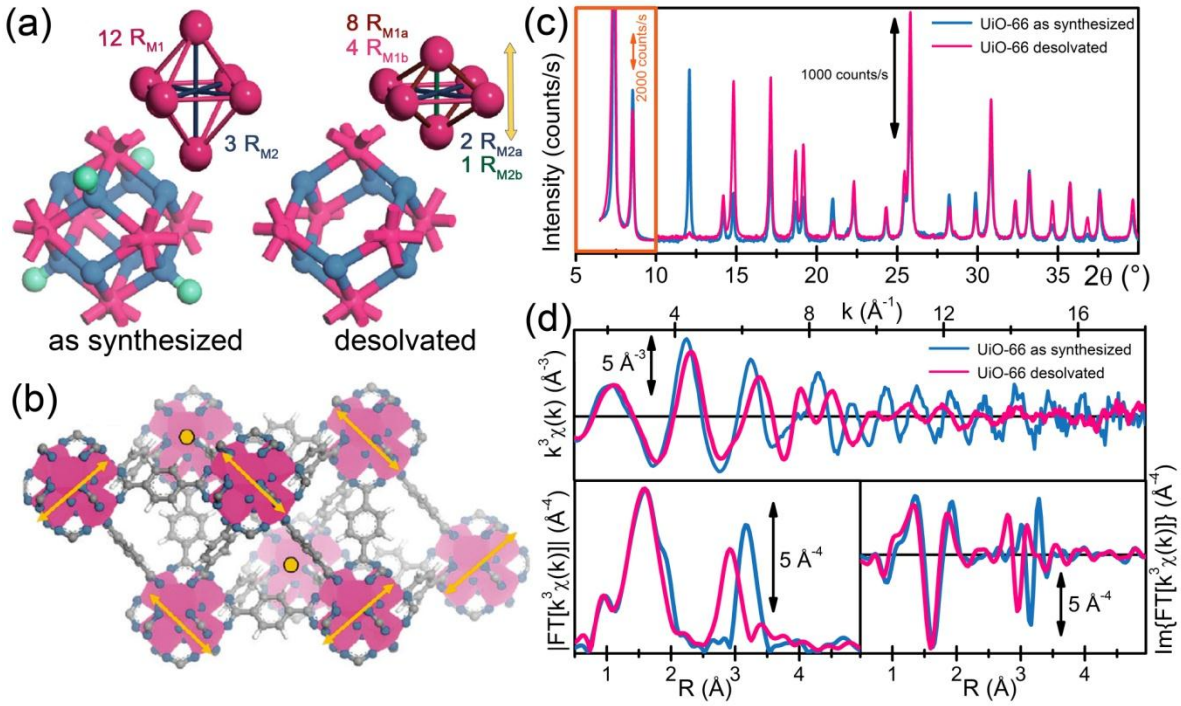

Figure 4. (a) Model of the effects of de-hydroxylation process on the UiO-66 $Zr_6O_4(OH)_4$ cornerstone (perfect octahedron with 12 equivalent R_{M1} sides and 3 equivalent R_{M2} diagonals), resulting in a distorted Zr_6O_6 cluster (squeezed octahedron, where both sides and diagonals split in two groups of equivalent distances, 12 R_{M1} → 8 R_{M1a} + 4 R_{M1b} and 3 R_{M2} → 2 R_{M2a} + 1 R_{M2b}). Magenta, blue and cyan colours refer to Zr, O and H atoms, respectively. In the top insets O and H atoms have been omitted for clarity. (b) Structure of the desolvated UiO-66 MOF, including one octahedral super-cage and two adjacent tetrahedral super-cages. Zr, O, C, and H atoms are represented in magenta, blue, grey, and white, respectively. The squeezing direction randomly coincides with one of the three diagonals of each Zr_6O_6 octahedron, and it is indicated by yellow arrows (or yellow points representing arrows pointing out of the page). (c, d) Effect of desolvation on UiO-66 observed by XRD and EXAFS (as-synthesized UiO-66, blue curves; desolvated UiO-66, at 300 K, in vacuo, magenta curves). (c): XRPD data collected with λ = 1.5406 Å. The patterns in the 10–40° 2θ-region have been amplified by a factor 4. (d) k^3-weighted *k*-space (top panel) and *R*-space (bottom panels, phase-uncorrected FT magnitude and imaginary part are reported in left and right part, respectively) EXAFS spectra. Adapted with permission from ref. [419]. Copyright (2011) American Chemical Society.

Valenzano *et al.* [419] have investigated the structural modifications undergone by the UiO-66 MOF after the desolvation process, resulting in the de-hydroxylated compound. Both XRPD and EXAFS were applied, in combination with density functional theory (DFT). Figure 4c shows the XRPD patters collected before and after the activation process. The two patters are remarkably similar: except for a significant intensity increase of the basal reflections, related to the removal of the electron density inside the framework pores [284, 285, 423], the position and intensity of the Bragg peaks remain substantially unchanged. As represented in Figure 4d, EXAFS points out a remarkably different situation: although the first coordination shell (Zr–O SS paths) is only slightly perturbed, the second shell signal shows pronounced modifications, which suggest an important splitting on the R_{M1} distances corresponding to the sides of the octahedral units. On the quantitative ground, the EXAFS spectrum of the hydroxylated MOF was successfully fitted using as starting guess the structure determined from the Rietveld refinement of the corresponding XRPD patterns. Conversely, it was impossible to achieve a satisfactory fit of the EXAFS data collected for the desolvated UiO-66 using the XRPD-based guess structure, refined within the highly symmetric *Fm-3m* space group.

This discrepancy between XRD and EXAFS response highlights how the de-hydroxylation process promotes a local structural distortion of the Zr-octaedral units, accompanied by a lowering in the coordination symmetry around the metal centres. In particular, EXAFS analysis assisted by period calculations performed with CRYSTAL code [424] at DFT level of theory, demonstrated a compression of the Zr_6O_6 octahedra in the desolvated MOF, occurring along a direction which randomly corresponds to one of the three diagonals. The squeezing results in the shortening of 8 of the 12 sides and the elongation of the other 4 sides (indicated respectively as R_{M1a} and R_{M1b} distances in Figure 4a, right model), clearly reflected by the shortening and splitting of the second shell EXAFS signal. Although much less evident in the EXAFS data plotted in Figure 4d, the erosion of the weak signal at ca. 4.17 Å in the FT magnitude spectrum is consistent with the splitting of diagonal R_{M2} bonds in two longer R_{M2a} and one shorter R_{M2b} distances and was clearly quantified in the analysis of the data. The random character of the distortion, occurring for all cornerstone units but without preferential orientation, causes the failure in its detection by XRPD. Conversely, focusing on the

local Zr coordination environment, the same experimental EXAFS spectrum is detected independently on which, out of the three diagonals, corresponds to the squeezing direction.
In conclusion, the example discussed so far highlights the high complementary character of structural information provided by EXAFS and XRD: a tight interplay between the two methods, possibly assisted by computational modelling, can be greatly helpful in to clarifying the structure of the most complex supramolecular architectures.

2.5.2 Time resolved EXAFS for *in situ* characterization

The conventional applications of XAS in the EXAFS region are related to steady-state characterization. For most of the chemically-relevant processes (those which reaction speed cannot be slowed down to the few-hours timescale [386, 387]) the standard acquisition schemes are not suitable to monitor the structural dynamics as the reaction proceeds in a controlled sample environment. Nevertheless, coupling the element-selectivity of EXAFS with a time-resolution which enable to follow *in situ* the structural dynamics in the local coordination environment of the absorber is a very attractive opportunity, with profound implications *e.g.* in catalysis, chemical synthesis and materials growth. For this reason, specialized experimental schemes has been proposed which allow sub-second EXAFS collection.
The standard experimental setup for EXAFS previously described (see Figure 3b for a schematic representation) works in step-scan mode, with acquisition times in the order of thousands of seconds. EXAFS spectra are collected by integrating for time interval Δt, adjustable to meet the specific experimental necessities, the counts on the detectors $I_0(E)$ and $I_1(E)$ (or $I_f(E)$ if fluorescence detection mode is employed) while maintaining the monochromator at the fixed energy E. After Δt, the data collection is paused until the monochromator has moved to the next energy point ($E + \Delta E$), where ΔE is the programmed energy step. This sequential procedure is repeated for all the required energies, with dead times in the collection while adjusting the incident energy. The overall integration time required for a satisfactory S/N ratio up to high k-values ranges from few tens of minutes to some hours, depending on the sample properties and to the target resolution in structural determination. With this respect, the smallness of the amplitude of the EXAFS oscillations is a serious barrier, possibly requiring data with a S/N ratio in the order of 10^{-4}: Conversely, XANES spectra of satisfactory quality (*e.g.* to monitor the edge position, Section 3.2.1) can be collected in less than one minute (as a S/N ratio of 10^{-2} is more than sufficient), using standard setups.
As discussed in details in a number of recent reviews [76, 147, 425, 426], two principal strategies have been developed to perform time-resolved EXAFS experiments: quick EXAFS (QEXAFS) [427-429] and energy dispersive EXAFS [428, 430-432].
The QEXAFS approach is directly derived from the standard setup discussed before, but focuses on the optimization of the movements of the monochromator system. The monochromator is driven in a continuous motion across the desired energy range, by geared stepper motors or a dc motor with encoder [147]. In this way $I_0(E)$ and $I_1(E)$ (or $I_F(E)$) are acquired "on the fly", by reading, saving and resetting the integrated counts of each detector for each Δt time interval. The latter is defined by the requested energy resolution ΔE and the rotation speed adopted by the monochromator. This acquisition mode ensures an accurate data normalization as in conventional experiments, with improved time resolution on the sub-second scale in the most recent implementations [433]. This value is an instrumental acquisition time and holds for concentrated samples only; for dilute samples a higher statistics is needed to obtain analyzable data, so that one should more realistically count for few tens of seconds for an EXAFS spectrum and few second for a XANES one.
Conversely, the energy dispersive approach (see Figure 5) implies a radical modification of the acquisition strategy. Here, the stepwise progression along the energy windows of interest is elegantly bypassed by simultaneously illuminating the sample with a focused X-ray beam containing the whole spectrum of energies required for the EXAFS acquisition. This is achieved using a bent "polychromator" crystal [434-438], which disperses the energies of an incoming X-ray white beam from the synchrotron. In addition, the polychromator focuses the X-rays onto the sample, located in its focal spot, before then diverging at the detector position. The transmitted intensities corresponding to the different energies of interest are thus measured "in one shot" using a position sensitive detector (*e.g.* a 2D CCD detector). This scheme implies that the incident X-ray intensity and the intensity transmitted by the sample have to be collected separately. This is obtained by positioning at the polychromator focal point nothing or the sample respectively. An additional acquisition is required for the collection of the reference sample. Using a dispersive setup, the time-resolution in EXAFS collection is limited by the detector read-out time, typically in the order of hundreds of ms (*e.g.* ~ 100 ms using the fast-readout low-noise FReLoN CCD camera [439] developed at the ESRF), although resolutions on the μs timescale have recently been demonstrated [440].
Improvements of the energy dispersive EXAFS setup, such as the *Turbo-XAS* one developed at ESRF ID24 [441], make possible to overcame the two major drawbacks of the technique, allowing the users to simultaneously measure $I_0(E)$, $I_1(E)$ and to collect spectra in fluorescence mode if needed.
Besides the obvious benefit of a significant reduction in the acquisition time, energy dispersive EXAFS is characterized by the absence of any movement of the optics during the spectrum acquisition (guarantying a potentially

high beam stability) and by the extremely small and stable horizontal focal spot that allows this setup to be potentially used for space resolved experiments also [438, 442-444].

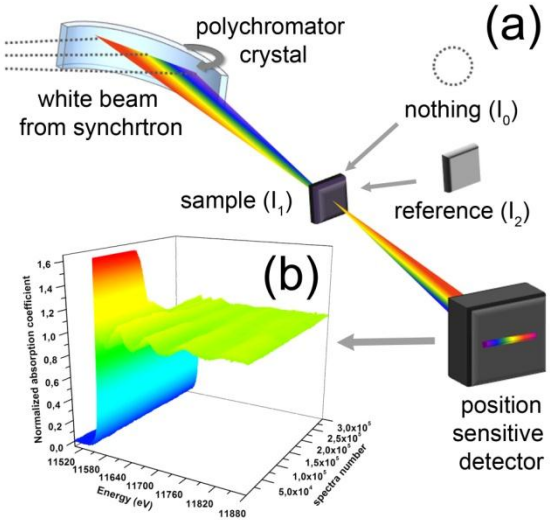

Figure 5. (a) Schematic representation of the experimental setup for energy dispersive EXAFS. (b) Example of time-resolved energy dispersive XAS spectra collected by Kong *et al.* [440] with 6 ms resolution while monotoring the thermolysis of $(NH_4)_2[PtCl_6]$. The analysis of these data provided direct structural evidence of *cis*-$PtCl_2(NH_3)_2$ as the intermediate, together with detailed insights in the reaction dynamics. The same setup has demonstrated to be capable of resolution down to 60 μs, faster than the evolution rate of the probed reaction. Part (b) reproduced with permission from ref. [440]. Copyright (2012) Nature Publishing Group (2012).

Both QEXAFS and energy dispersive EXAFS methods have been successfully integrated in multi-technique setups for *in situ* and *operando* characterization [76, 147, 155, 341, 426, 445-460], where for instance EXAFS is combined to XRPD or XRS methods for a simultaneous long- and short-range structural determination [64, 155, 276, 461] (see also Section 2.6.1), or to a suite of non-X-ray spectroscopic techniques, including IR, UV-Vis and mass spectroscopies [283, 286, 426, 459-468].

2.6 X-ray scattering techniques applied to disordered and partially ordered systems

The same fundamental physics and theoretical principles of XRD, that lead to the Bragg equation in crystalline solids, can be extended to the analysis of non-crystalline compounds and materials. Indeed, independently from the ordering level of the investigated system, the same link between the reciprocal and the real space (and *vice versa*) still holds, that is: the scattering amplitude is the FT of the electron density [213]. The related techniques are commonly referred to as X-ray scattering (XRS) methods [145, 146, 469, 470]. Indeed, a short-range ordered sample can be modelled as a statistical ensemble of randomly oriented sub-units, similarly to the micro-crystalline domains in a XRPD experiment. The correspondent signals are diffused in the entire reciprocal space (diffuse scattering): the 3D information is reduced to 1D and can be extracted (although not univocally) by theoretical modelling (and eventually fitting) of the isotropic scattering patterns [159, 471, 472].

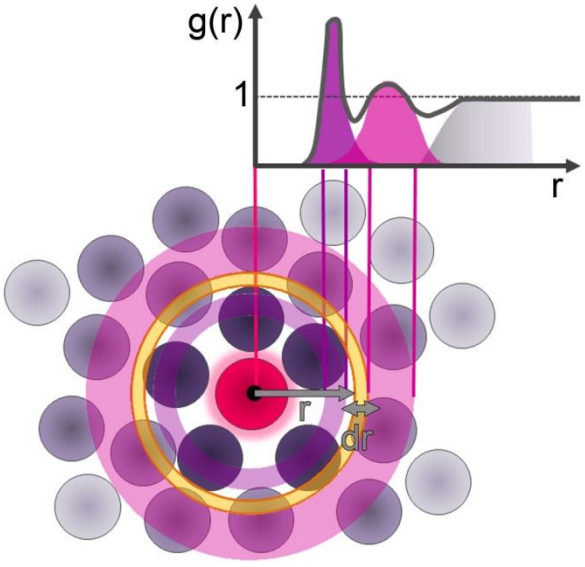

Figure 6. Scheme of the radial PDF $g(r)$. The radial PDF quantifies the correlation between the particles within a given system. In particular, $g(r)$ measures the average probability of finding a particle at a distance of r away from a given reference particle. The general algorithm to evaluate g(r) involves the determination of the number of particles within r and $r+dr$ (circular yellow shell in the figure) from the reference particle (depicted in magenta). In a sample showing short-range order, the $g(r)$ function shows a few oscillations before stabilizing at $g(r) = 1$, which correspond to local deviations from the isotropic condition, and are associated to the first coordination shells occurring at well-defined interatomic distances. Unpublished figure.

These conditions are mathematically mirrored by the Debye equation [213, 473], which represents the theoretical basis for the analysis of XRS experiments involving non-crystalline samples and relates the diffused scattering signal to the spatial arrangement of atoms in the probed sample volume (see Section 6.2.2). Especially while dealing with many-atoms systems (more than 500 atoms), the computation of the theoretical XRS curves can be speeded up by using the so-called radial pair distribution function (PDF) formalism [145, 474-479]. Partial radial PDFs for each kind of atomic pair present in the probed volume (constituted by elements i and j) are defined in such a way that the probability of finding a j-type atom at distance r from a i-type atom is equal to $4\pi r^2 g_{ij}(r)$, as schemed in Figure 6. Hence, the global radial PDF $g(r)$ is obtained by summing over all kind of i, j atoms the partial $g_{ij}(r)$. The FT of this sum, where each term $g_{ij}(r)$ is weighed by the product of the X-ray form factors of the two elements considered, $f_i f_j$, is proportional to the experimentally determined X-ray scattered intensity (see Section 6.2.2). Simplifying, the radial PDF can be pictured as a frequency histogram of the interatomic distances in the investigated system, which tends to a continuous distribution due to the huge number of sampled atomic pairs [145].
The nature of structural information achievable from XRS characterization and the details of data analysis/modelling are directly related to the specific sample features and experimental conditions. In particular, depending on the probed q-range (defined by the sampled 2θ angular interval and by the used λ), the WAXS (Wide Angle X-ray Scattering, sometimes referred to also as Large Angle X-ray Scattering, LAXS, or as X-ray solution scattering, XSS, when performed on solution phase systems) [159, 477] and SAXS (Small Angle X-ray Scattering) [480-482] techniques can be distinguished. WAXS covers an extended angular range, equivalent to that probed in XRD studies, yielding information on interatomic/intramolecular correlations. Conversely, SAXS collection is typically limited to the 0.5 – 50 mrad angular range (locating the detector at some meters from the sample and using an incident X-ray wavelength of ~ 1 Å) [482], hence providing information on inter-molecular correlations and inhomogeneities occurring on the nm-scale.
The WAXS technique is foremost applied in polymer science, for instance to identify ordered and disordered structures and to determine degree of crystallinity and size of crystallites [470, 483-486]. WAXS was also extensively employed since the end of the 60s in the analysis of solvated metal ions and complexes [487, 488], in particular for compounds containing high-Z elements (*e.g.* lanthanoids and actinoids), which ensure high contrast to the solvent environment, maintaining practical concentration values [312]. It is worth noting that before the breakthrough of synchrotron radiation and, consequently, of XAS spectroscopy (see Section 2.5), direct atomic-level structural information in the solution phase could be almost exclusively accessed by WAXS. The widespread diffusion of the EXAFS technique since the 90s limited the use of WAXS methods. Nevertheless, few recent examples can be found [489-493], often combined with EXAFS analysis.
In the SAXS region, the X-ray scattering signal is sensitive to shape and dimensions of macromolecules, typically between 1 and 100 nm in size [482] and to characteristic distances up to 150 nm [480] periodically repeating in partially ordered systems. These length-scales correspond for instance to the typical dimensions of biological macromolecules [494-499], of metallic nanoclusters [500-506] and of nanodomains in which synthetic polymeric chains self-organize [484, 486]. SAXS is therefore very appealing method for structural characterization of nanostructured systems, both in the solid state and in solution. The technique is perfectly suitable to monitor the synthesis of mesoscopic architectures, driven by the directional metal-ligands bonds and other weak intermolecular interactions involving the metal centres [325]. In this context, several SAXS studies recently appeared in the literature are focused on the characterization of MOFs, *e.g.* for the determination of the pores size distribution [507-511]. SAXS was also employed to characterize amino-acid-based metal assemblies [512] and other supramolecular coordination compounds [339].
Finally, let us introduce an advanced XRS characterization strategy, *i.e.* the pair distribution function (PDF) analysis (alternatively referred to as total scattering technique), referring the reader to the wide specialized literature on the topic for details [143-146, 310, 513-516]. This intriguing approach is increasingly contributing to the characterization of nano-crystalline and "structurally-challenged" [143] systems. PDF analysis is somehow the sum of XRPD and XRS methods, with something more than each of the addends. While the conventional XRPD approach is limited to the Bragg peaks analysis in the q-space, under the *a priori* assumption of long-range periodicity, the total scattering technique focuses on the signal coming from the crystalline components, *i.e.* Bragg peaks, but also on the diffuse scattering beneath the Bragg peaks, which carries out specific information on local deviations from the average structure (short-range correlations, which are the only ones contributing to the WAXS signal from *e.g.* amorphous solid or solutions). A proper data reduction of the row total scattering signal, including a careful removal of the

background due to extrinsic contributions and normalization [145, 517-519], allows the determination of the of total scattering structure function $S(q)$. $S(q)$ can be thus Fourier transformed into r-space to obtain the total PDF function $G(r)$, which is conceptually equivalent to the $g(r)$ function discussed before for case of systems only exhibiting short-range order.

It is worth noting how total scattering data treatment closely resembles that employed for the extraction of the EXAFS signal, introduced in Section 2.5. Beside the analogy in the extraction of the experimental signal, both the techniques allow the determination of the distribution of the interatomic distances, peaking at the R-positions where the most probable bond lengths are found, with no limitations for the application to disordered or partially-ordered systems. The interested reader can find a detailed comparison in the work by Filipponi *et al.* [520], where the inherent differences in the character of the $\chi(k)$ and $S(q)$ signals obtained from EXAFS and PDF experiments on single-component disordered systems are thoroughly discussed. In summary, three key points can be identified: (*i*) the PDF signal is not damped by the short photoelectron mean-free path and by the core hole life-time as the EXAFS one is: significant structural information is contained in the pair-correlations extending to much higher values of r (up to hundreds of Å, with high-resolution PDF analysis) than typically reachable by EXAFS (~ 5–8 Å); (*ii*) the total PDF function contains *not* atomically selective EXAFS-like information: $G(r)$ simultaneously includes contributions arising from the local environments of *all* the atomic species present in the sample, and their deconvolution requires additional complication in the data analysis; (*iii*) PDF data inherently contains only SS-like signals, hence no sophisticate data modelling strategies are required to tackle the MS contributions, as in the more advanced EXAFS analyses.

Concluding this overview on XRS methods, it is worth noting that for most of the techniques discussed in this Section, including WAXS, SAXS and total scattering, neutron-based variants exist, exploiting the specific advantages related to the use of neutrons (see Section 2.2), that are particularly suited for samples characterized by low-Z elements and in cases where high-q data collections are needed.

2.6.1 Advantages of synchrotron X-ray scattering

WAXS and SAXS experiments can be successfully performed using lab-scale setups based on high-performance X-ray tubes. Nevertheless, the use of synchrotrons ensures specific advantages, mainly related to the increased X-ray flux and to the possibility of tuning the energy of the incident X-rays to tailor the experimental conditions on the investigated system. These factors ensure a more practical data collection and a higher data quality, allowing to tackle also cases which are difficultly tractable, or definitely not doable, with laboratory instrumentation. It is worth noting that the energy tunability of synchrotron sources uniquely enables anomalous WAXS/SAXS experiments [86, 227, 313, 521], aiming to enhance the chemical contrast in the scattering signal (Section 2.7).

For instance, both flux and energy tunability are critical factors to unravel structures in solution with X-ray scattering methods [86]. Here, the huge solvent background present at practical concentrations complicates the extraction of solute-related information. With this respect, synchrotron high-energy X-ray scattering (HEXS) [312, 522] is recently becoming a versatile alternative for the structural characterization of solvated metal complexes and solution-phase speciation, bypassing these difficulties. In particular, the high-energy X-ray photons from third generation synchrotrons (> 60 keV, typically 100 keV) ensure higher penetration through solutions and improved statistics, allowing to access longer correlation ranges in the solution phase. Analogously to what is observed in total scattering analysis (*vide infra*), the extended range of momentum transfer probed using high-energy X-rays provides improved resolution in the radial PDF obtained by Fourier transforming the HEXS signal. Several examples can be found in the recent literature where the HEXS technique is employed, often in combination with L-edge XAS spectroscopy [523], to elucidate metal ion complexation in solution, in particular for lanthanides [524, 525] and actinides [312, 526-534]. Here, the high scattering power of the metal centre facilitates the extraction of the related correlations, upon careful subtraction of the background signal (*e.g.* from sample holder) and of the HEXS signal of pure solvent, where no metal ions are present. In several of the above mentioned studies, the solution phase structures unravelled by HEXS are compared to that obtained for the solid-state analogues refined by XRD, often highlighting insightful peculiarities of the solution phase structural chemistry of lanthanides and actinides.

In addition, as previously discussed for X-ray diffraction, the use of synchrotrons allows a drastic reduction of the acquisition time required to get structurally-significant XRS data. Nowadays, third generation sources allow acquisition time on the (sub)second scale, opening a brand-new range of possibilities for multi-scale time-resolved characterization. A variety of complex sample environments and *in situ* cells can be employed to "penetrate the black box" [76, 318, 535, 536] in which the reaction is evolving. Synchrotron SAXS setups developed for time-dependent studies [291, 537] allowed for instance to monitor crystallizations processes [288, 289, 291, 538] and self-assembly phenomena [539], and to determine transient intermediates in biomolecules folding [540]. Simultaneous SAXS/WAXS [288, 291, 537] and SAXS/WAXS/XAS are also worth to be mentioned, as well as experiments combining time-resolved X-ray scattering and thermal-analysis [541-543]. A scheme of the typical experimental setup allowing to simultaneously collect SAXS/WAXS/XAS data is reported in Figure 7.

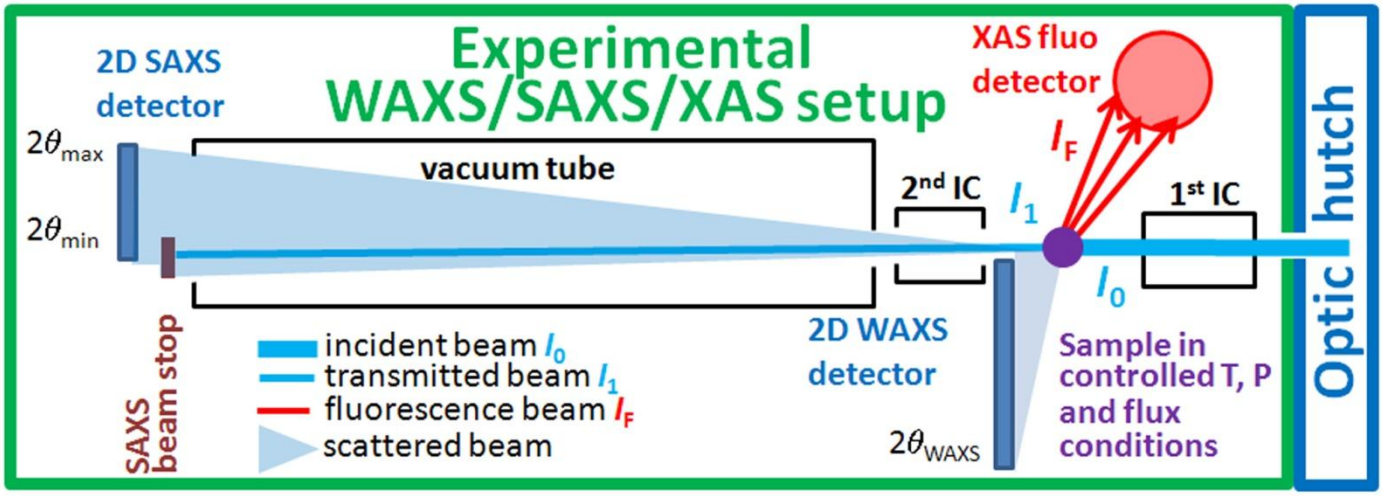

Figure 7. Schematic representation of an experimental setup able to simultaneously collect XAS (XANES and EXAFS), WAXS and SAXS data. The intensity of the monochromatized beam (I_0), coming from the optic hutch, is measured by the first ionization chamber. Then it interacts with the sample, typically hosted in a devoted cell, which allows to flux reagents and to heat the sample at the desired temperature, using adjustable heating ramps. Depending on the element concentration, the XAS spectrum can be obtained either measuring the transmitted beam (I_0) or the fluorescence one (I_0). The elastically scattered beam is collected in the high 2θ-region by the 2D WAXS detector located close to the sample and allowing to cover an angular interval up to $2\theta \sim 80$ °. Conversely, the small-angle fraction of the elastically-scattered beam enters a length-tunable vacuum tube and is collected by the 2D SAXS detector. The presence of a large vacuum tube of tunable length allows to reduce the $0–2\theta_{min}$ region obscured by the beamstop. The short reading/erasing deadtime of modern 2D detectors enable to perform time-resolved experiments with such an experimental setup. Such combined setup is available at a few beamlines worldwide, such as the BM26A DUBBLE beamline at the ESRF.

PDF analysis is more closely, although not exclusively, related to the use of third generation synchrotron sources. Indeed, to achieve an adequate *r*-space resolution of the peaks in the $G(r)$, it is crucial to extend the acquisition over a wide range of momentum transfer in *q*-space. In principle, *all* coherent scattering have to be acquired. In practice, data collection extended at least up to *q*-values such high as 20–30 $Å^{-1}$ [143, 146] is desirable to satisfactorily limit FT truncation errors. Nevertheless, the required *r*-space extension and resolution of the PDF should be evaluated case by case, also considering the intrinsic width of the PDF peaks due to thermal vibrations, to optimize the *q*-range to probe and determine the instrumental *q*-space resolution needed [516].

Being $q = 4\pi \sin\theta/\lambda$, and being the reachable θ_{max} typically ~ 70°, the maximum *q*-value experimentally accessible is limited by the wavelength of the incident X-ray beam, and short-wavelength X-rays (typically in the 0.27 – 0.12 Å range, *i.e.* from 45 to 100 keV in energy [143]) are sorely needed for high accuracy in real-space structural determination. These requirements can be satisfied using laboratory-scale Mo or Ag X-ray tubes, with acceptable results in term of r-space resolution. However, because of the inherent signal damping in the high-*q* region using X-rays, the extra flux provided by synchrotrons is a compelling advantage, and the highest resolution measurements are mostly performed at dedicated synchrotron beamlines. The multi-range local/global sensitivity of PDF analysis makes the technique particularly suitable to monitor *in situ* order → disorder (and *vice versa*) transitions in complex materials and supramolecular assemblies, occurring as a response to specific external inputs. The intensity provided by synchrotrons enables, as previously discussed for SAXS and WAXS, a faster total scattering data collection, ensuring a time resolution on the few-minutes scale, which is enough for several applications of interest in coordination chemistry.

2.7 Anomalous XRD and XRS in coordination chemistry: the charm of element- and site-selective structural characterization

As discussed in the previous Section, one of the crucial advantages of XAS spectroscopy with respect to XRD is its element-selectivity. Hereinafter we will discuss an advanced synchrotron-based strategy to add element-selectivity also to XRD and XRS techniques, *i.e.* anomalous scattering.

In Section 2.2 we have introduced the X-ray scattering factor (or atomic form factor) $f(q)$, discussing its behaviour as a function of *q* and of the atomic number *Z* of the scattering atom. Here we are more specifically interested in the dependence of *f* on the wavelength λ of the incoming X-ray beam employed for XRD/XRS experiments. With this respect, the X-ray scattering factor $f(\lambda)$ can be expressed as $f(\lambda) = f_0 + \Delta f(\lambda) = f_0 + \Delta f'(\lambda) + i\Delta f''(\lambda)$, where the complex λ-dependent term $\Delta f(\lambda)$ is referred to as anomalous scattering factor [477]. In conventional experiments, when working far from the X-ray absorption edges of the elements present in the sample, the anomalous contribution can be safely neglected: in these conditions $f(\lambda) \sim f_0$, resulting in a substantially wavelength-independent X-ray scattering factor. However, if the incident wavelength approaches an X-ray absorption edge, the $\Delta f'(\lambda)$ contribution

significantly influences the scattering signal, modifying the magnitude of the overall scattering factor ($\Delta f'$ (λ) term) and imparting a phase shift to the elastically scattered X-ray photons ($i\Delta f''$ (λ) term). Tuning the incident wavelength in the closest proximities of the edge (resonant conditions), the incident X-ray photons can interact with the bound inner electrons of the correspondent atom, be absorbed, and give photoelectric effect.

Importantly , the anomalous effects near an absorption edge for an atom contained in the sample, selectively enhance the contribution of that atom to the elastically scattered intensity [138, 228, 230, 544-546]. This phenomenon can be exploited in a variety of cases. The principal purely crystallographic application includes element-selective XRD/XRS experiments (contrast mode, more directly relevant to the field of coordination chemistry, *vide infra*) and efficient phasing (see the appendix, Section 6.2.1, for the definition of the phase problem in crystallography) in macromolecular crystallography (MAD method). Other intriguing approaches involve the hybridization of diffractometric and spectroscopic techniques. For instance, the diffraction signal for a specific atomic site or compound can be monitored by varying the wavelength of the incident X-ray beam across and absorption edge. Hence, the anomalous scattering contribution can be extracted, for instance to obtain a XAS-like signal resulting in site- and element-selective local structural information (Diffraction Anomalous Fine Structure, DAFS method).

The necessity of tuning the incident wavelength in the proximities of (and eventually across, for DAFS) one or more absorption edges rules out the use of laboratory setups for anomalous XRD/XRS experiments: these methods are uniquely performed at synchrotrons. In addition, the anomalous scattering is a minor contribution to the global elastic scattering signal. Consequently, also the high intensity of synchrotron X-rays beams is an important requirement for this kind of experiments. With this respect, during the last two decades impressive instrumental developments have taken place, yielding easier and faster wavelength tuning, better stability, energy resolution and control of the beam polarization. Nowadays, sophisticated control systems allows energy scanning and simultaneous flux maximization, while maintaining the scattering geometry; current setups typically ensure an energy resolution $\Delta E/E$ in the $10^{-5} - 10^{-4}$ range [230]. These improvements have recently enabled, for several favourable cases, applications of the technique also to powdered samples [229, 547, 548] and short-range ordered systems (*e.g.* anomalous SAXS, ASAXS [521, 549, 550] and anomalous WAXS, AWAXS [313]).

The idea of exploiting anomalous scattering (in particular the phase-shift term $\Delta f''$) to elegantly solve the phase problem in crystallography, was firstly proposed by Bijvoet, in an article dating back to 1949 [551]. However, due to the availability of more practical approaches allowing successful phasing in small molecules (heavy atom methods, direct methods, Patterson methods), this possibility remained unexploited for more than three decades. The situation drastically changed since the 1980's, when MAD phasing [136-138, 140, 141] at synchrotrons revolutionized the field of macromolecular crystallography. This synchrotron-based approach represented a turning point in biological structural sciences [220, 552-555], fostering the development of dedicated beamlines in the principal third generation facilities worldwide [142].

In chemical crystallography X-ray anomalous scattering is however mostly used to enhance the contrast between elements having similar atomic numbers, hence facilitating their discrimination in specific crystallographic positions [556-558] or, more in general, the solution of the structure for complex substituted compounds [559-562]. Alternatively, anomalous scattering is used to highlight the scattering of an element present in few % [563] or less, as is the case of metal centres in macromolecular structures [137].

Experimentally, anomalous studies in contrast mode involve the collection of at least one diffraction pattern with the incident X-ray wavelength tuned slightly below an absorption edge of the element of interest. The data collection has then to be repeated in the same condition but at a wavelength far below the selected edge. The differences in the intensities of these two patters are related to the variations in the $\Delta f'$ (λ) term of the selected "resonant scatterer", and allow to highlight its specific contribution. It is worth noting that the data collected after the absorption edge are inherently characterized by a worse S/N ratio, due to fluorescence effect (see also Section 2.3): this limitation can be partially overcome by using advanced detection systems, *e.g.* crystal analysers with an enlarged mosaicity [229].

Applications span a variety of research areas in solid state chemistry [138, 228-230, 564], including the discrimination of Zn and Ga in microporous materials [565] or of Pb and Bi in minerals [566], the investigation of the distribution of cations in multi-cationic zeolites [229, 567, 568], substitution of Cu by Fe, Co, Ni, and Zn in high-critical-temperature superconductor cuprates [556].

A few recent applications of contrast-mode anomalous X-ray diffraction specifically deal with the structural determination of coordination compounds, including multinuclear metal complexes [569-571] and MOFs [572].

A representative example is the study of Co−Co and Fe−Co bonds in a series of coordination complexes with formally mixed-valent $[M_2]^{3+}$ cores (where M = Fe, Z= 26; Co, Z = 27), by Zall *et al.* [570]. With a renewed synthetic route, the authors isolated both dicobalt homobimetallic and an Fe−Co heterobimetallic moieties (see Figure 8a), which cores show high-spin ground states and short metal−metal bond distances of 2.29 Å for Co−Co and 2.18 Å for Fe−Co. Anomalous X-ray scattering measurements at the Chem-MatCARS 15-ID-B beamline at the Advanced Photon Source (Argonne National Laboratory) played a key role in assigning the positions of Co and Fe atoms and in detecting and quantifying Fe/Co mixing. To determine the compositions of Fe/Co at the two independent metal sites, Zall *et al.*

refined in a least-squares scheme four anomalous diffraction datasets, collected spanning the absorption K-edges of Fe and Co (see Figure 8b). The refinement demonstrated that only a minor amount of metal-site mixing occurs in the heteronuclear complex: this compound is precisely described by the structure formula $(Fe_{0.94(1)}Co_{0.06(1)})(Co_{0.95(1)}Fe_{0.05(1)})L_{Ph}$, where L_{Ph} = phenyl-substituted tris(amidinato)amine, as depicted by the pie charts in Figure 8a.

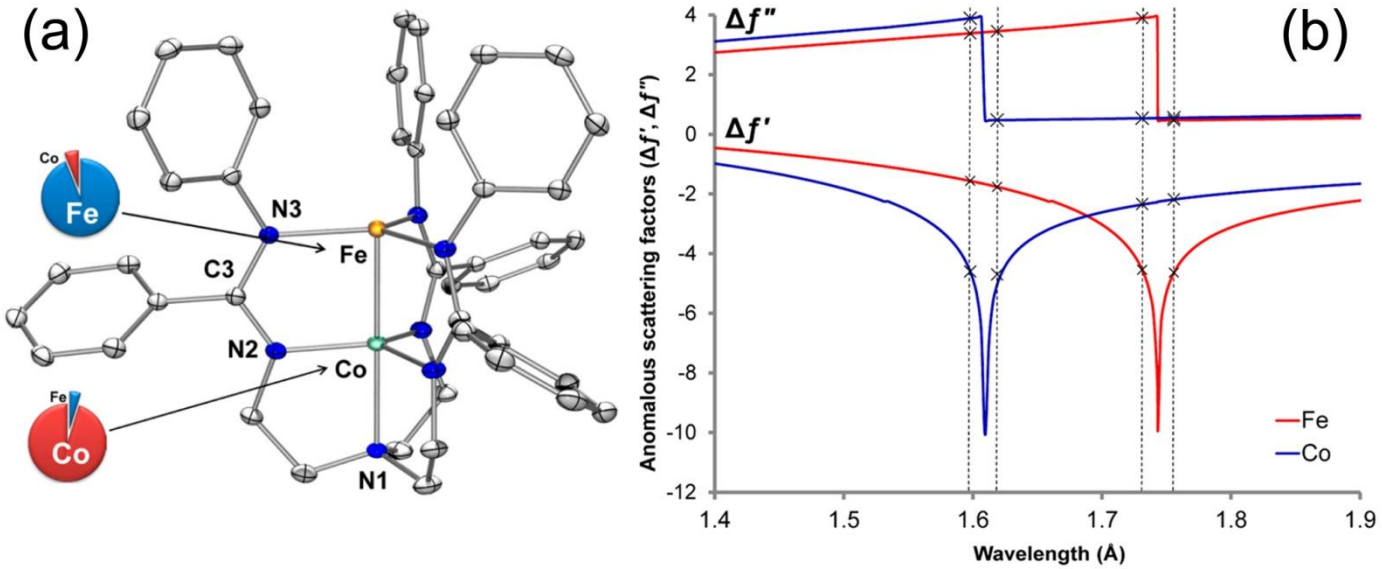

Figure 8. Example of X-ray anomalous scattering in contrast mode application to mixed-valent metal complexes. (a) Solid-state structure of the $Fe_{0.99}Co_{1.01}(L_{Ph})_4$ complex investigated by Zall *et al.* [570], at 50% probability (colour code: Co: cyan; Fe, yellow, N, blue, C, light grey; H atoms are omitted for clarity). The pie charts depict the percentages of Fe and Co present at each metal binding site, as quantified by the analysis of X-ray anomalous scattering data. (b) Real $\Delta f'$ (λ) and imaginary $\Delta f''$ (λ) parts of the anomalous contribution Δf (λ) to the X-ray scattering factor for Fe (red lines) and Co (blue lines) as a function of the incident X-ray wavelength. The four dotted vertical lines indicate the experimental wavelengths selected by Zall *et al.* for the anomalous experiments, spanning the Fe and Co absorption edges. Selected wavelengths are those that maximize the difference between the $\Delta f'$value of the two elements. The cross marks (×) indicate the $\Delta f'$ (λ) and $\Delta f''$ (λ) values for Fe and Co employed by the authors in the least-squares refinement to obtain the metal occupancies shown in the pie charts reported in part (a). Reproduced with permission from ref. [570]. Copyright (2013) American Chemical Society.

In addition, anomalous X-ray scattering was for instance employed to elucidate the elemental composition at each of the three metal-binding sites in novel trinuclear complexes, synthesized by from dinuclear metal species $(^{tbs}LH_2)M_2$ (M = Fe (Z = 26), Mn (Z = 25); $[^{tbs}L]^{6-}$ = [1,3,5-$C_6H_9(NC_6H_4$-*o*-NSi-$Me_2tBu)_3]^{6-}$ by Powers *et al.* [571]. Finally, a relevant example of the use of anomalous XRD in the structural characterization of MOFs is provided by Brozek *et al.* [572]. Here, the technique was applied to evaluate the relative cation occupation at two inequivalent metal sites in the Fe^{2+}-, Cu^{2+}-, and Zn^{2+}-exchanged analogues (Z = 26, 29 and 30, respectively) of the MnMnBTT MOF (BTT = 1,3,5-benzenetristetrazolate). Interestingly, the measurements on the whole series pointed out that the extent of cation exchange at Mn^{2+} sites is significantly influenced by the identity of the substituent metal.

As anticipated, among the structural techniques based on anomalous scattering, we have DAFS [89, 546, 573, 574]. Although DAFS so far has been scarcely applied to coordination compounds, a brief discussion of this method is deserved, considering its foreseeable diffusion in the close future and its analogies with XAS. Similarly to XAS, in a DAFS spectrum the near-edge region (DANES) and the extended region, characterized by an oscillatory fine structure (EDAFS) can be individuated. From DANES, in some favourable cases, it can be possible to distinguish the presence of atoms of the same element in different oxidation states in a specific crystallographic site (valence-difference contrast method [557, 575-577]). In addition, EDAFS spectra combine long-range information from diffraction and elementally-selective local sensitivity equivalent to that provided by EXAFS, enabling site- and chemical-selective structural characterization [546, 573, 574].

On the experimental ground, EDAFS collection is very demanding. Indeed it requires in the experimental hutch the same setup needed for XRPD and in the optic hutch a monochromator able to select the energy E delivered (and thus λ) with the same accuracy and speed needed to acquire an EXAFS spectrum. The DAFS data collection consists in measuring the intensity of a Bragg reflection $I_{h,k,l}(E)$ as a function of E for all values needed to obtain an EXAFS spectrum across one absorption edge of a selected element present in the sample. The result is an EXAFS-like spectrum that contains information of the local environment of the selected atom that contributes to the (h,k,l) reflection. To extract and quantitatively analyze the weak oscillations which modulate the total diffraction signal, an outstanding S/N ratio is required, implying the use of high-intensity incident X-ray beams, high-quality

diffractometers and very stable absorption-dedicated optics. It is worth noting that the EDAFS signal contains contributions from both the real, $\Delta f'(\lambda)$, and imaginary, $\Delta f''(\lambda)$, parts of the complex anomalous scattering factor, whereas EXAFS signal is proportional only to the imaginary part. Nevertheless, an EXAFS-like analysis procedure has been successfully applied to EDAFS spectra [546, 578]. The technique is commonly applied, also in combination with EXAFS, in the structural determination of complex nanostructural materials, where amorphous and crystalline phases coexist [579] (*e.g.* metal nanoclusters and low-dimensional semiconductor structures).

2.8 Magnetic resonance techniques: NMR and EPR - The laboratory way

The same principal concepts that are behind electron spin resonance (ESR) and nuclear magnetic resonance (NMR), but there are differences in the magnitude and signs of the magnetic interactions involved. Concerning NMR all nuclei having odd mass number possess the property of spin I which is an odd integral multiple of ½. Nuclei with even isotope number may have either spinless if the nuclear charge is even, or they can possess an integral I value of 1,2,3, etc.

The nucleus having both spin and charge possess a magnetic a magnetic moment μ. A nuclear spin behaves as a magnetic dipole which tends to align with an applied magnetic field and to interact with neighbouring dipoles. Quantum theory tells us that allowable nuclear spin states are quantized and in a macroscopic assembly the spin will distribute over the possible sites according to the Boltzmann law. In order to induce transition among the different spin levels an oscillating electromagnetic field can be applied to the system.

NMR spectroscopy [580-586] represents a powerful technique for structural investigation of metal complexes: the information provided by 1D spectra of NMR active metal nuclides as well as ^{1}H, ^{13}C, ^{15}N, ^{31}P data are well known to afford structural and electronic behaviour on inorganic and organometallic molecules [587, 588]. Furthermore 2D NMR techniques allows the detection of homo- (COSY, TOCSY) and heteronuclear (HMQC,HMBC) through-bond correlations [582, 585, 589]. All these methods represent an invaluable tool for structural assignment since they are very efficient for establishing connectivities. Other 2D experiments expressed designed for detecting homo- (NOESY, ROESY) and heteronuclear (HOESY) through-space interactions based on the nuclear Overhauser effect (nOe) provide information about the spatial structure of the metal complexes and the relative positions of the different atoms [590, 591]. The structural information are not only limited to a single molecule of the metal complex under investigation, since intermolecular NOE interactions are also present providing information about molecular environment. Intermolecular and interionic interactions as well as aggregation or encapsulation can be detected by Pulsed-field gradient spin-echo (PGSE) methodology [592].

NMR is a less sensitive method compared to synchrotron based techniques requiring much larger samples for analysis. Proton signals can be detect in modern high field NMR spectrometers higher than 400 MHz into the nanogram range (MW 300) allowing easily detection with the currently available cryoprobes.

For solid samples different chemical environments of the nuclei with non-null spin are detected by Solid State NMR (SSNMR) allowing to get information on structure of the solid complexes under investigation. Among all NMR parameters chemical shift, chemical shielding tensors (obtained by the evaluation of the chemical shift principal values from spinning sideband manifolds in low spinning samples), dipolar interaction, spin diffusion, and nuclear quadrupole coupling are the most important. In particular dipolar interactions are of paramount importance to measure internuclear distances or to establish connectivities for structure elucidation and have been extensively applied for investigating the geometric and electronic structure of solid transition metal complexes.

As was the case of EXAFS technique (Section 2.5), the local nature of the magnetic interaction probed by NMR allows to obtain structural information also on samples characterized by a low crystallinity, such as amorphous materials and nanomaterials, where single crystal diffraction methods fail. There are indeed several cases where NMR has been crucial in determining the crystal structure; the specialized literature often refers to such studies as to "NMR crystallography" [593-623].

Another important aspect of the study of transition metal complexes is related to the knowledge of molecular motions. Different spectroscopic and diffraction techniques involving elastic and inelasting scattering of particles like electrons, neutrons or photons have been used in order to provide information on a wide range of very fast processes that occur in nanoseconds down to very slow motions of the order of seconds. The great utility of solid state NMR lies in its intrinsic sensitivity to cover a wide timescale of a fluxional process (10^{2} to 10^{-10} s) [624].

In paramagnetic systems a large broadening of the NMR signals is observed mainly caused by the paramagnetic enhancement to nuclear transverse relaxation. Often the NMR signals are too broad to be detected for nuclei around the paramagnetic center with increasing broadening if the distance of the observed nuclei from the paramagnetic center is decreased. The effect depends also on the magnetogyric ratio, γ, of the observed nuclei and on the paramagnetic species present in the system. The broadening of the signals and spin diffusion phenomena introduce limitations to recovering distances via the usual SS-NMR experiments. Nevertheless a wealth of information can be extracted from the analysis of solid-state NMR signals of paramagnetic compounds, as the changes induced by the paramagnetic center depend in a well-defined way on the structure of the molecule. A large number of examples has

been reported where structural determination has been obtained from paramagnetic systems, mainly in biological fields [625] and references therein, [615, 626].
The technique has also been applied to characterize metal complexes. As an example, Groppo *et al.* [627] combined paramagnetic solid-state NMR, EXAFS, and Raman spectroscopies (supported by DFT calculations), to prove that the Cr center, in the cromocene (Cp_2Cr) complex, undergoes a spin-flip transition (from $2S+1 = 3$ to $2S+1 = 1$) during the CO addition reaction: $Cp_2Cr + CO \rightarrow Cp_2Cr(CO)$ [628, 629].
In ESR the magnetic moment of electron is considered and, as before for NMR, the interaction of this magnetic moment with the applied external magnetic field produces electron spin states at different energies that be investigated by applying an oscillating electromagnetic field. Whereas NMR is able to investigate mainly diamagnetic compounds (all electrons are paired); the ESR is an important spectroscopic technique for the study of paramagnetic species (unpaired electrons) such as free radicals, metal complexes, or triplet excited states of diamagnetic molecules. However NMR "chemical shift" is analogous to the "g factor" in ESR and substantial changes of the g factor in metal complexes, can be used to give information about the electronic structure of the transition metal complexes. Furthermore NMR coupling constant (J), in ESR, corresponds to the hyperfine coupling (or hyperfine splitting) constant. For many transition metal complexes having unpaired electrons ESR represents the technique of choice for providing information on the electronic structure in systems lacking long-range order on length scales that are not easily accessible by other techniques [630]. Magnetic parameters such as g values, hyperfine couplings, and nuclear quadrupole interactions are directly related to the electronic wavefunction and the local environment of the paramagnetic center. They can be used also for measuring distances between the nuclei and the unpaired electron up to ca. 1 nm or for providing information on the bonding of nuclei through nuclear quadrupole interactions. Pulse ESR techniques are particularly useful for the characterization transition metals on disordered systems: in ENDOR (electron nuclear double-resonance) [631, 632], the signal arises from the excitation of EPR and NMR transitions by microwave and radiofrequency irradiation, respectively, whereas in the ESEEM (electron-spin-echo envelope-modulation) [633] the nuclear transition frequencies are indirectly measured by the creation and detection of electron or nuclear coherences using only microwave pulses. ENDOR and ESEEM spectra often give complementary information.

3 Electronic characterization of coordination compounds

The knowledge of the electronic structure of a coordination compound is a fundamental step in understanding its structure (see Section 2) and in foreseeing its reactivity. Several spectroscopic techniques are available to shed light on the electronic structures of coordination complexes and related materials. In Section 3.1 we provide an overview on the most used spectroscopies, regardless of whether they are available at the laboratory scale or are synchrotron-based methods. Conversely, Section 3.2 is devoted to an in-depth discussion of synchrotron-specific spectroscopies.

3.1 Overview on the available techniques to determine the electronic structure

Scheme 2 reports a sketch of the electronic structure of a general transition metal atom embedded in a coordination compound. The 1*s*, 2*s*, $2p_{1/2}$ and $2p_{3/2}$ core levels are explicitly reported together with the n*s*, n*p*, n*d* (n = 3 or 4) and molecular orbitals (MO) valence levels. They are represented as partially overlapped owing to the facts that hybridization of metal atomic orbitals (AO) occurs because of ligand effect and that MO are obtained by linear combination of metal and ligands AO. All electronic spectroscopies are aimed to gain information on occupied and/or on unoccupied electronic states [634-636], that are separated by the Fermi level, defined as (E_F) in Scheme 2. The knowledge of occupied and unoccupied states allows to extract important information on the transition metal such as its oxidation state, its local geometry (tetrahedral, octahedral, square planar, etc…) and the chemical nature of its neighbours [637].
Photoelectron spectroscopies [638-642] (PES) are named UPS (exciting with $h\nu_0$ in the UV) or XPS (exciting with $h\nu_0$ in the X-rays) depending whether they probe valence or core occupied states. In some cases the acronym ESCA (electron spectroscopy for chemical analysis) is used instead of XPS. These experiments are performed using monochromatic photons of sufficiently high energy $h\nu_0$ to promote one electron to the continuum. Knowing $h\nu_0$ and measuring the electron kinetic energy *T*, according to the Einstein equation of the photoelectric effect [643], the electron binding energy *BE* can be obtained as: $BE = h\nu_0 - T$. The intensity of the photoelectron peak will be proportional to the occupied electron density of states. With the exception of advanced synchrotron-based setups, available in a few beamlines worldwide (see Section 3.2.4), the measure of the kinetic energy of an electron requires ultra-high vacuum conditions in the experimental chamber. On the other hand, the reduced free mean path of electrons inside condensed matter implies that PES techniques are surface sensitive techniques: typically 20-100 Å depending on the experimental conditions (average Z of the sample, adopted X-rays energy ($h\nu_0$) and their incidence angle etc…). This characteristic provides to PES strong potentialities, as in most of the techniques the response of the surface is overshadowed by the response of the bulk. Hence PES can be greatly informative, especially if combined with bulk-sensitive techniques.

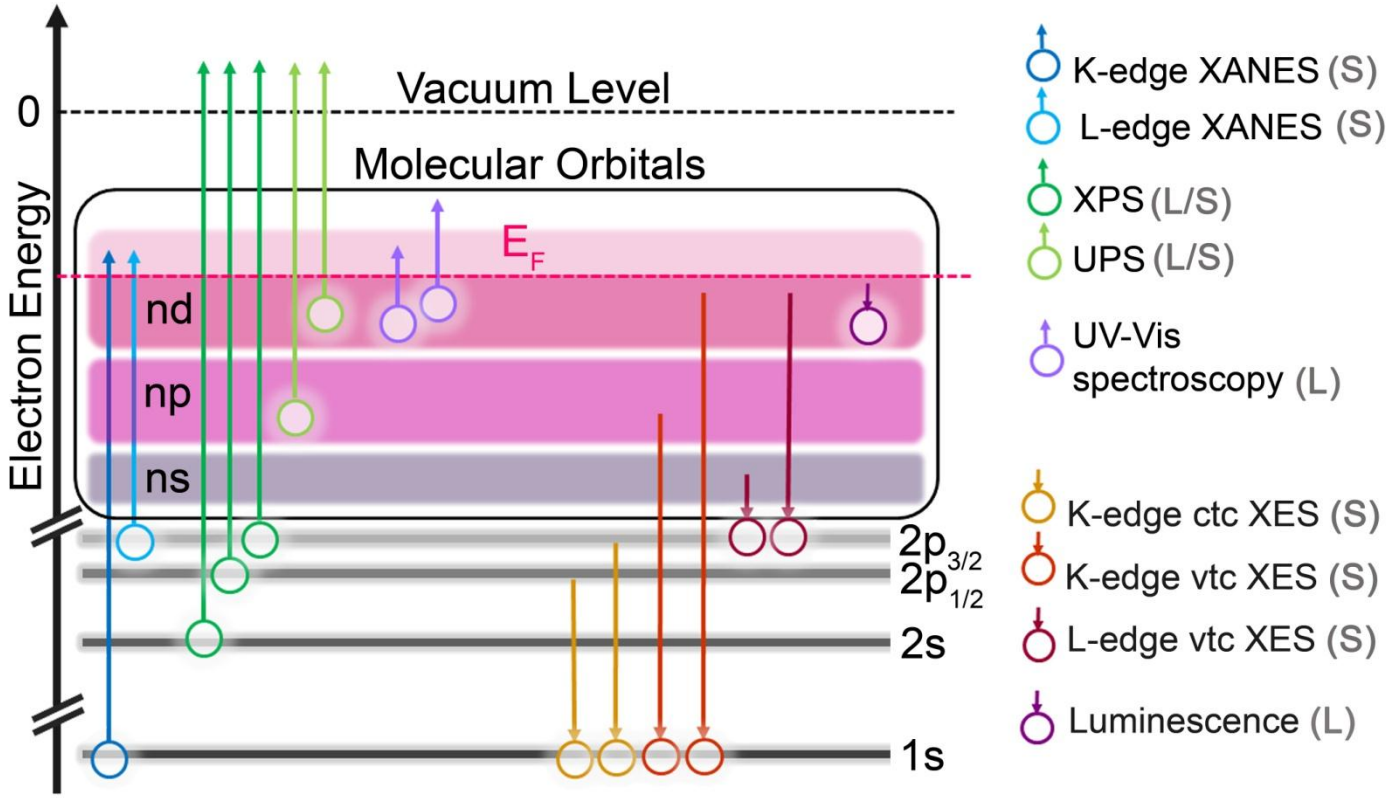

Scheme 2. Schematic representation of the core and valence electronic levels (n*s*, n*p*, n*d*) of a n*d*-transition atom included in a generic coordination compound; valence levels are overlapped to the molecular orbitals obtained by linear combination of metal and ligand atomic orbitals. The Fermi energy (E_F, dashed pink line) divides occupied from unoccupied states, while the 0-level of electron energy (dashed black line) divides bound from free electrons. The emission of an Auger electron is a three-level process alternative to XES and has been omitted in this scheme. For the specific case of X-rays/matter interaction, an alternative representation of the relevant processes is reported in Scheme 6, see appendix, Section 6.1 Unpublished figure inspired from [636].

UV-Vis and XAS (XANES region) spectroscopies promote into unoccupied states valence and core electrons, respectively. According to the Fermi Golden rule [644, 645], K- and L_1-edge XANES, promoting an *s*-electron, probes mainly unoccupied *p* states, while L_2- and L_3-edge XANES, promoting a *p*-electron, probe mainly unoccupied *s* and *d* states.

The processes UPS, XPS, UV-Vis (CT part) and XANES create a hole that is filled by an electron from the higher shells. The radiative decay of such processes can be followed by luminescence or X-ray emission spectroscopy (XES) depending weather we are dealing with valence or core holes. These spectroscopies are called de-excitation spectroscopies and are informative on the occupied states, as was the case for UPS and XPS. Due to the low efficiency of the process (particularly for valence to core transitions) and because of the high $\Delta E/E$ requested ($<10^{-4}$) the potentialities of XES spectroscopy can be fully exploited only at high brilliance beamlines hosted in III-generation synchrotrons. With these experimental setups, XES is combined to XANES (that create the core hole) so that the overall mechanism can be seen as a two-photons or photon in/photon out process. As an example, K-edge XANES creates a 1*s* core hole that can be filled by a $2p_{1/2}$ or $2p_{3/2}$ electron (core to core XES) or by a valence electron (valence to core XES). Having in mind the photon in/photon out scheme described so far, it becomes evident why XES has also been called inelastic X-ray scattering or Raman X-ray scattering. Core (valence) to core XES is able to obtain the same information as XPS (UPS) but using hard X-rays: this means that ultra-high vacuum conditions are not required and that information on the occupied electrons states can be obtained on materials in presence of solvent or in interaction with gas or liquid phases. Also the penetration depth of XES and PES are completely different. When comparison is made between valence to core XES and UV-Vis spectroscopies, the main differences are that UV-Vis has a better absolute energy resolution, while XES is able to detect *d-d* and charge transfer transitions also in an element selective way [37, 646] (see Section 3.2.2).

The low efficiency of the vtc-XES phenomenon implies that XES spectroscopy needs high flux available at the insertion device beamlines of the third generation synchrotron sources. Conversely XAS (particularly the less phonon-demanding XANES part) can, on concentrated samples, be performed also on laboratory instruments. Indeed, all the pioneering activity in XAS spectroscopy (1921-1971 period) has been carried out with X-ray tubes (see ref. [76] for an historical overview). Still in the age of synchrotrons, some laboratory instrumentation, mostly using a rotating anode as source, has been developed [647-650] and some interesting results have been obtained [651-657]. Obviously, the

investigated systems are limited to concentrated samples and long acquisition times are required, preventing time resolved studies to be done.
Finally, as anticipated in Section 2.5, it is worth to note that the photoelectric effect on core electrons can be also induced by high-energy electrons in TEMs, resulting in XAS-like spectra. The resulting electron energy-loss near edge structure (EELNES) spectra collected in the near edge region have, at least for low-*Z* edges, are competitive with those collected at synchrotron sources in terms of data quality. In this way, electronic information equivalent to that provided by XANES can be obtained at (sub)-nanometric spatial resolution, although suffering from the above-mentioned limitations of the electron-based methods.

3.2 The role of synchrotron characterization in the electronic determination of coordination compounds

As introduced in the previous Section, the use of synchrotron radiation allows a remarkable extension of the information on the electronic structure of coordination compounds. Hereinafter we will discuss the basic principles of the most common and informative synchrotron-based methods, also through a selection of relevant examples. First of all, we will describe the two highly-complementary XANES and XES techniques, which are mostly performed at third-generation synchrotrons (the key mathematical results for XANES and XES analysis are reported in the appendix, in Sections 6.3 and 6.4, respectively). Subsequently, we will point out the advantages related to synchrotron-based PES methods with respect to the conventional laboratory setups, with an emphasis on coordination chemistry applications.

3.2.1 XANES

The region including few tens of eV before and after the edge is usually called XANES for hard X-rays or NEXAFS (Near Edge XAFS) for soft X-rays [51, 53, 68, 410, 658-660]. This part of the spectrum mainly reflects the unoccupied atomic levels of the absorbing species and can be divided in pre-edge, edge and post-edge parts. The quantitative analysis of an X-ray absorption spectrum in this energy range can require calculations which are very demanding from the computational point of view. Nevertheless, as anticipated in Section 2.5, the remarkable progress in computational capabilities currently allows in many cases accurate interpretation and modelling of XANES spectra [50, 52, 53, 56, 405-409, 586, 661-670]. The technique is very sensitive not only to the bond length, but also to symmetry of the coordinated atoms, the distribution of charges and the potential around the absorbing atom. This makes the direct fitting of the spectra very difficult; the common approach is to start from a hypothetical structure and calculate a simulated spectrum, then compare it with the experimental curve and change systematically some of the physical parameters or atomic positions to improve the agreement.
The full MS approach is the only one possible to analyze XANES data, because the mean free path of the photoelectron near the edge is much greater. Several codes have been developed so far for the XANES simulation, as recently reviewed elsewhere [76, 90, 668]. Multiple scattering theories usually employ the muffin-tin approximation. Without entering into the theoretical details, it is worth mentioning that several computational methods haves been developed and successfully applied to avoid the restriction imposed by this approximation [52, 667, 671-673].
However, a qualitative interpretation of XANES spectra has been simultaneously developed during the years and it is commonly adopted as a first approximation. One of its more common uses is in fingerprinting, where the experimental spectrum measured on an unknown sample is compared to a selection of spectra obtained for reference compounds. As previously discussed with respect to EXAFS analysis (see Section 2.5), in order to compare different spectra it is first and foremost necessary to perform a proper normalization which requires an evaluation of the pre-edge and post edge trends and an estimation of the edge jump. Focusing on the XANES region, the most interesting features to be observed in this kind of analysis are pre-edge peaks, edge position and intensity of the top of the edge (known as "white line") [76, 90, 359, 674-678].
It is worth noting that the initial state of the electron is a core level with well-defined angular momentum quantum numbers l, m. Because of the orthogonality of spherical harmonics, the transition matrix element that describes the intensity of the absorption spectrum in the XANES region projects out only part of the final state wavefunction depending on the geometry and on the decreasing contribution of multipolar terms in the photoelectric interaction [90] (see Section 6.3). Hence, selection rules can be defined to determine the allowed transitions. Bearing in mind that the dipolar term is the dominant contribution of the photoelectric interaction, transitions with $\Delta l = \pm 1$ will be favoured. So the final states of K- and L_1-edges will contain *p* symmetry, while for L_2- and L_3-edges the final states will have an *s* or *d* character. Since *d* states are more localized then *p* states, usually L_2- and L_3-edges show a more pronounced white line. Thinking in terms of molecular orbitals, the atomic orbitals of the absorber will mix with the neighbours' orbitals, and the pre-edge transition strength will depend also on the symmetry of the site since in an inversion-symmetric site orbitals of different parity do not mix in an eigenfunction. For instance, in the case of a K-edge, transitions to *d*-states should have a very low probability. Nevertheless, when the coordination is tetrahedral, the inversion symmetry is broken and a sharp and intense pre-edge peak appears [359, 674, 677-687], while it is of very weak intensity for octahedral sites [414, 687-690].

To exemplify these concepts, the Ti K-edge XANES pre-edge features of Ti(IV) species hosted in microporous crystalline titanosilicates are reported in Figure 9a. Ti(IV) has 18 electrons, and its electronic configuration is $3s^2\ 3p^6\ 3d^0$, consequently, in absence of a significant *p-d* mixing, the pre-edge XANES features of Ti(IV) are very weak in intensity. This is the case of anatase and rutile forms of TiO_2 [687-690], where the local symmetry is O_h. Ti(IV) species hosted in TS-1 molecular sieve isomorphically substitute Si(IV) species and are consequently in a T_d-like symmetry [674, 677, 680, 683], see Figure 9b. As a consequence the ligands field on the local symmetry, a strong *p-d* mixing occurs, and Ti(IV) species exhibit only a partial occupation of 3p level. Consequently, the pre-edge peak in TS-1 is as high as 0.8 in normalized μx, see black curve in Figure 9a. Of interest is also the pre-edge peak measured by Prestipino *et al.* [691] on ETS-10 molecular sieve. Engelhard titanosilicate ETS-10 is a microporous crystalline material belonging to the family of Ti substituted silicates which framework is composed of corner-sharing [SiO_4] tetrahedra and [TiO_6] octahedra (see top of Figure 9c). [SiO_4] and [TiO_6] are linked through bridging oxygen atoms and form 12-membered rings [692, 693]. These rings give rise to two sets of perpendicular channels with an elliptical cross-section of 7.6 Å x 4.9 Å (Figure 9c, top). We notice that the [TiO_6] octahedra form linear ...–Ti–O–Ti–O–Ti–... chains within the ETS-10 framework [694, 695] (Figure 9c, bottom). Now, the local symmetry of [TiO_6] sites in ETS-10 is O_h and consequently ETS-10 is expected to have a XANES spectrum characterized by a very low pre-edge intensity. This is not what was found by Prestipino *et al.* [691] (grey curve in Figure 9a). This apparent contradiction has been explained by the authors considering the presence of defects along the ...–Ti–O–Ti–O–Ti–... chains: the terminal Ti atoms of the chain are no longer in O_h symmetry, but characterized by a C_{4V}-like environment. The experimental spectrum of ETS-10 (grey curve in Figure 9a) should then be the superimposition of the XANES spectra of regular and defective Ti sites, weighted by their abundance. Using FEFF8.2 code, Prestipino *et al.* computed the theoretical XANES spectra of octahedral and penta-coordnates sites of Ti(IV) hosted in ETS-4 titanosilicate (violet and red curves in Figure 9a, respectively) [691]. The local environments of such sites are similar to the regular and defective sites in ETS-10. The lack of an inversion center in the local environment of penta-coordinated Ti site (red curve in Figure 9a, C_{4V}-like environment) implies that a strong pre-edge feature is expected from the calculations; as a consequence, a relatively small fraction of defective (terminal) Ti sites in ETS-10 can justify the observed experimental spectrum [691].

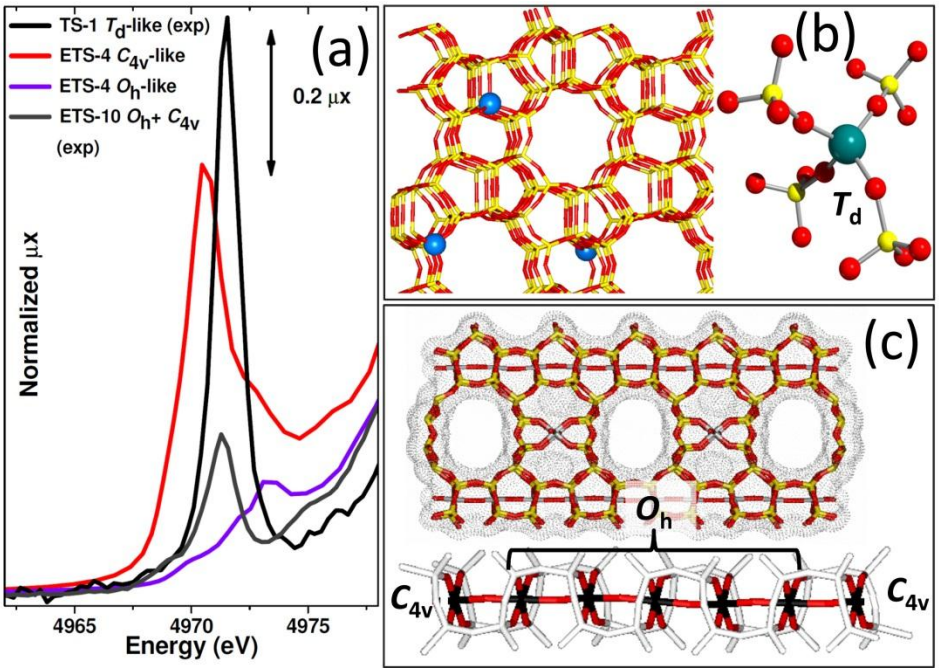

Figure 9. Effect of the local symmetry of Ti(IV) sites hosted in microporous titanosilicates on the intensity of the pre-edge peak of the Ti K-edge XANES spectra. Part (a): experimental Ti K-edge XANES spectra of thermally activated TS-1 (black line) and ETS-10 (grey line) titanosilicate molecular sieves. The red and the violet curves report respectively the theoretical spectra of pentacoorinated (C_{4v}-like) and octahedral (O_h-like) Ti sites of ETS-4 molecular sieve, computed with the FEFF8.2 code [664]. Part (b): 3D representation of TS-1 molecular sieve (left); zoom on the local environment of Ti(IV) sites exhibiting T_d-like symmetry. Part (c): 3D representation of ETS-10 molecular sieve (top); zoom on the local environment of Ti(IV) in the monoatomic –Ti–O–Ti–O–Ti– quantum wire showing the more abundant regular O_h-like sites and the defective C_{4V}-like sites, representing the terminal Ti atoms of the chain. Unpublished figure reporting spectra published by Prestipino *et al.* [691].

Another important information that can be extracted from XANES data is the oxidation state of the absorber, which can be gathered from the edge position [68, 76]. In fact, a higher oxidation state will correspond to higher edge energy, because it is more energetically expensive for the photoelectron to leave a positively charged (oxidized) atom. Figure 10 reports some exemplificative cases of this empirical rule. The first example, reported in part (a), refers to the catalyst used in the ethylene oxychlorination, a key step in the industrial PVC production [446, 696-700]. The

hydrated $CuCl_2$ phase, supported on γ-Al_2O_3 by the incipient wetness precipitation method, is reduced *in situ* by C_2H_4 at 500 K, resulting in an highly dispersed CuCl phase [698]. The example reported in part (b) concerns the reduction undergone by Cu^{2+} cations hosted in zeolitic systems upon thermal activation in vacuo at 400 °C, resulting in low coordinated Cu^{+} cations [701, 702]. Part (c) highlights the differences in the position of the absorption edge of Mn_2O_3 and MnO_2 bulk oxides. In addition, the effect on the Mn K-edge of the progressive substitution of Mn^{3+} cations by Mg^{2+} cations in the $LaMg_xMn_{1-x}O_3$ perovskite is reported in Figure 10d. These materials have been deeply investigated because of their magnetic properties [52, 703-707] and their use as high-temperature materials for catalytic combustion of methane [708-711]. In $LaMnO_3$ perovskite the manganese cations have a formal oxidation state of +3. The substitution of a fraction of trivalent manganese cations by divalent magnesium ones forces the remaining ones to increase their average oxidation state to guarantee the charge neutrality of the $LaMg_xMn_{1-x}O_3$ system. The progressive oxidation of Mn cation in the $LaMg_xMn_{1-x}O_3$ (x = 0.1, 0.2, 0.3 and 0.4) is clearly revealed by XANES analysis. Moreover, Figure 10e reports the XANES spectra collected *in situ* by Paulus *et al.* [386] on the $SrCoO_{2.5}$ brownmillerite system during the electrochemical intercalation of oxygen resulting in the final $SrCoO_{3.0}$ perovskite. In the starting material, the oxidation state of cobalt is +2, but the progressive insertion of O^{2-} anions implies the progressive oxidation of cobalt up to the final Co^{3+} state. The same group reported similar spectra for the $SrFeO_{2.5} \rightarrow SrFeO_{3.0}$ electrochemical oxidation in ref. [387]. Finally, Figure 10f reports the *in situ* reduction of the supported $Pd(OH)_2$ phase resulting in Pd^0 nanoparticles [712], of interest for the preparation of several hydrogenation catalysts, obtained by precipitation of the $Pd(OH)_2$ phase on high surface area carbons [713, 714].

Summarizing, XANES spectra are sensitive to both the oxidation and the coordination state of the absorbing element, being so informative on the formal charge of the absorber, on the nature and on the geometrical arrangement of its ligands. Such information can be extracted either performing accurate DFT calculations or according to a qualitative comparison with XANES spectra of known model compounds. This technique is consequently ideal to monitor distortions of the local geometry [89, 384], to follow in real time in situ red-ox reactions [386, 387, 445, 446, 700, 713, 714], to monitor the insertion of a ligand inside a coordination vacancy [379-381, 715-719], or a ligand displacement [720] and to monitor site reactivity [359, 676, 721, 722].

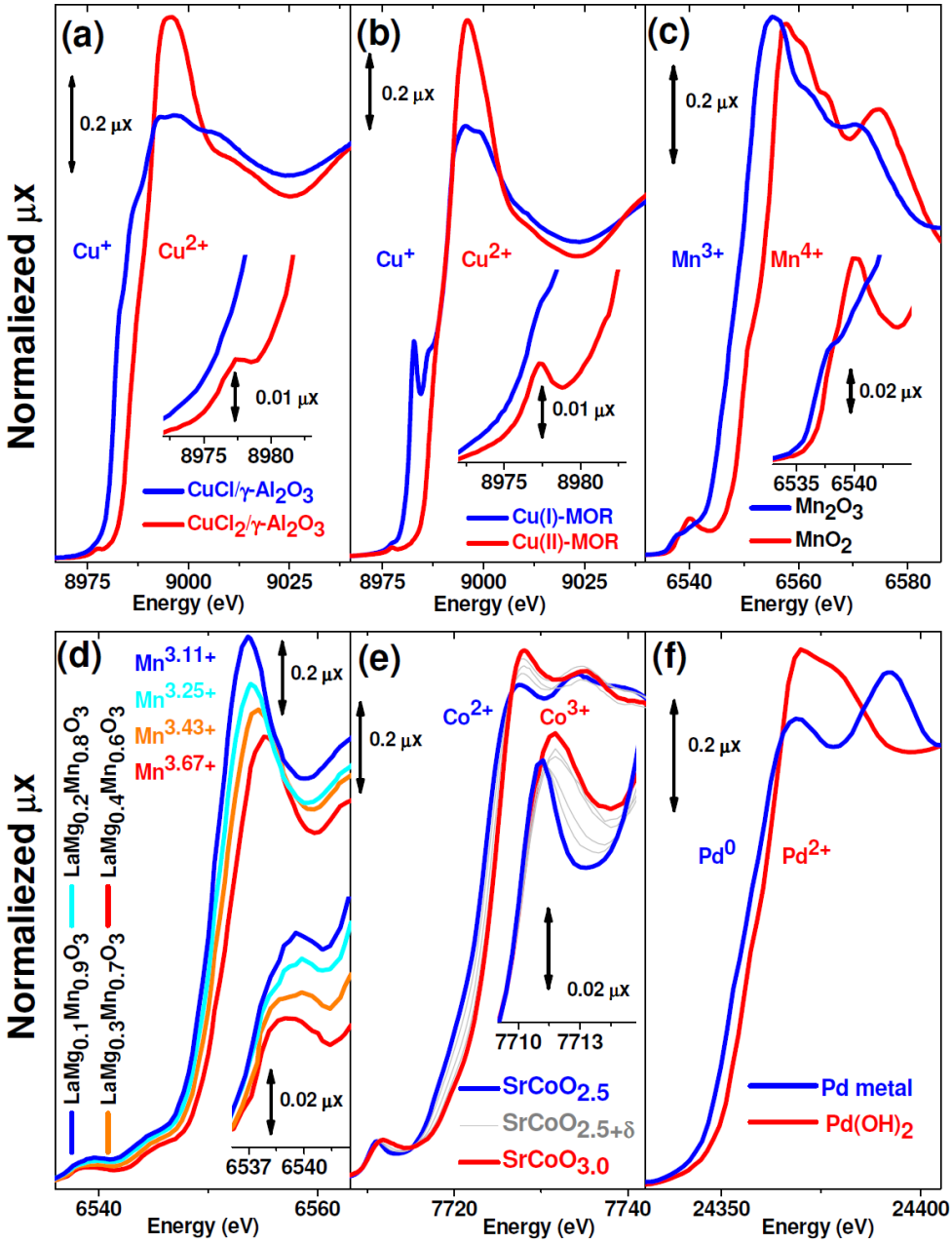

Figure 10. Examples of edge shifts in the XANES spectra caused by a change in the formal oxidation state of the absorbing atom. Part (a): hydrated $CuCl_2$ and anhydrous CuCl (formed upon *in situ* C_2H_4 reduction) hosted on high surface area γ-Al_2O_3 support [698]. Part (b): Hydrated Cu^{2+} and dehydrated Cu^{+} cations hosted in the channels of mordenite zeolite [702]. Part (c): Mn_2O_3 and MnO_2 bulk oxides (by courtesy of F. Geobaldo Politecnico of Turin). Part (d): $LaMg_xMn_{1-x}O_3$ perovskites (x = 0.1, 0.2, 0.3 and 0.4 by courtesy of F. Geobaldo Politecnico of Turin). Part (e) evolution from $SrCoO_{2.5}$ brownmillerite structure to $SrCoO_{3.0}$ perovskite structure upon *in situ* oxygen intercalation via electrochemical method [386]. Part (f): Highly dispersed $Pd(OH)_2$ phase precipitated on active carbons and successive metal nanoparticles formed upon H_2 reduction [712]. When pre-edge peaks are present, they have been magnified in the inset. Unpublished figure reporting spectra published in the quoted references.

3.2.2 XES and resonant-XES

The XANES process described in the previous paragraph implies the formation of a core hole in the metal center. Such exited state can undergo a radiative decay yielding X-rays emission of energy $\hbar\omega$: we refer to this process as X-ray emission spectroscopy (XES). Frequently, the excited state is induced by the absorption of photons in the X-ray region of the electromagnetic spectrum, but other particles (*i.e.* protons induced X-ray emission PIXE spectroscopy) can also be used [723-728].

The complex XES spectra can be fully interpreted by quantum mechanics calculations [116, 117, 120, 121, 729], however a comprehensive theoretical discussion is behind the aim of the present work and here we provide a simplified description using a one electron picture. We consider the case of a 3d-transition metal system with a 1s hole created by the transition of the 1s electron to the continuum by an incident photon (energy $\hbar\Omega$), see Figure 12. Such core hole can be filed by an electron from an upper level yielding the emission of a photon of energy $\hbar\omega$, that is measured during a XES experiment (see also Scheme 6 in the appendix, Section 6.1). The nomenclature of XES

spectroscopy is quite peculiar of the specialized literature and is hereafter briefly summarized. The transition of a 3p electron to a 1s hole (core-to-core or ctc-XES) gives rise to the Kβ main lines that are sensitive to the metal oxidation and spin state [730, 731], while the transition of a valence electron to the metal 1s hole gives rise to the valence-to-core (vtc)-XES that provides insights on the type, distance and number of ligands as well as to the metal oxidation and spin-state [117, 120-122, 732, 733]. It has been shown that these vtc-XES spectra can be effectively interpreted using ground state DFT calculation adopting the one-electron approximation [36, 38, 733-739]. As an example, Figure 11a reports the valence MOs (both eigenfunctions and eighenvalues) of $Ti(OH)_4$ and $Ti(OH)_6$ clusters in perfect T_d and O_h symmetry computed by Gallo *et al.* [38] at DFT level of theory using the ORCA 2008 *ab initio*/DFT code [670]. From such calculations, in the one electron approximation, the $|\langle 1s|\mathbf{O}|vMO_i\rangle|^2$ matrix element provides the probability that the $|1s\rangle$ core hole is filled by an electron coming from the i-th valence MOs $|vMO_i\rangle$, being **O** the transition operator, usually the dipole or quadrupole one, depending on the approximation. Consequently, the term $|\langle 1s|\mathbf{O}|vMO_i\rangle|^2$, properly weighted by the density of states of the valence MOs, provides the expected amplitude of the $|vMO_i\rangle \rightarrow |1s\rangle$ transition (Figure 11b). Then, the assignment of a finite broadening to the computed transitions yields the computed spectra reported in Figure 11c. This simple example underlines the strong interplay existing between XES experiments and corresponding DFT calculations. Indeed, DFT directly provides both the MOs and the corresponding energy levels (eigenfunctions and eigenvalues of the Schrödinger equation, some of them reported in Figure 11a,b); from the knowledge of MOs it is immediate to calculate the $|\langle 1s|\mathbf{O}|vMO_i\rangle|^2$ integrals, that provides the estimation of the intensity of the corresponding XES band, while from the difference of the eigenvalues, the theory predicts the expected $\hbar\omega_i = E_{MOi}, - E_{1s}$ energy where the XES band is expected to be observed.

Coming to the details of the selected examples, the vtc-XES of $Ti(OH)_6$ consists of two main peaks that involve $4t_{1u}$ and $5t_{1u}$ molecular orbitals (MOs), having strong O(2s) and O(2p) atomic character, respectively (Figure 11a,b). It is worth noting that, in such an ideal system, MOs which have the correct *ungerade* symmetry (in O_h) but small (*e.g.* $6t_{1u}$) or zero (*e.g.* $1t_{2u}$) Ti p-character (*i.e.* orbital moment l=1 with respect to Ti centre) do not significantly contribute to the spectra. The vtc-XES of the tetrahedral $Ti(OH)_4$ cluster is composed of three peaks. Each peak is associated with MOs with t_2-symmetry and thus Ti p-character. Note that, as already discussed for the XANES spectra (see Figure 9), the absence of inversion symmetry and thus possibility for pd-mixing in T_d symmetry increases the number of observed transitions in the Kß$_{2,5}$ region of vtc-XES. The interpretation of experimental XES spectra of Ti(IV) species T_d- and O_h-like geometries, like those of dehydrated TS-1 and of $CaTiO_3$ model compounds (Figure 11d), becomes straightforward once the previously described DFT study (Figure 11a−c) is taken into account.

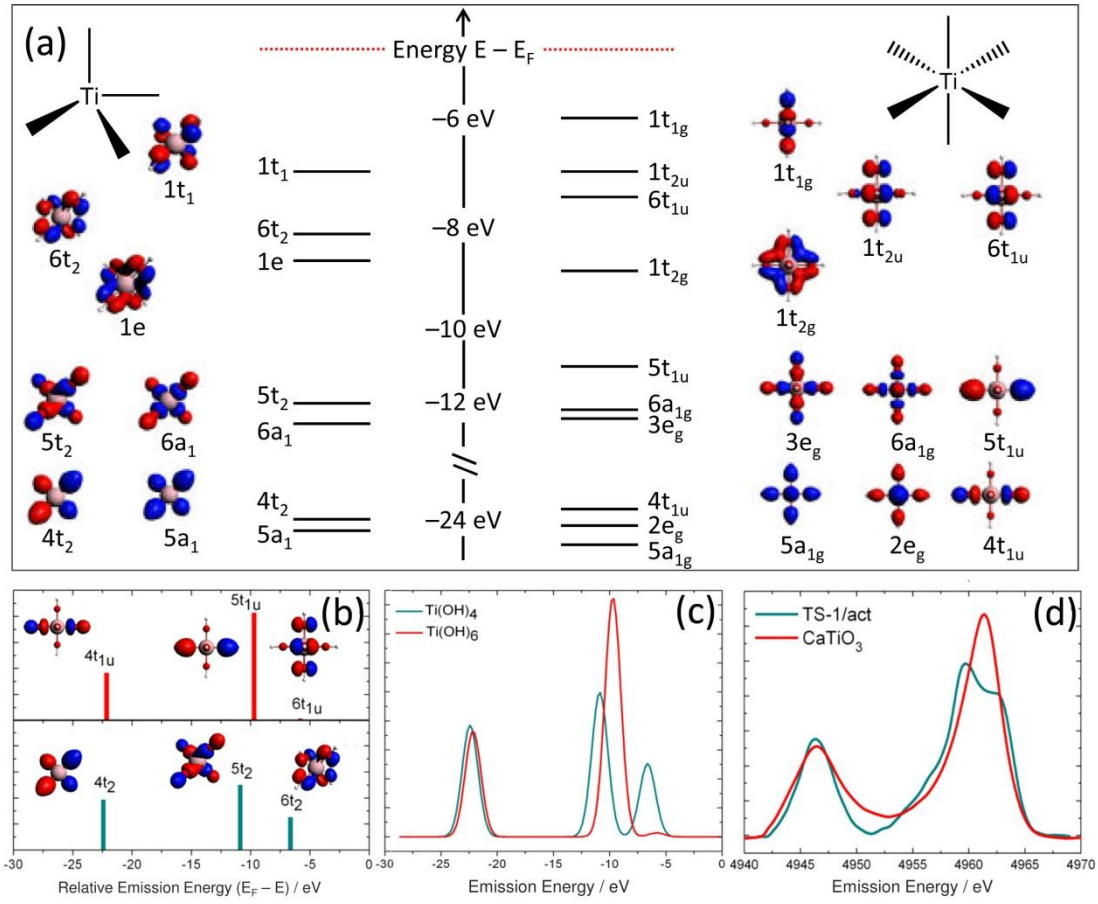

Figure 11. Part (a): calculated valence MOs for $Ti(OH)_4$ and $Ti(OH)_6$ clusters in perfect T_d and O_h symmetry, respectively. Part (b): Intensities for the vtc transitions and significant MOs of $Ti(OH)_4$ (bottom) and $Ti(OH)_6$ (top). Part (c): From the transitions

computed in part (b), the calculated vtc-XES spectra of $Ti(OH)_4$ (green line) and $Ti(OH)_6$ (red line) are obtained by assigning a finite broadening to the transition lines. Part (d): experimental vtc-XES of TS-1/act (green line) and $CaTiO_3$ (red line) used as model compounds for Ti(IV) in T_d- and O_h-like geometries, respectively. Unpublished figure reporting spectra and schemes published by Gallo *et al.* [37].

If the 1s electron is excited into an unoccupied level just above the Fermi energy E_F (see Figure 12c,d), the excitations are referred to as resonant (r). As before, we distinguish between decays of the intermediate state where the 1s hole is filled by a valence electron (rvtc-XES) or by another core electron (rctc-XES), see Figure 12 parts (c) and (d). In case of resonant excitation we define the energy transfer $\hbar(\Omega-\omega)$, which represents the energy that remains within the system [90, 740]. In this relatively young field of X-ray spectroscopy, the nomenclature is far to be univocal and resonant-XES is often also referred as resonant inelastic X-ray scattering (RIXS) or as resonant X-ray Raman. For rvtc-XES the net excitation can be as low as few eV, corresponding to the range of optical spectroscopy (charge transfer and d-d transitions), with the remarkable difference that rvtc-XES is element selective [37, 646, 741-744]. The Kramer-Heisemberg's formula, employed to describe non-resonant and resonant XES processes, is reported and briefly described in the appendix, Section 6.4.
An example of combined XAS/XES experiment is provided in Figure 12e. The techniques are able to follow the symmetry modification undergone by Ti(IV) atoms in T_d-like geometry upon coordination a fifth ligand (an adsorbed water molecule in this case) [36, 38, 674, 677, 680, 718].

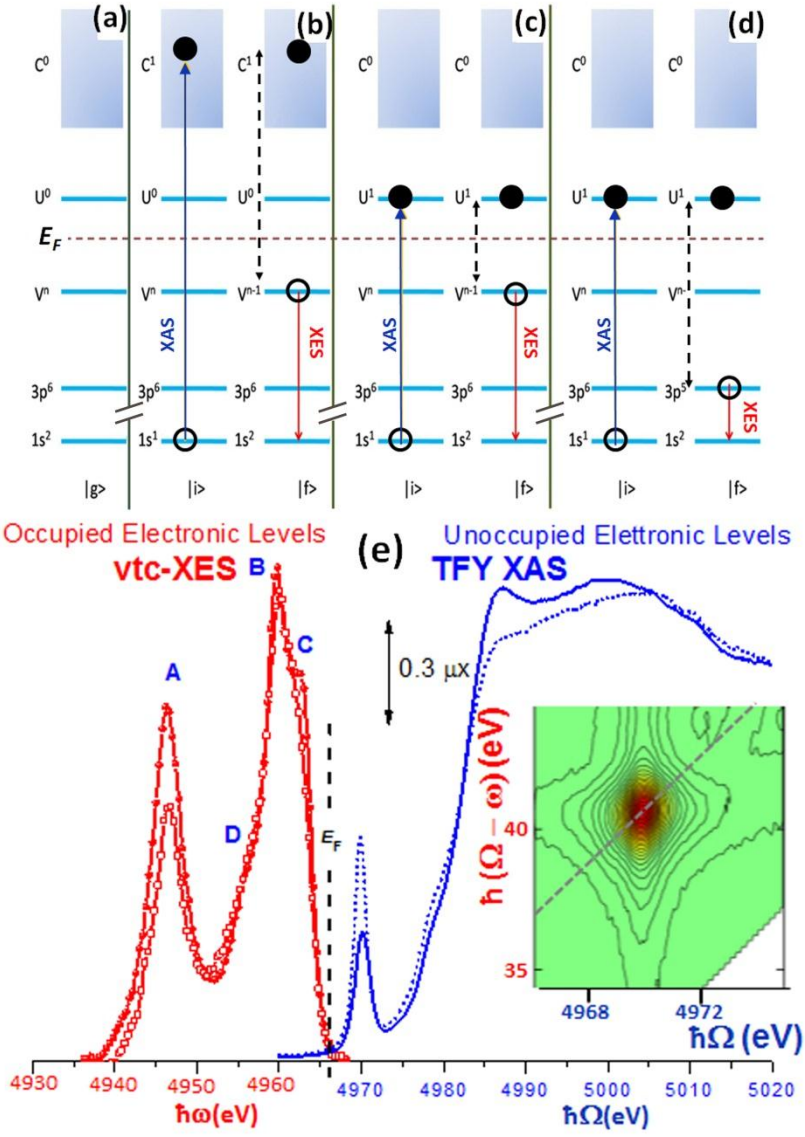

Figure 12. Parts (a-d): simplified representation, using a one electron picture, of: (a) the ground state |g> and the (b) vtc-XES; (c) rvtc-XES; and (d) rctc-XES processes. V^n indicates the number (n) of electrons in the valence molecular orbitals (V) just below the E_F. U indicates the unoccupied molecular orbitals just above the Fermi energy (E_F) and C the continuum excitations. The blue arrows represent the transition of the 1s electron due to the adsorption of an incoming photon of energy $\hbar\Omega$ to reach the intermediate state |i> (XAS or XANES spectra in part (e). The red arrow indicates the decay of an electron from a higher level to the core hole with final state |f>, accompanied by the emission of a photon of energy $\hbar\omega$ (XES spectra in part e). The energy transfer $\hbar(\Omega-\omega)$ is indicated with a dashed black arrow. Part (e): the combination of TFY-XAS (blue spectra) with vtc-XES (red

scattered spectra) allows the sampling of unoccupied and occupied molecular orbitals (MO) across E_F. The reported example indicates how the change of local symmetry of Ti(IV) species in T_d-like symmetry (dotted blue line and scattered full red spheres) to penta-coordination (solid blue line and scattered open red squares) upon adsorption of a water molecule is clearly visible by both XAS and XES spectroscopies. A detailed description of these spectra has been reported by Gallo *et al.* [36, 37]. The inset reports the corresponding rctc-XES map, where the dotted grey line shows the cut done to obtain the high-energy resolution fluorescence detected (HERFD) XANES spectrum (see Section 3.2.3). Reproduced with permission from [90], copyright IoP 2013.

Coming to the instrumentation needed to collect resonant XES spectra, besides the standard monochromator used to select the energy ħΩ of the incident X-ray beam (present in every XAS beamline), XES requires an additional X-ray spectrometer able to analyze the energy ħω of the fluorescence X-rays emitted by the sample in the de-excitation processes consequent to the creation of a core hole by the primary ħΩ beam. A description of the most used XES spectrometers can be found elsewhere [90, 123], here we just recall that they can be basically divided into (*i*) focusing Johansson-type monochromators in Rowland geometry, performing a scansion across the ħω spectral range of interest [745-753] and (*ii*) crystal analysers in von Hamos geometry, which uses a cylindrically curved crystal to produce a polychromatic line focus that disperses the X-rays with different energies onto a position sensitive detector [754-757, 758, Hudson, 2007 #799, Hasegawa, 2007 #800, Szlachetko, 2007 #801, Maeo, 2009 #802, Mattern, 2012 #803, Alonso-Mori, 2012 #804, Szlachetko, 2012 #805, Szlachetko, 2013 #807]. In Johansson-type spectrometers, the XES spectrum is acquired point per point, whereas in von Hamos-based instruments it is acquired in a single shot, without any motion of the optics, see Figure 13a. The latter set up is consequently more suitable for time resolved studies. With this respect, an example is reported in Figure 13b; in this study Szlachetko *et al.* [759] followed by non resonant (nr)-ctc XES (left) and XAS (right) spectroscopies with a sub-second time resolution, the decomposition of platinum acetylacetonate ($Pt(acac)_2$) in hydrogen induced by flash heating. The time resolved data reported in Figure 13b, clearly highlighted the presence of an intermediate reaction step (B) between the starting $Pt(acac)_2$ complex (A) and the final Pd^0 nanoparticles (C).

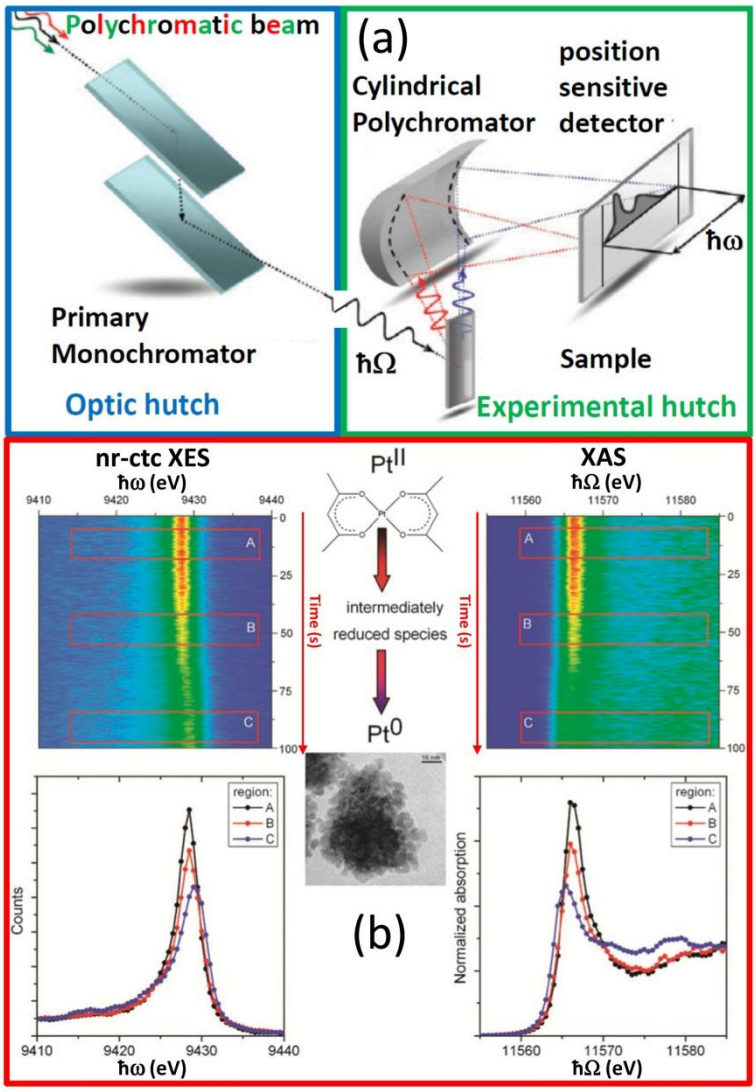

Figure 13. Part (a): Schematic representation of the von Hamos spectrometer available at the SuperXAS beamline of the SLS at the PSI. Part (b), top panel: In situ decomposition of $Pt(acac)_2$ under 5% H_2 in He at 150 °C followed by nr-ctc XES (left) and XAS (right) spectroscopies. Part (b), bottom panel: the data are reported in 2D plot with the time scale running from top to bottom. The corresponding 1D spectra from zones A, B and C are plotted in the lower panels. The suggested reaction path from $Pt(acac)_2$ to Pd^0 nanoparticles is drawn in the middle section of part (b). Adapted with permission from [759], copyright RSC 2012.

Summarizing, X-ray emission spectroscopy (XES) is a photon in/photon out process that probes the partially occupied density of electronic states of a material. In this regard it is, on one side, a complementary technique with respect to XANES (Section 3.2.1) which provides insights on the unoccupied states. The combination of XAS and XES is consequently highly informative in the characterization of the electronic, geometric and magnetic structure [36, 38, 39, 116, 117, 121-123, 732, 735, 740, 741, 760-766].
On the other side, XES is somehow related with PES spectroscopy (Section 3.2.5), that also probes the occupied density of states. The main advances of XES with respect to PES is the fact that XES uses hard X-rays, so allowing measurements of liquid and gases or of heterogeneous catalysts under reaction conditions. The main disadvantage is the low accessibility, as third generation synchrotron radiation beamlines are required.

3.2.3 High-energy resolution fluorescence detected (HERFD) XANES

In a conventional XANES experiment, one among the following signals deriving from the X-ray-matter interaction (see Scheme 6 in the appendix, Section 6.1) can be detected: (i) the transmitted photons; (ii) the total fluorescence yield (TFY), integrated over all the de-excitations related to the excited atomic species; (iii) the total or partial electron (TEY or PEY) decay of the sample, while scanning the incident photon energy $\hbar\Omega$ across the edge. In such experiments, besides the limits of the X-ray optics, there is a lower limit in the FWHM of the observed features (ΔE_{TFY}), that is set by the life-time broadening of the core hole of the selected edge: $\Delta E_{TFY} \approx \Gamma_{core} \equiv \hbar/\tau_{core}$, where τ_{core} is the life time of the core hole created by the absorbed X-ray. With the experimental setups reported in Figure 13a, it is possible to follow the evolution of the fluorescence emission at a given $\hbar\omega$ (corresponding to a particular fluorescence decay channel) upon scanning the incident photon energy $\hbar\Omega$. In such a way, being the decay transition due to an electron coming from an higher level (HL), that has a core hole with a longer τ_{HL} life-time ($\tau_{HL} >> \tau_{core}$), the resulting spectrum is characterized by and intrinsically lower broadening $\Delta E_{HERFD} \approx [(\Gamma_{core})^{-2} + (\Gamma_{HL})^{-2}]^{-½}$, where $\Gamma_{HL} \equiv \hbar/\tau_{HL}$, see dashed grey line in the inset of Figure 12e**.** This effectively leads to spectra with a higher energy resolution and sharper features [39, 76, 90, 122, 125, 767-770]. This life-time suppressed XANES is generally referred to as high-energy resolution fluorescence detected (HERFD) XANES and can be described as a partial fluorescence yields that should be treated in the framework of the Kramer-Heisenberg theory [121].
We conclude this section reminding that the HERFD mode allows also the collection of oxidation state-specific EXAFS spectra [117, 121]. This is possible in cases where the different oxidation states are characterized by slightly different florescence lines $\hbar\omega$, that can be selected with the analyser spectrometer (Figure 12e). With the same principle, also spin-selective EXAFS spectra can be recorded [771] because of the spin-sensitivity of the Kβ' fluorescence line.

3.2.4 X-ray magnetic circular dichroism or magnetic coordination compounds

The X-ray magnetic circular dichroism (XMCD) spectrum, $\mu_{XMCD}(E)$, is defined as the normalized difference spectrum of two XAS spectra collected in a magnetic field, one acquired with left circularly polarized beam, and one with right circularly polarized beam: $\mu_{XMCD}(E) = [\mu_L(E) - \mu_R(E)]/[\mu_L(E) + \mu_R(E)]$ [117]. To maximize the XMCD signal, the magnetization vector of the system is set either parallel or antiparallel to the polarization vector of the X-ray beam. A non-zero XMCD signal is observed only in magnetic systems and it gives information on the magnetic properties, such as spin and orbital magnetic moment. Consequently, XMCD is a major characterization tool for ferromagnetic metals, oxides and their surfaces, as well as for paramagnetic sites in bio-inorganic chemistry and coordination compounds [772]. The technique was able to bring new insight in the investigation of transition metal supported catalysts [582, 773, 774] and in bio-catalysis [775]. Usually, the XMCD measurement are performed at cryogenic temperatures and the XMCD signals are followed either by varying the magnetic field at constant temperature or by varying the temperature at fixed magnetic field [776].
In the field of coordination compounds, XMCD has been widely used in the investigation of single-molecule magnets [128-135]. In this regard, Badia-Romano *et al.* [135] have recently investigated the intra-molecular exchange interactions within the single-molecule magnet "butterfly" molecule $[Fe_3Ln(\mu_3\text{-}O)_2(CCl_3COO)_8(H_2O)(thf)_3]$, where Ln indicates a lanthanide atom (see Figure 14a for the structure of the Dy homologue), by combining XMCD, vibrating sample magnetometer (VSM) and *ab initio* simulations. Compounds with Ln = Gd and Dy, represent extreme cases where the rare earth center presents single-ion isotropic and uniaxial anisotropy. The Dy single-ion uniaxial anisotropy is estimated from *ab initio* calculations. Low-temperature (T ~ 2.5 K) hard X-ray XMCD at the Ln L_2, L_3 edges (Figure 14c,d) and VSM measurements as a function of the magnetic field indicate that the Ln moment dominates the

polarization of the molecule by the applied field. Within the $\{Fe_3LnO_2\}$ cluster (Figure 14a, right part) the Ln-Fe_3 sub-cluster interaction (Figure 14b) is determined to be antiferromagnetic in both Dy and Gd compounds, with values $J_{Dy\text{-}Fe3} = -0.4$ K and $J_{Gd\text{-}Fe3} = -0.25$ K, by fitting to spin Hamiltonian simulations that consider the competing effects of intra-cluster interactions and the external applied magnetic field. Authors found that in the uniaxial anisotropic $\{Fe_3DyO_2\}$ case, a field-induced reorientation of the Fe_3 and Dy spins from an antiparallel to a parallel orientation takes place at a threshold field ($\mu_0 H = 4$ T). In contrast, in isotropic $\{Fe_3GdO_2\}$ this reorientation was not observed [135]. Authors also measured the Fe K-edge XMCD signal, that however is very low, since Fe(III) has a quenched total orbital moment [135]. Indeed, for a d^5 ion, $L_z = 0$ in the 3d states and, consequently, a very low signal from is expected for the 1s to 4p excitations.

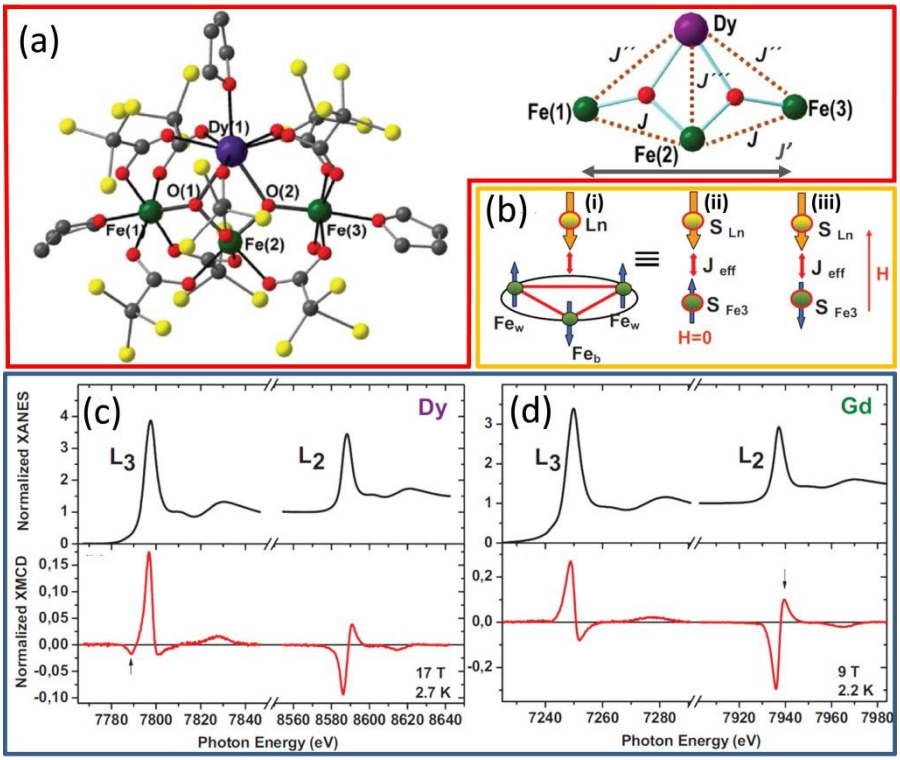

Figure 14. Part (a), left panel: structure of the $[Fe_3Dy(\mu_3\text{-}O)_2(CCl_3COO)_8(H_2O)(thf)_3]$ complex; part (a), right panel: the $\{Fe_3DyO_2\}$ magnetic core of the compound and the defined interatomic-exchange parameters. Part (b): scheme (i) represents the interaction Ln-Fe_3 (double headed arrow) within the $\{Fe_3LnO_2\}$ cluster (Ln = Gd or Dy). The Fe_3 group (red triangle) is substituted by a single spin S_{Fe3}. Simplified magnetic situations in cases null or high applied magnetic fields are reported in schemes (ii) and (iii), respectively. Part (c): Dy L_2- and L_3-edges XANES spectra (top) and XMCD signal (bottom) of $Fe_3Dy(\mu_3\text{-}O)_2(CCl_3COO)_8(H_2O)(thf)_3]$ complex. Part (d): as part (c) for the Gd homologue. Adapted with permission from [135], copyright APS 2013.

Wackerlin *et al.* [777] have provided combined XPS, XMCD experimental evidences, supported by DFT calculations, for an exchange-stabilized magnetic moment in a synthetically designed, non-planar and non-aromatic Co(II)-complex adsorbed on a ferromagnetic Ni substrate. Indirect magnetic coupling of Mg porphyrin to a ferromagnetic Co substrate was also investigated by the same group [778].

Furthermore, the electronic and magnetic properties of a star-shaped molecule exhibiting a ($Mn^{II}_4O_6$) core have been reported by Khanra *et al.* [779]. The peculiarity of this compound is weak magnetic coupling constants compared to other similar polyoxo compounds. This leads to complicated low-lying magnetic states, in which the ground state is not well separated from the upper-lying states, yielding a high-spin molecule with a giant magnetic moment of up to 20 μ_B/formula unit. Authors combined *ab initio* electronic band structure calculations with the study of local electronic structure around the Mn^{2+} ions with charge-transfer multiplet calculations, to fully interpret the multi-technique experimental data collected to characterize the compound, including XRD, magnetometry, XPS, XES and XMCD.

A last example is the study of two paramagnetic high-spin molecules $[Cr\{(CN)Ni(tetraethylenepentamine)\}_6](ClO_4)_9$ (intramolecular ferromagnetic coupling) and $[Cr\{(CN)Mn(N,N,N'\text{-}(tris(2\text{-}pyridylmethyl)\text{-}N'\text{-}methylethan)1,2\text{-}diamine)\}_6](ClO_4)_9 \cdot 3thf$ (intramolecular antiferromagnetic coupling) investigated by Arrio *et al.* [776] using XMCD. The X-ray absorption and dichroic spectra were calculated in the ligand field multiplet model to determine the crystal field parameters and the local orientation of the magnetic moments. The authors obtained the local magnetization curves at the Ni(II) and Mn(II) L_2- and L_3-edges for both molecules [776].

3.2.5 Photoelectron spectroscopy: basic principles and synchrotron applications

As introduced in Section 3.1, photoelectron spectroscopy (PES) detects the kinetic energy of the electrons escaped from the surface of the sample when soft X-ray (200-2000 eV) radiation or UV (10-45 eV) radiation are used (see Scheme 6 in the appendix, Section 6.1). In the first case the technique is usually called X-ray photoelectron spectroscopy (XPS) and allows the examination of core levels, whereas in the latter case we refer to ultraviolet photoelectron spectroscopy (UPS), able to obtain information on valence levels. PES has been successfully used to study the physical properties of transition metal complexes since in a typical experiment the electrons, emitted after excitation of the electronic states by photons of a specific energy, are sensitive to the atomic number of the emitting atom as well as to the principal quantum number of the bound electron, the angular momentum and the chemical environment. In addition, PES spectra afford information on electronic, magnetic and spatial structure of the transition metal complexes [640, 780-786].

UPS and XPS are sensitive methods which are widely used in catalyst investigations: if one considers XPS, the X-rays may penetrate deep into the sample, the ejected electrons have only a limited escape depth. With energies around 1400 eV, ejected electrons from depths typically greater than 10 nm (depending on the specific experimental conditions such as average Z of the sample, adopted X-rays energy and their incidence angle) are not contributing to primary photoelectric peaks since they have a low probability of leaving the surface without undergoing an energy loss event. Most of the methods for the investigation on metal complexes on catalytic surfaces are bulk sensitive and not surface sensitive, while only several atomic layers with a specific structure, that is not necessarily the same as the bulk structure, are directly participating in the catalytic process. Conventionally this technique operates at ultra-high vacuum conditions, with the pressure in the 10^{-10} mbar range required to allow the photoelectrons to reach the detector. There are few synchrotron-based XPS facilities worldwide where a complex differential pumping system allows XPS spectra to be collected at pressure of few mbar in the close vicinity of the sample surface [787-790]. However, besides these remarkable facilities, standard XPS and UPS setups remain (and will likely remain in the future) ultra-high vacuum instrumentations.

XPS (UPS) allows the investigation of almost all elements of the periodic table and it is able to detect core (and valence) bands affording considerable information about chemical structure. Furthermore the technique is giving information about absolute atomic concentration since the number of electrons recorded for a given transition is proportional to the number of atoms at the surface. In practice, however, an accuracy of 10% is typically quoted for routinely performed XPS atomic concentrations, because of the difficulty in quantifying readsorbtion processes. Nevertheless the precision of XPS makes the technique very powerful. The binding energy of a core-level electron depends also on the surroundings of atoms. Binding energy shift due to environment effects is usually named chemical shift. Non-equivalence of binding energies for an element in different chemical compounds can arise from various reasons such as difference in the formal oxidation and coordination states, different lattice parameters and so on. Then core level binding energies provide an accurate local probe of the electronic structure changes of an atom in different chemical environments and afford important information on surface reactivity changes. Core level XPS data also allow to probe the orbital mixing of the ligand and metal [791]. In principle, one can assume that the energies involved in a XPS experiment are well defined in terms of the binding energy of the electronic states of atoms, but the structure of 3s, 3p, and 2p XPS peaks of transition metals is additionally affected by a number of effects, among which the atomic multiplet splitting is the most important [120]. Secondarily, the XPS spectra are also influenced by several many-electron effects, such as the reduction of extension of the atomic multiplets due to the interaction of the states of the basic configuration with a lot of higher-lying excited configurations. To deal with this effect, we can assume that the multiplet structure is not violated, and consider the compression of multiplets by scaling the integrals of electrostatic interaction, with scaling factors typically in the 0.7 – 0.8 range [792].

In general, for the full interpretation of XPS spectra, DFT calculations are of paramount importance. For instance, DFT studies indicate that often final state contributions can be significant, in particular for noble metals like Cu and Ag, where the low density of states at the Fermi level yields a rather inefficient screening of the core hole [793, 794].

On the instrumental ground, for laboratory PES experiments, X-ray tubes (usually with Al or Mg cathode) and He gas-discharge lamps are used in XPS and UPS instruments. Although conventional high intensity sources provide discrete incident photon energies at high resolution, affording detailed information from the photoionization cross sections, they cannot be used to probe the photon energy dependence of XPS spectra.

Development of synchrotron radiation sources made available a continuous range of photon energies surpassing the intensity of conventional laboratory vacuum UV and X-ray tubes by several order of magnitudes. There are several advantages in the use of synchrotron light with respect to common laboratory X-ray sources, first of all the higher photon flux and the possibility of focusing of an X-ray beam into a small spot increase the spatial resolution. An additional benefit of the high photon flux is the possibility to increase the energy resolution ΔE in the determination of the electron kinetic energy obtained by improving the monochromaticity of the exciting photons. Moreover, the high collimation of synchrotron radiation beams is a crucial point in increasing the Δk resolution in angle-resolved PES experiments. However, the high photon flux has an important drawback in PES experiments, consisting in a high

electrinc charging of the sample; this makes SR-PES experiments on purely conducting samples difficult, needing accurate charge compensation with an electron gun. The experimental difficulties are even more severe for insulating powdered materials because it is virtually impossible to exactly compensate for each sample grain the positive charge induced by the X-ray beam with the negative charge induced by the electron gun. As a consequence the observed PES components are subjected by an energy broadening that hampers the potential energy resolution available using a synchrotron source. Finally, synchrotron light has the property of excitation energy tunability, which allows changing the information depth and the photoelectron cross section.

We report here some nice examples of the use of synchrotron XPS to address issues such as chemical bonding and structures in transition metal complexes. Hsin-Tien Chiu and coworkers found correlation between metal-ligand bond distance and XPS binding energies of the ligand in metal complexes. Specifically, they studied the variation of N 1s binding energy for several metal complexes such $Ta(NEtMe)_5$, *t*-BuN=$Ta(CH_2Bu\text{-}t)_3$, *t*-BuN=$Ta(NEtMe)_3$, *t*-BuN=$Ta(NEt_2)_3$, (*t*-BuN=)$_2$W(NHBu-*t*)$_2$, and N≡Cr(OBu-*t*)$_3$ [795].

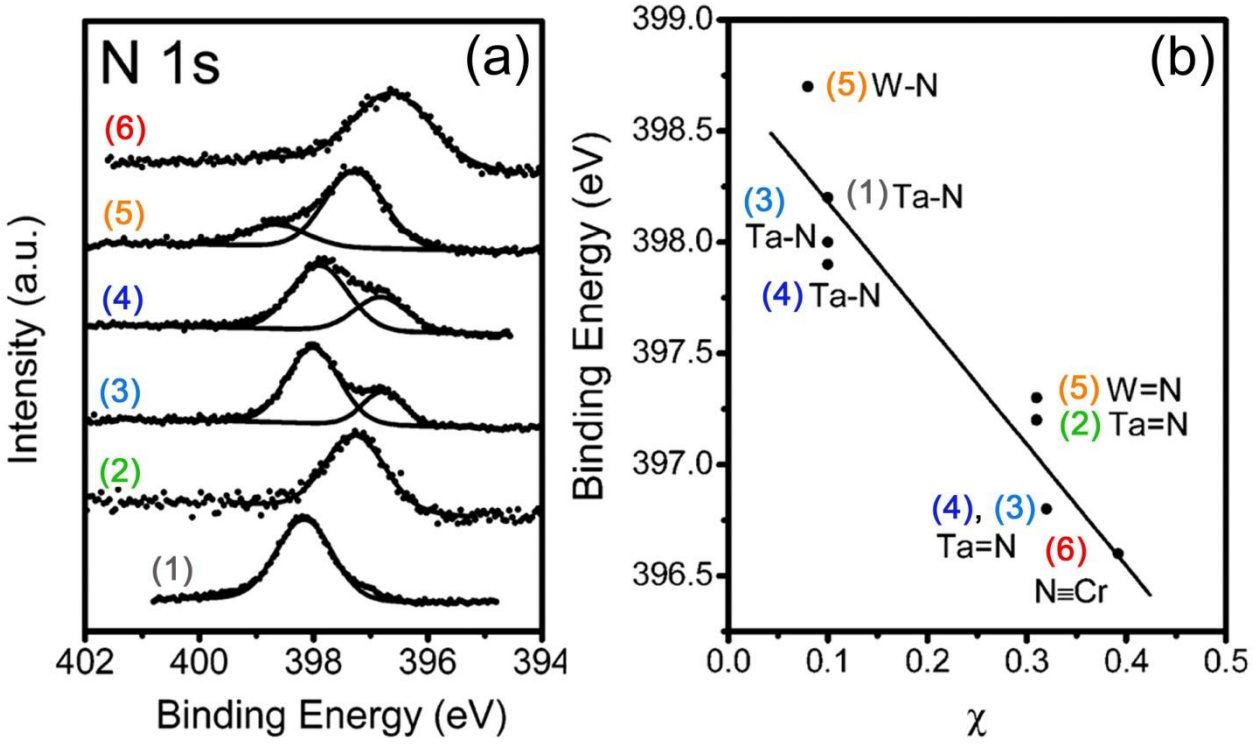

Figure 15. Part (a): N 1s synchrotron XPS for $Ta(NEtMe)_5$ (1), *t*-BuN=$Ta(CH_2Bu\text{-}t)_3$ (2), *t*-BuN=$Ta(NEtMe)_3$ (3), *t*-BuN=$Ta(NEt_2)_3$ (4), (*t*-BuN=)$_2$W(NHBu-*t*)$_2$ (5), and N≡Cr(OBu-*t*)$_3$ (6), adsorbed on Cu(111) surface at 300 K. Part (b): correlation of N 1s binding energies to χ parameter for $Ta(NEtMe)_5$ (1), *t*-BuN=$Ta(CH_2Bu\text{-}t)_3$ (2), *t*-BuN=$Ta(NEtMe)_3$ (3), *t*-BuN=$Ta(NEt_2)_3$ (4), (*t*-BuN=)$_2$W(NHBu-*t*)$_2$ (5), and N≡Cr(OBu-*t*)$_3$ (6). Adapted with permission from ref. [795]. Copyright (2003) American Chemical Society.

The *t*-BuN=$Ta(NEtMe)_3$ complex, exhibits two well resolved peaks at 398.0 and 396.8 eV with 3:1 integration (see curve (3) in Figure 15a), consistent with the stoichiometry ratio for two types of N atoms having three amido and one imido ligands. The shift toward higher binding energies of the W complex (curve (5) in Figure 15a) with respect to Ta complexes labelled as (3) and (4) is consistent with a larger Pauling electronegativity for W (2.36) than for Ta (1.5). The observed N 1s bonding energies values for various metal complexes follow the general trend: amido > imido > nitrido. The molecular orbital bonding picture indicates that the N atom of the ligands contributes more to the M–N bonding orbitals than the metal atom. The authors defined the parameter χ as: $\chi = (r_M + r_N) - R_{M-N}$, where r_M and r_N are the bonding radii of M and N and R_{M-N} is the M–N bond distance calculated from the crystallographic data. χ describes how the M–N bond gets shortened relative to the sum of the free atom values as the M–N bond.

The plotting of the N 1s binding energies as a function of the χ parameter is shown in Figure 15b. On the basis of XPS data it is possible to surmise that the observed N 1s binding energy values correlate better with the corresponding M–N bond distance than with bond-order parameters.

In 2003, Kobayashi and coworkers published the first report of XPS study by using as X-ray source a third generation synchrotron radiation facility [796]. In hard X-ray PES experiments (HXPES) using undulators, X-rays photon fluxes higher than 10^{11} photons/s can be obtained even after the reduction of bandwidths down to around 50 meV or less. In principle a total resolution of 60 meV can be achieved at 8 keV, but normally for practical purposes a total resolution of 200–250 meV is used [797]. HXPES has the advantage with respect to conventional photoemission spectroscopy to be a potentially bulk-sensitive technique measurements, due to the increased escape depth of the high-kinetic-energy

photoelectrons produced (typically > 5 nm [796]). The bulk-sensitivity of HXPES is realized by overcoming the problem of weak signal intensities due to the rapid decrease in photoionization cross section with increasing photon energy exploiting the enhanced incident photon flux from synchrotrons. Thus HXPES offers unique possibilities for detecting bulk electronic structures, and opens up the possibility of site-specific bulk-sensitive XPS [798, 799] when combined with the X-ray standing wave technique [800-802]. Such technique is widely used for the characterization of surfaces of materials, e.g. nanoscale advanced materials, electrodes of fuel cells, photocatalysts, etc [803], probing electronic structure, changes with ionization, and providing useful hints in the understanding of the physical properties and reactivity of such systems. The application on the study of metal complexes is much more limited, whereas HXPES characterization is mainly performed on thin films or heterogeneous catalysts. However this technique has been used also on metal complexes due to its ability to extract information on both initial and final state for systems involved in redox processes. Indeed, both the effect of electronic structure on redox processes and the changes in electronic structure that occur as a result of redox events can be extracted from this kind of XPS data [804].
In addition, the combined use of synchrotron-XPS and XANES can highlights subtle differences in the electronic structure and chemical bonding in closely-related coordination compounds. As an example, a combined gas phase synchrotron photoabsorption (XANES) and photoemission (XPS) experiment on ethyl-ferrocene, vinyl-ferrocene, and ethynyl-ferrocene, have been performed by Zanoni and coworkers. The closely related molecules differ only in the unsaturation degree of the C–C bond of the substituent group and the combination of the two techniques can afford information on the state of charge of the C atoms of the substituent group in the three molecules, and on the extent of conjugation of the C–C moiety with the cyclopentadienyl ring. XANES and XPS data are useful for investigating the preservation or loss of the unsaturation in the anchoring arm upon functionalization reaction of hydrocarbon-monosubstituted ferrocenes on surfaces [805]. High resolution C 1s XPS spectra of the three ferrocene derivatives in gas phase are reported in Figure 16.

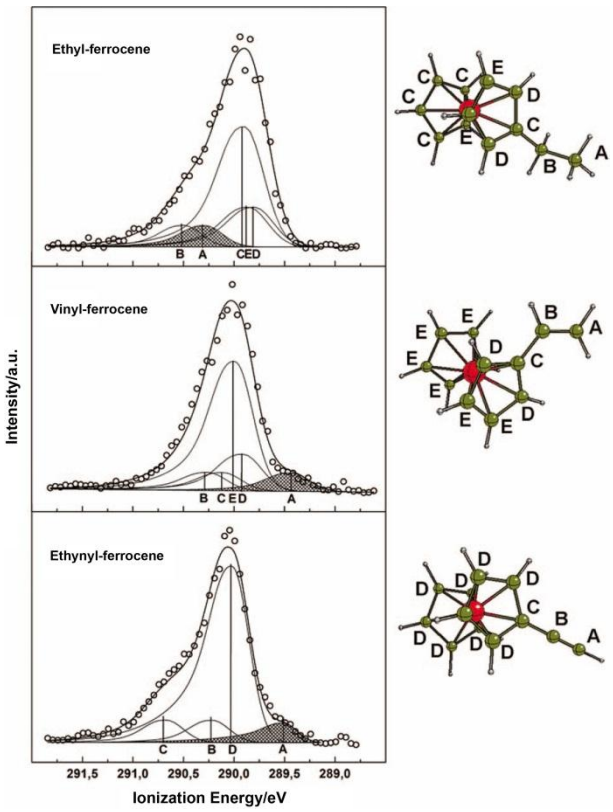

Figure 16. C 1 s XPS of ethyl-ferrocene, vinyl-ferrocene, and ethynyl-ferrocene (circles) obtained at 320 eV photon energy, reported with the results of the fitting procedure (solid lines). Theoretical ionization energies are represented by vertical bars. The different components are labelled according to the capital letters from A to E, which identify the non-equivalent carbon atoms in the molecules sketched on the right hand side. Adapted with permission from ref. [805]. Copyright (2012), AIP Publishing LLC.

The same carbon site in the different molecules shows different chemical shifts and distinctive trends of chemical shifts are observed for the A, B, and C atoms. The data have been rationalized in terms of initial and final state effects influencing the C 1s ionization energy value and related to the different mechanisms of electron conjugation between the ferrocene ring and the substituent, *i.e.* the σ/π hyperconjugation in ethyl-ferrocene and the π-conjugation in vinyl-ferrocene, and ethynyl-ferrocene.

4 Applications in catalysis

We will discuss separately applications in homogeneous catalysis (Section 3.1) and applications in heterogeneous catalysis (Section 3.2). Before entering in the discussion, we will present some concepts of general validity.
The main goal of the present section is to describe the synchrotron radiation methodologies (mainly XAS and XES) that allow to understand, at the molecular level, the structure of the catalytic site and its modification along the whole cycle. The vast majority of the cases catalysts do not exhibit long range order. This is obviously the case for homogeneous catalysis, where reactants, products and catalysts are in the liquid phase. For heterogeneous catalysis, in which the reaction is confined to the interface between the catalyst (a solid phase) and the reactants that are either in the liquid or in the gaseous phases, the lack of long range order still holds in most of the cases. In fact in order to maximize such interface most of the solid supports are high surface area materials (10^2–10^3 m^2 g^{-1}) with a very poor crystallinity (e.g. γ-Al_2O_3 [445, 696, 697, 806], active carbons [713, 807, 808] or polymers [809, 810]) or amorphous (e.g. silica [359, 811]). This implies that usually XRD [213] cannot be used to determine the structure of the catalytic active centres. This makes EXAFS the most suited characterization technique to understand the structure of the catalytic sites [62-64, 74, 76, 147, 460, 812], while XANES [67, 68, 76] and XES [76, 117, 122, 125, 324] are informative for its electronic structure. Exception to this statement is made for two main classes of crystalline microporous catalysts, where XRD has played a role: we are speaking about zeolites [285, 813-815] (that are industrially widely used) and metal-organic frameworks [816] (MOFs, which are of potential interest in the near future [817, 818]). However, also for zeolites and MOFs, when XRD data have been complemented by a XAS study, a better understanding of the material was achieved [64, 67, 79, 147].
The great benefit of XAS and XES spectroscopies applied to catalyst investigation is related to the high penetration depth of hard X-rays, allowing to measure catalysts under operation conditions, i.e. in presence of reactants and products from the gas or liquid phases. This is a mandatory step to understand all the intermediate steps. The strong connection between catalysis and XAS is testified by the large number of contributions related to catalysis (from 7 up to 19%) presented in the fifteen XAS conferences that have taken place in the last three decades (since 1981 in Daresbury, UK, to 2012 in Beijing, China) and by the number of contributions related to XAS (from 16 to 28%) that have been presented in the four conferences on *operando* spectroscopy (from 2003 in Lunteren, NL, to 2012 in Brookhaven US), see ref. [76] for a detailed statistic.
Section 4.1 is devoted to discuss the characterization of homogeneous catalysts, while in section 4.2 we will treat the case of heterogeneous catalysts. For sake of brevity, the case of *quasi-homogeneous* catalysis [819-823] will not be discussed.

4.1 Homogeneous catalysis

The great advantage of homogeneous catalysis is that the structure of the precursor of the active species is perfectly known. It is the complex dissolved in the solution, often named as "precatalyst" [824], the structure of which can be determined in the solid phase by diffraction techniques and/or by solid state NMR. Once dissolved in the solution, the structure of the complex will undergo relaxation of bond lengths and angles that can be monitored by EXAFS and NMR. In case of paramagnetic species also EPR can be used. The entity of such distortion is solvent dependent as different solvent molecules (polar, apolar) interact differently with the complex. Accurate DFT studies, with a periodic approach for the solid state, and with a cluster approach (including the solvent effects), can validate the experimental findings. The critical point is that the precatalyst is converted to the true catalysts in the reaction medium (eventually with the use of an activator) and that its structure may in some cases significantly differ from that of the well-characterized precatalyst.
Homogeneous catalysts represent an ideal playground for XAS spectroscopies because the dilution of the active molecule inside a liquid medium implies a perfect homogeneous dispersion of the absorbing X-ray sites in the solvent. This implies that the optical thickness of the sample, $\mu(E)x$, is uniform and that the quality of an EXAFS data collection will not be deteriorated by small fluctuation of the X-ray beam on the sample along the long energy scan needed to collect a full EXAFS spectrum. This is particularly true when the metal center of the coordination compound is a high Z-element, because its K-edge will occur in the hard X-ray region, where the molecules of the solvent are weakly absorbing X-rays. This fact allows to compensate the usually high dilution of the complex (usually few mM) by a large thickness of the samples, making in some cases possible a measure in transmission mode. This is the case of 10 mM $[Ru(bpy)_2(AP)_2]^{2+}$ in water (see Figure 17).

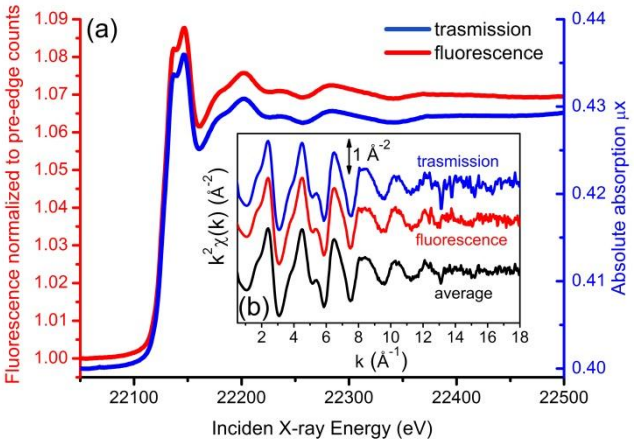

Figure 17. Part (a) pre-edge subtracted Ru K-edge absorption spectra of 10 mM $[Ru(bpy)_2(AP)_2]^{2+}$ in water collected in fluorescence and in transmission modes, red and blue curves, respectively. Fluorescence data have been normalized imposing the average pre-edge counts to unit; the contribution of Ru fluorescence is around 8% of the background. Transmission data have been plotted imposing the pre-edge μx absorption equal to 0.4, as expected by 0.6 cm of water at 22100 eV. The low edge jump of the spectrum collected in transmission mode is remarkable ($\Delta\mu x = 0.03$). Parts (b): k^2-weighted $\chi(k)$ function obtained averaging along the three scans the fluorescence (red top curves) and the transmission (blue middle curves) EXAFS spectra. The bottom black curves report the $k^2\chi(k)$ function obtained averaging the fluorescence and the transmission $k^2\chi(k)$ functions. Part (a) unpublished, part (b) adapted with permission from [396], copyright (2009) IoP.

At the Ru K-edge (22.1 keV) the X-ray absorption length in water is larger than 1.5 cm. This allowed Salassa *et al.* [396] to use a sufficiently thick sample holder to obtain in transmission mode and edge jump of ($\Delta\mu x = 0.05$). The fluorescence signal was also collected simultaneously.

The quality of the $k^2\chi(k)$ functions obtained from the spectra measured in transmission mode (blue curves in Figure 17b) is impressive for a sample with so low edge jump, and it is due to the high homogeneity of the solution and to the high stability of beamline (BN29 at the ESRF). Authors performed the EXAFS data analysis on both the fluorescence and transmission data sets obtaining, within experimental errors, the same values for all the optimized parameters. This fact allowed them to average the fluorescence and transmission data sets, resulting in the black spectrum in Figure 17b. The same data analysis was then repeated for the final averaged data set, resulting in optimized parameters compatible with those obtained in the two previous analyses, but characterized by smaller error bars [396]. The same group has investigated with synchrotron techniques (using both X-ray absorption and X-ray scattering) the structure of several ruthenium complexes in solution such as $[Ru(bpy)(AP)_4]^{2+}$ [396], $[Ru(bpy)_2(AP)_2]^{2+}$ [396] $[Ru(bpy)_2(AP)(H_2O)]^{2+}$ [396], cis-$[Ru(bpy)_2(CO)Cl]^{+}$ [720], cis-$[Ru(bpy)_2(py)_2]^{2+}$ [825-828] (AP = 4-aminopyridyne; py = pyridine; bpy = 2-2′-bipyridyne).

In the following we will provide an overview on the recent studies that, exploiting synchrotron based techniques, contributed in improving the knowledge of catalysts working in homogeneous conditions for: polymerization reactions (section 4.1.1); oligomerization or cyclization reactions (section 4.1.2); isomerization reactions (section 4.1.3); and coupling reactions (section 4.1.4).

4.1.1 Polymerization reactions

Hu *et al.* [829] reported a complete study on the synthesis and characterization of Group IV metal complexes (Ti, Zr and Hf) that contain a tetradentate dianionic [OSSO]-carborane ligand $[(HOC_6H_2tBu_2\text{-}4,6)_2(CH_2)_2S_2C_2\text{-}(B_{10})H_{10}]$. Reactions of $TiCl_4$ and $Ti(OiPr)_4$ with the [OSSO]-type ligand afforded a six-coordinated titanium complex $[Ti(OC_6H_2)tBu_2\text{-}4,6)_2(CH_2)_2S_2C_2\text{-}(B_{10}H_{10})Cl_2]$ and a four-coordinated titanium complex $[Ti(OC_6H_2tBu_2\text{-}4,6)_2\text{-}(CH_2)_2S_2C_2(B_{10}H_{10})(OiPr)_2]$, respectively. $ZrCl_4$ and $HfCl_4$ were treated with the [OSSO]-type ligand to give a six-coordinated zirconium complex $[Zr(OC_6H_2tBu_2\text{-}4,6)_2\text{-}(CH_2)_2S_2C_2(B_{10}H_{10})Cl_2(thf)_2]$ and a six-coordinated hafnium complex $[Hf(OC_6H_2tBu_2\text{-}4,6)_2(CH_2)_2S_2C_2\text{-}(B_{10}H_{10})Cl_2]$. All the complexes were fully characterized by IR, ^1H and ^{13}C NMR spectroscopy, and elemental analysis. The authors also provided single crystal XRD studies on the titanium complexes, founding the expected different coordination geometry due to steric hindrance effects. The local atomic environment of the metal center in the zirconium and in the hafnium complexes was further confirmed by Zr K- and Hf L_3-edge EXAFS analysis, respectively [829]. Corresponding XANES spectra confirmed the expected charge on the metal site. Authors demonstrated that the six-coordinated titanium complex shows a good activity toward ethylene polymerization as well as toward copolymerization of ethylene with 1-hexene in the presence of methylaluminoxane (MAO) as cocatalyst (up to 1060 kg[mol(Ti)]$^{-1}$h^{-1} in the case of 10 atm of ethylene pressure).

4.1.2 Oligomerization and cyclization reactions

The group of Brückner [830] combined *operando* EPR under elevated ethylene pressure and *in situ* XAS to discriminate between active and deactivating Cr species in the ethylene tetramerization reaction. Authors founded that, starting from Cr(III) in the $Cr(acac)_3$ precursor, a (PNP)Cr(II)-$(CH_3)_2$ complex (PNP = bidentate diphosphinoamine) is formed upon adding bidentate diphosphinoamine and modified methylaluminoxane (MMAO), which is the active species that converts ethylene to 1-octene by passing a reversible redox cycle, while reduction to Cr(I) leads to deactivation.

Miyoshi *et al.* [831] deeply investigated the aerobic intermolecular cyclization of acrylic acid with 1-octene to afford α-methylene-γ-butyrolactones, catalysed by the $Pd(OCOCF_3)_2/Cu(OAc)_2{\cdot}H_2O$ system. They found that the accumulation of water generated from oxygen during the reaction causes deactivation of the Cu co-catalyst. This prevents regeneration of the active Pd catalyst and, thus, has a harmful influence on the progress of the cyclization reaction. They concluded that both the substrate conversion and product yield are efficiently improved by continuous removal of water from the reaction mixture. Authors provided also a convincing model explaining the cyclization mechanism. Pd K-edge EXAFS data agree with the existence of the intermediates bearing acrylate (Pd–O bond), η^3-C_8H_{15} (Pd–C bond), or $C_{11}H_{19}O_2$ (Pd–C bond) moieties on the Pd center as the resting-state compounds. Furthermore, Cu K-edge XANES data showed that not only Cu(II), but also Cu(I), species are present when the reaction proceeds efficiently. Authors concluded that the Cu(II) species is partially reduced to the Cu(I) species when the active Pd catalytic species are regenerated [831].

4.1.3 Isomerization reactions

Jennerjahn *et al.* [832] investigated a selective iron-catalysed mono-isomerization of olefins, which allows for the selective generation of 2-olefins. In particular, the isomerization of 1-octene has been performed in diglyme solvent on a large library of iron complexes, $[Fe_3(CO)_{12}]$, $[Fe_2(CO)_9]$, $[Fe(CO)_5]$, $[Fe(CO)_4]$, $Na_2[Fe(CO)_4]$, $[Fe(BF_4)_2]$, $[CpFe(CO)_2]^-$ and $Na_2[Fe(CN)_5NO]$ and in different basic or acidic environments. Using only iron carbonyl complexes without water and base resulted in a mixture of internal olefins. Conversely, yields in 2-octene higher than 92% were obtained with $[Fe_3(CO)_{12}]$ and $Na_2[Fe(CO)_4]$ complexes; in both cases KOH was added to the reaction solution [832]. DFT calculations were used to define the reaction path, with the corresponding activation barriers for the different transition states, for the isomerization reaction of 1- to 2-butene catalysed by $[Fe_3(CO)_{12}]$. EXAFS spectra were collected on the $[Fe_3(CO)_{12}]$ precatalyst (both in the solid state and in diglyme solution), proving the stability of the triiron dodecacarbonyl complex in solution. Then a third EXAFS spectrum was collected after 30 minutes of 1-octene isomerization reaction in diglyme/KOH at room temperature. The stability of the Fe_3 cluster under reaction condition was supported by the coordination number $N_{Fe–Fe} = 1.7 \pm 0.3$ ($N_{Fe–Fe} = 1.8 \pm 0.3$ before reaction; ideally $N_{Fe–Fe} = 2$ for an iron trimer). In the course of isomerization of 1-octene, authors found $N_{Fe–C} = 2{,}0 \pm 0.5$, a value that is in agreement with the two stable complexes computed by DFT with either 1-butene or 2-butene coordinated to the iron complex.

4.1.4 Coupling and addition reactions

According to the organic chemistry nomenclature [833, 834], addition reaction, takes place when two or more molecules combine to form a larger one. This implies that addition reactions require the presence of reactants having multiple bonds, such as alkenes (C=C), alkynes (C≡C) or molecules containing carbonyl (C=O) or imine (C=N) groups. Conversely, a coupling reaction concerns two hydrocarbon fragments that are coupled, usually with the aid of a metal catalyst [835].

In the themed issue of PCCP on "recent developments in X-ray absorption spectroscopy", Bauer, and Gastl used as example the iron-catalysed Michael addition reaction to provide a complete survey over synchrotron radiation and laboratory methods in homogeneous catalysis [466]. The authors reported a thorough investigation of the catalytic cycle by combining conventional X-ray absorption spectroscopy (XANES and EXAFS), RIXS and multi-dimensional spectroscopy. The catalytically active compound formed in the first step of the Michael reaction of methyl vinyl ketone with 2-oxocyclopentanecarboxylate was elucidated *in situ* by RIXS spectroscopy. The reduced catalytic activity of $FeCl_3{\cdot}6H_2O$ compared to $Fe(ClO_4)_3{\cdot}9H_2O$ was explained by the formation of a $[Fe^{III}Cl_4^-]_3[Fe^{III}$(2-oxocyclopentanecarboxylate-H)$_2(H_2O)_2^+][H^+]_2$ complex. Chloride was identified as catalyst poison with a combined XAS and UV-Vis study, which revealed that Cl^- binds quantitatively to the available iron centres that are deactivated by formation of $[FeCl_4^-]$. *Operando* studies in the course of the reaction of methyl vinyl ketone with 2-oxocyclopentanecarboxylate by combined XAS-Raman spectroscopy allowed the exclusion of changes in the oxidation state and the octahedral geometry at the iron site; a reaction order of two with respect to methyl vinyl ketone and a rate constant of $k = 1.413\ min^{-2}$ were determined by analysis of the C=C and C=O vibration bands. In the same work, the authors also report the technical detail of a dedicated experimental set-up designed to perform a simultaneous three-dimensional spectroscopic study (XAS, UV-Vis and Raman) of homogeneous catalytic reactions under *operando* conditions.

Fiddy *et al.* [836] reported a Pd K-edge EXAFS study on the Mizoroki-Heck coupling [837] of selected aryl bromides with acrylates catalysed by a series of Pd complexes of bidentate pyridyl-, picolyl-, diphenylphosphinoethyl- and diphenylphosphinomethyl-functionalised N-heterocyclic carbene. Authors reported that the catalyst activity is dependent on the type of solvent and base used and the nature of the "classical" donors of the mixed-donor bidentate ligand and its bite angle. They reported a mechanistic model for the pyridine-functionalised N-heterocyclic carbene complexes based on an *in situ* EXAFS study under dilute catalyst conditions (2 mM). The model involves pre-dissociation of the pyridine functionality and oxidative addition of aryl bromide in the early stages of the reaction, as well as formation of monomeric and dimeric Pd species at the time of substrate conversion.
Among all the data reported by Fiddy *et al.* [836] we will focus here on the results obtained on the Pd bromine carbene system, scheme (2) in Figure 18c. Authors used the EXAFS spectra of the Pd bromine carbene precatalyst in the solid state (curves 1 in Figure 18a,b) to check phases and amplitude functions generated by EXCURV98 [838-840]. The molecule was then diluted in N-methylpyrrolidone at 2 mM and measured in fluorescence mode to check whether any significant structural changes occur in solution (curves 2 in Figure 18a,b). Authors were able to reproduce the EXAFS spectrum of the solid phase with a four shell fit resulting in two C atoms at 2.02 Å, one N atom at 2.21 Å and one Br at 2.48 Å, in excellent agreement with XRD data where the three distances were refined at 2.002, 2.168 and 2.489 Å, respectively [841]. Note that the Pd-O distance of 2.002 Å is actually the average of two independent distances at 1.970 and 2.034 Å that cannot be resolved by EXAFS in a three shell fit. Comparable results were obtained from the fit of the sample in solution: resulting in two C atoms at 2.01 Å, one N atom at 2.20 Å and one Br at 2.48 Å. The Pt-O and the Pt-N contribution were obtained with Debye-Waller factors comparable with those obtained in the solid phase, while a much larger Debye-Waller factor was needed to reproduce the Pd-Br contribution in the liquid phase. Besides these technical aspects, authors concluded that the complex is stable in N-methylpyrrolidone solution at room temperature and that its first shells ligands remain bound even in a polar solvent [836].–

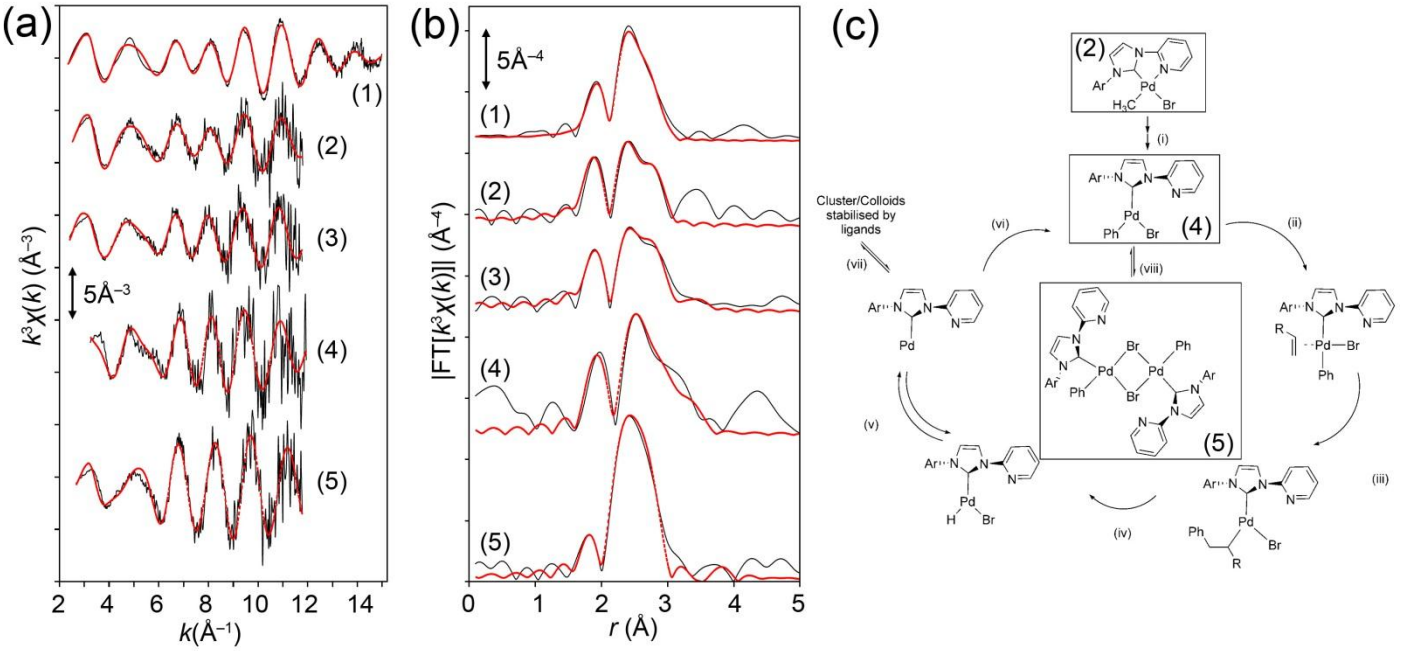

Figure 18. Part (a): Pd K-edge k^3-weighted EXAFS (phase-shift corrected for C back-scatterer atoms) of the Pd bromine carbene precatalyst, in the solid-state form (1) and in solution (2 mM in N-methylpyrrolidone) (2) and of the catalyst during the Mizoroki–Heck conditions at different reaction times and temperatures: 5 min at 353 K (3): 5 min at 403 K (4) and 20 min at 403 K (5). Black and red lines represent the experimental and theoretical fits respectively, the latter derived from spherical wave analysis in EXCURV98 [838-840]. Reported times represent the total reaction time at the given temperature; after reaction, the solution was quenched to room temperature and six EXAFS scans have been collected. Part (b): as part (a) for the corresponding carbon phase-shift-corrected FT. Spectrum (1) was measured in transmission mode, spectra (2)-(5) were collected in fluorescence mode. Part (c): Proposed mechanism for the Mizoroki–Heck reaction of bromoacetophenone with butyl acrylate (observed species characterized by EXAFS indicated by boxes labelled with the number referring to the corresponding spectrum; the remainder are all plausible transient species). Adapted with permission from [836], copyright Wiley (2007).

Fiddy *et al.* [836] used EXAFS analysis to face the following open questions: (i) Are Pd nanoparticles formed during the reaction? (ii) Is there evidence for the generation of Pd^0 by reductive elimination of 2-methylimidazolium salts from the starting precatalyst? (iii) Does the pyridine arm of the bidentate ligand detach from Pd during the catalysis? (iv) Is there any observable loss of bromide during the reaction that could offer an alternative possibility for alkene coordination?
Hence, butyl acrylate and p-bromoacetophenone were injected into the cell containing the 2mM solution of the Pd bromine carbene precatalyst. The liquid was gradually heated at 10 K min^{-1} up to the reaction temperature (403 K).

During this process, at certain intervals, the cell was rapidly cooled to 263 K to quench the reaction, thereby providing a "snapshot" of the intermediate species present in solution. The progress of the reaction was monitored under the same temperature regime by taking aliquots and analysing quantitatively the reaction mixture by gas chromatography [836].
The catalytic solution at room temperature (curves 3 in Figure 18a,b), before heating provided a structure with almost identical parameters to those observed for the non-catalytic N-methylpyrrolidone solution (curves 2 in Figure 18a,b). A second measurement was made after the catalytic solution had reached 353 K for 5 min. (curves 4 in Figure 18a,b). After this first heating step, the Pd pre-catalyst remained basically intact: the EXAFS analysis resulted in: two C at 2.03 Å, one N at 2.19 Å and one Br at 2.49 Å. However the fit was obtained with a relatively high Debye–Waller factor for the Pd-N shell [836]. Authors explained this observation either as the consequence of the weakening of the Pd–N_{py} bond or as the fact that some of the bidentate ligand acts as monodentate [836].
The EXAFS signal of the catalyst heated to 403 K for 5 min showed a significant change (curves 4 in Figure 18a,b). In this case the experimental EXAFS spectrum was reproduced using only two shells, namely: two C atoms at 2.01 Å and one Br atom at 2.48 Å. Any attempt to add a third Pd-N shell failed. This was interpreted as the break of the Pd–N_{py} bond (scheme 4 in Figure 18c) and the consequent creation of a site coordination vacancy on Pd thus allowing the co-ordination of the olefin, reaction (ii), Figure 18c. Prolonging the reaction time at 403 K the EXAFS spectrum underwent an additional important modification (curves 5 in Figure 18a,b). The experimental spectrum was reconstructed using two C at 2.00 Å and two Br at 2.45 Å and one Pd at 2.74 Å, justifying the structural model of the Pd-dimeric complex reported in scheme 5 of Figure 1c.
Summarizing, the EXAFS results reported in Figure 18a,b allowed the authors to suggest the catalytic cycle reported in Figure 18c, that is closely related to the mechanistic model already postulated by Evans *et al.* [842] in which a dimeric species acts as the starting catalyst. Note that the formation of a dimeric species is also consistent with the reaction profile and the model postulated by De Vries, in which the species involved in the actual catalytic cycle are monomeric and dimeric species and not soluble palladium colloids [843].
We finally close this section briefly mentioning the study of Benson *et al.* [844] who recently investigated the electronic states of rhenium bipyridyl electrocatalysts for CO_2 reduction combining Re L_3-edge XAS (10.5 keV) with DFT calculations. Authors were able to explain the high selectivity of the [Re(bpy)$(CO)_3$Cl] family of catalysts for the reduction of CO_2 in the presence of significant concentrations of H^+ sources.

4.2 Heterogeneous catalysis

Nowadays, XAS-based methods on heterogeneous catalysts have become very advanced [76]: time-resolved and *in situ*/*operando* measurements have become standard [147, 282, 445, 446, 812]and enhanced space resolution has become available[154, 155, 314, 845]. Furthermore, X-ray emission spectroscopy (XES) is more frequently used: HERFD [122, 767, 846] and valence band RIXS [847, 848] yield the electronic structure of the filled and unfilled density of states that is relevant to the bonding of the catalytic center. A small fraction of studies on heterogeneous catalysts deals with supported organometallic complexes and most of these, although not exclusively, are heterogenized homogeneous complexes [65, 678, 686, 849-861]. In contrast to supported metals and oxides, which contain many different surface sites and defects, the structure of organometallic complexes is precisely defined and obtaining structure – performance relations is more accessible. In a recent review, Takakusagi and coworkers summarized the structural determination of complexes on single crystal surfaces using total reflection fluorescence XAS [862], illustrating how the well-defined nature of the complexes facilitates structural characterization and its relation to performance. In this paragraph we summarize a selected number of typical examples and, even though this section focuses on X-ray absorption, we propose a quick survey of the literature about determining structure – performance relations that highlights how a single method generally does not provide definite answers while combining different methods, including theory, yields the desired relations. In most if not all cases, the defined nature of the complex contributed to the understanding of the structure – performance relationships.

4.2.1 Supported metathesis catalysts, an early example

A very early example of a heterogeneous complex was investigated at the SRS Daresbury in the early nineties. In this study, Mosselmans and coworkers investigated an alumina-supported molybdenum olefin metathesis catalyst during pretreatment and under catalytically-relevant conditions [863]. To this end, the catalyst was exposed to propylene. The time resolution achieved during the experiment was in the range of minutes, and was sufficient to observe the structural changes during the pretreatment using the XANES. In olefin metathesis, a carbon – carbon double bond is broken and a new one is formed. This redistribution of fragments of olefins is commercially applied in the synthesis of higher olefins from α-olefins in the SHELL higher olefins process [864]. More modern applications are found in the pharmaceutical industry. Metathesis remains a very active field of research and heterogenization of the organometallic complex is a main goal that could be of great benefit for the industrial processes. The question addressed by Mosselmans and coworkers was: what is the structure of the molybdenum complex on the alumina support and can the structure of the adsorbed complex be determined during reaction? Fitting of the EXAFS data of the $Mo_2(CH_3CO_2)_4$-

derived catalysts identified, after exposure to propylene, the presence of two carbon atoms at the short distance of 1.88 Å and two oxygen atoms at 2.06 Å. The latter were attributed to oxygen atoms that tethered the complex to the surface. The former were assigned to the possible alkylidene, $Mo=C_xH_y$, which is the proposed intermediate in the Chauvin mechanism. In this mechanism, for which Chauvin was awarded the Nobel-prize together with Grubbs and Schrock, a [2+2] cycloaddition of an alkene double bond to a transition metal alkylidene forms a metallacyclobutane intermediate. The metallacyclobutane can revert to give either the original species or a new alkene and alkylidene.

4.2.2 Tuning selectivity by supported rhodium complexes

Over the years, Gates and co-workers have synthesized many metal complexes on various supports and determined their structure and catalytic performance [865-876]. They highlighted that the support has a strong and defining influence on the structure of the complex or particle and as a result on the catalytic performance [877]. A recent series of publications [873, 878, 879] nicely illustrates the power of X-ray absorption-based methods to determine the structure or supported organometallic complexes and to relate the structure to catalytic performance, in this case selectivity. Besides X-ray absorption, complementary methods (notably infrared spectroscopy and detailed kinetic analysis) were necessary to yield the catalyst structures and the structure – performance relations. Molecular rhodium catalysts on support were obtained from rhodium acetylacetonate ($Rh(C_2H_4)_2$). The supports used were faujasite in proton and sodium form (zeolite HY and NaY) and magnesia (MgO). The different catalytic behaviour observed for the different supported Rh complexes was explained in terms of different electronic properties and different extent of the electron transfer to the ligands. When supported on HY, the mononuclear complex dimerized ethylene to butane with 76% selectivity. Hydrogenation occurred when the support was MgO, even in case of monomers, and NaY. Moreover, after reductive pretreatment, rhodium clusters active in hydrogenation were formed. Table 1 shows the fitted EXAFS parameters of the complex supported on HY and MgO. Scheme 3 illustrates the structure of rhodium complexes on zeolite and relates it to catalytic performance. After deposition on HY and MgO, a mononuclear complex was formed and in the case of HY it was selective to dimerization of ethylene. After reductive treatment (entry 2), part of the mononuclear clusters transformed into rhodium clusters that were active in hydrogenation, yielding mainly ethane. Dimers formed on MgO after reductive treatment (entry 5), and like the mononuclear specie on MgO yielded hydrogenation only.

Table 1. Structure and selectivity of Rh complexes on different supports. The reaction selectivity of ethylene conversion is to dimerization or hydrogenation.

Entry	Rhodium nucleation	Support	Rh – Rh coordination number	Rh – Rh bond length	Selectivity to dimerization / hydrogenation
1 (as synthesized)	mononuclear	HY	undetected	undetected	76 / 24
2 (after reduction)	mononuclear and clusters	HY	1.9	2.70	8 / 89
3 (during reaction)	mononuclear	HY	undetected	undetected	---
4 (as synthesized)	mononuclear	MgO	undetected	undetected	0 / 100
5 (after reduction)	dimers	MgO	1.0	2.71	0 / 100

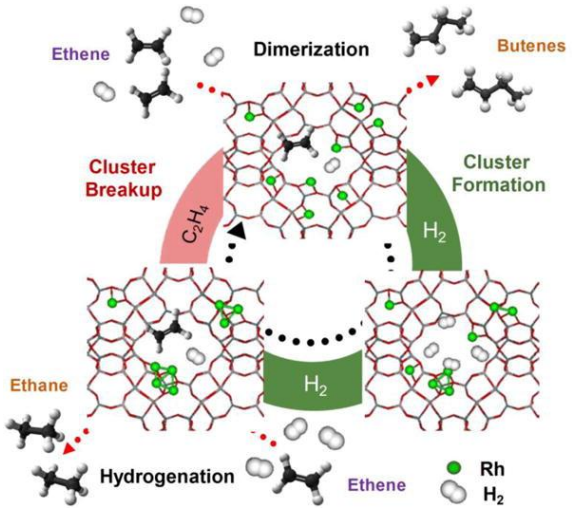

Scheme 3. Summary of structure and catalyst performance of rhodium complexes on support. Depending on support and on the conditions, the catalyst adopts a different structure, which either dimerizes or hydrogenates ethylene. Mononuclear $Rh(C_2H_4)_2$ on

the aluminium sites in zeolite HY selectively and uniquely yields butenes; reduction yields clusters that primarily hydrogenate ethylene to ethane. Reproduced with permission from ref. [879]. Copyright (2008) Elsevier.

Thus, the authors identified the roles of the zeolitic acid site and of adsorption of the $Rh(C_2H_4)_2$ complex on the zeolite above aluminium sites. If such structure was not formed, dimerization did not occur. Also, as soon as rhodium-rhodium bonds were formed, which is indicative of small clusters, ethylene primarily underwent hydrogenation, even in the case of HY as support. The authors stressed rightfully that the synthesis of well-defined structures was essential to relate the differing catalytic selectivity to structural changes in the supported complex at the molecular scale. The solid support functions as a ligand to the organometallic complex, thus affecting its structure and catalytic performance.

4.2.3 Solid porous ligands for catalysis by gold on support

Catalysis by gold is a very active field of research and gold catalysts have recently been added to the toolbox of organic synthesis [880-882]. The most promising applications are cyclo-isomerization and C – C coupling reactions. Most of these are homogeneous catalysts (see section 4.1.4). Gold (sub)nanometer particles on support is also active for many reactions, such as water gas shift, CO oxidation, and hydrogenation reactions [872, 883]. Gold becomes active as its size decreases to below one nm or if it is cationic, however the literature is not consensual about that. Homogeneous gold complexes are versatile and ligand modification affects their catalytic performance. Gold complexes on support are much less studied that those in the homogeneous phase, even though the advantage of using heterogeneous catalysts is obvious as product separation from catalyst and thus catalyst re-use becomes easy.

Recently, Vaclavik *et al.* described a Au(I) catalyst on a support, that was called solid porous ligand [884]. The support was a MOF functionalized with a phosphine group, yielding a P-MOF [885-887]. In homogeneous catalysis phosphines are universal ligands to transition metals that find widespread application in catalysis. Having a heterogeneous porous material that contains phosphine functional groups combines the benefits of structural versatility of homogeneous catalysis with the separation of heterogeneous ones. Using as linker the 4,4′,4″-phosphinetriyltribenzoic acid (tcpp; Scheme 4) and zirconium as inorganic unit, the P-MOF called LSK-1 was synthesized, obtaining a partial crystalline material characterized by a BET surface area (or number) of 1025 m^2/g. Such large numbers are indicative of the large microporous volume. Electron microscopy identified the presence of structural units of about 0.5 nm, which could be columns of the inorganic $[Zr_6O_4(OH)_4]^{12+}$ units, connected by the organic linkers and separated by the micropores. Post-synthetic modification of the P-ligand with chloro(tetrahydrothiophene)gold , yielded the catalyst-precursor (LSK-1)-Au-Cl. Removal of chlorine was achieved by forming a gold-alkyne complex, that was the active catalyst (LSK-1)-Au-PA. The catalyst was active in the hydration of phenylacetylene and could be re-used four times, showing a significant loss of activity only after the first use. Gold catalysts are excellent catalysts also for oxazole synthesis (Scheme 5). Very large activity of the Au-P-MOF was observed, even faster than comparable homogeneous catalysts from literature [888, 889]. No gold reduction was observed, which commonly occurs in homogeneous gold catalysts. Because of the promising catalytic results, this catalyst was extensively characterized, including diffraction and NMR on all relevant elements that are NMR active. However, the gold center could not be directly observed with any of the methods, thus L_3 RIXS and HERFD XAS were used to determine the gold oxidation state. Gold has a nominal oxidation state of +1 in the complex. RIXS and HERFD XAS at the Au L_3 edge yield the gold electronic structure, which relates to oxidation state. Figure 19 shows the L_3 RIXS and the HERFD XAS of (LSK-1)-Au-Cl. The high resolution data enable precise identification of spectral features [122, 125, 767, 846]. The intermediate white line intensity in the catalyst unambiguously identified the oxidation state of +1 of the gold complex: a careful comparison of its white line intensity to that of reference compounds enabled making the identification. In agreement with the indirect evidence of electron microscopy and P NMR no evidence of gold reduction or black gold formation was observed.

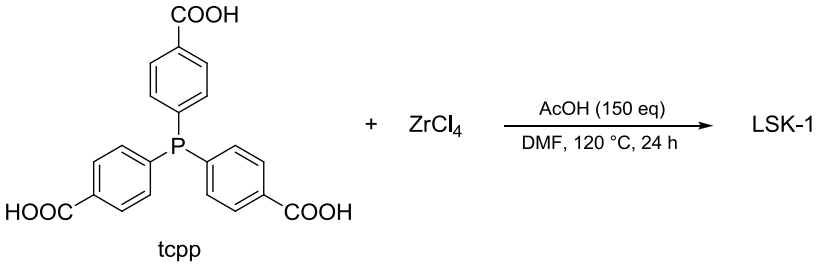

Scheme 4. Linker and inorganic unit used to synthesize the P-MOF called LSK-1. Further modification with gold precursors yields a Au(I) on support catalyst.

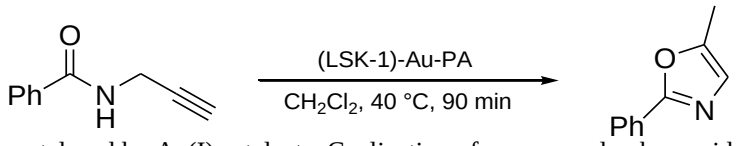

Scheme 5. Oxazole synthesis is catalysed by Au(I) catalysts: Cyclization of a propargylcarboxamide to oxazole.

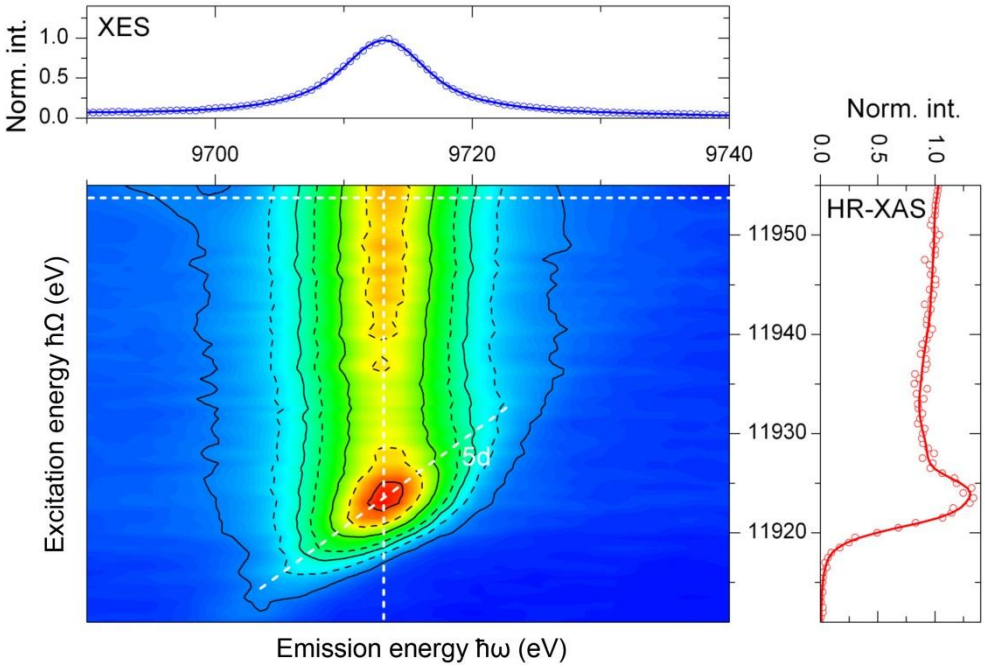

Figure 19. RIXS map of (LSK-1)-Au-Cl. On top is the X-ray emission spectrum. On the right the high resolution XAS is given. The intermediate white line intensity is indicative of the presence of Au(I). Adapted with permission from ref. [884]. Copyright (2013) WILEY-VCH.

4.2.4 Silica supported polymerization catalysts

Reactions of silica surface with organometallic species are of fundamental importance in heterogeneous catalysis [14, 17, 20, 359, 678, 686, 890, 891 Corker, 1996 #457, 892-904]. The large use of amorphous silica as support for many heterogeneous catalysts is due to its high surface area, thermal and mechanical stability. In most of the cases, the active phase is formed upon reaction of the well defined organometallic precursors with surface silanol groups, whose concentration and type can be tuned by changing the temperature of the pre-treatments[359, 905]. When the grafting procedure is performed on a highly dehydroxylated silica, the grafted metal species can assume a single-site character [17, 906]. Several heterogeneous catalysts for olefin polymerization are supported on amorphous silica; the silica types involved are porous, with high specific surface areas and potentially reactive surface hydroxyl groups almost entirely upon the pore walls [907]. The first developed polyolefin catalyst based on silica was the Phillips catalyst for ethylene polymerization, where the active sites are diluted chromium centres [359, 908-910]. In such a case it was demonstrated that silica does not only play the role of an inert support, but directly influences the properties of the grafted chromium species in terms of accessibility, coordination ability and flexibility [359, 890, 908-911]. Indeed, Weckhuysen et al first [912], and Groppo *et al.* [359, 678, 686] successively showed that, upon grafting of H_2CrO_4 on high surface area silica, tetrahedral Cr(VI) species are obtained (left structure in the scheme in Figure 20a). These species are characterized by the typical sharp 1s→3pd electronic transition (red XANES spectrum in Figure 20a) typical of 3d transition elements in T_d-like geometry (vide supra the discussion related to Figure 9). The corresponding FT of the EXAFS spectrum (see inset) is dominated by a component at very low R due to the Cr=O double bond, being the Cr–O single bond with the silica surface just an high-R shoulder of the main component. Upon reduction in CO at 623 K, Cr(II) species characterized by an high coordinative unsaturation are obtained (see scheme and related XANES spectrum, blue curve in Figure 20a). The high coordinative unsaturation of such Cr(II) species is testified by the ability to coordinate, at liquid nitrogen temperature, up to three CO ligands, see green spectrum in Figure 20b showing an intense second shell peak due to the strong multiple scattering contribution typical of linear metal carbonyls [715, 716, 858, 890, 913]. The direct structural proof that an important rearrangement of the local environment of the Cr(II) site at the silica surface occurs upon CO adsorption has been obtained by the experiment of Gianolio *et al.* [890], summarized in Figure 20b. The Cr–O distance of 1.86 ± 0.03 Å of the reduced Cr(II) species (blue spectrum) is stretched to 1.935 ± 0.007 Å upon formation of surface $>Cr^{II}(CO)_3$ adducts, being the CO

molecules located at 1.995 ± 0.008 Å [890]. This experimental evidence supported previous Raman study by Damin *et al.* [914].

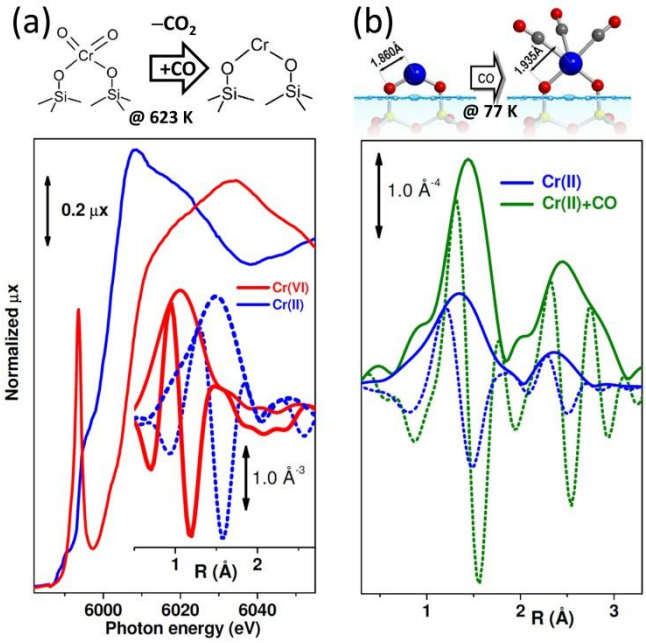

Figure 20. Part (a) top: scheme of the reaction followed by XAS. Part (a) bottom: XANES spectra of the *oxidized* (red curve) and *CO-reduced* (blue curve) Cr/SiO_2 systems. The inset reports the modulus and the imaginary part (full and doted curves, respectively) of the k^2-weighted, phase-uncorrected, FT of the EXAFS signals collected together with the XANES spectra reported in the main part. Part (b) top: scheme of the reaction followed by XAS (Cr blue, O red, C grey, Si yellow). Part (b) bottom: k^3-weighted, phase-uncorrected, FT of the EXAFS signals collected at 77 K on the reduced catalyst before (blue) and after (green) CO adsorption. Unpublished figure reporting experimental data from refs [359] and [890] for parts (a) and (b), respectively.

Amorphous silica was successively employed as a support also for Ti-based Ziegler-Natta catalysts for ethylene polymerization [907, 915, 916]. The simple combination of titanium tetrachloride on silica yielded low-reactivity catalysts; however, the combination of a magnesium compound with a porous silica material, followed by reaction with titanium tetrachloride, resulted in a catalyst showing an enhanced reactivity and the excellent handling and polymer particle control characteristic of Phillips' chromium catalysts [907, 915, 916]. In the frame of a wider work devoted to the physical–chemical characterization of silica-supported Ziegler-Natta catalysts based on tetrahydrofuranates of $TiCl_4$ and $MgCl_2$, Groppo *et al.* performed a detailed spectroscopic investigation on the reactivity of titanium chloride tetrahydrofuranates ($TiCl_4(thf)_2$ and $TiCl_3(thf)_3$) towards a polymer-grade silica and on the structure of the resulting Ti-grafted sites [811, 917].

The determination of the structure case of Ti chloride tetrahydrofuranate complexes grafted on silica discussed was very complex, for two main reasons. First, the starting complexes are six-folded coordinated and are less reactive with respect to the pure metal chlorides due to the presence of the thf ligands. Second, the employed silica was not highly dehydroxylated, therefore, the number of possible structures resulting from the grafting of the Ti complexes is theoretically much larger than those hypothesized for $TiCl_4$ alone on highly dehydroxylated silica [918, 919]. While the occurrence of Ti grafting through surface ≡SiOH groups can be easily demonstrated by IR spectroscopy (by looking at the consumption of the IR absorption bands due to surface ≡SiOH groups in the ν(O–H) stretching region [920, 921]), insight into the geometric and electronic structure of the grafted Ti sites was obtained by Groppo *et al.* combining UV-Vis, XANES, EXAFS and XES spectroscopies [811]. These techniques clearly evidenced a structural and electronic modification of the $TiCl_4(thf)_2$ precursor upon grafting on the SiO_2 surface, see Figure 21a-d.

To understand the potential complexity of the situation, we should imagine that, on a structural point of view, the grafting of $TiCl_4(thf)_2$ on the silica surface should occur through the loss of some ligand (Cl or thf) and the formation of new Si–O–Ti bonds. Grafted Ti(IV) species should then be characterized by three different fist shell ligands: Ti–O bonds from thf, Ti–O bonds form the silica surface and Ti–Cl bonds. Without any additional constraints from independent techniques the EXAFS fit was highly instable because of the too high correlation between bond distances, coordination numbers and Debye-Waller factors of the three contributions [811]. Authors first hypothesized that the number of new Si–O–Ti bonds substitutes all ligands that have been lost, in this case once end up with a six-fold coordinated Ti (s-models in the top part of Figure 21e). Authors optimized, at DFT level (using the ORCA 2008 code [670]), the structures obtained forming 1, 2, 3 or 4 Si–O–Ti bonds with the silica surface resulting in eleven different cases (clusters s1-s11) depending whether each Si–O–Ti bond resulted from the loss of a Cl or of a thf ligand. Then authors hypothesized that the $TiCl_4(thf)_2$ precursors form n Si–O–Ti bonds with the surface (n= 1-4), losing n+1

(resulting in penta-coordinated Ti centres, p1-p11 clusters) or n+2 (resulting in tetra-coordinated Ti centres) ligands. From the structure of the optimized clusters authors computed the theoretical XES spectra and compared them to the experimental one (Figure 21e). Authors defined and agreement factor θ between computed and experimental XES spectra and ranked the different simulations on the basis of θ. None of the tetra-coordinated cluster was able to satisfactory reproduce the experimental spectrum, the same holds for a dimeric species, proving the isolated nature of the grafted Ti species [811]. Among the 32 different simulated clusters those resulting in the best θ values are reported in the top part of Figure 21e and the corresponding simulated XES spectra are reported in the bottom part.
In the same work, Groppo *et al.* [811] also investigated the catalyst obtained by grafting $TiCl_3(thf)_3$ Ti(III) precursor. All the experimental data allowed the authors to conclude that both structural and electronic properties of silica-supported samples are very similar, irrespective of the starting precursor, *i.e.* $TiCl_4(thf)_2$ or $TiCl_3(thf)_3$. In both cases, most of the chlorine ligands originally surrounding the Ti sites were substituted by oxygen ligands upon grafting on silica, as happens for the more reactive and geometrically different $TiCl_4$ precursor [918, 919]. The electronic properties of silica-supported Ti sites are largely different from those of the corresponding precursors, and in both cases most of the grafted Ti sites have a formal oxidation state of +4. Besides the interest in Ziegler-Natta catalysis, the study of Groppo *et al.* [811] is of relevance in the field of organometallic chemistry and reactivity of metal-oxide surfaces towards organometallic compounds and demonstrated the key role of the synergic use of complementary experimental techniques to get insights into the properties of the grafted sites [922].

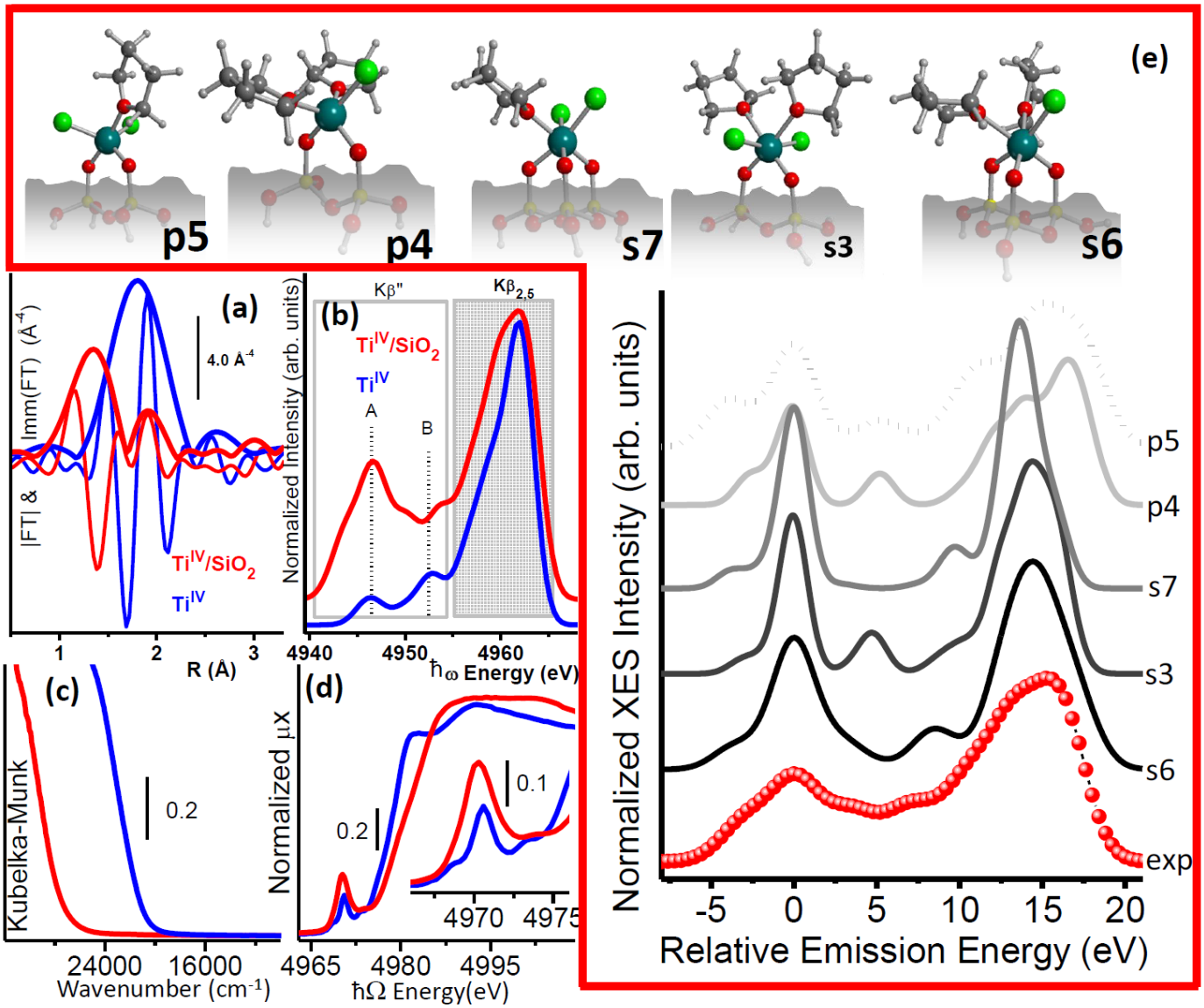

Figure 21. Part (a): Phase-uncorrected modulus (bold lines) and imaginary parts (lines) of the $k^3\chi(k)$ EXAFS function for Ti^{IV}/SiO_2 grafted on silica (red) and of the $TiCl_4(thf)_2$ precursor (blue). Parts (b): as part (a) for the vtc-XES spectra. The Kβ" and $K\beta_{2,5}$ regions are indicated with white and grey boxes, respectively. A and B features identify oxygen and chlorine ligands, respectively. Part (c): as part (a) for the UV-Vis spectra. Part (d): as part (a) for the XANES spectra. Part (e): experimental XES spectrum of Ti^{IV}/SiO_2 reported in part (b) (exp) and selection of spectra simulated by means of the minimal clusters p5, p4, s7, s3, and s6. The labells refer to the names of the clusters reported in the upper part. The spectra have been translated for clarity. In order to evaluate the agreement between the simulated and the experimental vtc-XES spectra the zero of the energy was shifted to

the maximum of the Kβ" characteristic of oxygen ligands. Unpublished figure reporting spectra and schemes published in ref. [811].

4.3 Photoactive coordination compounds

Photoexcited states of coordination compound play key roles in luminescent materials and in processes and devices converting solar energy to fuels or electricity, such as photocatalysis and dye-sensitized solar cells (DSSCs). In this section we review the literature concerning the use of synchrotron radiation techniques to characterize photoactive coordination compounds applied in the fields of luminescence, photocatalysis and solar energy conversion.

4.3.1 Luminescent coordination compounds

Johansson and coworker [923] employed a combination of HXPES and XAS to map the electronic structure of the complexes $[Fe(bpy)_3]^{2+}$, $[Ru(bpy)_3]^{2+}$ and $[Os(bpy)_3]^{2+}$ (bpy = 2,2′-bipyridine). They compared experimental results and electronic structure calculations to explain the trends observed in oxidation potentials and absorption spectra of these coordination compounds, in terms of metal ligand interactions and spin orbit coupling. The HXPES measurements show that the C 1s peaks for the three complexes are quite similar, indicating a low contribution of the metal in the spectra. The main component largely contains two features separated by 1.0 eV and with an intensity ratio of about 2:3. The general structure may be expected from the pyridine structure with two out of the five carbons bonding to nitrogen. The N 1s peaks are also rather similar in term of peak width, but the binding energy varies. The shift was attributed to a different interaction between the N and the different metal centres, as confirmed by the N K-edge XAS measurements. The spectra of the highest occupied electronic structure (see Figure 22) display a trend towards higher binding energy of the intensity maximum, passing from $[Fe(bpy)_3]^{2+}$ to $[Ru(bpy)_3]^{2+}$ and $[Os(bpy)_3]^{2+}$. However, a clear splitting is observed in the HXPES spectrum of $[Os(bpy)_3]^{2+}$. Being the lowest binding energy states (HOMO levels) closely connected to the redox potential, the authors related the fine structure in the HXPES spectrum of $[Os(bpy)_3]^{2+}$ to the abnormal trend in the oxidation potentials of the three complexes, which are 1.03, 1.20, and 0.81 V vs SCE for $[Fe(bpy)_3]^{2+}$, $[Ru(bpy)_3]^{2+}$ and $[Os(bpy)_3]^{2+}$ (in acetonitrile), respectively. The HXPES spectrum of $[Os(bpy)_3]^{2+}$ displays an asymmetric structure that can be deconvoluted with two peaks having an intensity ratio of 2:1. These transitions were modelled using relativistic CASSCF (complete active space self-consistent field) calculations including spin orbit coupling. The calculations showed that the fine structure in the HXPES spectrum of $[Os(bpy)_3]^{2+}$ is primarily due to a large spin orbit coupling in the final Os(d5) state, explaining the anomaly in the trend of oxidation potentials of the three complexes. The influence of the different metal ions on the state formed upon light absorption was investigated by N K-edge XAS. Comparing the N K-edge spectra for the three complexes, clear differences are observed. In particular, the third peak shows a strong energy shift. The first two peaks were attributed to π* resonances. The third resonance was related to a nitrogen σ* orbital directed toward the metal center and mixed with a metal d orbital. This explains the large shift in energy for the different complexes due to differences in interaction with the different metals. The difference between π* and σ* excitations increased for $[Fe(bpy)_3]^{2+}$ to $[Ru(bpy)_3]^{2+}$ and to $[Os(bpy)_3]^{2+}$. Finally, the energy difference between the energy of the highest occupied valence structure and the energy of the lowest N K-edge XAS resonance explains the trends observed in UV-Vis excitation spectra and specifically the decrease in excitation energy for $[Os(bpy)_3]^{2+}$ compared to $[Ru(bpy)_3]^{2+}$.

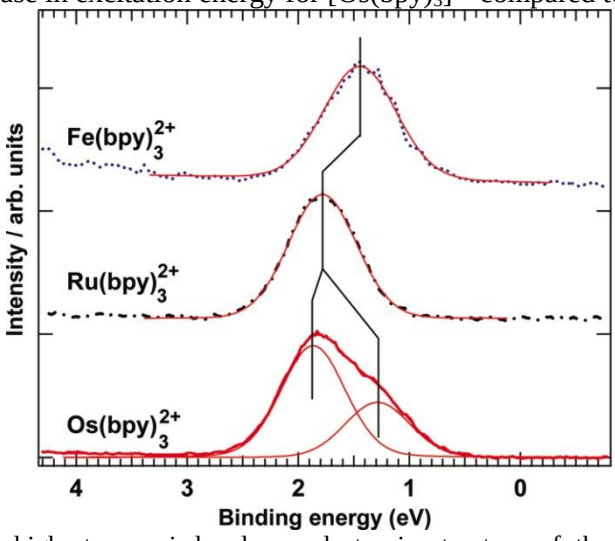

Figure 22 HXPES spectra of the highest occupied valence electronic structure of the complexes measured at 2800 eV. Reproduced with permission from ref. [923]. Copyright (2010) AIP Publishing.

In 2007, Pascu and coworkers presented a study concerning the synthesis and characterization of a new family of M(II) bis(thiosemicarbazonato) complexes (M = Ni, Cu and Zn) [924]. The authors aimed to obtain potentially biologically active metal complexes suitable as imaging probes and therapeutic agents. The Zn and Cu complexes

were found to be highly cytotoxic in MCF-7 cancer cell lines, the Zn complex is intrinsically fluorescent while the Cu complex could be of interest as a PET imaging reagent. The three complexes were characterized in solution by spectroscopic methods, while their solid state structures were determined by single crystal XRD. However, the crystals obtained for the Zn and Cu complexes were extremely small and weakly diffracting and a synchrotron radiation source was necessary to collect data suitable for structure solution and refinement.

In the attempt of developing artificial photosynthetic systems, Takahashi and Kobuke prepared a zinc complex of bis(1-methylimidazolyl)-m-gable porphyrin, capable to self-assemble into macrocyclic porphyrin arrays by slipped-cofacial dimer formation, through non-covalent bonds [925, 926]. The authors isolated two different assemblies that gave round-shaped particles on solid substrates, when analysed by atomic force and scanning tunneling microscopies. To determine the exact aggregation number, they investigated the system using synchrotron radiation SAXS. The plot of scattering intensity versus the square modulus of the scattering vector (Guinier analysis) provided radius of gyrations for the predominant component that are compatible with the radius of hexameric and pentameric macrorings. Interestingly, the porphyrin macrorings did not show any fluorescence quenching by assembly formation, suggesting that the macrorings of gable porphyrins represent a good model for an artificial light-harvesting complex.

Recently, Martínez Casado and coworkers reported two luminescent MOFs based on Pb(II) complexes [927], having formulas $[Pb_2(btr)_4(4,4'\text{-bpy})(H_2O)]_n$ and $[Pb_2(btr)_4(bpe)(H_2O)]_n$ (where btr = butyrate; 4,4′-bpy = 4,4′-bipyridine and bpe = 1,2-bis(4-pyridyl)ethane). The two materials present interesting optical properties. When excited by UV radiation they show intense fluorescence with structured emission bands, denoting a strong ligand-centred (LC) character. The emission lifetime values, in the nanosecond scale, indicate that despite the high atomic number, the intersystem crossing (ISC) is not efficient enough to promote the population of triplet states, likely due to the relative ionic character of the metal–ligand bond. Nevertheless, the large Stokes shifts reveal that ground and excited states are significantly distorted to each other. Both materials present very similar structures that where solved by synchrotron radiation single crystal XRD. The metal ions are organized in dinuclear units, where the Pb atoms are bonded through double μ-oxo-carboxylate from two btr ligands and one μ-aqua which are linked by means of four oxo-carboxylate bridges to two adjacent dinuclear entities, building a double metal-chain. The 4,4′-bpy and bpe act as bismonodentate ligands, linking two consecutive Pb(II) chains, to achieve the final 3D architecture. The btr tiles fill the interstitial voids among the double chains, avoiding the inclusion of crystallization water molecules in the structures.

Recently, Stock and coworkers synthesized five new bismuth carboxylates based on pyromellitic, trimellitic and trimesic acids as linkers [928]. Their luminescence properties are dominated by a combination of short-lived linker fluorescence and long-lived Bi(III) phosphorescence, characteristic of Bi(III)-containing solids. Exceptionally long Bi(III) emission decay times of about 1 ms were observed at room temperature. The crystal structures of the new compounds were determined using laboratory single crystal XRD data. To get a better understanding of product formation, the authors monitored the crystallization processes by *in situ* energy-dispersive X-ray diffraction (EDXRD), see Section 2.3.2. EDXRD has widely been applied to follow the crystallization (extract kinetic parameters, detect crystalline intermediates and observe phase transformations). In EDXRD studies, intense white-beam synchrotron radiation is employed to achieve high time resolution (< 1 min) while using conventional reaction vessels in the experiments. The white beam is sufficiently intense to penetrate steel or glass autoclaves, and thus reactions can be investigated without imposing an external influence on the reaction mixture provided no beam-sensitive solvents are used. The *in situ* EDXRD experiments showed that bismuth carboxylates crystallize after very short reaction times and crystalline intermediates appear within minutes. In addition, the authors were able to isolate two intermediates by quenching of the reaction mixtures. Their crystal structures were resolved using laboratory and synchrotron XRPD data and allowed to establish a possible reaction pathway. Considering such results, the authors suggest that due to the long reaction times commonly used in the synthesis of bismuth carboxylates (usually days, up to a week), metastable intermediates may generally be overlooked and several systems should therefore be reinvestigated.

Lanthanide complexes with organic ligands have photoluminescence properties that are favourable for a broad range of optical applications. However, they suffer of poor thermal stability and low mechanical strength. One solution is to immobilize the complexes in a stable rigid matrix.

Carlos, Gonçalves and coworkers obtained an enhanced Eu(III) luminescence by immobilizing the complex $Eu(NTA)_3{\cdot}2H_2O$ (NTA = 1-(2-naphthoyl)-3,3,3-trifluoroacetonate) in the ordered mesoporous silica MCM-41 functionalized with a chelating pyrazolylpyridine ligand covalently anchored to the support (MCM-41-L2) [929]. The supported material MCM-41-L2/Eu was characterized employing a combination of vibrational spectroscopy and ab initio calculations. Moreover, Eu L_3-edge XAS spectra were measured in the solid state at room temperature for $Eu(NTA)_3{\cdot}2H_2O$, MCM-41-L2/Eu, and for the model complex $Eu(NTA)_3L1$ (L1 = ethyl[3-(2-pyridyl)-1-pyrazolyl]acetate). The normalized XANES data reveal single, intense edge resonances at 6.981 keV, in agreement with the Eu(III) reference compound $EuCl_3{\cdot}6H_2O$. The absence of any additional peaks to the low energy side of the Eu(III) resonance confirms that the samples do not contain any divalent or intermediate-valent Eu. For $Eu(NTA)_3L1$ and MCM-41-L2/Eu, the amplitude and frequency of the oscillations on the high energy side of the Eu(III) resonance

are identical, indicating very similar local Eu coordination environments. For the adduct $Eu(NTA)_3$(1,10-phenantroline), the Eu–O distance was found to be in agreement with the single crystal XRD data. The refined coordination numbers for the first shell indicate a contribution from the neutral ligands in addition to the six oxygen atoms of the NTA groups. The replacement of the H_2O ligands in $Eu(NTA)_3 \cdot 2H_2O$ by bidentate pyrazolylpyridine ligands could not be confirmed by the EXAFS analysis alone, due to the similarity of the backscattering amplitudes and phases for O and N atoms. However, there is a visual match between the EXAFS spectrum of MCM-41-L2/Eu and the model complex $Eu(NTA)_3$L1. The second shell fitted to the Eu L_3-edge EXAFS of the three compounds corresponds mainly to the C atoms of the NTA CO groups.

Hasegawa and coworker used molecular thin film techniques to obtain polarized electronic transition of lanthanide (III) complexes. In particular the authors report the first observation of a polarized ff-emission in a Tb(III) complex having 1,10-phenanthroline as a ligand, on a polyvinyl alcohol (PVA) film surface [930]. The emissive film was produced by spin-coating acetonitrile solutions of Tb(III) after treatment with 1,10-phenanthroline solutions on stretched PVA films. The electronic behaviour and the coordination between the ligand and metal ion are strongly correlated, thus Hasegawa and coworker performed XAFS measurements to get information on the local structure of Tb(III) on the PVA film. The EXAFS spectra at the Tb L_3-edge of the Tb(III)-phenanthroline compound on the stretched and the unstretched PVA film show that the mean bond distances between Tb(III) and its nearest neighbour atoms of the 1,10-phenanthroline ligand on the film are close to those of the reference samples $Tb(NO_3)_3H_2O$ and [Tb(1,10-phenanthroline)$_2(NO_3)_3$]. The FT of the EXAFS spectrum, in the first coordination shell region, shows that the mean atomic distances between Tb(III) and the coordinating atoms and the coordination number on the stretched/unstretched films are similar to those in the reference samples. However, at higher distances there are differences in the spectral features around 3–4 Å between the PVA film samples and [Tb(1,10-phenanthroline)$_2(NO_3)_3$]. This indicates that the Tb(III) compound on the PVA film has a slightly different coordination environment compared to that in [Tb(1,10-phenanthroline)$_2(NO_3)_3$].

Rocha, Paz and coworkers investigated the use of rare-earth elements as metallic nodes in the construction of photoluminescent layered lanthanide MOFs. They obtained a series of coordination polymers with carboxylate- and phosphonate-based organic linkers, namely $[Ln(H_3NMP)] \cdot 1.5H_2O$ (where Ln = La, Pr, Nd, Sm, Eu and H_6NMP = bis(phosphonomethyl)aminomethylphosphonic acid) [931], $[Ln(H_2cmp)(H_2O)]$ (where Ln = Y, La, Pr, Nd, Sm, Eu, Gd, Tb, Dy, Ho, Er and H_5cmp = 2-(bis(phosphonomethyl)amino)acetic acid) [932] and $[Ln(H_2cmp)] \cdot xH_2O$ (where Ln = Nd, Eu, H_5cmp = 2-(bis(phosphonomethyl)amino)acetic acid and $x < 1$) [933]. The authors reported the synthesis, structural characterization, catalytic activity, and photophysical properties of the new materials. Due to the small crystallite size and to the occurrence of connection mistakes during self-assembly of the organic ligands and rare-earth centres, materials could only be isolated as microcrystalline powders. Hence, the authors combined synchrotron radiation (micro-crystal and high-signal-to-noise powder diffraction) and high-resolution solid-state NMR techniques in order to unveil the structural details of these materials. XRPD data and information from solid-state NMR revealed layered materials built up from single crystallographically independent Ln(III) centres, in a highly distorted dodecahedral coordination environment. Connectivity through H_3NMP^{3-} or H_2cmp^{3-} anionic ligands leads to undulated tapes of Ln(III). Inter-tape connections are assured by the bridging deprotonated phosphonate groups, leading to the formation of a neutral two-dimensional network. Individual layers close pack, mediated by hydrogen bonding interactions. In the $[Ln(H_2cmp)(H_2O)]$ system, the H_2cmp^{3-} anion behaves as a heptadentate ligand and one water molecule is present in the first coordination sphere of the lanthanides. This coordinated water has an important impact on the photoluminescence properties, acting as a highly efficient non-radiative channel. On the contrary, water is not included in the first coordination sphere in the case of $[Ln(H_3NMP)] \cdot 1.5H_2O$ and $[Ln(H_2cmp)] \cdot xH_2O$, where uncoordinated water molecules of crystallization occupy the interlayer spaces. Variable-temperature XRPD reveals that the $[Ln(H_3NMP)] \cdot 1.5H_2O$ system is structurally robust and removal of the water molecules leads to a new crystalline phase with a smaller interlayer space.

The coordination complex tris(8-hydroxyquinolinato)aluminium (Alq_3) is one of the most attractive electroluminescent compounds, successfully used as green emitter and electron transport material in several OLEDs. Despite this, there have been few studies using synchrotron techniques meant to characterize the electronic structure of Alq_3 and to monitor the chemical processes that Alq_3 may undergo during fabrication or degradation of light-emitting devices [934-937].

In 2008, DeMasi *et al.* reported an extensive experimental and theoretical investigation of the electronic structure of thin films of Alq_3 using a combination of XAS, XES (and RIXS) and XPS, together with DFT calculations [938]. The C and N K-edge XAS spectra were in agreement with earlier XAS studies [934, 936]. The XPS measurements at the C, N and O 1s core levels were performed to probe the valence band electronic structure of Alq_3. After aligning the main features, the valence band XPS results are in excellent agreement with the DFT calculated total density of states and with earlier studies [934, 939]. XPS measurements at both N and O 1s core levels display single peaks at binding energies of 400.1 and 531.6 eV, respectively. Conversely, XPS measurement of the C 1s reveals a broad peak centred at a binding energy of 285.3 eV, which can be deconvoluted into three components corresponding to C atoms in C–C,

C–H, and C–N/O environments. For what concern XES measurements, high resolution measurements using a Nordgren-type instrument with narrow entrance slits require a small photon spot with a high photon flux, and long collection times. These conditions lead to significant photon-induced beam damage in Alq_3. The authors bypassed the beam damage problem by continuously translating the Alq_3 films in front of the focused X-ray beam. Figure 23 compares the C, N, and O K-edge XES spectra for both stationary and continuously translated Alq_3 films, and illustrates clearly the effect of the X-ray photon beam.

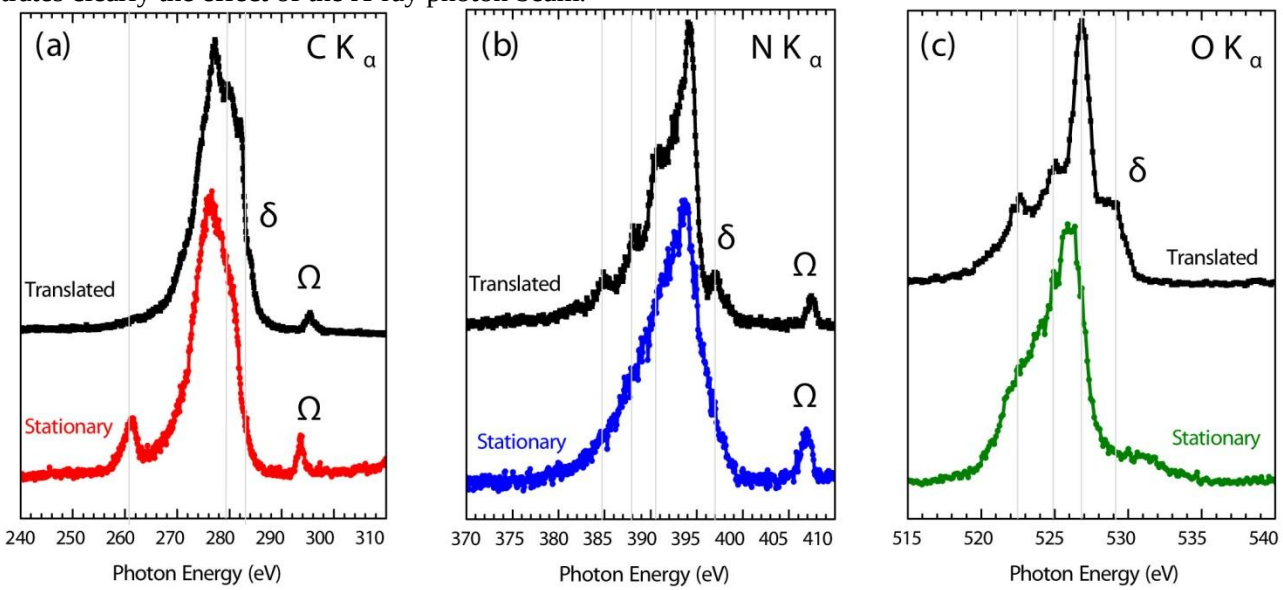

Figure 23. (a) carbon, (b) nitrogen, and (c) oxygen K-edge XES spectra from translated and stationary Alq_3 films, collected with incident excitation energies of 293.2, 407.7, and 539.0 eV, respectively. The feature identified as Ω refers to the elastically scattered photons while the emission from the HOMO state is labelled with δ. Reproduced with permission from ref. [938]. Copyright (2008), AIP Publishing LLC.

The N K-edge XES spectrum from the stationary film shows fewer spectral features and less definition than that from the translated film Figure 23b. This is expected since valence band features are particularly sensitive to any changes related to broken molecular bonds. The feature at 397.0 eV marked as δ can be identified as emission from the HOMO state. The absence of this feature in the spectra from the stationary films highlights how electronic structure information obtained from beam-damaged samples is problematic. The different results obtained from translated and stationary films are consistent with the conclusions from the XPS studies that Alq_3 partly decomposes by ejecting nitrogen out of the molecule [935]. For the O K-edge XES spectra, a distinct change in the overall spectral shape is also noted. A significant broadening and energy shift of the emission from the HOMO state δ in the XES spectrum from the damaged film can be seen in Figure 23c. Less dramatic changes between the emission from translated and stationary films are observed in the C K-edge XES spectra. This is due to the broad range of binding energies exhibited by the C 1s states as a result of the different local bonding environments of the C atoms. RIXS measurements were performed to probe the C, N and O 2p partial densities of states. A good agreement was found with the results of DFT calculations. Furthermore, RIXS at the C K-edge is shown to be able to measure the partial density of states associated with individual C sites of the molecule.

In a paper by Mao and coworkers [940], XAS and XES have been applied to investigate the effect of carbon nanotube (CNT) on the performance of OLEDs. The authors reported that the incorporation of a CNT layer, between the cathode and the organic layer, enhances the electron injection efficiency and the luminance characteristics of OLEDs, due to the increasing of the electric field. In addition, they examined the influence of CNT incorporation on the LUMO and HOMO levels of the organic material. XAS and XES measurements were performed at the C K-edge on OLEDs based on the complex Alq_3. The XES spectra of Alq_3, used to yield the HOMO level of molecule, do not show any significant change after incorporating CNTs. In contrast, the LUMO level as derived from the XAS spectra exhibits a reduction of approximately 0.3 eV after CNT incorporation. These results indicate that the incorporation of CNT could effectively decrease the barrier for electron injection, thus contributing to the improved OLED device performance.

The degradation due to exposure to light of materials commonly used in OLEDs is the principal weakness of these devices. In a recent paper, Brito, Rocco and coworkers [941] monitored the degradation mechanisms caused by light exposure of Alq_3 thin films. They monitored the UV photodegradation through XAS at the C, N, O K-edges and Al L-edges and XPS at the C, N, O 1s core levels and Al at the 2s and 2p core levels. The light exposure was simulated using three UV irradiation wavelengths, namely 254, 365 and 307 nm. The unoccupied molecular orbitals (LUMOs) of Alq_3 were probed using XANES in TEY mode. Attenuation of peak intensities was observed for all irradiations, although exposure at 254 and 365 nm caused larger degradation, as observed by results at the C and N K-edge. This

was attributed to changes in the chemical environment with damage of the π-system of the molecule with consequent loss of electroluminescence and electron transport properties, and formation of dark emissive zones. XPS measurements from non-irradiated and irradiated Alq_3 thin films at 307 nm were also performed. While the Al peaks were less affected, changes in peak intensities and energy shifts for C, N and O were much more dramatic, this was related to the breakdown of charge conductivity.

4.3.2 Photocatalysts

A promising way to address the challenges of securing cheap and renewable energy sources is to design catalysts capable of promoting light-induced water-splitting into hydrogen and oxygen. The enzyme responsible for water oxidation in all oxygenic photosynthetic organisms (photosystem II, PS II) is characterized by a core containing a Mn_4CaO_4 cluster. The history of the structural research on the Mn_4CaO_4 cluster in photosystem II overlaps the history of the development of the experimental method of XAS, and the background of XAS studies on photosystem II has been reviewed in detail [942-945].

The Mn_4CaO_4 cluster has inspired the development of synthetic manganese catalysts for solar energy production [946]. An efficient manganese water-oxidation photocatalyst was prepared by doping a tetranuclear manganese cluster $[Mn_4O_4L_6]^+$ (L = diarylphosphinate), into a Nafion polymer matrix coated on a glassy carbon electrode [947-951]. This device was shown to sustain water oxidation catalysis for an extended period on illumination with visible light and application of a potential bias. However, the structure of this system was reanalysed by Hocking, Spiccia *et al.* by *in situ* Mn K-edge XAS studies, in order to elucidate the mechanism of catalysis [952, 953]. They found that the cluster embedded in Nafion dissociates during catalytic cycling, generating Mn(II) compounds which are then reoxidized to form dispersed nanoparticles of a disordered Mn(III/IV) oxide phase. The XANES spectrum following loading into Nafion (Figure 24, State 1) shows a significant shift in the XANES intensity to lower energy, which is consistent with the reduction of the Mn(III/IV) centres to mononuclear Mn(II) species. This peak is lost upon electro-oxidation, the XANES becomes similar to that of the initial $[Mn_4O_4L_6]^+$ and typical of an oxidized Mn(III/IV) product (Figure 24, State 2). However, a careful analysis of the EXAFS reveals that the material formed upon electro-oxidation is more ordered. Exposure of an electrode in State 2 to light releases O_2 while regenerating the Mn(II) species (Figure 24, State 3). An electrode in State 3 could be immersed in electrolyte and oxidized electrochemically to State 4 giving XANES and EXAFS consistent with the disordered Mn(III/IV) oxide phase deposited on the original electrode (Figure 24). The existence of two clean isosbestic points in repeat experiments indicates a reproducible interconversion between reduced Mn(II) species and the oxidized Mn(III/IV) oxide phase. Finally, the water oxidation activity was found to be comparable to that obtained with other Mn(II) compounds in Nafion. This study demonstrated that the metal complex is essentially a precursor of water-oxidation catalysts, providing an accessible source of metal ions needed for the assembly of a high-surface-area material with high catalytic activity. The behaviour of Mn in Nafion therefore parallels its broader biogeochemistry, which is dominated by cycles where light sensitive Mn(III/IV) oxides are produced by bacteria, and then dissolve by photoreduction to Mn(II) and oxygen [953].

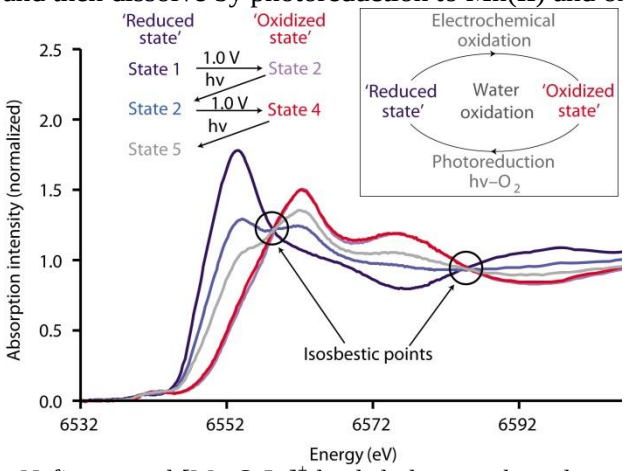

Figure 24. Mn K-edge XANES of a Nafion-coated $[Mn_4O_4L_6]^+$-loaded glassy carbon electrode measured in different "states" of photochemical cycling. State 1 = initial load; State 2 = State 1 + 1.0 V (versus Ag/AgCl) applied potential in electrolyte; State 3 = State 2 + 40 minutes of light excitation in electrolyte; State 4 = State 3 + 1.0 V applied potential in electrolyte; State 5 = State 4 + 20 minutes of light excitation in electrolyte. Two clean isosbestic points can be observed indicating that repeated cycling between an oxidized birnessite-like state and a reduced Mn(II) state can be achieved. Adapted with permission from ref. [952]. Copyright (2011) Nature Publishing Group.

Light-induced water-splitting to generate reactive species is only half of the goal of artificial photosynthesis. The long-standing project is to mimic plants and other photosynthetic organisms to make high-energy chemicals, such as H_2 or reduced forms of carbon. Many green algae and cyanobacteria contain an enzyme that can convert the released

protons into dihydrogen. An ideal solution would be if H_2 could be produced by a direct photocatalytic water splitting reaction.

The first real single-component bifunctional catalytic system was reported by Sakai *et al.* using the [Pt(tpy)Cl]Cl complex (tpy = 2,2′:6′,2″-terpyridine), which acts both as a photosensitizer and H_2-evolving catalyst in aqueous media under visible-light illumination [954]. The formation of the hydride-diplatinum(II, III) by cooperative action of adjacent Pt complexes was postulated to occur as intermediate species. However, evidence of the local structure and electronic transition during the photocatalytic processes was vague and some earlier studies suggest that the metallic Pt(0) is the main contributor to catalytic activity. Yamashita and coworkers investigated such system to gain direct information about the nature and coordination chemistry of active species, in particular to determine whether the active Pt species are in a monomeric or colloidal form. They performed *in situ* XAS measurements of the reaction mixtures under visible irradiation, to determine changes in the electronic structure and chemical environment of the [Pt(tpy)Cl]Cl during photocatalytic H_2 evolution [955]. As evidenced by XANES and EXAFS results, there is no evidence of Pt(II) species being converted to colloidal platinum during H_2 reaction, demonstrating that the Pt(II) monomeric species are the active catalyst.

The integration of metal complexes with nanostructured porous inorganic materials having rigid structures has been intensively investigated in order to construct functional supramolecular materials. Recently, Yamashita and coworkers reported two new hybrid photocatalyst obtained by intercalation of [Pt(tpy)Cl]Cl into layered niobate ($K_4Nb_6O_{17}$) or into mesoporous silica (MCM-48), with the aim of developing recyclable photocatalysts [956-958]. The exploitation of host−guest interactions within restricted spaces confers the new supramolecular materials unique photoluminescence and photocatalytic properties. Unlike the free Pt complex in solution, the intercalated Pt complexes in close proximity to each other exhibit photoluminescence emission due to the ^{3}MMLCT (triplet metal–metal-to-ligand charge-transfer transition), moreover H_2 evolution in aqueous media in the presence of EDTA under visible-light irradiation is achieved. The photocatalytic activity significantly varies according to the amount of Pt loadings, in good accordance with the increasing intensity of the luminescence emission. XAS measurements were conducted to elucidate the electronic structure and chemical environment of the Pt complex in the supramolecular materials. Pt L_3-edge XANES spectra show that anchored samples have slightly higher intensity peaks compared to free [Pt(tpy)Cl]Cl; suggesting that the intercalated Pt species are in a slightly electron-deficient state, because of the decrease in σ-donor electrons by replacement of chloride by a nitrogen (MCM-48) or an oxygen ($K_4Nb_6O_{17}$) atom at the fourth coordination site. In the Pt L_3-edge EXAFS spectra, all samples show a strong peak around 1.5 Å that can be ascribed to a Pt−N bond and a small second shell at ca. 2.4 Å, attributable to adjacent carbon atoms. This validates a tridentate binding structure for Pt(II). In the case of the [Pt(tpy)Cl]Cl complex, an additional peak due to the Pd−Cl bond is observed around 1.8 Å. This peak completely disappears after the intercalation step, suggesting that the intercalation is accompanied by the replacement of the fourth coordinated ligand from chloride to nitrogen (MCM-48) or oxygen ($K_4Nb_6O_{17}$) atoms. The samples with high Pt loadings exhibit an additional peak at around 3.5 Å, ascribed to the short Pt···Pt interactions. The authors suggested that such intercalated complexes behave as a single-component bifunctional catalysts capable of visible-light photosensitization associated with the ^{3}MMLCT excited states and hydrogenic activation to evolve H_2. Moreover, the XAS spectrum of the recovered material after the photocatalytic reaction is identical to that of the fresh catalyst, indicating no changes in the electronic configuration and local structures. This was interpreted as clear evidence that the molecular species rather than a colloidal form are responsible for the catalysis.

Recently, Rosseinsky and coworkers reported two porphyrin MOFs based on Al-carboxylate coordination chemistry: H_2TCPP[AlOH]$_2$ and ZnTCPP[AlOH]$_2$, where TCPP = *meso*-tetra(4-carboxyphenyl)porphyrin [959]. The two compounds demonstrated to be active photosensitizer for visible-light-driven water-splitting, in a system using colloidal Pt as catalyst. The crystal structures of the new materials were solved and refined from synchrotron XRPD and confirmed by solid-state NMR spectroscopy. The linker consists of four benzoate groups around the central porphyrin core. Each porphyrin is coordinated to eight aluminium centres through the four carboxylate groups, each bridging two aluminium units. The aluminium coordination consists of four carboxylate-derived oxygen atoms in the equatorial plane and two μ_2 axial OH^- bridging adjacent Al(III) centres to form an infinite $Al(OH)O_4$ chain. The Zn^{2+} ion in ZnTCPP[AlOH]$_2$ is at the center of the porphyrin ring, in square planar coordination.

4.3.3 Dyes for solar energy conversion

Dye-sensitized solar cells (DSSCs) based on nanostructured titanium dioxide (TiO_2) have become an active field of research, because they are a promising low-cost alternative to conventional solid-state photovoltaic devices. Interactions between the dye and the semiconductor material play a key role in the efficiency of DSSCs because they influence the electron transfer process. Synchrotron-radiation techniques are perfect tools to study the interface properties of dye/semiconductor in DSSCs. As already highlighted by Lee *et al.* [960], several groups have studied the electron transfer mechanism occurring between dyes and TiO_2 using XAS, XRD and XPS.

Ju and coworkers reported a XAS study at the Ti K-edge of a nanocomposite prepared by self-assembly of the Ru dye N3 (*cis*-diisothiocyanatobis(4,4′-dicarboxy-2,2′-bipyridine)ruthenium(II)) on the surface of 10–20 nm TiO_2 anatase nanoparticles [961]. The parameters obtained by fitting the EXAFS data evidenced a change in the coordination numbers of Ti (from 4.0 to 2.7) and O (from 1.6 to 2.2) atoms in the nanocomposite respect to the free nanoparticles. This was interpreted as an effect of the reconstruction of the Ti local structure at the interface upon coordination of the metal complex on the TiO_2 surface.
Similarly, Shklover and coworkers characterized the Ru complexes N719 and black dye (respectively *cis*-diisothiocyanatobis(4-carboxylic-4′-carboxylate-2,2′-bipyridine)ruthenium(II) and triisothiocyanato(4,4′,4″-tricarboxy-2,2′:6′,2″-terpyridine)ruthenium(II)) supported on nanocristalline TiO_2 anatase using Ti K-edge XAS in combination with out-of-plane XRD and XPS analysis [962]. The uniform enhancement of the pre-edge peaks in the XANES spectra was suggested to correspond to higher distortions of a local Ti coordination in the coated samples, as this is forbidden in the centrosymmetric octahedral environment. Moreover, the coordination numbers of Ti and O were drastically diminished if compared with those of the uncoated sample (Ti, from 4.6 to 2.8; O, from 2.7 to 1.4). Such results were ascribed to a strong distortion of the local environment of Ti atoms caused by the dye coating. However, it should be noted that both XAS spectra measured in transmission mode by Ju and coworkers and FY at Ti K-edge measured by Shklover and coworkers are mostly bulk techniques which are not surface-sensitive.
XPS provides information concerning the energy matching between the orbitals of the dye and the metal oxide valence band and regarding the chemical transformation of the dye at the dye/metal oxide interface.
In terms of XPS studies, the electronic and molecular structure of dyes adsorbed onto nanostructured TiO_2 anatase, have been studied in a number of publications [963-966].
Rensmo and coworkers conducted XAS and XPS studies on a series of Ru-polypyridine complexes (including N3, N719 and black dye) for DSSC application [963, 964, 967, 968]. Their XPS measurements provided information concerning the energy matching between the orbitals of the dye and the TiO_2 (anatase) valence and conduction bands. The position of the HOMO of the complex is shown to be correlated with the metal core levels (Ru 3d) and is basically related to the electrostatic potential at the metal site. Accordingly, negative ligands move the HOMO level toward lower binding energies. The lowest HOMO binding energy was obtained for complexes N3 and N719 which are the most efficient complexes found to date as sensitizers in the nanostructured solar cells. Concerning the bonding of the complexes to the TiO_2 surface, the C 1s, O 1s, N 1s, and S 2p spectra support the general picture of bonding via the carboxyl groups of a single ligand of the complex. In the case of N3, N719 and black dye, a fraction of the isothiocyanate groups also interacts with the TiO_2 surface through the sulfur atoms on the basis of their S 2p spectra. From the O 1s spectrum of N719, they deduced the oxydrilic units in carboxylic acid groups to be at a larger distance from the TiO_2 surface than carboxylated oxygen, indicating that N719 is anchored to the TiO_2 surface through carboxylated groups. Moreover, from the N 1s spectrum, the tetrabutylammonium counterions were found to be at the surface, although the amounts were clearly smaller than expected from the molecular formula.
Similary, O'Shea and coworkers reported an XPS and XANES experimental study of the bonding geometry and electronic coupling of N3 adsorbed on TiO_2 (rutile) [966]. They found that the carboxyl groups of a single ligand of the complex deprotonate so that its O atoms bond to Ti atoms of the substrate, and one of the isothiocyanate groups bonds via a S atom to an O atom of the substrate (see Figure 25). DFT calculations supported that this geometry is energetically more favourable than the bonding of one carboxylic group from each ligand.

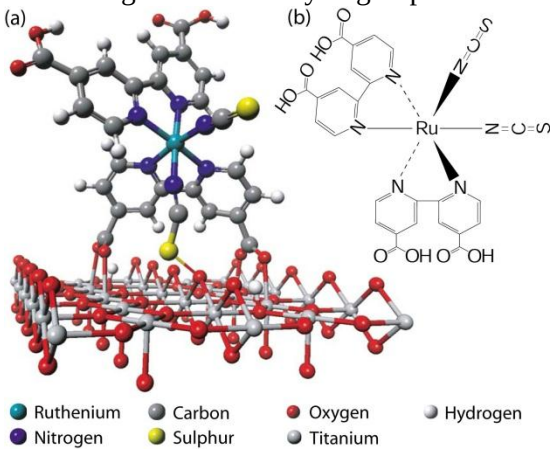

Figure 25. (a) N3 molecule adsorbed on TiO_2, calculated at the DFT-GGA level (see ref. [966] for details), and (b) chemical structure of the N3 molecule. Reproduced with permission from ref. [966]. Copyright (2008), AIP Publishing LLC.

Schwanitz and coworkers investigated the interaction of the Ru dye N3 on nanocrystalline films of anatase TiO_2 [965], using highly surface sensitive synchrotron-induced photoelectron spectroscopy (both XPS and UPS). The HOMO of the adsorbed sensitizer N3 was found 1.6 eV above the TiO_2 valence band, while the LUMO lies 0.17 eV above the Fermi level. Moreover, the authors evaluated the influence of the solvent on the alignment of the dye HOMO level

versus the substrate valence band, demonstrating that the HOMO position of the adsorbed dye changes in the presence of the solvent. In particular, the dye binding energy positions changes upon coadsorption of acetonitrile solvent molecules. A new induced dipole, or the modification of an existing surface dipole, shifts the HOMO by 150 meV and N 1s of the dye NCS group by approximately 200 meV to higher binding energies.
Recently, Demopoulos and coworkers investigated the electronic properties of N719 adsorbed onto TiO_2 (anatase) combining XAS (in TEY mode, to improve surface/interface sensitivity) and XPS [960].
The Ti 2p and O 1s XPS spectra showed that adsorption of the dye on TiO_2 leads to a change of the surface dipole and/or a change in the Fermi level position in the band gap, which shifts all the core levels of TiO_2.
Conversely, even employing the surface-sensitive TEY mode, the Ti L- or K-edge XAS data did not show any structural changes in terms of crystal field modification after dye adsorption to the TiO_2 surface, in contrast to what previously reported by Ju and coworkers and by Shklover and coworkers using transmission or FY mode. This was attributed to the fact that even with the surface-sensitive TEY mode (probing depth of 5-10 nm) most of the XANES signal comes from Ti and O atoms far from the dye-TiO_2 interface and, as such, observing these changes was not feasible in transmission or FY mode. On the other hand, the C K-edge XANES spectral changes revealed that additional electronic states occur between N719 molecules and TiO_2 surface. The authors proposed that electronic interactions do not only occur through the covalent bonding of the anchoring groups but also through the aromatic π electron density of the bipyridine rings and the d states found in TiO_2. The N K-edge did not display additional electronic states, however, the orientation measurements in the N K-edge showed that the intensity for the N 1s $\rightarrow \pi^*$ resonance peak increased at 30°, indicating that the sp2 conjugated π bond in the bipyridine groups is more aligned with the TiO_2 substrate at 30° than 90° to the surface and further suggesting that this type of geometry favours electronic aromatic interaction between the TiO_2 surface and the N719 molecules. This was further confirmed via XPS analysis by monitoring the bipyridine group whose N 1s XPS peak was found to shift to higher energy for dye-coated TiO_2. Furthermore, in the N 1s and S 2p XPS spectra, the NCS peaks of dye-coated TiO_2 are shifted toward higher energy, indicating that there exists an additional H-bonding interaction of the isothiocyanate ligand of the dye molecule with the TiO_2 surface groups (OH/H_2O).
In order to shed light on the possible causes for the different behaviour of ZnO and TiO_2 as materials in DSSCs, Rensmo and coworkers also investigated by XPS the interaction of N3 and nanostructured ZnO, comparing the results with those obtained for nanostructured TiO_2 anatase [968]. Even for a low dye coverage of the ZnO surface, differences in the surface molecular structure were observed comparing the O 1s, N 1s, and S 2p signals. These differences in the XPS signals were interpreted as differences in molecular adsorption geometry or also as a consequence of dye aggregation. The energy matching between the dye and ZnO was found to be similar to that of the dye/TiO_2 system. However, the electronic structure of the isothiocyanate ligand is found to be affected by the adsorption to the ZnO surface. This is interpreted as an effect of an interaction between the isothiocyanate sulfur and zinc sites on the surface or with dissolved zinc ions during dye sensitization. This interaction also has implications on the electronic structure of the dye valence levels, resulting in a broadening in the HOMO level structure.

5 Conclusions and perspectives

We have illustrated how synchrotron radiation based techniques (anomalous scattering, XAS, XES) have had considerable impact to understand the structural and electronic properties of coordination compounds. Insights on their reactivity can be obtained using *in situ*, *operando*, time-resolved techniques. Importantly, the use of complementary methods, such as laboratory techniques (XRD, SAXS, luminescence and UV-Vis) and DFT calculations, is greatly helpful in assisting the analysis of synchorotron data, reinforcing the robustness of the derived results. The advantages in the use of synchrotron radiation sources for X-ray based techniques usually performed at the laboratory scale (such as XRD, XRS and PES) have also been discussed. Finally, in this review we have presented a large number of significant examples, showing the importance of the synergic use of different complementary techniques in the structural and electronic characterization of coordination compounds.
We foresee in the next future the following advances in the use of synchrotron radiation techniques in the characterization of coordination compounds:

(i) Equipment to perform *in situ* and *operando* experiments will become more readily available at most of the XAS beamlines worldwide.

(ii) Time resolved techniques, such as laser pump-X-ray probe and fast data recording methods (quick XAS and energy dispersive XAS) have shown a great development in the last decade and will further develop in the future, conjugating a faster response with a number of independent characterization techniques available on line and allowing *e.g.* parallel IR, UV-Vis, and Raman investigations. Hopefully, improved and readily available data-analysis programs will be developed to take full advantage of the rapid data-taking.

(iii) XES based techniques, nowadays still available only on very few beamlines worldwide, will allow a much deeper knowledge of the electronic structure of the metal center, being able to probe with hard X-rays both the density of both occupied and non-occupied states. These methods will allow to access XPS-like information on coordination complexes in interaction with gases and liquids.

(iv) High-energy resolution fluorescence detected XAS will allow oxidation state-specific EXAFS (separate EXAFS signals in samples containing the same element in different oxidation states) [117, 121] and spin-selective EXAFS spectra collection [771].
(v) Till now, in the large majority of the published papers, XANES has been used only as a qualitative support of the hypothesized structures, based on the evolution of edge, pre edge and post edge features. Quantitative results were extracted from XANES data mainly in comparison with the experimental XANES spectra of model compounds. Publications where hypothesized local structures are used to compute a XANES spectrum are still limited in number, but the remarkable progress made by XANES codes will change this situation. We foresee that the simulation of the XANES spectra will be used more and more frequently to confirm or discard local structures hypothesized from the refinement of EXAFS or diffraction data [717].
(vi) Total scattering (PDF) experiments, will be able to bridge the gap between EXAFS, dominating the 0–30 Å diameter interval, and XRPD, informative in the 80–bulk interval.
(vii) X-ray magnetic circular dichroism (X-MCD), coupled with more conventional techniques, such as visible light MCD and EPR, will bring new insight in the investigation of transition metal coordination compounds.

6 Appendix – X-ray-matter interactions and related techniques: a compendium of the key mathematical results

6.1 X-ray-matter interactions

As underlined in the introduction, we limited as much as possible the use of mathematical equations along the text in order to increase its readibillity and to allow the reader to focus on the scientific issues rather than on the complex mathematical formalism that describes the interaction of X-rays with matter. To partially overcome this lack, a brief summary of the most relevant concepts and related equations is reported in this brief appendix. For further details on the topics treated hereinafter, the reader is referred to the specialized literature quoted along the text.
A simplified representation of the principal X-rays/matter interactions relevant to the structural and electronic characterization of coordination compounds is reported in Scheme 6. In summary, the incident X-ray beam is primary absorbed (according to Lambert-Bear law [166, 969, 970]) or elastically scattered (I_S) by the sample. The radiation not absorbed nor scattered is transmitted through the sample (I_T). At typical X-ray energies, the absorption of a photon generally promotes the expulsion of a core-electron (photoelectrical effect, with a kinetic energy T given by $T = \hbar\Omega - E_K$, being $\hbar\Omega$ the energy of the incoming photon and E_K the binding energy of the electron in the K-shell); the resulting core-hole is then filled by an electron from an outer shell. The excess energy can be released with the emission of characteristic X-rays (X-ray fluorescence, XRF, I_F), which are X-ray photons with energy equal to the difference between the two electronic levels involved ($\hbar\omega_{K\alpha} = E_K - E_{Li}$ or $\hbar\omega_{K\beta} = E_K - E_{Mj}$, i = I, II or III; j = I, II, III, IV or V). Alternatively, the excess energy, instead of being released as a photon, can be transmitted to a second electron that is in turn extracted from the outer electronic levels (Auger electron), which kinetic energy does not depend on the the energy of the incoming photon ($\hbar\Omega$) but on the binding energies of the three involved electronic levels: $T_{Auger} = E_K - E_{Li} - E_{Mj}$. For both these decay channels, the probability of X-ray or electron emission is directly proportional to the X-ray absorption probability. In general, photoelectric absorption is dominant for high-atomic number (Z) elements, while the probability of the Auger effect increases with a decrease in the difference of the corresponding energy states. This means that: (*i*) for a hole crearted in a given shell (K or L) the Auger recombination increases by decreasing the atomic number Z (*i.e.* it is higher for the low-Z atoms); (*ii*) for a given atomic number Z, the Auger recombination increases by moving from a core hole generated in the K-, L- or M-shells [971].

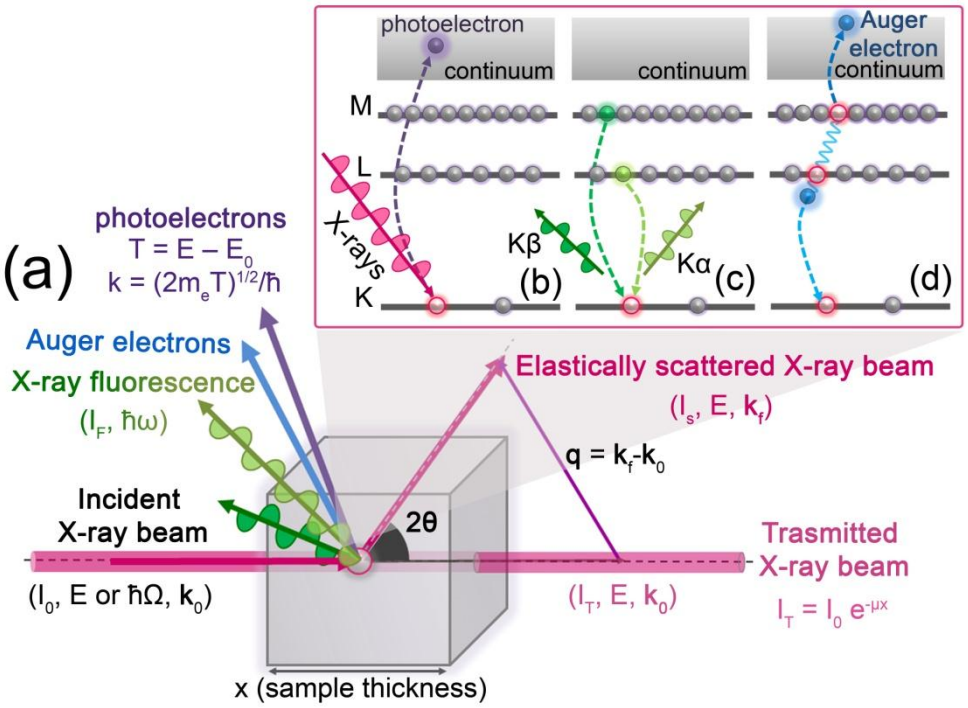

Scheme 6. (a) Schematic representation of the principal X-rays/matter interactions relevant to the structural and electronic characterization of coordination compounds. The scheme reports: the incident X-ray beam (intensity I_0, energy E or $\hbar\Omega$, wavevector $\boldsymbol{k}_0$); the transmitted X-ray beam (intensity $I_T = I_0 \exp(-\mu x)$, where μ is the X-ray absorption coefficient of the sample and x the sample thickness, energy E and wavevector $\boldsymbol{k}_0$); the elastically scattered X-ray beam (intensity I_S, energy E, wavevector $\boldsymbol{k}_f$, with $|\boldsymbol{k}_f|=|\boldsymbol{k}_0|$), the scattering angle 2θ and the scattering vector $\boldsymbol{q} = \boldsymbol{k}_f - \boldsymbol{k}_0$ are also indicated; the emission of photoelectrons (kinetic energy $T = E - E_0$, where E_0 indicates the energy of the core level from which the photoelectron has been extracted: $E_0 = E_K$, or E_{Li}, or E_{Mj}), Auger electrons and X-ray fluorescence photons (intensity I_F and energy $\hbar\omega$). The inset reports schemes of (b) photoelectric effect, resulting in the creation of a core-hole, and two of its possible decay channels: (c) X-ray fluorescence and (d) Auger effect.

Hereinafter we report a brief compendium of the key mathematical passages and results describing the principal X-ray/matter interactions and the related characterization techniques discussed in the main text, focusing in particular on X-ray elastic scattering, X-ray absorption and X-ray emission. The interested reader can refer to the wide literature quoted in the Sections of the main text devoted to the related techniques (X-ray elastic scattering: Section 2.2 (XRD) and 2.6 (XRS); X-ray absorption: Section 2.5 (EXAFS) and 3.2.1 (XANES); X-ray emission: Section 3.2.2) for an extensive and systematic discussion of the matter.

6.2 X-ray Elastic Scattering

When a X-ray plane wave of wavevector $\boldsymbol{k}$ arrives at a generic sample having an electron density $\rho_e(\boldsymbol{r})$, the amplitude of the elastically scattered X-ray wave $A(\boldsymbol{q})$ is expressed by eq. (1).

$$A(\boldsymbol{q}) = \int \rho_e(\boldsymbol{r}) e^{-i\boldsymbol{q}\cdot\boldsymbol{r}} d\boldsymbol{r} \qquad (1)$$

where the integration runs on the X-ray illuminated sample volume (typically, from several μm^3 to few mm^3), $\rho_e(\boldsymbol{r})$ is the electron density of the sample and $\boldsymbol{q} = \boldsymbol{k} - \boldsymbol{k}_0$ is the wave vector proportional to the momentum transfer during the elastic scattering interaction (scattering vector), of modulus given by eq. (2).

$$q = |\boldsymbol{q}| = \frac{4\pi \sin\theta}{\lambda} \qquad (2)$$

The X-ray scattering amplitude $A(\boldsymbol{q})$ and the sample electron density $\rho_e(\boldsymbol{r})$, expressed as a function of the 3D coordinate $\mathbf{r}$, are linked by a Fourier transform operation, as evidenced in eq. (1). This relation is of key importance and highlights the structural sensitivity of the X-ray techniques based on elastic scattering. Experimentally, we are however limited to measure only the square modulus of the scattering amplitude $A(\boldsymbol{q})$, that is the scattered intensity $I(\boldsymbol{q})$, eq. (3).

$$I(\boldsymbol{q}) = |A(\boldsymbol{q})|^2 = \left| \int \rho_e(\boldsymbol{r}) e^{-i\boldsymbol{q}\cdot\boldsymbol{r}} d\boldsymbol{r} \right|^2 \qquad (3)$$

This yield to the so-called "*phase problem*", hampering the direct Fourier inversion of eq. (1) to reconstruct $\rho_e(\boldsymbol{r})$ from a suitable set of X-ray scattering/diffraction data (see below).

Eq. (1) can be further developed by expressing the global electron density $\rho_e(\boldsymbol{r})$ as a superimposition of the individual atomic electron densities centred in the nuclear positions $\boldsymbol{r}_n$:

$$\rho_e(\boldsymbol{r}) = \sum_n \rho_n(\boldsymbol{r}) \otimes \delta(\boldsymbol{r} - \boldsymbol{r}_n) = \sum_n \rho_n(\boldsymbol{r} - \boldsymbol{r}_n) \quad (4)$$

where ρ_n is the electron density of the n^{th} atom, the vector $\boldsymbol{r}$ describes a generic position from the origin of the reference system, the symbol $\otimes$ represents the convolution product and δ is the Dirac delta-function.
By combining eq. (1) and (4) it is possible to express the scattering amplitude $A(\boldsymbol{q})$ in the reference system of the $\boldsymbol{r}_n$ positions as follows:

$$A(\boldsymbol{q}) = \sum_n f_n(\boldsymbol{q})\, e^{-i\boldsymbol{q}\cdot\boldsymbol{r}_n} \quad (5)$$

where the index n runs over all atoms included in the X-ray illuminated sample volume (typically in the order of $N_a \sim 6 \times 10^{23}$) and where $f_n(\boldsymbol{q})$ is the so-called atomic form factor (or X-ray scattering factor) for the n^{th} atom [159, 471], which is the Fourier transform of the atomic electron density, as evidenced in eq. (6):

$$f_n(\boldsymbol{q}) = \int \rho_n(\boldsymbol{r}) e^{-i\boldsymbol{q}\cdot\boldsymbol{r}} d\boldsymbol{r} \quad (6)$$

Eq. (6) is conceptually very differet from eq. (1) because here the integral runs in the volume where the atomic electron density $\rho_n(\boldsymbol{r})$ is significantly different from zero, *i.e.* over few Å^3. Under the assumption of spheric symmetry of the scattering atoms, $f_n(\boldsymbol{q})$ can be expressed as a function of the modulus of $\boldsymbol{q}$, *i.e.* as $f_n(q)$. The scattered intensity can be therefore written as in eq. (7):

$$I(\boldsymbol{q}) = \left| \sum_n f_n(q)\, e^{-i\boldsymbol{q}\cdot\boldsymbol{r}_n} \right|^2 \quad (7)$$

As discussed in the main text (see Section 2.2), the atomic form factor describes the X-ray scattering properties of a specific atom, as determined by the shape of its electron density (spatial charge distribution in the atomic orbitals). Having spatially extended orbitals instead of point-charges (with respect to the wavelength of the incoming X-ray wave) causes a reduction in the coherently scattered intensity. This reduction will be more efficient the larger either $\boldsymbol{q}$ or $\boldsymbol{r}$ become, because the phase shift among the $d\boldsymbol{r}$ regions where the integral is performed is determined by the scalar product $\boldsymbol{q}\cdot\boldsymbol{r}$ in the second term of eq. (6), resulting in the steep decrease in $f(q)$ values as q increases [972].
It is also worth noting that, for some applications (see Section 2.7 in the main text), the anomalous scattering of X-rays has to be considered. Correspondingly, the definition of the atomic form factor is extended, including a complex anomalous scattering contribution [138], according to eq. (8):

$$f(q,E) = f(q) + \Delta f(E) = f(q) + \Delta f'(E) + i\Delta f''(E) \quad (8)$$

The $\Delta f(E)$ contribution, dependent on the incident X-ray energy (or wavelength), is added to the atomic form factors f defined above, with its real and imaginary parts indicating a magnitude variation and a phase shift of the scattered wave, respectively. Nevertheless, working at energies far from any X-ray absorption edges of the elements present in the sample, anomalous scattering factors $\Delta f'$ and $\Delta f''$ are negligible with comparison to f [973].

6.2.1 X-ray diffraction from long-range ordered systems

The periodic arrangement of atoms in long-range ordered systems (crystals) allows further elaboration of the term $|\Sigma_n \exp(-i\boldsymbol{q}\cdot\boldsymbol{r}_n)|^2$ in eq. (7). Here, the unit cell is periodically repeated in the three spatial dimensions. In particular, for a crystal lattice including N_1, N_2 and N_3 atoms along x, y, and z respectively, the position $\boldsymbol{r}_n$ of the n^{th} atom can be expressed as:

$$\boldsymbol{r}_n = n_1\boldsymbol{a} + n_2\boldsymbol{b} + n_3\boldsymbol{c} \quad (9)$$

with (n_1; n_2; n_3) integer numbers and ($\boldsymbol{a}$; $\boldsymbol{b}$; $\boldsymbol{c}$) primitive vectors of the crystal lattice. Expressing $\boldsymbol{r}_n$ as in eq.(9), the $|\Sigma_n \exp(-i\boldsymbol{q}\cdot\boldsymbol{r}_n)|^2$ term in eq. (7) can be developed as follows:

$$\left| \sum_n e^{-i\boldsymbol{q}\cdot\boldsymbol{r}_n} \right|^2 = \left| \sum_n e^{-i\boldsymbol{q}\cdot(n_1\boldsymbol{a}+n_2\boldsymbol{b}+n_3\boldsymbol{c})} \right|^2 = \left| \sum_{n_1=0}^{N_1-1} e^{-i\boldsymbol{q}\cdot(n_1\boldsymbol{a})} \right|^2 \cdot \left| \sum_{n_2=0}^{N_2-1} e^{-i\boldsymbol{q}\cdot(n_2\boldsymbol{b})} \right|^2 \cdot \left| \sum_{n_3=0}^{N_3-1} e^{-i\boldsymbol{q}\cdot(n_3\boldsymbol{c})} \right|^2 \quad (10)$$

It can be demonstrated that, under suitable conditions, each of the factors of general form $|\Sigma_j \exp[-i\boldsymbol{q}\cdot(j\boldsymbol{l})]|^2$ (with $j = n_1$, n_2, n_3 and $\boldsymbol{l} = \boldsymbol{a}$, $\boldsymbol{b}$, $\boldsymbol{c}$) in eq. (10) is zero unless the scalar product $\boldsymbol{q}\cdot\boldsymbol{l}$ is equal to an integer multiple of 2π. This condition on $\boldsymbol{q}$-values allowing constructive interference, and thus detectable scattered intensity, results in the Laue equations [157, 159, 974]:

$$q\cdot\boldsymbol{a} = 2\pi\, h;\; q\cdot\boldsymbol{b} = 2\pi\, k;\; q\cdot\boldsymbol{c} = 2\pi\, l \quad (11)$$

where (h; k; l) $\in \mathbf{Z}$ are also known as Miller indexes.

The periodic order in crystalline systems allows to limit the structural analysis to the unit cell, greatly reducing the number of atoms to consider. With this respect, we can define the structure factor $F(\boldsymbol{q})$ as:

$$F(\boldsymbol{q}) = \sum_n f_n(q)\, e^{-i\boldsymbol{q}\cdot\boldsymbol{r}_n} \tag{12}$$

where now the index n runs exclusively over the atoms within the unit cell and $f_n(q)$ is the atomic form factor of the n^{th} atom in the unit cell. This is a very important point, because, comparing eq. (5) with eq. (12), the translational symmetry of a crystalline lattice allows to reduce the number of terms included in the sum from the whole number of atoms in the sample (a fraction of the Avogadro's number) to a number that, depending on the complexity of the unit cell, can range from few units to some thousands. Having this fact in mind, it becomes clear that the quantitative extraction of structural data from non periodical short-range orderd systems (amorphous solids, liquids and gases) is much more demanding and less informative (see Section 6.2.2 in this appendix).

By expressing the positions $\boldsymbol{r}_n$ of the N atoms within the unit cell by their dimensionless fractional coordinates (x_n, y_n, z_n), *i.e.* $\boldsymbol{r}_n = x_n\boldsymbol{a} + y_n\boldsymbol{b} + z_n\boldsymbol{c}$, and considering the Laue conditions, eq. (11), for a detectable reflection, the structure factor, now indexed using the Miller index (h, k, l), can be expressed as in eq. (13), commonly referred to as the structure factor equation:

$$F_{hkl} = \sum_{n=0}^{N} f_n\, e^{-2\pi i(h\boldsymbol{x}_n + k\boldsymbol{y}_n + l\boldsymbol{z}_n)} = |F_{hkl}|e^{i\varphi(h,k,l)} \tag{13}$$

The third-hand term in eq. (13) highlights how F_{hkl} is a complex quantity, that can be expressed in terms of amplitude and phase: in particular, $\varphi(h,k,l)$ is the phase associated with the point in reciprocal space of coordinates (h, k, l).

Exploiting, within the unit cell volume, the Fourier relation between atomic form factor and atomic electron density, eq. (6), we can rewrite eq. (13) as:

$$F_{hkl} = \int_{cell} \rho(x,y,z) e^{-2\pi i(hx+ky+lz)}\, dxdydz \tag{14}$$

where $\rho(x,y,z)$ represents the electron density value in the point of coordinates (x, y, z) within the unit cell volume, on which the integration is performed.

Assuming that the structure factor F_{hkl} is fully determined, both in its amplitude and phase, it is possible to invert eq. (14) as follows:

$$\rho(x,y,z) = \frac{1}{V}\sum_{h,k,l} |F_{hkl}|e^{i\varphi(h,k,l)}\, e^{2\pi i(hx+ky+lz)} \tag{15}$$

where V is the unit cell volume, and the integral has been replaced by a summation over the discrete ensamble of collected (and indexed) *hkl* reflections. Consequently, what is obtained is a discrete approximation of the continuous $\rho(x,y,z)$ function, evaluated on the finest possible grid of (x, y, z) points within the unit cell, exploiting in each point the whole diffraction dataset.

Unfortunatelly, the direct inversion of the structure factor equation, eq. (14) and (15), is not straightforwardly practicable. Indeed, only $|F_{hkl}| \propto (I_{hkl})^{1/2}$ can be obtained from the experiment, while any information about the phase $\varphi(h,k,l)$, which carries out a major part of the structural information, is unavoidably lost ("*phase problem*"). Nevertheless, several methods have been developed to tackle this problem, allowing to determine the $\varphi(h,k,l)$ values in correspondence of increasingly complex structures [975-977]. The commonest phasing methods suitable in chemical crystallography (indicatively for units cells containing up to 10^3 atoms) include Patterson methods [978-980] and *ab initio* or direct methods [204]. More sophisticate strategies allows to solve the phase problem in macromolecular crystallography, such as molecular replacement [980, 981], charge flipping methods [982] and the synchrotron-based methods exploiting anomalous X-ray diffraction [137, 138, 553, 983].

Finally, it is worth to note that the spatial resolution of the resulting electron density $\rho(x,y,z)$, computed from eq. (15) after the determination of the phases, is generally quantified using the minimum appreciable distance, d_{min}. More specifically, a given diffraction dataset allows us to discriminate the electron densities between two points (x,y,z) and (x',y',z') in the unit cell only if the distance between the two points is larger than d_{min}. The d_{min} value is related by the Bragg law to the maximim angle θ_{max} (or maximum q-value $|\boldsymbol{q}_{max}|$) at which a Bragg peak is detected above the noise level in that given dataset:

$$d_{min} = \frac{\lambda}{2sin\theta_{max}} = \frac{2\pi}{|\boldsymbol{q}_{max}|} \tag{16}$$

Hence, to improve the resolution level, we can reduce the incident X-ray wavelength and collect high-quality data at higher q-values: as discussed in the main text (see Section 2.3), both these strategies are made much more effective by the use of synchrotron sources

6.2.2 X-ray scattering from short-range ordered systems

In short-range ordered systems, such as gases, liquids, solutions and amorphous materials, the probed volume is constituted by a statistical ensemble of randomly oriented structural units (*e.g.* molecules), exhibiting local

correlations, which result in local deviations from the average density of the sample. In these conditions, the general expression of the X-ray scattered intensity, eq. (7), after having explicitely developed the square modulus operation ($|z|^2 = z\,z^*$, $z \in \mathbf{C}$):

$$I(\boldsymbol{q}) = \left|\sum_n f_n(q) e^{-i\boldsymbol{q}\cdot\boldsymbol{r}_n}\right|^2 = \left[\sum_n f_n(q) e^{-i\boldsymbol{q}\cdot\boldsymbol{r}_n}\right]\left[\sum_m f_m(q) e^{i\boldsymbol{q}\cdot\boldsymbol{r}_m}\right] = \sum_n \sum_m f_n(q) f_m(q) e^{-i\boldsymbol{q}\cdot(\boldsymbol{r}_n - \boldsymbol{r}_m)} \qquad (17)$$

can be isotropically averaged on all possible orientations [159, 472, 477], yielding to the Debye equation [473]:

$$\langle I(\boldsymbol{q})\rangle_\Omega = I(q) = \sum_n \sum_m f_n(q) f_m(q) \frac{\sin(\boldsymbol{q}\cdot\boldsymbol{r}_{nm})}{\boldsymbol{q}\cdot\boldsymbol{r}_{nm}} \qquad (18)$$

where $\langle\ \ \rangle_\Omega$ indicates an average over the solid angle Ω, the indexes n, m run over all the system atoms, and r_{nm} is the distance between n^{th} and m^{th} atom, which is now the only "radial" spatial coordinate employed in the expression of the scattered X-ray intensity $I(q)$.

On the contrary of what is achieved, after phasing, from XRD data on long-range ordered systems, here a univocal reconstruction of the three-dimensional electron density from the measured $I(q)$ is impossible, due to the inherent reduction in the information level of one-dimensional XRS data. Nonetheless, eq. (18) can be employed to simulate and compare to experimental data the scattering signal from a series of candidate structures, obtained from *a priori* knowledge of the investigated system. A more practical (and computationally-friendly, for the sake of simulation) expression of the Debye equation can be obtained in terms of radial pair distribution functions (PDF) $g_{\alpha\beta}(r)$ [474-476]. As discussed in Section 2.6 of the main text, radial PDF are defined in such a way that the probability of finding a β-type atom at distance r from an α-type atom (where α, β indicate a specific chemical element) is equal to $4\pi r^2 g_{\alpha\beta}(r)$. Using the formalism of RDF, eq. (18) can be rewritten as follows [159]:

$$I(q) = \sum_\alpha N_\alpha^2 f_\alpha^2(q) + \sum_\beta \sum_{\alpha\neq\beta} \frac{N_\alpha N_\beta}{V} f_\alpha(q) f_\beta(q) \int_0^\infty (g_{\alpha\beta}(r) - 1) \frac{\sin(qr)}{qr} 4\pi r^2 dr \qquad (19)$$

where the indexes α and β run over all the atomic species (elements) included in the sample, N_α and N_β are the numbers of α-type and β-type atoms, respectively, and V the volume of the sample probed by X-rays.

6.3 X-ray Absorption spectroscopy

The physical principles yielding to the XAS signal (see Sections 2.5 and 3.2.1 in the main text for EXAFS and XANES, respectively) can be described in terms of scattering theory. In the framework of a simplified one-electron picture, in the non relativistic approximation, we can model the photoelectrical absorption process as a transition from an initial state ψ_i, including the incident X-ray photon of energy $E = \hbar\Omega$ and a core-electron characterized by a binding energy E_0, and a final state ψ_f, including the core-hole formed after photoionization, and the excited photoelectron. For $E < E_0$ (*i.e.* in the XANES pre-edge region), the photoelectron is promoted to empty bound states near the Fermi level. Conversely, for $E > E_0$ (edge, XANES post-edge and EXAFS regions), the electron is excited to the continuum. In these conditions, the free electron can be described as a spherical wave diffusing from the absorber atom [56, 91], which wavevector k is given by eq. (20):

$$k = \frac{\sqrt{2m_e T}}{\hbar} = \frac{\sqrt{2m_e(\hbar\Omega - E_0)}}{\hbar} \qquad (20)$$

where m_e is the electron mass, $\hbar$ is the reduced Planck constant and $T = \hbar\Omega - E_0$ is the kinetic energy of the diffusing photoelectron. When the absorber is surrounded by other atoms, the photoelectron is scattered by the electrons of the atomic neighbours, resulting in a modification of its wavefunction. The final state is thus constituted by a superimposition of the outgoing wave diffusing from the absorber and the waves backscattered by the neighbouring atoms, exhibiting a phase difference $\Delta\varphi = k(2d)$, with d indicating the interatomic distance between the absorber and its scattering atomic neighbour.

More specifically, the transition rate $T_{i\to f}$ from an initial state $|i\rangle$ to a final state $|f\rangle$, in presence of a time-dependent perturbation, is generally given by the Fermi's golden rule [644, 645], eq. (21):

$$T_{i\to f} = \frac{2\pi}{\hbar} |\langle f|H'|i\rangle|^2 \, \rho_i(\text{occ}) \, \rho_f(\text{unocc}) \qquad (21)$$

where ρ_i(occ) and ρ_f(unocc) indicate the density of the occupied initial states and of the unoccupied final states, respectively, and where H' is the Hamiltonian describing the perturbation.

In particular, for a transition induced by photoelectric absorption, the Fermi's golden rule can be specified as in eq. (22), being the transition rate $T_{i\to f}$ proportional to the X-ray absorption coefficient μ monitored in a XAS experiment:

$$\mu \propto \left|\langle\psi_f|\hat{\boldsymbol{\epsilon}}\cdot\boldsymbol{r}\ \ e^{i\boldsymbol{k}\cdot\boldsymbol{r}}|\psi_i\rangle\right|^2 \delta(E_f - E_i - \hbar\Omega) \qquad (22)$$

where $\hat{\boldsymbol{\epsilon}}$ is the X-rays polarization versor, $\hbar\boldsymbol{k}$ and $\hbar\Omega$ are the photoelectron momentum and energy, respectively, E_i and E_f are the energies of the initial and final state, and δ is the Dirac delta-function.

To quantitatively interpret the fine structure in the XAS spectrum, it is necessary to evaluate the matrix element $\langle\psi_f|\hat{\boldsymbol{\epsilon}}\cdot\boldsymbol{r}\ e^{i\boldsymbol{k}\cdot\boldsymbol{r}}|\psi_i\rangle$ in eq. (22). The expression can be simplified by expanding the exponential $e^{i\boldsymbol{k}\cdot\boldsymbol{r}}$ as a series, *i.e.* $\hat{\boldsymbol{\epsilon}}\cdot\boldsymbol{r}\ e^{i\boldsymbol{k}\cdot\boldsymbol{r}} \sim \hat{\boldsymbol{\epsilon}}\cdot\boldsymbol{r}\ (1 + i\boldsymbol{k}\cdot\boldsymbol{r} + \cdots)$, where the first term indicates the dominant electrical dipole interaction, while the following are related to electrical quadrupole (weaker than the dipole interaction of a factor in the order of the fine structure constant $\alpha \sim 1/137$ [122, 984]) and higher-order multipoles. Under these assumptions, several methods have been developed to perform the full calculation. The commonest strategy is the multiple scattering approach [985, 986], where the potential is modelled as a sum of separated atomic contributions.

Exploiting the Green's function [987], it is also possible to express the absorption coefficient μ as the sum of two terms, separately accounting for the contribution from the "isolated" absorber (μ_0) and from the scattering effects related to the presence of atomic neighbours around the absorber (χ):

$$\mu = \mu_0(1 + \chi) \tag{23}$$

The scattering term χ can be further expressed as a sum of contributions due to all possible scattering events. With this respect, Stern, Sayers and Lytle [46-49] derived a useful formula in single scattering approximation (EXAFS equation), expressing χ as a function of the photoelectron wavenumer k:

$$\chi(k) = -S_0^2 \sum_i \frac{N_j}{kR_i^2} |f_i(k)|\, e^{-2R_i/\lambda_e} e^{-2k\sigma_i^2} \sin(2kR_i + 2\delta_1(k) + \arg(f_i(k))) \tag{24}$$

The sum-index i in eq. (24) runs over the different "coordination shells" (group of atoms of the same chemical element, located at similar distances from the absorber); S_0^2 is the amplitude reduction factor [988], N_i is the number of atoms included in the i^{th} shell (coordination number), R_i is the average distance of the i^{th} shell, σ_i is the Debye-Waller factor depending on the mean square variation about the average of the individual atomic distances for the i^{th} shell and on the thermal vibrations along the bond axis for included atoms, $|f_i(k)|$ and $\arg[f_i(k)]$ are the modulus and the phase of the complex electron scattering amplitude respectively, $\delta_1(k)$ is a phase depending on the absorber, and λ_e is the photoelectron mean free path.

It is worth to note that the EXAFS equation can be successfully applied only for photoelectron energy sufficiently higher than E_0 (EXAFS region), where single scattering events are dominant. Indeed, at relatively lower energies after the absorption edge, the path expansion could not converge, due to the higher scattering probability (full multiple scattering regime). In this region (commonly referred to as XANES post-edge region) more complex and computationally-demanding strategies have to be applied, inclusing *e.g.* the Haydock's recursion method [989], the full matrix inversion [990] and the finite difference method [52, 690].

6.4 X-ray emission spectroscopy

As discussed in the main text (see Section 3.2.2), after excitation with X-ray incident energy $\hbar\Omega$ well above an absorption edge of the element of interest, the excited system can relax filling the photo-induced core-hole by radiative decay from a continuum state, resulting in a *non-resonant* X-ray emission or X-ray fluorescence line. The XES technique relies in the detection of these emitted photons as a function of their energy ($\hbar\omega$) with an energy resolution at least of the same order of the core hole lifetime broadening. Alternatively, if the system is *resonantly* excited to a localized state (tuning the incident X-ray energy $\hbar\Omega$ to an absorption feature in proximity of the Fermi level), and the subsequent radiative decay is monitored with lifetime energy resolution, the technique is referred to as resonant-XES (r-XES) or resonant inelastic X-ray scattering (RIXS).

Both non-resonant XES and r-XES can be described in a common theoretical framework [122, 123, 125, 740, 991], modelling the underlying physics as a two-level photon scattering process *via* the Kramers-Heisenberg equation [116], eq. (25):

$$F(\hbar\Omega, \hbar\omega) = \sum_f \left| \sum_n \frac{\langle f|T_2|n\rangle\langle n|T_1|g\rangle}{E_g - E_n + \hbar\Omega - i\frac{\Gamma_{INT}}{2}} \right|^2 \cdot \frac{\frac{\Gamma_{FIN}}{2\pi}}{(E_g - E_n + \hbar\Omega - \hbar\omega)^2 + \frac{\Gamma^2{}_{FIN}}{4}} \tag{25}$$

Eq. (25) expresses the scattered X-ray intensity $F(\hbar\Omega, \hbar\omega)$ as a function of the incident ($\hbar\Omega$) and emitted ($\hbar\omega$) X-ray energy, and of the energies of the electronic configurations; g, n and f indicates the electron wavefunctions for the starting (ground) state, the intermediate and the final state, respectively. Corresponding energies are indicated as E_g, E_n and E_f. Γ_{INT} and Γ_{FIN} express the intermediate and final state lifetime broadenings (in term of FWHM); the operators T_1 and T_2 describe the absorption and the emission of an X-ray photon, respectively. The energy difference $\hbar\Omega - \hbar\omega$ represents the energy transfer occurring during the inelastic scattering process.

7 Acknowledgements

The authors would like to thank Dr. Elena Groppo (University of Turin, Italy) for valuable discussions on the polymerization catalysts and Dr. Luca Salassa (CIC biomaGUNE, San Sebastián, Spain) for stimulating comments that were greatly helpful in developing our manuscript. CL is indebted with F. Geobaldo (Politecnico of Turin, Italy)

for the synthesis of the oxides which unpublished XANES spectra have been reported in Fig. 10c,d. This work has been supported by “Progetti di Ricerca di Ateneo-Compagnia di San Paolo-2011- Linea 1”, ORTO11RRT5 project and by the Mega-grant of the Russian Federation Government to support scientific research under the supervision of leading scientist at Southern Federal University, No.14.Y26.31.0001.

8 Acronyms

bpy	2,2′-bipyridine
AO	Atomic Orbitals
ASAXS	Anomalous Small-Angle X-ray Scattering
AWAXS	Anomalous Wide Angle X-ray Scattering
CT	Charge Transfer
ctc-XES	core-to-core XES
DAFS	Diffraction Anomalous Fine Structure
DANES	Diffraction Anomalous Near-Edge Structure
DFT	Density Functional Theory
DSSC	Dye-Sensitized Solar Cell
DW	Debye-Waller
EDAFS	Extended Diffraction Anomalous Fine Structure
EDXRD	Energy-Dispersive X-ray Diffraction
EELNES	Electron Energy-Loss Near Edge Structure
EPR	Electron Paramagnetic Resonance
ESCA	Electron Spectroscopy for Chemical Analysis
EXAFS	Extended X-ray Absorption Fine Structure
EXELFS	EXtended Energy-Loss Fine Structure
FT	Fourier Transform
FY	Fuorescence Yield
HERFD	High-Energy Resolution Fluorescence Detected
HEXS	High-Energy X-ray Scattering
HXPES	Hard X-ray PES
HOMO	Highest Occupied Molecular Orbital
IR	InfraRed
ISC	InterSystem Crossing
LAXS	Large Angle X-ray Scattering
LC	Ligand-Centred
LUMO	Lowest Unoccupied Molecular Orbital
MAD	Multi-wavelength Anomalous Dispersion
MO	Molecular Orbital
MOF	Metal-Organic Framework
MS	Multiple-Scattering
ND	Neutron Diffraction
NEXAFS	Near Edge XAFS
NMR	Nuclear Magnetic Resonance
OLEDs	Organic Light-Emitting Diodes.
PEY	Partial Electron Yield
PDF	Pair Distribution Function
PES	PhotoElectron Spectroscopy
XMCD	X-ray Magnetic Circular Dichroism
QEXAFS	Quick EXAFS
RIXS	Resonant Inelastic X-ray Scattering
rctc-XES	resonant ctc-XES
rvtc-XES	resonant vtc-XES
SAXS	Small-Angle X-ray Scattering
SS	Single-Scattering
TEM	Transmission Electron Microscopy
TEY	Total Electron Yield
TFY	Total Fluorescence Yield
thf	tetrahydrofurane
UPS	Ultraviolet Photoelectron Spectroscopy
UV-Vis	UltraViolet–Visible

vtc-XES	valence-to-core XES
XAFS	X-ray Absorption Fine Structure
XANES	X-ray Absorption Near Edge Structure
XAS	X-ray Absorption Spectroscopy
XES	X-ray Emission Spectroscopy
XPS	X-ray Photoelectron Spectroscopy
XRD	X-ray Diffraction
XRPD	X-ray Powder Diffraction
XRS	X-ray Scattering
XSS	X-ray Solution Scattering
WAXS	Wide Angle X-ray Scattering

9 References

[1] C. Bianchini, A. Meli, M. Peruzzini, F. Vizza, F. Zanobini, Coord. Chem. Rev., 120 (1992) 193-208.
[2] G.F. de Sa, O.L. Malta, C.D. Donega, A.M. Simas, R.L. Longo, P.A. Santa-Cruz, E.F. da Silva, Coord. Chem. Rev., 196 (2000) 165-195.
[3] A.D. Phillips, L. Gonsalvi, A. Rornerosa, F. Vizza, M. Peruzzini, Coord. Chem. Rev., 248 (2004) 955-993.
[4] A.Y. Robin, K.M. Fromm, Coord. Chem. Rev., 250 (2006) 2127-2157.
[5] M. Caporali, L. Gonsalvi, A. Rossin, M. Peruzzini, Chem. Rev., 110 (2010) 4178-4235.
[6] S.P. de Visser, J.U. Rohde, Y.M. Lee, J. Cho, W. Nam, Coord. Chem. Rev., 257 (2013) 381-393.
[7] G. Kedarnath, V.K. Jain, Coord. Chem. Rev., 257 (2013) 1409-1435.
[8] L.M. Mirica, J.R. Khusnutdinova, Coord. Chem. Rev., 257 (2013) 299-314.
[9] P. Portius, M. Davis, Coord. Chem. Rev., 257 (2013) 1011-1025.
[10] T.S. Li, S. Kaercher, P.W. Roesky, Chem. Soc. Rev., 43 (2014) 42-57.
[11] Y. Iwasawa, Adv. Catal., 35 (1987) 187-264.
[12] H.H. Lamb, B.C. Gates, H. Knozinger, Angew. Chem.-Int. Edit., 27 (1988) 1127-1144.
[13] Y. Iwasawa, Accounts Chem. Res., 30 (1997) 103-109.
[14] J.M. Basset, F. Lefebvre, C. Santini, Coord. Chem. Rev., 178 (1998) 1703-1723.
[15] A.C. Franville, D. Zambon, R. Mahiou, Y. Troin, Chem. Mat., 12 (2000) 428-435.
[16] J. Guzman, B.C. Gates, Dalton Trans., (2003) 3303-3318.
[17] C. Coperet, M. Chabanas, R.P. Saint-Arroman, J.M. Basset, Angew. Chem.-Int. Edit., 42 (2003) 156-181.
[18] J.C. Fierro-Gonzalez, S. Kuba, Y.L. Hao, B.C. Gates, J. Phys. Chem. B, 110 (2006) 13326-13351.
[19] M. Tada, Y. Iwasawa, Coord. Chem. Rev., 251 (2007) 2702-2716.
[20] E.A. Quadrelli, J.M. Basset, Coord. Chem. Rev., 254 (2010) 707-728.
[21] G.A. Ozin, Adv. Mater., 4 (1992) 612-649.
[22] A. Malek, G. Ozin, Adv. Mater., 7 (1995) 160-163.
[23] L.X. Song, L. Bai, X.M. Xu, J. He, S.Z. Pan, Coord. Chem. Rev., 253 (2009) 1276-1284.
[24] M. Peruzzini, L. Gonsalvi, A. Romerosa, Chem. Soc. Rev., 34 (2005) 1038-1047.
[25] J. Bravo, S. Bolano, L. Gonsalvi, M. Peruzzini, Coord. Chem. Rev., 254 (2010) 555-607.
[26] P. Ravindran, R. Vidya, P. Vajeeston, A. Kjekshus, H. Fjellvag, J. Solid State Chem., 176 (2003) 338-374.
[27] P. Frank, M. Benfatto, R.K. Szilagyi, P. D'Angelo, S. Della Longa, K.O. Hodgson, Inorg. Chem., 44 (2005) 1922-1933.
[28] E.I. Solomon, B. Hedman, K.O. Hodgson, A. Dey, R.K. Szilagyi, Coord. Chem. Rev., 249 (2005) 97-129.
[29] A.R. Jaszewski, R. Stranger, R.J. Pace, J. Phys. Chem. A, 112 (2008) 11223-11234.
[30] E.M. Sproviero, J.P. McEvoy, J.A. Gascon, G.W. Brudvig, V.S. Batista, Photosynth. Res., 97 (2008) 91-114.
[31] E.M. Sproviero, J.A. Gascon, J.P. McEvoy, G.W. Brudvig, V.S. Batista, Coord. Chem. Rev., 252 (2008) 395-415.
[32] F.M.F. de Groot, Inorg. Chim. Acta, 361 (2008) 850-856.
[33] S.G. Ebbinghaus, H.P. Abicht, R. Dronskowski, T. Muller, A. Reller, A. Weidenkaff, Prog. Solid State Chem., 37 (2009) 173-205.
[34] X.L. Tan, M. Fang, X.K. Wang, Molecules, 15 (2010) 8431-8468.
[35] P. Gatt, R. Stranger, R.J. Pace, J. Photochem. Photobiol. B-Biol., 104 (2011) 80-93.
[36] E. Gallo, C. Lamberti, P. Glatzel, Phys. Chem. Chem. Phys., 13 (2011) 19409-19419.
[37] E. Gallo, C. Lamberti, P. Glatzel, Inorg. Chem., 52 (2013) 5633-5635.
[38] E. Gallo, F. Bonino, J.C. Swarbrick, T. Petrenko, A. Piovano, S. Bordiga, D. Gianolio, E. Groppo, F. Neese, C. Lamberti, P. Glatzel, ChemPhysChem, 14 (2013) 79-83.
[39] K.A. Lomachenko, C. Garino, E. Gallo, D. Gianolio, R. Gobetto, P. Glatzel, N. Smolentsev, G. Smolentsev, A.V. Soldatov, C. Lamberti, L. Salassa, Phys. Chem. Chem. Phys., 15 (2013) 16152-16159.
[40] G. Margaritondo, J. Synchrotron Rad., 2 (1995) 148-154.
[41] K. Wille, Rep. Prog. Phys., 54 (1991) 1005-1068.
[42] M.E. Couprie, J.M. Filhol, C. R. Phys., 9 (2008) 487-506.
[43] G. Margaritondo, Introduction to synchrotron radiation, Oxford University Press, New York, 1988.
[44] G. Margaritondo, Surf. Rev. Lett., 7 (2000) 379-387.
[45] D.H. Bilderback, P. Elleaume, E. Weckert, J. Phys. B-At. Mol. Opt. Phys., 38 (2005) S773-S797.
[46] D.E. Sayers, E.A. Stern, F.W. Lytle, Phys. Rev. Lett., 27 (1971) 1204-1207.
[47] E.A. Stern, Phys. Rev. B, 10 (1974) 3027-3037.
[48] E.A. Stern, D.E. Sayers, F.W. Lytle, Phys. Rev. B, 11 (1975) 4836-4846.
[49] F.W. Lytle, D.E. Sayers, E.A. Stern, Phys. Rev. B, 11 (1975) 4825-4835.

[50] C.R. Natoli, Near Edge Absorption Structure in the Framework of the Multiple Scattering Model. Potential Resonance or Barrier Effects?, in: A. Bianconi, L. Incoccia, S. Stipcich (Eds.) EXAFS and Near Edge Structure, Springer, Berlin, 1983, pp. 43-56.
[51] A. Bianconi, XANES spectroscopy, in: D.C. Koningsberger, R. Prins (Eds.) X-Ray Absorption: Principles, Applications, Techniques of EXAFS, SEXAFS and XANES, John Wiley & Sons, New York, 1988, pp. 573-662.
[52] Y. Joly, Phys. Rev. B, 63 (2001) art. n. 125120.
[53] J.J. Rehr, A.L. Ankudinov, Coord. Chem. Rev., 249 (2005) 131-140.
[54] A. Filipponi, A. Di Cicco, C.R. Natoli, Phys. Rev. B, 52 (1995) 15122-15134.
[55] A. Filipponi, A. Di Cicco, Phys. Rev. B, 52 (1995) 15135-15149.
[56] J.J. Rehr, R.C. Albers, Rev. Mod. Phys., 72 (2000) 621-654.
[57] J.C.J. Bart, Adv. Catal., 34 (1986) 203-296.
[58] J.C.J. Bart, G. Vlaic, Adv. Catal., 35 (1987) 1-138.
[59] J.H. Sinfelt, Accounts Chem. Res., 20 (1987) 134-139.
[60] R. Prins, D.C. Koningsberger, Catalysis, in: D.C. Koningsberger, R. Prins (Eds.) X-Ray Absorption: Principles, Applications, Techniques of EXAFS, SEXAFS and XANES, John Wiley & Sons, New York, 1988, pp. 321.
[61] H. Kuroda, T. Yokoyama, K. Asakura, Y. Iwasawa, Faraday Discuss., 92 (1991) 189-198.
[62] J.H. Sinfelt, G.D. Meitzner, Accounts Chem. Res., 26 (1993) 1-6.
[63] J. Evans, Chem. Soc. Rev., 26 (1997) 11-19.
[64] B.S. Clausen, H. Topsoe, R. Frahm, Adv. Catal., 42 (1998) 315-344.
[65] O. Alexeev, B.C. Gates, Top. Catal., 10 (2000) 273-293.
[66] D. Bazin, L. Guczi, Appl. Catal. A-Gen., 213 (2001) 147-162.
[67] J.M. Thomas, G. Sankar, Accounts Chem. Res., 34 (2001) 571-581.
[68] M. Fernandez-Garcia, Catal. Rev. Sci. Engin., 44 (2002) 59–121.
[69] A.E. Russell, A. Rose, Chem. Rev., 104 (2004) 4613-4635.
[70] S.R. Bare, T. Ressler, Adv. Catal., 52 (2009) 339-465.
[71] A.J. Foster, R.F. Lobo, Chem. Soc. Rev., 39 (2010) 4783-4793.
[72] U. Bentrup, Chem. Soc. Rev., 39 (2010) 4718-4730.
[73] A.I. Frenkel, A. Yevick, C. Cooper, R. Vasic, Annu. Rev. Anal. Chem., 4 (2011) 23-39.
[74] A.I. Frenkel, Chem. Soc. Rev., 41 (2012) 8163-8178.
[75] S. Muratsugu, M. Tada, Accounts Chem. Res., 46 (2013) 300-311.
[76] S. Bordiga, E. Groppo, G. Agostini, J.A. van Bokhoven, C. Lamberti, Chem. Rev., 113 (2013) 1736-1850.
[77] Y.E. Alexeev, B.I. Kharisov, T.C. Hernandez Garcia, A.D. Garnovskii, Coord. Chem. Rev., 254 (2010) 794-831.
[78] M.A. Denecke, Coord. Chem. Rev., 250 (2006) 730-754.
[79] S. Bordiga, F. Bonino, K.P. Lillerud, C. Lamberti, Chem. Soc. Rev., 39 (2010) 4885-4927.
[80] M.S. Queen, B.D. Towey, K.A. Murray, B.S. Veldkamp, H.J. Byker, R.K. Szilagyi, Coord. Chem. Rev., 257 (2013) 564-578.
[81] K.C. Szeto, C. Prestipino, C. Lamberti, A. Zecchina, S. Bordiga, M. Bjorgen, M. Tilset, K.P. Lillerud, Chem. Mat., 19 (2007) 211-220.
[82] K.C. Szeto, K.P. Lillerud, M. Tilset, M. Bjorgen, C. Prestipino, A. Zecchina, C. Lamberti, S. Bordiga, J. Phys. Chem. B, 110 (2006) 21509-21520.
[83] A. Rossin, B. Di Credico, G. Giambastiani, M. Peruzzini, G. Pescitelli, G. Reginato, E. Borfecchia, D. Gianolio, C. Lamberti, S. Bordiga, J. Mater. Chem., 22 (2012) 10335-10344.
[84] L.R. Sharpe, W.R. Heineman, R.C. Elder, Chem. Rev., 90 (1990) 705-722.
[85] H.D. Abruna, G.M. Bommarito, H.S. Yee, Accounts Chem. Res., 28 (1995) 273-279.
[86] A.K. Cheetham, A.P. Wilkinson, Angew. Chem.-Int. Edit., 31 (1992) 1557-1570.
[87] S.H. Tolbert, A.P. Alivisatos, Annu. Rev. Phys. Chem., 46 (1995) 595-625.
[88] J.G. Chen, Surf. Sci. Rep., 30 (1997) 5-152.
[89] C. Lamberti, Surf. Sci. Rep., 53 (2004) 1-197.
[90] L. Mino, G. Agostini, E. Borfecchia, D. Gianolio, A. Piovano, E. Gallo, C. Lamberti, J. Phys. D-Appl. Phys., 46 (2013) art. n. 423001.
[91] F. Boscherini, X-Ray Absorption Fine Structure in the Study of Semiconductor Heterostructures and Nanostructures in: C. Lamberti, G. Agostini (Eds.) Characterization of Semiconductor Heterostructures and Nanostructures (Second Edition), Elsevier, Amsterdam, 2013, pp. 259-310.
[92] E.D. Crozier, J.J. Rehr, R. Ingalls, Amorphous and liquid systems, in: D.C. Koningsberger, R. Prins (Eds.) X-Ray Absorption, John Wiley and Sons, New York, 1988, pp. 663.
[93] A. Filipponi, J. Phys.-Condes. Matter, 13 (2001) R23-R60.
[94] C. Hardacre, Ann. Rev. Mater. Res., 35 (2005) 29-49.
[95] G. Hahner, Chem. Soc. Rev., 35 (2006) 1244-1255.

[96] B. Watts, H. Ade, Mater. Today, 15 (2012) 148-157.
[97] Y. Moritomo, M. Takachi, Y. Kurihara, T. Matsuda, Adv. Mater. Sci. Eng., (2013) art. n. 967285.
[98] A. Manceau, M.A. Marcus, N. Tamura, Rev. Mineral. Geochem., 49 (2002) 341-428.
[99] W.P. Gates, X-ray absorption spectroscopy, in: F. Bergaya, B.K.G. Theng, G. Lagaly (Eds.) Handbook of Clay Science, Elsevier, Amsterdam, 2006, pp. 789-864.
[100] L. Bertrand, M. Cotte, M. Stampanoni, M. Thoury, F. Marone, S. Schoder, Phys. Rep.-Rev. Sec. Phys. Lett., 519 (2012) 51-96.
[101] D.M. Goltz, Anal. Lett., 45 (2012) 314-329.
[102] M. Cotte, J. Susini, J. Dik, K. Janssens, Accounts Chem. Res., 43 (2010) 705-714.
[103] G.P. Diakun, Nature, 344 (1990) 83-84.
[104] P.J. Riggsgelasco, T.L. Stemmler, J.E. Pennerhahn, Coord. Chem. Rev., 144 (1995) 245-286.
[105] J.G. Parsons, M.V. Aldrich, J.L. Gardea-Torresdey, Appl. Spectrosc. Rev., 37 (2002) 187-222.
[106] L. Pellerito, L. Nagy, Coord. Chem. Rev., 224 (2002) 111-150.
[107] J.E. Penner-Hahn, Coord. Chem. Rev., 249 (2005) 161-177.
[108] R.W. Strange, M. Ellis, S.S. Hasnain, Coord. Chem. Rev., 249 (2005) 197-208.
[109] R. Ortega, A. Carmona, I. Llorens, P.L. Solari, J. Anal. At. Spectrom., 27 (2012) 2054-2065.
[110] L. Rulisek, U. Ryde, Coord. Chem. Rev., 257 (2013) 445-458.
[111] R. Sarangi, Coord. Chem. Rev., 257 (2013) 459-472.
[112] G. Sarret, E. Smits, H.C. Michel, M.P. Isaure, F.J. Zhao, R. Tappero, Adv. Agronomy, 119 (2013) 1-82.
[113] A.A. Hummer, A. Rompel, Adv. Protein Chem. Struct. Biol., 93 (2013) 257-305.
[114] A.A. Hummer, A. Rompel, Metallomics, 5 (2013) 597-614.
[115] E.Z. Kurmaev, V.R. Galakhov, S.N. Shamin, Crit. Rev. Solid State Mat. Sci., 23 (1998) 65-203.
[116] A. Kotani, S. Shin, Rev. Mod. Phys., 73 (2001) 203-246.
[117] F. de Groot, Chem. Rev., 101 (2001) 1779-1808.
[118] A. Nilsson, J. Electron Spectrosc. Relat. Phenom., 126 (2002) 3-42.
[119] A. Nilsson, L.G.M. Pettersson, Surf. Sci. Rep., 55 (2004) 49-167.
[120] F. de Groot, Coord. Chem. Rev., 249 (2005) 31-63.
[121] F. de Groot, A. Kotani, Core Level Spectroscopy of Solids, CRC Press, London, 2008.
[122] P. Glatzel, U. Bergmann, Coord. Chem. Rev., 249 (2005) 65-95.
[123] U. Bergmann, P. Glatzel, Photosynth. Res., 102 (2009) 255-266.
[124] P. Glatzel, M. Sikora, M. Fernandez-Garcia, Eur. Phys. J.-Spec. Top., 169 (2009) 207-214.
[125] J. Singh, C. Lamberti, J.A. van Bokhoven, Chem. Soc. Rev., 39 (2010) 4754-4766.
[126] R. Guillemin, S. Carniato, L. Journel, W.C. Stolte, T. Marchenko, L. El Khoury, E. Kawerk, M.N. Piancastelli, A.C. Hudson, D.W. Lindle, M. Simon, J. Electron Spectrosc. Relat. Phenom., 188 (2013) 53-61.
[127] A. Kotani, Mod. Phys. Lett. B, 27 (2013) art. n. 1330012.
[128] E. Dujardin, S. Ferlay, X. Phan, C. Desplanches, C.C.D. Moulin, P. Sainctavit, F. Baudelet, E. Dartyge, P. Veillet, M. Verdaguer, J. Am. Chem. Soc., 120 (1998) 11347-11352.
[129] B. Donnio, E. Riviere, E. Terazzi, E. Voirin, C. Aronica, G. Chastanet, D. Luneau, G. Rogez, F. Scheurer, L. Joly, J.P. Kappler, J.L. Gallani, Solid State Sci., 12 (2010) 1307-1313.
[130] F. Moro, V. Corradini, M. Evangelisti, R. Biagi, V. De Renzi, U. del Pennino, J.C. Cezar, R. Inglis, C.J. Milios, E.K. Brechin, Nanoscale, 2 (2010) 2698-2703.
[131] M.J. Rodriguez-Douton, M. Mannini, L. Armelao, A.L. Barra, E. Tancini, R. Sessoli, A. Cornia, Chem. Commun., 47 (2011) 1467-1469.
[132] M. Mannini, E. Tancini, L. Sorace, P. Sainctavit, M.A. Arrio, Y. Qian, E. Otero, D. Chiappe, L. Margheriti, J.C. Cezar, R. Sessoli, A. Cornia, Inorg. Chem., 50 (2011) 2911-2917.
[133] J. Dreiser, K.S. Pedersen, T. Birk, M. Schau-Magnussen, C. Piamonteze, S. Rusponi, T. Weyhermuller, H. Brune, F. Nolting, J. Bendix, J. Phys. Chem. A, 116 (2012) 7842-7847.
[134] R. Westerstrom, J. Dreiser, C. Piamonteze, M. Muntwiler, S. Weyeneth, H. Brune, S. Rusponi, F. Nolting, A. Popov, S.F. Yang, L. Dunsch, T. Greber, J. Am. Chem. Soc., 134 (2012) 9840-9843.
[135] L. Badia-Romano, F. Bartolome, J. Bartolome, J. Luzon, D. Prodius, C. Turta, V. Mereacre, F. Wilhelm, A. Rogalev, Phys. Rev. B, 87 (2013) art. n. 184403.
[136] R. Fourme, M. Chiadmi, R. Kahn, Multiwavelength Anomalous Diffraction in protein crystallography: phase calculations, experimental procedures and results, in: A. Bianconi, A.C. Castellano (Eds.) Biophysics and Synchrotron Radiation, Springer, Berling, 1987, pp. 32-40.
[137] W.A. Hendrickson, Science, 254 (1991) 51-58.
[138] J.L. Hodeau, V. Favre-Nicolin, S. Bos, H. Renevier, E. Lorenzo, J.F. Berar, Chem. Rev., 101 (2001) 1843-1867.
[139] Z. Dauter, Curr. Opin. Struct. Biol., 12 (2002) 674-678.

[140] J.R. Helliwell, Macromolecular Crystallography with Synchrotron Radiation, Cambridge University Press, Cambridge, 2005.
[141] E.M.H. Duke, L.N. Johnson, Proc. R. Soc. A-Math. Phys. Eng. Sci., 466 (2010) 3421-3452.
[142] A. Cassetta, A.M. Deacon, S.E. Ealick, J.R. Helliwell, A.W. Thompson, J. Synchrot. Radiat., 6 (1999) 822-833.
[143] S.J.L. Billinge, M.G. Kanatzidis, Chem. Commun., (2004) 749-760.
[144] S.J.L. Billinge, I. Levin, Science, 316 (2007) 561-565.
[145] T. Egami, S.J.L. Billinge, Underneath the Bragg Peaks: Structural Analysis of Complex Materials, Elsevier Science, Oxford, 2012.
[146] E.S. Bozin, P. Juhás, S.J.L. Billinge, Local structure of bulk and nanocrystalline semiconductors using total scattering method, in: C. Lamberti, G. Agostini (Eds.) Characterization of Semiconductor Heterostructures and Nanostructures (II Ed.), Elsevier, Amsterdam, 2013, pp. 289-330.
[147] M.A. Newton, A.J. Dent, J. Evans, Chem. Soc. Rev., 31 (2002) 83-95.
[148] L.X. Chen, Angew. Chem.-Int. Edit., 43 (2004) 2886-2905.
[149] C. Bressler, M. Chergui, Chem. Rev., 104 (2004) 1781-1812.
[150] C. Bressler, M. Chergui, Annu. Rev. Phys. Chem., 61 (2010) 263-282.
[151] M. Rahman, P.R. Bolton, J. Evans, A.J. Dent, I. Harvey, S. Diaz-Moreno, Faraday Discuss., 122 (2003) 211-222.
[152] A.O. Er, J. Chen, P.M. Rentzepis, J. Appl. Phys., 112 (2012) art. n. 031101.
[153] E. Borfecchia, C. Garino, L. Salassa, C. Lamberti, Phil. Trans. R. Soc. A, 371 (2013) art. n. 20120132.
[154] J.D. Grunwaldt, C.G. Schroer, Chem. Soc. Rev., 39 (2010) 4741-4753.
[155] A.M. Beale, S.D.M. Jacques, B.M. Weckhuysen, Chem. Soc. Rev., 39 (2010) 4656-4672.
[156] G. Martinez-Criado, E. Borfecchia, L. Mino, C. Lamberti, Micro and nano X-ray beams, in: C. Lamberti, G. Agostini (Eds.) Characterization of Semiconductor Heterostructures and Nanostructures (Second Edition), Elsevier, Amsterdam, 2013, pp. 361-412.
[157] W. Friedrich, P. Knipping, M. von Laue, Bayerische Akademie der Wissenschaften, (1912) 303-322.
[158] R.W. James, The Optical Principles of the Diffraction of x-rays, G. Bell and Sons Ltd., 1948.
[159] B.E. Warren, X-ray Diffraction, Dover, New York, 1969.
[160] C. Giacovazzo, Fundamentals of Crystallography, Oxford University Press, Oxford, 2002.
[161] G.P. Thomson, A. Reid, Nature, 119 (1927) 890-890.
[162] G.P. Thomson, Nature, 120 (1927) 802-802.
[163] G.P. Thomson, Contemporary Phys., 9 (1968) 1-15.
[164] D.B. Williams, C.B. Carter, Transmission Electron Microscopy, Plenum, New York, 1996.
[165] M. De Graef, Introduction to Conventional Transmission Electron Microscopy, Cambridge University Press, Cambridge, 2003.
[166] P. Atkins, Physical Chemistry 3rd Edition Oxford University Press, Oxford, 1986.
[167] C.G. Shull, E.O. Wollan, W.C. Koehler, Phys. Rev., 84 (1951) 912-921.
[168] C.G. Shull, Rev. Mod. Phys., 67 (1995) 753-757.
[169] W.G. Williams, Polarized Neutrons, Clarendon Press, Oxford, 1988.
[170] T. Chatterji, Neutron Scattering from Magnetic Materials, Elsevier Science, Amsterdam, 2005.
[171] R.J. Harrison, Rev. Mineral. Geochem., 63 (2006) 113-143.
[172] M. Chergui, A.H. Zewail, ChemPhysChem, 10 (2009) 28-43.
[173] M.P. Seah, W.A. Dench, Surf. Interface Anal., 1 (1979) 2-11.
[174] X. Zou, S. Hovmoller, Acta Crystallogr. Sect. A, 64 (2008) 149-160.
[175] T.E. Weirich, J.L. Lábár, X. Zou, in, Springer, Dordrecht, 2006.
[176] X. Zou, S. Hovmöller, P. Oleynikov, Electron Crystallography: Electron Microscopy and Electron Diffraction, Oxford University Press, New York, 2011.
[177] I. Hargittai, Stereochemical Applications of Gas-Phase Electron Diffraction, Part A: The Electron Diffraction Technique, VHC, Weinheim, Germany, 1988.
[178] V.P. Spiridonov, N. Vogt, J. Vogt, Struct. Chem., 12 (2001) 349-376.
[179] H. Fleischer, D.A. Wann, S.L. Hinchley, K.B. Borisenko, J.R. Lewis, R.J. Mawhorter, H.E. Robertson, D.W.H. Rankin, Dalton Trans., (2005) 3221-3228.
[180] I. Hargittai, Gas-phase electron diffraction for molecular structure determination, in: T.E. Weirich, J.L. Lábár, X. Zou (Eds.) Electron Crystallography: Novel Approaches for Structure Determination of Nanosized Materials, Springer, Dordrecht, 2006.
[181] D. Denysenko, M. Grzywa, M. Tonigold, B. Streppel, I. Krkljus, M. Hirscher, E. Mugnaioli, U. Kolb, J. Hanss, D. Volkmer, Chem.-Eur. J., 17 (2011) 1837-1848.
[182] H.F. Greer, W.Z. Zhou, Crystallogr. Rev, 17 (2011) 163-185.

[183] C. Wiktor, S. Turner, D. Zacher, R.A. Fischer, G. Van Tendeloo, Microporous Mesoporous Mat., 162 (2012) 131-135.
[184] O.I. Lebedev, F. Millange, C. Serre, G. Van Tendeloo, G. Ferey, Chem. Mat., 17 (2005) 6525-6527.
[185] J. Cravillon, S. Munzer, S.J. Lohmeier, A. Feldhoff, K. Huber, M. Wiebcke, Chem. Mat., 21 (2009) 1410-1412.
[186] R.J.T. Houk, B.W. Jacobs, F. El Gabaly, N.N. Chang, A.A. Talin, D.D. Graham, S.D. House, I.M. Robertson, M.D. Allendorf, Nano Lett., 9 (2009) 3413-3418.
[187] M. Yamada, S. Yonekura, J. Phys. Chem. C, 113 (2009) 21531-21537.
[188] T.D. Bennett, A.L. Goodwin, M.T. Dove, D.A. Keen, M.G. Tucker, E.R. Barney, A.K. Soper, E.G. Bithell, J.C. Tan, A.K. Cheetham, Phys. Rev. Lett., 104 (2010) art. n. 115503.
[189] J.P. Glusker, M. Lewis, M. Rossi, Crystal Structure Analysis for Chemists and Biologists, Wiley, New York, 1994.
[190] W. Clegg, Crystal Structure Determination, Oxford University Press, Incorporated, Oxford, 1998.
[191] W. Clegg, X-ray Diffraction, in: J.A. McCleverty, T.J. Meyer (Eds.) Comprehensive Coordination Chemistry II Elsevier Ltd., Oxford, 2003
[192] A.J. Blake, W. Clegg, J.M. Cole, Crystal structure analysis: principles and practice, Oxford University Press, New York, 2009.
[193] J.P. Glusker, K.N. Trueblood, Crystal Structure Analysis: A Primer, Oxford University Press, New York, 2010.
[194] R.E. Dinnebier, S.J.L. Billinge, Powder Diffraction: Theory and Practice, Royal Society of Chemistry, Cambridge, 2008.
[195] C.R. Groom, F.H. Allen, Wiley Interdiscip. Rev.-Comput. Mol. Sci., 1 (2011) 368-376.
[196] F.H. Allen, Acta Crystallogr. Sect. B-Struct. Sci., 58 (2002) 380-388.
[197] Cambridge Structural Database Entries: Summary Statistics 2013 (http://www.ccdc.cam.ac.uk/Lists/ResourceFileList/stats_entries_Jan2013.pdf).
[198] J.I. Langford, D. Louer, Rep. Prog. Phys., 59 (1996) 131-234.
[199] A. Altomare, C. Cuocci, A. Moliterni, R. Rizzi, Single crystal and powder XRD techniques: an overview, in: A. Dibenedetto, M. Aresta (Eds.) Inorganic Micro- and Nanomaterials. Synthesis and Characterization, De Gruyter, Berlin, 2013, pp. 57-91.
[200] H. Rietveld, Acta Crystallogr., 22 (1967) 151-152.
[201] H. Rietveld, J. Appl. Crystallogr., 2 (1969) 65-71.
[202] R.A. Young, D.B. Wiles, J. Appl. Crystallogr., 15 (1982) 430-438.
[203] R.A. Young, The Rietveld Method, Oxford University Press, 1995.
[204] C. Giacovazzo, Direct Phasing in Crystallography: Fundamentals and Applications, Oxford University Press, Oxford, 1998.
[205] D. Louer, Acta Crystallogr. Sect. A, 54 (1998) 922-933.
[206] W.I.F. David, in, Oxford University Press, Oxford, 2002.
[207] P.E. Werner, L. Eriksson, M. Westdahl, J. Appl. Crystallogr., 18 (1985) 367-370.
[208] A. Altomare, C. Giacovazzo, A. Guagliardi, A.G.G. Moliterni, R. Rizzi, J. Appl. Crystallogr., 33 (2000) 1305-1310.
[209] C. Giacovazzo, A. Altomare, C. Cuocci, A.G.G. Moliterni, R. Rizzi, J. Appl. Crystallogr., 35 (2002) 422-429.
[210] A. Altomare, R. Caliandro, M. Camalli, C. Cuocci, I. da Silva, C. Giacovazzo, A.G.G. Moliterni, R. Spagna, J. Appl. Crystallogr., 37 (2004) 957-966.
[211] D.J. Tranchemontagne, J.L. Mendoza-Cortes, M. O'Keeffe, O.M. Yaghi, Chem. Soc. Rev., 38 (2009) 1257-1283.
[212] A. Bacchi, M. Carcelli, P. Pelagatti, Crystallogr. Rev, 18 (2012) 253-279.
[213] E. Borfecchia, D. Gianolio, G. Agostini, S. Bordiga, C. Lamberti, Local and long order structural determination by combining EXAFS and diffraction techniques, in: F.X. Llabrés i Xamena, J. Gascón (Eds.) Metal Organic Frameworks as Heterogeneous Catalysts, RSC, Cambridge, 2013, pp. 143-208.
[214] V.F. Sears, Neutron News, 3 (1992) 26-37.
[215] G.E. Bacon, Neutron diffraction, Clarendon Press, Oxford, 1975.
[216] S.W. Lovesey, T. Springer, in, Springer-Verlag, Berlin, 1977.
[217] J. Baruchel, Neutron and synchrotron radiation for condensed matter studies: Applications to solid state physics and chemistry, Springer-Verlag, Berlin, 1994.
[218] C.C. Wilson, Single Crystal Neutron Diffraction from Molecular Materials, World Scientific, Singapore, 2000.
[219] G.J. Long, Neutron Diffraction, in: J.A. McCleverty, T.J. Meyer (Eds.) Comprehensive Coordination Chemistry II Elsevier Ltd., Oxford, 2003.
[220] M.P. Blakeley, M. Cianci, J.R. Helliwell, P.J. Rizkallah, Chem. Soc. Rev., 33 (2004) 548-557.
[221] M.P. Blakeley, Crystallogr. Rev, 15 (2009) 157-218.

[222] G.L. Squires, Introduction to the Theory of Thermal Neutron Scattering, Cambridge University Press, Cambridge, 2012.
[223] V.J. Murphy, D. Rabinovich, T. Hascall, W.T. Klooster, T.F. Koetzle, G. Parkin, J. Am. Chem. Soc., 120 (1998) 4372-4387.
[224] T. Yildirim, M.R. Hartman, Phys. Rev. Lett., 95 (2005) art. n. 215504.
[225] M.T. Weller, P.F. Henry, V.P. Ting, C.C. Wilson, Chem. Commun., (2009) 2973-2989.
[226] R.E. Morris, W.T.A. Harrison, J.M. Nicol, A.P. Wilkinson, A.K. Cheetham, Nature, 359 (1992) 519-522.
[227] G. Materlik, C.J. Sparks, K. Fischer, Resonant anomalous X-ray scattering: theory and applications, Elsevier, Amsterdam, 1994.
[228] J.R. Helliwell, M. Helliwell, V. Kaucic, N.Z. Logar, Eur. Phys. J.-Spec. Top., 208 (2012) 245-257.
[229] H. Palancher, S. Bos, J.F. Berar, I. Margiolaki, J.L. Hodeau, Eur. Phys. J.-Spec. Top., 208 (2012) 275-289.
[230] C. Vettier, Eur. Phys. J.-Spec. Top., 208 (2012) 3-14.
[231] Y. Joly, S.D. Matteo, O. Bunau, Eur. Phys. J.-Spec. Top., 208 (2012) 21-38.
[232] P. Calandra, V. Turco Liveri, A. Longo, Colloid Polymer Sci., 279 (2001) 1112-1117.
[233] G. Portale, A. Longo, L. D'Ilario, A. Martinelli, R. Caminiti, Appl. Phys. Lett., 85 (2004) 4798-4800.
[234] G. Portale, A. Longo, L. D'Ilario, A. Martinelli, R. Caminiti, V. Rossi Albertini, J. Appl. Cryst., 40 (2007) 218-231.
[235] D. Altamura, R. Lassandro, F.A. Vittoria, L. De Caro, D. Siliqi, M. Ladisa, C. Giannini, J. Appl. Cryst., 45 (2012) 869-873.
[236] L. De Caro, D. Altamura, F.A. Vittoria, G. Carbone, F. Qiao, L. Manna, C. Giannini, J. Appl. Cryst., 45 (2012) 1228-1235.
[237] C. Giannini, D. Siliqi, O. Bunk, A. Beraudi, M. Ladisa, D. Altamura, S. Stea, F. Baruffaldi, Sci. Rep., 2 (2012) art. n. 435.
[238] C. Giannini, D. Altamura, B.M. Aresta, T. Sibillano, D. Siliqi, L. De Caro, Lens-less scanning X-ray microscopy with XAS amd WAXS contrast, in: A. Dibenedetto, M. Aresta (Eds.) Inorganic Micro- and Nanomaterials. Synthesis and Characterization, De Gruyter, Berlin, 2013, pp. 137-156.
[239] A.C. Bloomer, U.W. Arndt, Acta Crystallogr. Sect. D-Biol. Crystallogr., 55 (1999) 1672-1680.
[240] W. Clegg, J. Chem. Soc.-Dalton Trans., (2000) 3223-3232.
[241] E.E. Koch, in, North Holland Pub. , Amsterdam, 1983.
[242] J. Baruchel, Neutron and Synchrotron Radiation for Condensed Matter Studies. Vol. 1: Theory, Instruments and Methods, Springer-Verlag, Berlin, 1993.
[243] P.J. Duke, Synchrotron Radiation. Pruduction and Properties, Oxford University Press, Oxford, 2000.
[244] G. Margaritondo, Elements of Synchrotron Light: For Biology, Chemistry, and Medical Research, Oxford University Press, New York, 2002.
[245] Y. Kubota, M. Takata, T.C. Kobayashi, S. Kitagawa, Coord. Chem. Rev., 251 (2007) 2510-2521.
[246] G.R. Castro, J. Synchrot. Radiat., 5 (1998) 657-660.
[247] C. Meneghini, G. Artioli, A. Balerna, A.F. Gualtieri, P. Norby, S. Mobilio, J. Synchrot. Radiat., 8 (2001) 1162-1166.
[248] T. Ikeda, A. Nisawa, M. Okui, N. Yagi, H. Yoshikawa, S. Fukushima, J. Synchrot. Radiat., 10 (2003) 424-429.
[249] A.N. Fitch, J. Res. Natl. Inst. Stand. Technol., 109 (2004) 133-142.
[250] M. Knapp, C. Baehtz, H. Ehrenberg, H. Fuess, J. Synchrot. Radiat., 11 (2004) 328-334.
[251] F.F. Ferreira, E. Granado, W. Carvalho, S.W. Kycia, D. Bruno, R. Droppa, J. Synchrot. Radiat., 13 (2006) 46-53.
[252] J. Wang, B.H. Toby, P.L. Lee, L. Ribaud, S.M. Antao, C. Kurtz, M. Ramanathan, R.B. Von Dreele, M.A. Beno, Rev. Sci. Instrum., 79 (2008) art. n. 085105.
[253] S.P. Thompson, J.E. Parker, J. Potter, T.P. Hill, A. Birt, T.M. Cobb, F. Yuan, C.C. Tang, Rev. Sci. Instrum., 80 (2009) art. n. 075107.
[254] X.B. Shi, S. Ghose, E. Dooryhee, J. Synchrot. Radiat., 20 (2013) 234-242.
[255] W. Parrish, J.I. Landford, 2.3 Powder and related techniques: X-ray techniques, in: E. Prince (Ed.) International Tables for Crystallography, Mathematical, Physical and Chemical Tables, Kluwer Academic Published for the International Union of Crystallography, Dordrecht, 2004, pp. 42-79.
[256] G.L. Marra, A.N. Fitch, A. Zecchina, G. Ricchiardi, M. Salvalaggio, S. Bordiga, C. Lamberti, J. Phys. Chem. B, 101 (1997) 10653-10660.
[257] P. Coppens, D. Cox, E. Vlieg, I.K. Robinson, Synchrotron radiation crystallography, Academic Press, London, 1992.
[258] T.S. Koritsanszky, P. Coppens, Chem. Rev., 101 (2001) 1583-1627.
[259] P. Coppens, B. Iversen, F.K. Larsen, Coord. Chem. Rev., 249 (2005) 179-195.
[260] P. Coppens, Angew. Chem.-Int. Edit., 44 (2005) 6810-6811.

[261] D. Chopra, J. Phys. Chem. A, 116 (2012) 9791-9801.
[262] C. Gatti, P. Macchi, in, Springer, Dordrecht, 2012.
[263] P. Macchi, Crystallogr. Rev, 19 (2013) 58-101.
[264] C. Gatti, Phys. Scr., 87 (2013) art. n. 048102.
[265] R.F. Stewart, J. Chem. Phys., 58 (1973) 1668-1676.
[266] N.K. Hansen, P. Coppens, Acta Crystallogr. A, 34 (1978) 909-921.
[267] P. Macchi, A. Sironi, Coord. Chem. Rev., 238 (2003) 383-412.
[268] B.B. Iversen, F.K. Larsen, A.A. Pinkerton, A. Martin, A. Darovsky, P.A. Reynolds, Inorg. Chem., 37 (1998) 4559-4566.
[269] S. Pillet, G. Wu, V. Kulsomphob, B.G. Harvey, R.D. Ernst, P. Coppens, J. Am. Chem. Soc., 125 (2003) 1937-1949.
[270] P. Macchi, A.J. Schultz, F.K. Larsen, B.B. Iversen, J. Phys. Chem. A, 105 (2001) 9231-9242.
[271] J. Overgaard, H.F. Clausen, J.A. Platts, B.B. Iversen, J. Am. Chem. Soc., 130 (2008) 3834-3843.
[272] H.F. Clausen, J. Overgaard, Y.S. Chen, B.B. Lversen, J. Am. Chem. Soc., 130 (2008) 7988-7996.
[273] B.S. Clausen, G. Steffensen, B. Fabius, J. Villadsen, R. Feidenhansl, H. Topsoe, J. Catal., 132 (1991) 524-535.
[274] J.W. Couves, J.M. Thomas, D. Waller, R.H. Jones, A.J. Dent, G.E. Derbyshire, G.N. Greaves, Nature, 354 (1991) 465-468.
[275] A.J. Dent, M.P. Wells, R.C. Farrow, C.A. Ramsdale, G.E. Derbyshire, G.N. Greaves, J.W. Couves, J.M. Thomas, Rev. Sci. Instrum., 63 (1992) 903-906.
[276] G. Sankar, P.A. Wright, S. Natarajan, J.M. Thomas, G.N. Greaves, A.J. Dent, B.R. Dobson, C.A. Ramsdale, R.H. Jones, J. Phys. Chem., 97 (1993) 9550-9554.
[277] A.J. Dent, G.N. Greaves, M.A. Roberts, G. Sankar, P.A. Wright, R.H. Jones, M. Sheehy, D. Madill, C.R.A. Catlow, J.M. Thomas, T. Rayment, Nucl. Instrum. Methods Phys. Res. B, 97 (1995) 20-22.
[278] B.S. Clausen, H. Topsoe, Combined EXAFS/XRD methods, in: Y. Iwasawa (Ed.) X-ray absorption fine structure for catalysts and surfaces, World Scientific, Singapore, 1996, pp. 345-353.
[279] I.J. Shannon, T. Maschmeyer, G. Sankar, J.M. Thomas, R.D. Oldroyd, M. Sheehy, D. Madill, A.M. Waller, R.P. Townsend, Catal. Lett., 44 (1997) 23-27.
[280] T. Shido, R. Prins, Curr. Opin. Solid State Mat. Sci., 3 (1998) 330-335.
[281] G. Sankar, J.M. Thomas, Top. Catal., 8 (1999) 1-21.
[282] J.D. Grunwaldt, B.S. Clausen, Top. Catal., 18 (2002) 37-43.
[283] A.I. Frenkel, Q. Wang, N. Marinkovic, J.G. Chen, L. Barrio, R. Si, A.L. Camara, A.M. Estrella, J.A. Rodriguez, J.C. Hanson, J. Phys. Chem. C, 115 (2011) 17884-17890.
[284] M. Milanesio, G. Artioli, A.F. Gualtieri, L. Palin, C. Lamberti, J. Am. Chem. Soc., 125 (2003) 14549-14558.
[285] G. Agostini, C. Lamberti, L. Palin, M. Milanesio, N. Danilina, B. Xu, M. Janousch, J.A. van Bokhoven, J. Am. Chem. Soc., 132 (2010) 667-678.
[286] A. Kubacka, A. Iglesias-Juez, A. Martinez-Arias, M. Di Michiel, M.A. Newton, M. Fernandez-Garcia, ChemCatChem, 4 (2012) 725-737.
[287] M. Epple, J. Therm. Anal., 42 (1994) 559-593.
[288] K. Westesen, B. Siekmann, M.H.J. Koch, Int. J. Pharm., 93 (1993) 189-199.
[289] B.S. Hsiao, K.H. Gardner, D.Q. Wu, B. Chu, Polymer, 34 (1993) 3986-3995.
[290] D.J. Jensen, E.M. Lauridsen, L. Margulies, H.F. Poulsen, S. Schmidt, H.O. Sorensen, G.B.M. Vaughan, Mater. Today, 9 (2006) 18-25.
[291] S. Nikitenko, A.M. Beale, A.M.J. van der Eerden, S.D.M. Jacques, O. Leynaud, M.G. O'Brien, D. Detollenaere, R. Kaptein, B.M. Weckhuysen, W. Bras, J. Synchrot. Radiat., 15 (2008) 632-640.
[292] H.E. Huxley, K.C. Holmes, J. Synchrot. Radiat., 4 (1997) 366-379.
[293] A. Bruckner, Catal. Rev.-Sci. Eng., 45 (2003) 97-150.
[294] M. von Laue, Nobel Lectures, Physics, (1914) 1901–1921.
[295] J. Hajdu, I. Andersson, Annu. Rev. Biophys. Biomolec. Struct., 22 (1993) 467-498.
[296] Z. Ren, D. Bourgeois, J.R. Helliwell, K. Moffat, V. Srajer, B.L. Stoddard, J. Synchrot. Radiat., 6 (1999) 891-917.
[297] I. Schlichting, Accounts Chem. Res., 33 (2000) 532-538.
[298] M.H.J. Koch, N.A. Dencher, D. Oesterhelt, H.J. Plohn, G. Rapp, G. Buldt, Embo J., 10 (1991) 521-526.
[299] M. Reconditi, Rep. Prog. Phys., 69 (2006) 2709-2759.
[300] J.S.O. Evans, R.J. Francis, D. Ohare, S.J. Price, S.M. Clark, J. Flaherty, J. Gordon, A. Nield, C.C. Tang, Rev. Sci. Instrum., 66 (1995) 2442-2445.
[301] R. Caminiti, V.R. Albertini, Int. Rev. Phys. Chem., 18 (1999) 263-299.
[302] K. Tamura, M. Inui, S. Hosokawa, Rev. Sci. Instrum., 70 (1999) 144-152.

[303] I.A. Denks, C. Genzel, Nucl. Instrum. Methods Phys. Res. Sect. B-Beam Interact. Mater. Atoms, 262 (2007) 87-94.
[304] C. Genzel, I.A. Denks, J. Gibmeler, M. Klaus, G. Wagener, Nucl. Instrum. Methods Phys. Res. Sect. A-Accel. Spectrom. Dect. Assoc. Equip., 578 (2007) 23-33.
[305] R.J. Francis, S.J. Price, J.S.O. Evans, S. Obrien, D. Ohare, S.M. Clark, Chem. Mat., 8 (1996) 2102-2108.
[306] F. Millange, R.I. Walton, D. O'Hare, J. Mater. Chem., 10 (2000) 1713-1720.
[307] R.I. Walton, F. Millange, D. O'Hare, A.T. Davies, G. Sankar, C.R.A. Catlow, J. Phys. Chem. B, 105 (2001) 83-90.
[308] H. Xia, Q. Xia, A.L. Ruoff, Phys. Rev. B, 47 (1993) 12925-12928.
[309] T.S. Duffy, G.Y. Shen, D.L. Heinz, J.F. Shu, Y.Z. Ma, H.K. Mao, R.J. Hemley, A.K. Singh, Phys. Rev. B, 60 (1999) 15063-15073.
[310] J.L. Hodeau, R. Guinebretiere, Appl. Phys. A-Mater. Sci. Process., 89 (2007) 813-823.
[311] A.L. Harris, J.K. Brown, C.B. Harris, Ann. Rev. Phys. Chem., 39 (1988) 341-366.
[312] K.E. Knope, L. Soderholm, Chem. Rev., 113 (2013) 944-994.
[313] D. Bazin, L. Guczi, J. Lynch, Appl. Catal. A-Gen., 226 (2002) 87-113.
[314] J.D. Grunwaldt, J.B. Wagner, R.E. Dunin-Borkowski, ChemCatChem, 5 (2013) 62-80.
[315] S.R. Zhang, L. Nguyen, Y. Zhu, S.H. Zhan, C.K. Tsung, F. Tao, Accounts Chem. Res., 46 (2013) 1731-1739.
[316] C. Lamberti, C. Prestipino, S. Bordiga, A.N. Fitch, G.L. Marra, Nucl. Instrum. Methods Phys. Res. B, 200 (2003) 155-159.
[317] G. Turnes Palomino, S. Bordiga, A. Zecchina, G.L. Marra, C. Lamberti, J. Phys. Chem. B, 104 (2000) 8641-8651.
[318] M.G. O'Brien, A.M. Beale, B.M. Weckhuysen, Chem. Soc. Rev., 39 (2010) 4767-4782.
[319] J. Lee, O.K. Farha, J. Roberts, K.A. Scheidt, S.T. Nguyen, J.T. Hupp, Chem. Soc. Rev., 38 (2009) 1450-1459.
[320] M.J. Prakash, M.S. Lah, Chem. Commun., (2009) 3326-3341.
[321] B.L. Chen, S.C. Xiang, G.D. Qian, Acc. Chem. Res., 43 (2010) 1115-1124.
[322] Y. Liu, W.M. Xuan, Y. Cui, Adv. Mater., 22 (2010) 4112-4135.
[323] L.Q. Ma, W.B. Lin, Designing Metal-Organic Frameworks for Catalytic Applications, in: M. Schroder (Ed.) Functional Metal-Organic Frameworks: Gas Storage, Separation and Catalysis, 2010, pp. 175-205.
[324] F. Bonino, C. Prestipino, G. Agostini, A. Piovano, D. Gianolio, L. Mino, E. Gallo, C. Lamberti, Catalyst characterization by XAS and XES spectroscopies: in situ and operando experiments, in: F. Boscherini, C. Meneghini, S. Mobilio (Eds.) Synchrotron Radiation: Basics, Methods and Applications, Springer, Berlin, 2014.
[325] B.J. Holliday, C.A. Mirkin, Angew. Chem.-Int. Edit., 40 (2001) 2022-2043.
[326] F.A. Cotton, C. Lin, C.A. Murillo, Accounts Chem. Res., 34 (2001) 759-771.
[327] P.H. Dinolfo, J.T. Hupp, Chem. Mat., 13 (2001) 3113-3125.
[328] S.S. Sun, A.J. Lees, Coord. Chem. Rev., 230 (2002) 171-192.
[329] H.W. Roesky, M. Andruh, Coord. Chem. Rev., 236 (2003) 91-119.
[330] N.C. Gianneschi, M.S. Masar, C.A. Mirkin, Accounts Chem. Res., 38 (2005) 825-837.
[331] B.H. Ye, M.L. Tong, X.M. Chen, Coord. Chem. Rev., 249 (2005) 545-565.
[332] N.B. Debata, D. Tripathy, D.K. Chand, Coord. Chem. Rev., 256 (2012) 1831-1945.
[333] D. Philp, J.F. Stoddart, Angew. Chem.-Int. Edit., 35 (1996) 1155-1196.
[334] S. Leininger, B. Olenyuk, P.J. Stang, Chem. Rev., 100 (2000) 853-907.
[335] S.R. Seidel, P.J. Stang, Accounts Chem. Res., 35 (2002) 972-983.
[336] D.M. Vriezema, M.C. Aragones, J. Elemans, J. Cornelissen, A.E. Rowan, R.J.M. Nolte, Chem. Rev., 105 (2005) 1445-1489.
[337] J.R. Nitschke, Accounts Chem. Res., 40 (2007) 103-112.
[338] B.H. Northrop, Y.-R. Zheng, K.-W. Chi, P.J. Stang, Accounts Chem. Res., 42 (2009) 1554-1563.
[339] R. Chakrabarty, P.S. Mukherjee, P.J. Stang, Chem. Rev., 111 (2011) 6810-6918.
[340] M.A. Banares, Catal. Today, 100 (2005) 71-77.
[341] A.I. Frenkel, J.A. Rodriguez, J.G.G. Chen, ACS Catal., 2 (2012) 2269-2280.
[342] T.K. Kim, J.H. Lee, M. Wulff, Q.Y. Kong, H. Ihee, ChemPhysChem, 10 (2009) 1958-1980.
[343] H. Ihee, Acc. Chem. Res. , 42 (2009) 356-366.
[344] H. Ihee, M. Wulff, J. Kim, S. Adachi, Int. Rev. Phys. Chem., 29 (2010) 453-520.
[345] L.X. Chen, X. Zhang, J. Phys. Chem. Lett., (2013) 4000-4013.
[346] H. Bertagnolli, T.S. Ertel, Angew. Chem.-Int. Edit., 33 (1994) 45-66.
[347] P. D'Angelo, R. Spezia, Chem.-Eur. J., 18 (2012) 11162-11178.
[348] R.C. Nelson, J.T. Miller, Catal. Sci. Technol., 2 (2012) 461-470.
[349] P. D'Angelo, N.V. Pavel, J. Synchrot. Radiat., 8 (2001) 173-177.
[350] G. Chillemi, P. D'Angelo, N.V. Pavel, N. Sanna, V. Barone, J. Am. Chem. Soc., 124 (2002) 1968-1976.

[351] P. D'Angelo, V. Barone, G. Chillemi, N. Sanna, W. Meyer-Klaucke, N.V. Pavel, J. Am. Chem. Soc., 124 (2002) 1958-1967.
[352] P. D'Angelo, M. Benfatto, S. Della Longa, N.V. Pavel, Phys. Rev. B, 66 (2002) art. n. 064209.
[353] P. D'Angelo, M. Benfatto, J. Phys. Chem. A, 108 (2004) 4505-4514.
[354] P. D'Angelo, P.E. Petit, N.V. Pavel, J. Phys. Chem. B, 108 (2004) 11857-11865.
[355] P. D'Angelo, V. Migliorati, L. Guidoni, Inorg. Chem., 49 (2010) 4224-4231.
[356] V. Migliorati, G. Mancini, G. Chillemi, A. Zitolo, P. D'Angelo, J. Phys. Chem. A, 115 (2011) 4798-4803.
[357] V. Migliorati, G. Mancini, S. Tatoli, A. Zitolo, A. Filipponi, S. De Panfilis, A. Di Cicco, P. D'Angelo, Inorg. Chem., 52 (2013) 1141-1150.
[358] G. Vlaic, D. Andreatta, P.E. Colavita, Catal. Today, 41 (1998) 261-275.
[359] E. Groppo, C. Lamberti, S. Bordiga, G. Spoto, A. Zecchina, Chem. Rev., 105 (2005) 115-183.
[360] S.S. Hasnain, K.O. Hodgson, J. Synchrot. Radiat., 6 (1999) 852-864.
[361] D.S. Auld, Biometals, 14 (2001) 271-313.
[362] J.N. Chan, Z.Y. Huang, M.E. Merrifield, M.T. Salgado, M.J. Stillman, Coord. Chem. Rev., 233 (2002) 319-339.
[363] A. Levina, R.S. Armstrong, P.A. Lay, Coord. Chem. Rev., 249 (2005) 141-160.
[364] J. Barber, J.W. Murray, Coord. Chem. Rev., 252 (2008) 233-243.
[365] R. Gabbianelli, M. Dorazio, F. Pacello, P. Oneill, L. Nicolini, G. Rotilio, A. Battistoni, Biol. Chem., 385 (2004) 749-754.
[366] I. Toro, C. Petrutz, F. Pacello, M. D'Orazio, A. Battistoni, K. Djinovic-Carugo, J. Mol. Biol., 386 (2009) 406-418.
[367] P. D'Angelo, S. Della Longa, A. Arcovito, M. Anselmi, A. Di Nola, G. Chillemi, J. Am. Chem. Soc., 132 (2010) 14901-14909.
[368] D.R. Sandstrom, F.W. Lytle, Ann. Rev. Phys. Chem., 30 (1979) 215-238.
[369] P.A. Lee, P.H. Citrin, P. Eisenberger, M. Kincaid, Rev. Mod. Phys., 53 (1981) 769-806.
[370] B.K. Teo, D.C. Joy, EXAFS Spectroscopy: Techniques and Applications Plenum, New York, 1981.
[371] E.A. Stern, Theory of EXAFS, in: D.C. Koningsberger, R. Prins (Eds.) X-Ray Absorption: Principles, Applications, Techniques of EXAFS, SEXAFS and XANES, John Wiley & Sons, New York, 1988, pp. 3-51.
[372] A. Bianconi, L. Inoccia, S. Stipcich, in, Springer, London, 2012.
[373] D.E. Sayers, B.A. Bunker, Data analysis, in: D.C. Koningsberger, R. Prins (Eds.) X-Ray Absorption: Principles, Applications, Techniques of EXAFS, SEXAFS and XANES, John Wiley & Sons, New York, 1988, pp. 211.
[374] T. Yokoyama, Theory and parameters of EXAFS, in: Y. Iwasawa (Ed.) X-ray absorption fine structure for catalysts and surfaces, World Scientific, Singapore, 1996, pp. 9-32.
[375] K. Asakura, Analysis of EXAFS, in: Y. Iwasawa (Ed.) X-ray absorption fine structure for catalysts and surfaces, World Scientific, Singapore, 1996, pp. 33-58.
[376] J. Penner-Hahn, X-ray Absorption Spectroscopy, in: J.A. McCleverty, T.J. Meyer (Eds.) Comprehensive Coordination Chemistry II Elsevier Ltd., Oxford, 2003
[377] F. Boscherini, X-ray absorption fine structure in the study of semiconductor heterostructures and nanostructures, in: C. Lamberti (Ed.) Characterization of Semiconductor Heterostructures and Nanostructures, Elsevier, Amsterdam, 2008, pp. 289-330.
[378] E. Borfecchia, G. Agostini, S. Bordiga, E. Groppo, C. Garino, R. Gobetto, A. Agostino, L. Mino, M. Truccato, D. Gianolio, A. Piovano, G. Martinez-Criado, L. Salassa, C. Lamberti, Structural and electronic characterization of nano-sized inorganic materials by X-ray Absorption Spectroscopies, in: A. Dibenedetto, M. Aresta (Eds.) Inorganic Micro- and Nanomaterials. Synthesis and Characterization, De Gruyter, Berlin, 2013, pp. 93-136.
[379] F. Bonino, S. Chavan, J.G. Vitillo, E. Groppo, G. Agostini, C. Lamberti, P.D.C. Dietzel, C. Prestipino, S. Bordiga, Chem. Mater., 20 (2008) 4957-4968.
[380] S. Chavan, F. Bonino, J.G. Vitillo, E. Groppo, C. Lamberti, P.D.C. Dietzel, A. Zecchina, S. Bordiga, Phys. Chem. Chem. Phys., 11 (2009) 9811-9822.
[381] S. Chavan, J.G. Vitillo, E. Groppo, F. Bonino, C. Lamberti, P.D.C. Dietzel, S. Bordiga, J. Phys. Chem. C, 113 (2009) 3292-3299.
[382] E. Groppo, C. Prestipino, C. Lamberti, P. Luches, C. Giovanardi, F. Boscherini, J. Phys. Chem. B, 107 (2003) 4597-4606.
[383] C. Lamberti, E. Groppo, C. Prestipino, S. Casassa, A.M. Ferrari, C. Pisani, C. Giovanardi, P. Luches, S. Valeri, F. Boscherini, Phys. Rev. Lett., 91 (2003) art. n. 046101.
[384] P. Luches, S. D'Addato, S. Valeri, E. Groppo, C. Prestipino, C. Lamberti, F. Boscherini, Phys. Rev. B, 69 (2004) art. n. 045412.
[385] E. Groppo, C. Prestipino, C. Lamberti, R. Carboni, F. Boscherini, P. Luches, S. Valeri, S. D'Addato, Phys. Rev. B, 70 (2004) art. n. 165408.
[386] R. Le Toquin, W. Paulus, A. Cousson, C. Prestipino, C. Lamberti, J. Am. Chem. Soc., 128 (2006) 13161-13174.

[387] A. Piovano, G. Agostini, A.I. Frenkel, T. Bertier, C. Prestipino, M. Ceretti, W. Paulus, C. Lamberti, J. Phys. Chem. C, 115 (2011) 1311-1322.
[388] C. Lamberti, S. Bordiga, M. Salvalaggio, G. Spoto, A. Zecchina, F. Geobaldo, G. Vlaic, M. Bellatreccia, J. Phys. Chem. B, 101 (1997) 344-360.
[389] C. Lamberti, S. Bordiga, A. Zecchina, M. Salvalaggio, F. Geobaldo, C.O. Arean, J. Chem. Soc.-Faraday Trans., 94 (1998) 1519-1525.
[390] G. Berlier, G. Spoto, S. Bordiga, G. Ricchiardi, P. Fisicaro, A. Zecchina, I. Rossetti, E. Selli, L. Forni, E. Giamello, C. Lamberti, J. Catal., 208 (2002) 64-82.
[391] G. Berlier, G. Spoto, P. Fisicaro, S. Bordiga, A. Zecchina, E. Giamello, C. Lamberti, Microchem. J., 71 (2002) 101-116.
[392] A. Zecchina, M. Rivallan, G. Berlier, C. Lamberti, G. Ricchiardi, Phys. Chem. Chem. Phys., 9 (2007) 3483-3499.
[393] M. Braglia, G. Dai, S. Mosso, S. Pascarelli, F. Boscherini, C. Lamberti, J. Appl. Phys., 83 (1998) 5065-5068.
[394] M. Braglia, G. Dai, S. Mosso, S. Pascarelli, F. Boscherini, A. Balerna, C. Lamberti, J. Appl. Phys., 85 (1999) 7987-7988.
[395] M. Braglia, G. Dai, S. Mosso, C. Meneghini, A. Balerna, F. Boscherini, C. Lamberti, J. Synchrot. Radiat., 6 (1999) 509-511.
[396] L. Salassa, D. Gianolio, C. Garino, G. Salassa, E. Borfecchia, T. Ruiu, C. Nervi, R. Gobetto, R. Bizzarri, P.J. Sadler, C. Lamberti, J. Phys. Conf. Ser., 190 (2009) art. n. 012141.
[397] C. Lamberti, S. Bordiga, F. Bonino, C. Prestipino, G. Berlier, L. Capello, F. D'Acapito, F.X.L.I. Xamena, A. Zecchina, Phys. Chem. Chem. Phys., 5 (2003) 4502-4509.
[398] R.F. Pettifer, O. Mathon, S. Pascarelli, M.D. Cooke, M.R.J. Gibbs, Nature, 435 (2005) 78-81.
[399] M.P. Ruffoni, R.F. Pettifer, S. Pascarelli, A. Trapananti, O. Mathon, J. Synchrot. Radiat., 14 (2007) 421-425.
[400] B.-K. Teo, P.A. Lee, J. Am. Chem. Soc., 101 (1979) 2815-2832.
[401] A.G. McKale, B.W. Veal, A.P. Paulikas, S.K. Chan, G.S. Knapp, J. Am. Chem. Soc., 110 (1988) 3763-3768.
[402] H.H. Zhang, B. Hedman, K.O. Hodgson, X-ray Absorption Spectroscopy and EXAFS Analysis: The Multiple-Scattering Method and Applications in Inorganic and Bioinorganic Chemistry, Inorganic Electronic Structure and Spectroscopy, in: E.I. Solomon, A.B.P. Lever (Eds.) Inorganic Electronic Structure and Spectroscopy: Methodology, Wiley, New York, 1999.
[403] A. Di Cicco, J. Synchrot. Radiat., 10 (2003) 46-50.
[404] B.K. Teo, Bond Angle Determination by EXAFS: A New Dimension, in: A. Bianconi, L. Inoccia, S. Stipcich (Eds.) Exafs and Near Edge Structure: Proceedings of the International Conference Frascati, Italy, September 13-17, 1982, Springer, London, 2012.
[405] M.F.d.G. Frank, J. Phys. Conf. Ser., 190 (2009) art. n. 012004.
[406] Y. Joly, O. Bunau, J.E. Lorenzo, R.M. Galera, S. Grenier, B. Thompson, J. Phys. Conf. Ser., 190 (2009) art. n. 012007.
[407] K. Hatada, K. Hayakawa, J. Chaboy, N.C. R., J. Phys. Conf. Ser., 190 (2009) art. n. 012010.
[408] M. Benfatto, S. Della Longa, Journal of Physics: Conference Series, 190 (2009) art. n. 012031.
[409] J.J. Kas, J. Vinson, N. Trcera, D. Cabaret, E.L. Shirley, J.J. Rehr, J. Phys. Conf. Ser., 190 (2009) art. n. 012009.
[410] T. Fujikawa, J. Phys. Soc. Jpn., 60 (1991) 3904-3919.
[411] V. Serin, G. Zanchi, J. Sevely, Microsc. Microanal. Microstruct., 3 (1992) 201-212.
[412] M.X. Qian, M. Sarikaya, E.A. Stern, Ultramicroscopy, 59 (1995) 137-147.
[413] M. Sarikaya, M. Qian, E.A. Stern, Micron, 27 (1996) 449-466.
[414] P. Rez, J.M. MacLaren, D.K. Saldin, Phys. Rev. B, 57 (1998) 2621-2627.
[415] M.S. Moreno, K. Jorissen, J.J. Rehr, Micron, 38 (2007) 1-11.
[416] A. Sakdinawat, D. Attwood, Nat. Photonics, 4 (2010) 840-848.
[417] G.E. Ice, J.D. Budai, J.W.L. Pang, Science, 334 (2011) 1234-1239.
[418] J.H. Cavka, S. Jakobsen, U. Olsbye, N. Guillou, C. Lamberti, S. Bordiga, K.P. Lillerud, J. Am. Chem. Soc., 130 (2008) 13850-13851.
[419] L. Valenzano, B. Civalleri, S. Bordiga, M.H. Nilsen, S. Jakobsen, K.-P. Lillerud, C. Lamberti, Chem. Mater., 23 (2011) 1700-1718.
[420] S. Chavan, J.G. Vitillo, D. Gianolio, O. Zavorotynska, B. Civalleri, S. Jakobsen, M.H. Nilsen, L. Valenzano, C. Lamberti, K.P. Lillerud, S. Bordiga, Phys. Chem. Chem. Phys., 14 (2012) 1614-1626.
[421] J. Jakobsen, D. Gianolio, D. Wragg, M.H. Nilsen, H. Emerich, S. Bordiga, C. Lamberti, U. Olsbye, M. Tilset, K.P. Lillerud, Phys. Rev. B, 86 (2012) art. n. 125429.
[422] D. Gianolio, J.G. Vitillo, B. Civalleri, S. Bordiga, U. Olsbye, K.P. Lillerud, L. Valenzano, C. Lamberti, J. Phys. Conf. Ser., 430 (2013) art. n. 012134.

[423] J. Hafizovic, M. Bjorgen, U. Olsbye, P.D.C. Dietzel, S. Bordiga, C. Prestipino, C. Lamberti, K.P. Lillerud, J. Am. Chem. Soc., 129 (2007) 3612-3620.
[424] R. Dovesi, R. Orlando, B. Civalleri, C. Roetti, V.R. Saunders, C.M. Zicovich-Wilson, Z. Kristallogr., 220 (2005) 571-573.
[425] A.J. Dent, Top. Catal., 18 (2002) 27-35.
[426] A.M. Beale, A.M.J. van der Eerden, K. Kervinen, M.A. Newton, B.M. Weckhuysen, Chem. Commun., (2005) 3015-3017.
[427] J.D. Grunwaldt, M. Beier, B. Kimmerle, A. Baiker, M. Nachtegaal, B. Griesebock, D. Lutzenkirchen-Hecht, J. Stotzeld, R. Frahm, Phys. Chem. Chem. Phys., 11 (2009) 8779-8789.
[428] S. Khalid, W. Caliebe, P. Siddons, I. So, B. Clay, T. Lenhard, J. Hanson, Q. Wang, A.I. Frenkel, N. Marinkovic, N. Hould, M. Ginder-Vogel, G.L. Landrot, D.L. Sparks, A. Ganjoo, Rev. Sci. Instrum., 81 (2010) art. n. 015105.
[429] C. Prestipino, O. Mathon, R. Hino, A. Beteva, S. Pascarelli, J. Synchrot. Radiat., 18 (2011) 176-182.
[430] S. Diaz-Moreno, D.T. Bowron, J. Evans, Dalton Trans., 2005 (2005) 3814-3817.
[431] M. Tromp, J.R.A. Sietsma, J.A. van Bokhoven, G.P.F. van Strijdonck, R.J. van Haaren, A.M.J. van der Eerden, P. van Leeuwen, D.C. Koningsberger, Chem. Commun., (2003) 128-129.
[432] D.T. Bowron, S. Diaz-Moreno, Anal. Chem., 77 (2005) 6445-6452.
[433] J. Singh, M. Nachtegaal, E.M.C. Alayon, J. Stotzel, J.A. van Bokhoven, ChemCatChem, 2 (2010) 653-657.
[434] F. D'acapito, F. Boscherini, A. Marcelli, S. Mobilio, Rev. Sci. Instrum., 63 (1992) 899-901.
[435] M. Hagelstein, C. Ferrero, U. Hatje, T. Ressler, W. Metz, J. Synchrot. Radiat., 2 (1995) 174-180.
[436] A. San-Miguel, M. Hagelstein, J. Borrel, G. Marot, M. Renier, J. Synchrot. Radiat., 5 (1998) 1396-1397.
[437] S. Pascarelli, T. Neisius, S. De Panfilis, M. Bonfim, S. Pizzini, K. Mackay, S. David, A. Fontaine, A. San Miguel, J.P. Itie, M. Gauthier, A. Polian, J. Synchrot. Radiat., 6 (1999) 146-148.
[438] S. Pascarelli, O. Mathon, Phys. Chem. Chem. Phys., 12 (2010) 5535-5546.
[439] J.C. Labiche, O. Mathon, S. Pascarelli, M.A. Newton, G.G. Ferre, C. Curfs, G. Vaughan, A. Homs, D.F. Carreiras, Rev. Sci. Instrum., 78 (2007) art. n. 091301.
[440] Q.Y. Kong, F. Baudelet, J. Han, S. Chagnot, L. Barthe, J. Headspith, R. Goldsbrough, F.E. Picca, O. Spalla, Sci Rep, 2 (2012) art. n. 1018.
[441] S. Pascarelli, T. Neisius, S. De Panfilis, J. Synchrot. Radiat., 6 (1999) 1044-1050.
[442] S. Pascarelli, O. Mathon, M. Munoz, T. Mairs, J. Susini, J. Synchrot. Radiat., 13 (2006) 351-358.
[443] G. Aquilanti, O. Mathon, S. Pascarelli, J. Synchrot. Radiat., 16 (2009) 699-706.
[444] G. Aquilanti, S. Pascarelli, O. Mathon, M. Munoz, O. Narygina, L. Dubrovinsky, J. Synchrot. Radiat., 16 (2009) 376-379.
[445] C. Lamberti, C. Prestipino, F. Bonino, L. Capello, S. Bordiga, G. Spoto, A. Zecchina, S.D. Moreno, B. Cremaschi, M. Garilli, A. Marsella, D. Carmello, S. Vidotto, G. Leofanti, Angew. Chem.-Int. Edit., 41 (2002) 2341-2344.
[446] N.B. Muddada, U. Olsbye, L. Caccialupi, F. Cavani, G. Leofanti, D. Gianolio, S. Bordiga, C. Lamberti, Phys. Chem. Chem. Phys., 12 (2010) 5605-5618.
[447] D. Gianolio, N.B. Muddada, U. Olsbye, C. Lamberti, Nucl. Instrum. Met. Phys. Res. B, 284 (2012) 53-57.
[448] H. Topsoe, J. Catal., 216 (2003) 155-164.
[449] N. Weiher, E. Bus, B. Gorzolnik, M. Moller, R. Prins, J.A. van Bokhoven, J. Synchrot. Radiat., 12 (2005) 675-679.
[450] J.L. Fulton, J.C. Linehan, T. Autrey, M. Balasubramanian, Y. Chen, N.K. Szymczak, J. Am. Chem. Soc., 129 (2007) 11936-11949.
[451] F.J. Scott, C. Roth, D.E. Ramaker, J. Phys. Chem. C, 111 (2007) 11403-11413.
[452] R. Rousseau, G.K. Schenter, J.L. Fulton, J.C. Linehan, M.H. Engelhard, T. Autrey, J. Am. Chem. Soc., 131 (2009) 10516-10524.
[453] N. Guo, B.R. Fingland, W.D. Williams, V.F. Kispersky, J. Jelic, W.N. Delgass, F.H. Ribeiro, R.J. Meyer, J.T. Miller, Phys. Chem. Chem. Phys., 12 (2010) 5678-5693.
[454] J. Melke, A. Schoekel, D. Dixon, C. Cremers, D.E. Ramaker, C. Roth, J. Phys. Chem. C, 114 (2010) 5914-5925.
[455] P.J. Ellis, I.J.S. Fairlamb, S.F.J. Hackett, K. Wilson, A.F. Lee, Angew. Chem.-Int. Edit., 49 (2010) 1820-1824.
[456] K. Paredis, L.K. Ono, S. Mostafa, L. Li, Z.F. Zhang, J.C. Yang, L. Barrio, A.I. Frenkel, B.R. Cuenya, J. Am. Chem. Soc., 133 (2011) 6728-6735.
[457] M. Hubner, D. Koziej, M. Bauer, N. Barsan, K. Kvashnina, M.D. Rossell, U. Weimar, J.D. Grunwaldt, Angew. Chem.-Int. Edit., 50 (2011) 2841-2844.
[458] A.M. Beale, A.M.J. van der Eerden, S.D.M. Jacques, O. Leynaud, M.G. O'Brien, F. Meneau, S. Nikitenko, W. Bras, B.M. Weckhuysen, J. Am. Chem. Soc., 128 (2006) 12386-12387.
[459] M. Bauer, G. Heusel, S. Mangold, H. Bertagnolli, J. Synchrot. Radiat., 17 (2010) 273-279.
[460] M.A. Newton, W. van Beek, Chem. Soc. Rev., 39 (2010) 4845-4863.

[461] A. Hornes, A.B. Hungria, P. Bera, A.L. Camara, M. Fernandez-Garcia, A. Martinez-Arias, L. Barrio, M. Estrella, G. Zhou, J.J. Fonseca, J.C. Hanson, J.A. Rodriguez, J. Am. Chem. Soc., 132 (2010) 34-35.
[462] M.A. Newton, A.J. Dent, S.G. Fiddy, B. Jyoti, J. Evans, Catal. Today, 126 (2007) 64-72.
[463] D. Gamarra, C. Belver, M. Fernandez-Garcia, A. Martinez-Arias, J. Am. Chem. Soc., 129 (2007) 12064-12065.
[464] C. Mondelli, D. Ferri, J.D. Grunwaldt, F. Krumeich, S. Mangold, R. Psaro, A. Baiker, J. Catal., 252 (2007) 77-87.
[465] F. Klasovsky, J. Hohmeyer, A. Bruckner, M. Bonifer, J. Arras, M. Steffan, M. Lucas, J. Radnik, C. Roth, P. Claus, J. Phys. Chem. C, 112 (2008) 19555-19559.
[466] M. Bauer, C. Gastl, Phys. Chem. Chem. Phys., 12 (2010) 5575-5584.
[467] J.P. Holgado, M.D. Soriano, J. Jimenez-Jimenez, P. Concepcion, A. Jimenez-Lopez, A. Caballero, E. Rodriguez-Castellon, J.M.L. Nieto, Catal. Today, 155 (2010) 296-301.
[468] D. Gamarra, M. Fernandez-Garcia, C. Belver, A. Martinez-Arias, J. Phys. Chem. C, 114 (2010) 18576-18582.
[469] Y. Waseda, The structure of non-crystalline materials: liquids and amorphous solids, McGraw-Hill International Book Co., New York, 1980.
[470] N. Stribeck, X-Ray Scattering of Soft Matter, Springer, Berlin, 2007.
[471] A. Guinier, X-ray Diffraction, Dover, New York, US, 1963.
[472] G.A. Martynov, J. Mol. Liq., 106 (2003) 123-130.
[473] P. Debye, Ann. der Physik, 46 (1915) 809-823.
[474] J.G. Kirkwood, E.M. Boggs, J. Chem. Phys., 10 (1942) 394-402.
[475] B.R.A. Nijboer, L. Van Hove, Phys. Rev., 85 (1952) 777-783.
[476] B. Widom, J. Chem. Phys., 41 (1964) 74-77.
[477] A. Guinier, X-ray Diffraction in Crystals, Imperfect Crystals, and Amorphous Bodies, Dover, Toronto, 1994.
[478] R. Zallen, The Physics of Amorphous Solids, Wiley, Weinheim, 2008.
[479] D.S. Sivia, Elementary Scattering Theory: For X-ray and Neutron Users, Oxford University Press, Oxford, 2011.
[480] O. Glatter, O. Kratky, Small angle x-ray scattering, Academic Press, London, 1982.
[481] L.A. Feigin, D.I. Svergun, Structure analysis by small angle X-ray and neutron scattering, Plenum Press, New York, 1987.
[482] G. Portale, A. Longo, Small Angle X-ray scattering for the study of nanostructures and nanostructured materials, in: C. Lamberti, G. Agostini (Eds.) Characterization of Semiconductor Heterostructures and Nanostructures (II Ed.), Elsevier, Amsterdam, 2013, pp. 289-330.
[483] M.D. Foster, Crit. Rev. Anal. Chem., 24 (1993) 179-241.
[484] B. Chu, B.S. Hsiao, Chem. Rev., 101 (2001) 1727-1761.
[485] Y. Nozue, Y. Shinohara, Y. Amemiya, Polym. J., 39 (2007) 1221-1237.
[486] Y.A. Akpalu, Polym. Rev., 50 (2010) 1-13.
[487] G. Johansson, Adv. Inorg. Chem., 39 (1992) 159-232.
[488] H. Ohtaki, T. Radnai, Chem. Rev., 93 (1993) 1157-1204.
[489] I. Persson, L. Eriksson, P. Lindqvist-Reis, P. Persson, M. Sandstrom, Chem.-Eur. J., 14 (2008) 6687-6696.
[490] N. Torapava, I. Persson, L. Eriksson, D. Lundberg, Inorg. Chem., 48 (2009) 11712-11723.
[491] J. Krakowiak, D. Lundberg, I. Persson, Inorg. Chem., 51 (2012) 9598-9609.
[492] A. Fuchs, D. Lundberg, D. Warminska, I. Persson, J. Phys. Chem. B, 117 (2013) 8502-8511.
[493] J. Mahler, I. Persson, R.B. Herbert, Dalton Trans., 42 (2013) 1364-1377.
[494] J. Lipfert, S. Doniach, Small-angle X-ray scattering from RNA, proteins, and protein complexes, in: Annu. Rev. Biophys. Biomolec. Struct., Annual Reviews, Palo Alto, 2007, pp. 307-327.
[495] C.D. Putnam, M. Hammel, G.L. Hura, J.A. Tainer, Q. Rev. Biophys., 40 (2007) 191-285.
[496] M.R. Wasielewski, Accounts Chem. Res., 42 (2009) 1910-1921.
[497] H.D.T. Mertens, D.I. Svergun, J. Struct. Biol., 172 (2010) 128-141.
[498] R.P. Rambo, J.A. Tainer, Curr. Opin. Struct. Biol., 20 (2010) 128-137.
[499] C.E. Blanchet, D.I. Svergun, Small-Angle X-Ray Scattering on Biological Macromolecules and Nanocomposites in Solution, in: M.A. Johnson, T.J. Martinez (Eds.) Annual Review of Physical Chemistry, Vol 64, Annual Reviews, Palo Alto, 2013, pp. 37-54.
[500] M.T. Reetz, M. Winter, R. Breinbauer, T. Thurn-Albrecht, W. Vogel, Chem.-Eur. J., 7 (2001) 1084-1094.
[501] P. Calandra, A. Longo, V.T. Liveri, J. Phys. Chem. B, 107 (2003) 25-30.
[502] G. Beaucage, H.K. Kammler, S.E. Pratsinis, J. Appl. Crystallogr., 37 (2004) 523-535.
[503] H. Borchert, E.V. Shevehenko, A. Robert, I. Mekis, A. Kornowski, G. Grubel, H. Weller, Langmuir, 21 (2005) 1931-1936.
[504] M.M. Maye, I.I.S. Lim, J. Luo, Z. Rab, D. Rabinovich, T.B. Liu, C.J. Zhong, J. Am. Chem. Soc., 127 (2005) 1519-1529.

[505] C.W. Scheeren, G. Machado, S.R. Teixeira, J. Morais, J.B. Domingos, J. Dupont, J. Phys. Chem. B, 110 (2006) 13011-13020.
[506] V. Valtchev, L. Tosheva, Chem. Rev., 113 (2013) 6734-6760.
[507] C.S. Tsao, M.S. Yu, T.Y. Chung, H.C. Wu, C.Y. Wang, K.S. Chang, H.L. Chent, J. Am. Chem. Soc., 129 (2007) 15997-16004.
[508] C.S. Tsao, C.Y. Chen, T.Y. Chung, C.J. Su, C.H. Su, H.L. Chen, U.S. Jeng, M.S. Yu, P.Y. Liao, K.F. Lin, Y.R. Tzeng, J. Phys. Chem. C, 114 (2010) 7014-7020.
[509] M. Klimakow, P. Klobes, A.F. Thunemann, K. Rademann, F. Emmerling, Chem. Mat., 22 (2010) 5216-5221.
[510] J. Juan-Alcaniz, M. Goesten, A. Martinez-Joaristi, E. Stavitski, A.V. Petukhov, J. Gascon, F. Kapteijn, Chem. Commun., 47 (2011) 8578-8580.
[511] A. Mallick, E.M. Schon, T. Panda, K. Sreenivas, D.D. Diaz, R. Banerjee, J. Mater. Chem., 22 (2012) 14951-14963.
[512] K. Ogata, D. Sasano, T. Yokoi, K. Isozaki, R. Yoshida, T. Takenaka, H. Seike, T. Ogawa, H. Kurata, N. Yasuda, H. Takaya, M. Nakamura, Chem.-Eur. J., 19 (2013) 12356-12375.
[513] B.H. Toby, T. Egami, Acta Crystallogr. A, 48 (1992) 336-346.
[514] D.A. Keen, J. Appl. Crystallogr., 34 (2001) 172-177.
[515] M. Fernandez-Garcia, A. Martinez-Arias, J.C. Hanson, J.A. Rodriguez, Chem. Rev., 104 (2004) 4063-4104.
[516] T. Proffen, H. Kim, J. Mater. Chem., 19 (2009) 5078-5088.
[517] T. Proffen, S.J.L. Billinge, J. Appl. Cryst., 32 (1999) 572-575.
[518] X. Qiu, J.W. Thompson, S.J.L. Billinge, J. Appl. Cryst., 37 (2004) 678.
[519] C.L. Farrow, P. Juhas, J.W. Liu, D. Bryndin, E.S. Bozin, J. Bloch, T. Proffen, S.J.L. Billinge, J. Phys.-Condes. Matter, 19 (2007) art. n. 335219.
[520] A. Filipponi, J. Phys.-Condes. Matter, 6 (1994) 8415-8427.
[521] G. Goerigk, K. Huber, N. Mattern, D.L. Williamson, Eur. Phys. J.-Spec. Top., 208 (2012) 259-274.
[522] C.J. Benmore, ISRN Materials Science, 2012 (2012) 19.
[523] M.R. Antonio, L. Soderholm, X-ray absorption spectroscopy of the actinides, in: L.R. Morss, J. Fuger, N. Edelstein (Eds.) Chemistry of the Actinide and Transactinide Elements, Springer, Dordrecht, 2006, pp. 3086.
[524] P. Nockemann, B. Thijs, K. Lunstroot, T.N. Parac-Vogt, C. Gorller-Walrand, K. Binnemans, K. Van Hecke, L. Van Meervelt, S. Nikitenko, J. Daniels, C. Hennig, R. Van Deun, Chem.-Eur. J., 15 (2009) 1449-1461.
[525] L. Soderholm, S. Skanthakumar, R.E. Wilson, J. Phys. Chem. A, 113 (2009) 6391-6397.
[526] L. Soderholm, S. Skanthakumar, J. Neuefeind, Anal. Bioanal. Chem., 383 (2005) 48-55.
[527] S. Skanthakumar, M.R. Antonio, R.E. Wilson, L. Soderholm, Inorg. Chem., 46 (2007) 3485-3491.
[528] R.E. Wilson, S. Skanthakumar, P.C. Burns, L. Soderholm, Angew. Chem.-Int. Edit., 46 (2007) 8043-8045.
[529] C. Hennig, A. Ikeda, K. Schmeide, V. Brendler, H. Moll, S. Tsushima, A.C. Scheinost, S. Skanthakumar, R. Wilson, L. Soderholm, K. Servaes, C. Gorrler-Walrand, R. Van Deun, Radiochim. Acta, 96 (2008) 607-611.
[530] K.E. Knope, R.E. Wilson, S. Skanthakumar, L. Soderholm, Inorg. Chem., 50 (2011) 8621-8629.
[531] L. Soderholm, S. Skanthakumar, R.E. Wilson, J. Phys. Chem. A, 115 (2011) 4959-4967.
[532] R.E. Wilson, S. Skanthakumar, C.L. Cahill, L. Soderholm, Inorg. Chem., 50 (2011) 10748-10754.
[533] C. Walther, J. Rothe, B. Schimmelpfennig, M. Fuss, Dalton Trans., 41 (2012) 10941-10947.
[534] Y.J. Hu, K.E. Knope, S. Skanthakumar, L. Soderholm, Eur. J. Inorg. Chem., 2013 (2013) 4159-4163.
[535] C. Lamberti, C. Prestipino, S. Bordiga, G. Berlier, G. Spoto, A. Zecchina, A. Laloni, F. La Manna, F. D'Anca, R. Felici, F. D'Acapito, P. Roy, Nucl. Instrum. Meth. B, 200 (2003) 196-201.
[536] F.C. Meunier, Chem. Soc. Rev., 39 (2010) 4602-4614.
[537] W. Bras, G.E. Derbyshire, A.J. Ryan, G.R. Mant, A. Felton, R.A. Lewis, C.J. Hall, G.N. Greaves, Nucl. Instrum. Methods A, 326 (1993) 587-591.
[538] S. Nojima, K. Kato, S. Yamamoto, T. Ashida, Macromolecules, 25 (1992) 2237-2242.
[539] D. Grosso, F. Babonneau, P.A. Albouy, H. Amenitsch, A.R. Balkenende, A. Brunet-Bruneau, J. Rivory, Chem. Mat., 14 (2002) 931-939.
[540] D.J. Segel, A. Bachmann, J. Hofrichter, K.O. Hodgson, S. Doniach, T. Kiefhaber, J. Mol. Biol., 288 (1999) 489-499.
[541] W. Bras, G.E. Derbyshire, A. Devine, S.M. Clark, J. Cooke, B.E. Komanschek, A.J. Ryan, J. Appl. Crystallogr., 28 (1995) 26-32.
[542] P. Zalden, G. Aquilanti, C. Prestipino, O. Mathon, B. Andre, M. Wuttig, M.V. Coulet, J. Synchrot. Radiat., 19 (2012) 806-813.
[543] P. Zalden, G. Aquilanti, C. Prestipino, O. Mathon, B. Andre, M.V. Coulet, J. Non-Cryst. Solids, 377 (2013) 30-33.
[544] W. Göran, Phys. Scr., 21 (1980) 535-542.

[545] Y. Waseda, Anomalous X-Ray Scattering for Materials Characterization: Atomic-Scale Structure Determination, Springer, Berlin, 2002.
[546] H. Renevier, M.G. Proietti, Grazing Incidence Diffraction Anomalous Fine Structure in the Study of Structural Properties of Nanostructures, in: C. Lamberti, G. Agostini (Eds.) Characterization of Semiconductor Heterostructures and Nanostructures (Second Edition), Elsevier, Amsterdam, 2013, pp. 311-359.
[547] P.D. Battle, S.J. Blundell, A.I. Coldea, E.J. Cussen, M.J. Rosseinsky, J. Singleton, L.E. Spring, J.F. Vente, J. Mater. Chem., 11 (2001) 160-167.
[548] Y.G. Zhang, A.P. Wilkinson, P.L. Lee, S.D. Shastri, D.M. Shu, D.Y. Chung, M.G. Kanatzidis, J. Appl. Crystallogr., 38 (2005) 433-441.
[549] T. Vad, H.G. Haubold, N. Waldofner, H. Bonnemann, J. Appl. Crystallogr., 35 (2002) 459-470.
[550] P. Andreazza, H. Khelfane, O. Lyon, C. Andreazza-Vignolle, A.Y. Ramos, M. Samah, Eur. Phys. J.-Spec. Top., 208 (2012) 231-244.
[551] J.M. Bijvoet, Proc. Acad. Sci. Amst., 52 (1949) 313.
[552] W.A. Hendrickson, Trends Biochem.Sci., 25 (2000) 637-643.
[553] S.E. Ealick, Curr. Opin. Chem. Biol., 4 (2000) 495-499.
[554] U. Heinemann, G. Illing, H. Oschkinat, Curr. Opin. Biotechnol., 12 (2001) 348-354.
[555] U. Heinemann, K. Bussow, U. Mueller, P. Umbach, Accounts Chem. Res., 36 (2003) 157-163.
[556] R.S. Howland, T.H. Geballe, S.S. Laderman, A. Fischercolbrie, M. Scott, J.M. Tarascon, P. Barboux, Phys. Rev. B, 39 (1989) 9017-9027.
[557] M. Helliwell, J. Synchrot. Radiat., 7 (2000) 139-147.
[558] D.E. Freedman, T.H. Han, A. Prodi, P. Muller, Q.Z. Huang, Y.S. Chen, S.M. Webb, Y.S. Lee, T.M. McQueen, D.G. Nocera, J. Am. Chem. Soc., 132 (2010) 16185-16190.
[559] M.A.G. Aranda, D.C. Sinclair, J.P. Attfield, A.P. Mackenzie, Phys. Rev. B, 51 (1995) 12747-12753.
[560] M.D. Marcos, M.A.G. Aranda, D.C. Sinclair, J.P. Attfield, Physica C, 235 (1994) 967-968.
[561] J.M. Joubert, R. Cerny, M. Latroche, A. Percheron-Guegan, K. Yvon, J. Appl. Crystallogr., 31 (1998) 327-332.
[562] M. Latroche, J.M. Joubert, A. Percheron-Guegan, P.H.L. Notten, J. Solid State Chem., 146 (1999) 313-321.
[563] R. Magalhaes-Paniago, G. Medeiros-Ribeiro, A. Malachias, S. Kycia, T.I. Kamins, R.S. Williams, Phys. Rev. B, 66 (2002) art. n. 245312.
[564] M. Cianci, J.R. Helliwell, M. Helliwell, V. Kaucic, N.Z. Logar, G. Mali, N.N. Tusar, Crystallogr. Rev., 11 (2005) 245-335.
[565] M. Helliwell, J.R. Helliwell, V. Kaucic, N.Z. Logar, S.J. Teat, J.E. Warren, E.J. Dodson, Acta Crystallogr. Sect. B-Struct. Sci., 66 (2010) 345-357.
[566] R. Wulf, Acta Crystallogr. Sect. A, 46 (1990) 681-688.
[567] A.P. Wilkinson, A.K. Cheetham, S.C. Tang, W.J. Reppart, J. Chem. Soc.-Chem. Commun., (1992) 1485-1487.
[568] H. Palancher, J.L. Hodeau, C. Pichon, J.F. Berar, J. Lynch, B. Rebours, J. Rodriguez-Carvajal, Angew. Chem.-Int. Edit., 44 (2005) 1725-1729.
[569] X.F. Zhang, D.G. Huang, Y.S. Chen, R.H. Holm, Inorg. Chem., 51 (2012) 11017-11029.
[570] C.M. Zall, L.J. Clouston, V.G. Young, K.Y. Ding, H.J. Kim, D. Zherebetskyy, Y.S. Chen, E. Bill, L. Gagliardi, C.C. Lu, Inorg. Chem., 52 (2013) 9216-9228.
[571] T.M. Powers, N.X. Gu, A.R. Fout, A.M. Baldwin, R. Hernandez Sanchez, D.M. Alfonso, Y.-S. Chen, S.-L. Zheng, T.A. Betley, J. Am. Chem. Soc., 135 (2013) 14448-14458.
[572] C.K. Brozek, A.F. Cozzolino, S.J. Teat, Y.S. Chen, M. Dinca, Chem. Mat., 25 (2013) 2998-3002.
[573] H. Stragier, J.O. Cross, J.J. Rehr, L.B. Sorensen, C.E. Bouldin, J.C. Woicik, Phys. Rev. Lett., 69 (1992) 3064-3067.
[574] I.J. Pickering, M. Sansone, J. Marsch, G.N. George, J. Am. Chem. Soc., 115 (1993) 6302-6311.
[575] A.F. Jensen, Z.W. Su, N.K. Hansen, F.K. Larsen, Inorg. Chem., 34 (1995) 4244-4252.
[576] S. Sasaki, T. Toyoda, K. Yamawaki, K. Ohkubo, J. Synchrot. Radiat., 5 (1998) 920-922.
[577] T. Toyoda, S. Sasaki, M. Tanaka, Am. Miner., 84 (1999) 294-298.
[578] M.G. Proietti, H. Renevier, J.L. Hodeau, J. Garcia, J.F. Berar, P. Wolfers, Phys. Rev. B, 59 (1999) 5479-5492.
[579] A.I. Frenkel, A.V. Kolobov, I.K. Robinson, J.O. Cross, Y. Maeda, C.E. Bouldin, Phys. Rev. Lett., 89 (2002) art. n. 285503.
[580] K. Wüthrich, J. Biol. Chem., 265 (1990) 22059-22062.
[581] A.I. Popov, K. Hallenga, Modern NMR Techniques and their Application in Chemistry, Marcel Dekker, Inc., New York, 1991.
[582] W.R. Croasmun, R.M.K. Carlson, Two-Dimensional NMR Spectroscopy: Applications for Chemists and Biochemists, Wiley, New York, 1994.
[583] M. Pons, NMR in Supramolecular Chemistry, Kluwer, Dordrecht, 1999.

[584] N.E. Jacobsen, NMR Spectroscopy Explained: Simplified Theory, Applications and Examples for Organic chemistry and Structural Biology, Wiley, 2007.
[585] V. Friebolin, S. Marten, K. Albert, Magn. Reson. Chem., 48 (2010) 111-116.
[586] J. Keeler, Understanding NMR Spectroscopy (2nd edition), Wiley, Chichester, 2012.
[587] L. Ronconi, P.J. Sadler, Coord. Chem. Rev., 252 (2008) 2239-2277.
[588] P.S. Pregosin, Coord. Chem. Rev., 252 (2008) 2156-2170.
[589] W. von Philipsborn, Chem. Soc. Rev., 28 (1999) 95-105.
[590] A. Macchioni, Eur. J. Inorg. Chem., (2003) 195-205.
[591] H.P. Mo, T.C. Pochapsky, Prog. Nucl. Magn. Reson. Spectrosc., 30 (1997) 1-38.
[592] B. Binotti, A. Macchioni, C. Zuccaccia, D. Zuccaccia, Comments Inorganic Chem., 23 (2002) 417-450.
[593] F. Taulelle, Solid State Sci., 6 (2004) 1053-1057.
[594] R.K. Harris, Solid State Sci., 6 (2004) 1025-1037.
[595] R.K. Harris, Analyst, 131 (2006) 351-373.
[596] B. Elena, G. Pintacuda, N. Mifsud, L. Emsley, J. Am. Chem. Soc., 128 (2006) 9555-9560.
[597] C.J. Pickard, E. Salager, G. Pintacuda, B. Elena, L. Emsley, J. Am. Chem. Soc., 129 (2007) 8932-8933.
[598] D.H. Brouwer, J. Am. Chem. Soc., 130 (2008) 6306-6307.
[599] E. Salager, R.S. Stein, C.J. Pickard, B. Elena, L. Emsley, Phys. Chem. Chem. Phys., 11 (2009) 2610-2621.
[600] D.M. Grant, M.D. Halling, Concepts Magn. Reson. Part A, 34A (2009) 217-237.
[601] R.K. Harris, R.E. Wasylishen, M.J. Duer, NMR Crystallography, John Wiley & Sons, Chichester, 2009.
[602] A.L. Webber, L. Emsley, R.M. Claramunt, S.P. Brown, J. Phys. Chem. A, 114 (2010) 10435-10442.
[603] J.F. Lai, D. Niks, Y.C. Wang, T. Domratcheva, T.R.M. Barends, F. Schwarz, R.A. Olsen, D.W. Elliott, M.Q. Fatmi, C.E.A. Chang, I. Schlichting, M.F. Dunn, L.J. Mueller, J. Am. Chem. Soc., 133 (2011) 4-7.
[604] C. Martineau, B. Bouchevreau, Z.J. Tian, S.J. Lohmeier, P. Behrens, F. Taulelle, Chem. Mat., 23 (2011) 4799-4809.
[605] C. Luchinat, G. Parigi, E. Ravera, M. Rinaldelli, J. Am. Chem. Soc., 134 (2012) 5006-5009.
[606] E. Davies, M.J. Duer, S.E. Ashbrook, J.M. Griffin, J. Am. Chem. Soc., 134 (2012) 12508-12515.
[607] X. Filip, I.G. Grosu, M. Miclaus, C. Filip, Crystengcomm, 15 (2013) 4131-4142.
[608] H. Colas, L. Bonhomme-Coury, C.C. Diogo, F. Tielens, F. Babonneau, C. Gervais, D. Bazin, D. Laurencin, M.E. Smith, J.V. Hanna, M. Daudon, C. Bonhomme, Crystengcomm, 15 (2013) 8840-8847.
[609] D.V. Dudenko, J.R. Yates, K.D.M. Harris, S.P. Brown, Crystengcomm, 15 (2013) 8797-8807.
[610] D.H. Brouwer, Solid State Nucl. Magn. Reson., 51-52 (2013) 37-45.
[611] D.H. Brouwer, K.P. Langendoen, Crystengcomm, 15 (2013) 8748-8762.
[612] F.A. Perras, I. Korobkov, D.L. Bryce, Crystengcomm, 15 (2013) 8727-8738.
[613] T. Pawlak, P. Paluch, K. Trzeciak-Karlikowska, A. Jeziorna, M.J. Potrzebowski, Crystengcomm, 15 (2013) 8680-8692.
[614] V.R. Seymour, E.C.V. Eschenroeder, M. Castro, P.A. Wright, S.E. Ashbrook, Crystengcomm, 15 (2013) 8668-8679.
[615] A. Bhaumik, C. Luchinat, G. Parigi, E. Ravera, M. Rinaldelli, Crystengcomm, 15 (2013) 8639-8656.
[616] S. Macholl, D. Tietze, G. Buntkowsky, Crystengcomm, 15 (2013) 8627-8638.
[617] F. Taulelle, B. Bouchevreau, C. Martineau, Crystengcomm, 15 (2013) 8613-8622.
[618] M.R. Chierotti, R. Gobetto, Crystengcomm, 15 (2013) 8599-8612.
[619] S.M. Santos, J. Rocha, L. Mafra, Cryst. Growth Des., 13 (2013) 2390-2395.
[620] B. Bouchevreau, C. Martineau, C. Mellot-Draznieks, A. Tuel, M.R. Suchomel, J. Trebosc, O. Lafon, J.P. Amoureux, F. Taulelle, Chem. Mat., 25 (2013) 2227-2242.
[621] M. Baias, J.N. Dumez, P.H. Svensson, S. Schantz, G.M. Day, L. Emsley, J. Am. Chem. Soc., 135 (2013) 17501-17507.
[622] J.S. Stevens, S.J. Byard, C.C. Seaton, G. Sadiq, R.J. Davey, S.L.M. Schroeder, Phys. Chem. Chem. Phys., 16 (2014) 1150-1160.
[623] M. Miclaus, I.G. Grosu, X. Filip, C. Tripon, C. Filip, Crystengcomm, 16 (2014) 299-303.
[624] M.R. Chierotti, R. Gobetto, Eur. J. Inorg. Chem., (2009) 2581-2597.
[625] G. Pintacuda, G. Kervern, Modern Nmr Methodology, 335 (2013) 157-200.
[626] I. Bertini, C. Luchinat, G. Parigi, R. Pierattelli, Dalton Trans., (2008) 3782-3790.
[627] J. Estephane, E. Groppo, J.G. Vitillo, A. Damin, D. Gianolio, C. Lamberti, S. Bordiga, E.A. Quadrelli, J.M. Basset, G. Kervern, L. Emsley, G. Pintacuda, A. Zecchina, J. Phys. Chem. C, 114 (2010) 4451-4458.
[628] J. Estephane, E. Groppo, A. Damin, J.G. Vitillo, D. Gianolio, C. Lamberti, S. Bordiga, C. Prestipino, S. Nikitenko, E.A. Quadrelli, M. Taoufik, J.M. Basset, A. Zecchina, J. Phys. Chem. C, 113 (2009) 7305-7315.
[629] J. Estephane, E. Groppo, J.G. Vitillo, A. Damin, C. Lamberti, S. Bordiga, A. Zecchina, Phys. Chem. Chem. Phys., 11 (2009) 2218-2227.

[630] J.A. Weil, J.R. Bolton, J.E. Wertz, Electron paramagnetic resonance: Elementary theory and applications, Wiley-interscience, New York, 1994.
[631] W.B. Mims, Proc. R. Soc. A, 283 (1965) 452-457.
[632] D.M. Murphy, R.D. Farley, Chem. Soc. Rev., 35 (2006) 249-268.
[633] A. Schweiger, G. Jeschke, Principles of pulse electron paramagnetic resonance., Oxford University Press, Oxford UK, 2001.
[634] D.N. Sathyanarayana, Electronic Absorption Spectroscopy and Related Techniques, Universities Press (India) Ltd, Bangalore, 2001.
[635] A.M. Ellis, E.M. Feher, T.G. Wright, Electronic and Photoelectron Spectroscopy: Fundamentals and Case Studies, Cambridge University Press, Cambridge, 2005.
[636] F. Bonino, C. Lamberti, S. Chavan, J.G. Vitillo, S. Bordiga, Characterization of MOFs by combined vibrational, and electronic spectroscopies, in: F.X. Llabrés i Xamena, J. Gascón (Eds.) Metal-Organic Frameworks in heterogeneous catalysis, RSC, Cambridge, 2013, pp. 76-142.
[637] B.N. Figgis, M.A. Hitchman, Ligand Field Theory and Its Applications, Wiley, New York, 2000.
[638] C.T. Au, A.F. Carley, M.W. Roberts, Int. Rev. Phys. Chem., 5 (1986) 57-87.
[639] I.S. Tilinin, A. Jablonski, W.S.M. Werner, Prog. Surf. Sci., 52 (1996) 193-335.
[640] A.P. Pijpers, R.J. Meier, Chem. Soc. Rev., 28 (1999) 233-238.
[641] S. Hüfner, Photoelectron Spectroscopy: Principles and Applications (3^{ed} Edition), Springer, Berlin, 2003.
[642] P. van der Heide, X-ray Photoelectron Spectroscopy: An introduction to Principles and Practices, Wiley, Hoboken, 2012.
[643] A. Einstein, Anal. Phys., 322 (1905) 132-148.
[644] P.A.M. Dirac, Proc. Roy. Soc. (London) A, 114 (1927) 243-265.
[645] E. Fermi, Nuclear Physics, University of Chicago Press, Chicago, 1950.
[646] L. Mino, V. Colombo, J.G. Vitillo, C. Lamberti, S. Bordiga, E. Gallo, P. Glatzel, A. Maspero, S. Galli, Dalton Trans., 41 (2012) 4012-4019.
[647] G.S. Knapp, H. Chen, T.E. Klippert, Rev. Sci. Instrum., 49 (1978) 1658-1666.
[648] G.G. Cohen, D.A. Fischer, J. Colbert, N.J. Shevchik, Rev. Sci. Instrum., 51 (1980) 273-277.
[649] S. Khalid, R. Emrich, R. Dujari, J. Shultz, J.R. Katzer, Rev. Sci. Instrum., 53 (1982) 22-33.
[650] K. Tohji, Y. Udagawa, T. Kawasaki, K. Masuda, Rev. Sci. Instrum., 54 (1983) 1482-1487.
[651] S. Okada, T. Tonuma, Y. Uebo, J.-i. Yamaki, J. Power Sources, 119-121 (2003) 621-625.
[652] T. Kyomen, R. Yamazaki, M. Itoh, Phys. Rev. B, 68 (2003) art. n. 104416.
[653] T. Kyomen, R. Yamazaki, M. Itoh, Chem. Mater., 15 (2003) 4798-4803.
[654] K. Inoue, K. Shinoda, S. Suzuki, Y. Waseda, Materials Transact., 49 (2008) 466-470.
[655] H. Yoshida, S.-i. Nonoyama, Y. Yazawa, T. Hattori, Catal. Today, 153 (2009) 156-161.
[656] A.A. Guda, N. Smolentsev, J. Verbeeck, E.M. Kaidashev, Y. Zubavichus, A.N. Kravtsova, O.E. Polozhentsev, A.V. Soldatov, Solid State Commun., 151 (2011) 1314-1317.
[657] I.S. Rodina, A.N. Kravtsova, A.V. Soldatov, G.E. Yalovega, Y.V. Popov, N.I. Boyko, Optics Spectrosc., 115 (2013) 858-862.
[658] P.J. Durham, Theory of XANES, in: D.C. Koningsberger, R. Prins (Eds.) X-Ray Absorption: Principles, Applications, Techniques of EXAFS, SEXAFS and XANES, John Wiley & Sons, New York, 1988, pp. 53-84.
[659] N. Kosugi, Theory and analysis of XANES: MO approach, in: Y. Iwasawa (Ed.) X-ray absorption fine structure for catalysts and surfaces, World Scientific, Singapore, 1996, pp. 60-76.
[660] A. Bianconi, J. Garcia, M. Benfatto, Top. Curr. Chem., 145 (1988) 29-67.
[661] P.J. Durham, Multiple Scattering Calculations of XANES, in: A. Bianconi, L. Incoccia, S. Stipcich (Eds.) EXAFS and Near Edge Structure, Springer, Berlin, 1983, pp. 37-42.
[662] A. Bianconi, J. Garcia, M. Benfatto, A. Marcelli, C.R. Natoli, M.F. Ruizlopez, Phys. Rev. B, 43 (1991) 6885-6892.
[663] T.A. Tyson, K.O. Hodgson, C.R. Natoli, M. Benfatto, Phys. Rev. B, 46 (1992) 5997-6019.
[664] A.L. Ankudinov, B. Ravel, J.J. Rehr, S.D. Conradson, Phys. Rev. B, 58 (1998) 7565-7576.
[665] J.J. Rehr, A.L. Ankudinov, J. Synchrot. Radiat., 8 (2001) 61-65.
[666] G. te Velde, F.M. Bickelhaupt, E.J. Baerends, C.F. Guerra, S.J.A. Van Gisbergen, J.G. Snijders, T. Ziegler, J. Comput. Chem., 22 (2001) 931-967.
[667] Y. Joly, J. Synchrot. Radiat., 10 (2003) 58-63.
[668] Y. Joly, Interaction of Polarized Light with Matter, in: E. Beaurepaire, H. Bulou, F. Scheurer, K. J-P (Eds.) Magnetism and Synchrotron Radiation: New Trends, Springer, Berlin, 2010, pp. 77-126.
[669] F. Neese, ORCA, an ab initio DFT and semiempirical electronic structure package, version 2.7, University of Bonn: Bonn, Germany, (2009).
[670] F. Neese, Wiley Interdisciplinary Rev.: Comput. Mol. Sci., 2 (2012) 73-78.

[671] D. Ahlers, G. Schutz, V. Popescu, H. Ebert, J. Appl. Phys., 83 (1998) 7082-7084.
[672] T. Huhne, H. Ebert, Solid State Commun., 109 (1999) 577-582.
[673] K. Schwarz, P. Blaha, S.B. Trickey, Mol. Phys., 108 (2010) 3147-3166.
[674] S. Bordiga, S. Coluccia, C. Lamberti, L. Marchese, A. Zecchina, F. Boscherini, F. Buffa, F. Genoni, G. Leofanti, G. Petrini, G. Vlaic, J. Phys. Chem., 98 (1994) 4125-4132.
[675] S. Bordiga, R. Buzzoni, F. Geobaldo, C. Lamberti, E. Giamello, A. Zecchina, G. Leofanti, G. Petrini, G. Tozzola, G. Vlaic, J. Catal., 158 (1996) 486-501.
[676] C. Prestipino, G. Berlier, F.X. Llabrés i Xamena, G. Spoto, S. Bordiga, A. Zecchina, G.T. Palomino, T. Yamamoto, C. Lamberti, Chem. Phys. Lett., 363 (2002) 389-396.
[677] S. Bordiga, F. Bonino, A. Damin, C. Lamberti, Phys. Chem. Chem. Phys., 9 (2007) 4854-4878.
[678] G. Agostini, E. Groppo, S. Bordiga, A. Zecchina, C. Prestipino, F. D'Acapito, E. van Kimmenade, P.C. Thune, J.W. Niemantsverdriet, C. Lamberti, J. Phys. Chem. C, 111 (2007) 16437-16444.
[679] E. Paris, A. Mottana, G. Dellaventura, J.L. Robert, European Journal of Mineralogy, 5 (1993) 455-464.
[680] S. Bordiga, F. Boscherini, S. Coluccia, F. Genoni, C. Lamberti, G. Leofanti, L. Marchese, G. Petrini, G. Vlaic, A. Zecchina, Catal. Lett., 26 (1994) 195-208.
[681] X.T. Gao, S.R. Bare, J.L.G. Fierro, M.A. Banares, I.E. Wachs, J. Phys. Chem. B, 102 (1998) 5653-5666.
[682] X.T. Gao, S.R. Bare, B.M. Weckhuysen, I.E. Wachs, J. Phys. Chem. B, 102 (1998) 10842-10852.
[683] G. Ricchiardi, A. Damin, S. Bordiga, C. Lamberti, G. Spanò, F. Rivetti, A. Zecchina, J. Am. Chem. Soc., 123 (2001) 11409-11419.
[684] E.A. Eilertsen, S. Bordiga, C. Lamberti, A. Damin, F. Bonino, B. Arstad, S. Svelle, U. Olsbye, K.P. Lillerud, ChemCatChem, 3 (2011) 1869-1871.
[685] E.A. Eilertsen, F. Giordanino, C. Lamberti, S. Bordiga, A. Damin, F. Bonino, U. Olsbye, K.P. Lillerud, Chem. Commun., 47 (2011) 11867-11869.
[686] E. Groppo, C. Prestipino, F. Cesano, F. Bonino, S. Bordiga, C. Lamberti, P.C. Thune, J.W. Niemantsverdriet, A. Zecchina, J. Catal., 230 (2005) 98-108.
[687] T. Yamamoto, X-Ray Spectrometry, 37 (2008) 572-584.
[688] Z.Y. Wu, G. Ouvrard, P. Gressier, C.R. Natoli, Phys. Rev. B, 55 (1997) 10382-10391.
[689] F. Farges, G.E. Brown, J.J. Rehr, Phys. Rev. B, 56 (1997) 1809-1819.
[690] Y. Joly, D. Cabaret, H. Renevier, C.R. Natoli, Phys. Rev. Lett., 82 (1999) 2398-2401.
[691] C. Prestipino, P.L. Solari, C. Lamberti, J. Phys. Chem. B, 109 (2005) 13132-13137.
[692] M.W. Anderson, O. Terasaki, T. Ohsuna, A. Philippou, S.P. Mackay, A. Ferreira, J. Rocha, S. Lidin, Nature, 367 (1994) 347-351.
[693] M.W. Anderson, O. Terasaki, T. Ohsuna, P.J.O. Malley, A. Philippou, S.P. Mackay, A. Ferreira, J. Rocha, S. Lidin, Philos. Mag. B, 71 (1995) 813-841.
[694] E. Borello, C. Lamberti, S. Bordiga, A. Zecchina, C.O. Arean, Appl. Phys. Lett., 71 (1997) 2319-2321.
[695] C. Lamberti, Microporous Mesoporous Mat., 30 (1999) 155-163.
[696] G. Leofanti, M. Padovan, M. Garilli, D. Carmello, A. Zecchina, G. Spoto, S. Bordiga, G.T. Palomino, C. Lamberti, J. Catal., 189 (2000) 91-104.
[697] G. Leofanti, M. Padovan, M. Garilli, D. Carmello, G.L. Marra, A. Zecchina, G. Spoto, S. Bordiga, C. Lamberti, J. Catal., 189 (2000) 105-116.
[698] G. Leofanti, A. Marsella, B. Cremaschi, M. Garilli, A. Zecchina, G. Spoto, S. Bordiga, P. Fisicaro, G. Berlier, C. Prestipino, G. Casali, C. Lamberti, J. Catal., 202 (2001) 279-295.
[699] G. Leofanti, A. Marsella, B. Cremaschi, M. Garilli, A. Zecchina, G. Spoto, S. Bordiga, P. Fisicaro, C. Prestipino, F. Villain, C. Lamberti, J. Catal., 205 (2002) 375-381.
[700] N.B. Muddada, U. Olsbye, G. Leofanti, D. Gianolio, F. Bonino, S. Bordiga, T. Fuglerud, S. Vidotto, A. Marsella, C. Lamberti, Dalton Trans., 39 (2010) 8437-8449.
[701] G. Turnes Palomino, P. Fisicaro, S. Bordiga, A. Zecchina, E. Giamello, C. Lamberti, J. Phys. Chem. B, 104 (2000) 4064-4073.
[702] F.X. Llabrés i Xamena, P. Fisicaro, G. Berlier, A. Zecchina, G.T. Palomino, C. Prestipino, S. Bordiga, E. Giamello, C. Lamberti, J. Phys. Chem. B, 107 (2003) 7036-7044.
[703] J. Blasco, J. Garciá, G. Subías, M.C. Sánchez, Phys. Rev. B, 70 (2004) art. n. 094426.
[704] T.R.N. Kutty, P. Philip, J. Phys.: Condens. Matter, 12 (2000) 7747-7758.
[705] J.H. Zhao, T. Song, H.P. Kunkel, Z. Zhou, R.M. Roshko, G. Williams, J. Phys.: Condens. Matter, 12 (2000) 6903-6918.
[706] J. Philip, T.R.N. Kutty, Mater. Chem. Phys., 73 (2002) 220-226.
[707] J.H. Zhao, H.P. Kunkel, X.Z. Zhou, G. Williams, Phys. Rev. B, 66 (2002) art. n. 184428.
[708] G. Saracco, G. Scibilia, A. Iannibello, G. Baldi, Appl. Catal. B: Environ., 8 (1996) 229-244.
[709] G. Saracco, F. Geobaldo, G. Baldi, Appl. Catal. B: Environ., 20 (1999) 277-288.

[710] S. Cimino, S. Colonna, S. De Rossi, M. Faticanti, L. Lisi, I. Pettiti, p. Portaz, J. Catal., 205 (2002) 309-317.
[711] M.F.M. Zwinkels, S.G. Jaras, P.G. Menon, T.A. Griffin, Catal. Rev. Sci. Eng., 35 (1993) 319-358.
[712] G. Agostini, E. Groppo, A. Piovano, R. Pellegrini, G. Leofanti, C. Lamberti, Langmuir, 26 (2010) 11204-11211.
[713] R. Pellegrini, G. Leofanti, G. Agostini, E. Groppo, M. Rivallan, C. Lamberti, Langmuir, 25 (2009) 6476-6485.
[714] R. Pellegrini, G. Agostini, E. Groppo, A. Piovano, G. Leofanti, C. Lamberti, J. Catal., 280 (2011) 150-160.
[715] C. Lamberti, G.T. Palomino, S. Bordiga, G. Berlier, F. D'Acapito, A. Zecchina, Angew. Chem.-Int. Edit., 39 (2000) 2138-2141.
[716] C. Prestipino, L. Capello, F. D'Acapito, C. Lamberti, Phys. Chem. Chem. Phys., 7 (2005) 1743-1746.
[717] E. Borfecchia, S. Maurelli, D. Gianolio, E. Groppo, M. Chiesa, F. Bonino, C. Lamberti, J. Phys. Chem. C, 116 (2012) 19839-19850.
[718] S. Bordiga, A. Damin, F. Bonino, A. Zecchina, G. Spanò, F. Rivetti, V. Bolis, C. Prestipino, C. Lamberti, J. Phys. Chem. B, 106 (2002) 9892-9905.
[719] V. Bolis, A. Barbaglia, S. Bordiga, C. Lamberti, A. Zecchina, J. Phys. Chem. B, 108 (2004) 9970-9983.
[720] L. Salassa, T. Ruiu, C. Garino, A.M. Pizarro, F. Bardelli, D. Gianolio, A. Westendorf, P.J. Bednarski, C. Lamberti, R. Gobetto, P.J. Sadler, Organometallics, 29 (2010) 6703-6710.
[721] F. Bonino, A. Damin, G. Ricchiardi, M. Ricci, G. Spano, R. D'Aloisio, A. Zecchina, C. Lamberti, C. Prestipino, S. Bordiga, J. Phys. Chem. B, 108 (2004) 3573-3583.
[722] C. Prestipino, F. Bonino, S. Usseglio, A. Damin, A. Tasso, M.G. Clerici, S. Bordiga, F. D'Acapito, A. Zecchina, C. Lamberti, ChemPhysChem, 5 (2004) 1799-1804.
[723] E.F. Garman, G.W. Grime, Prog. Biophys. Mol. Biol., 89 (2005) 173-205.
[724] R. Lobinski, C. Moulin, R. Ortega, Biochimie, 88 (2006) 1591-1604.
[725] R. Ortega, Metallomics, 1 (2009) 137-141.
[726] L. Mandic, S. Fazinic, M. Jaksic, Phys. Rev. A, 80 (2009) art. n. 042519.
[727] K. Tsuji, K. Nakano, Y. Takahashi, K. Hayashi, C.U. Ro, Anal. Chem., 84 (2012) 636-668.
[728] O.T. Butler, W.R.L. Cairns, J.M. Cook, C.M. Davidson, J. Anal. At. Spectrom., 28 (2013) 177-216.
[729] A. Kotani, Eur. Phys. J. B, 47 (2005) 3-27.
[730] G. Peng, F.M.F. de Groot, K. Hamalainen, J.A. Moore, X. Wang, M.M. Grush, J.B. Hastings, D.P. Siddons, W.H. Armstrong, O.C. Mullins, S.P. Cramer, J. Am. Chem. Soc., 116 (1994) 2914-2920.
[731] G. Vanko, T. Neisius, G. Molnar, F. Renz, S. Karpati, A. Shukla, F.M.F. de Groot, J. Phys. Chem. B, 110 (2006) 11647-11653.
[732] U. Bergmann, C.R. Horne, T.J. Collins, J.M. Workman, S.P. Cramer, Chem. Phys. Lett., 302 (1999) 119-124.
[733] K.M. Lancaster, M. Roemelt, P. Ettenhuber, Y.L. Hu, M.W. Ribbe, F. Neese, U. Bergmann, S. DeBeer, Science, 334 (2011) 974-977.
[734] G. Smolentsev, A.V. Soldatov, J. Messinger, K. Merz, T. Weyhermuller, U. Bergmann, Y. Pushkar, J. Yano, V.K. Yachandra, P. Glatzel, J. Am. Chem. Soc., 131 (2009) 13161-13167.
[735] J.C. Swarbrick, Y. Kvashnin, K. Schulte, K. Seenivasan, C. Lamberti, P. Glatzel, Inorg. Chem., 49 (2010) 8323-8332.
[736] N. Lee, T. Petrenko, U. Bergmann, F. Neese, S. DeBeer, J. Am. Chem. Soc., 132 (2010) 9715-9727.
[737] M.U. Delgado-Jaime, B.R. Dible, K.P. Chiang, W.W. Brennessel, U. Bergmann, P.L. Holland, S. DeBeer, Inorg. Chem., 50 (2011) 10709-10717.
[738] J.J. Kas, J.J. Rehr, J.A. Soininen, P. Glatzel, Phys. Rev. B, 83 (2011) art. n. 235114.
[739] J.J. Kas, J.J. Rehr, M. Tromp, R.J. Thomas, P. Glatzel, J. Phys. Conf. Ser., 430 (2013) art. n. 012003.
[740] P. Glatzel, M. Sikora, G. Smolentsev, M. Fernandez-Garcia, Catal. Today, 145 (2009) 294-299.
[741] G. Ghiringhelli, N.B. Brookes, E. Annese, H. Berger, C. Dallera, M. Grioni, L. Perfetti, A. Tagliaferri, L. Braicovich, Phys. Rev. Lett., 92 (2004) art. n. 117406.
[742] S. Huotari, T. Pylkkanen, G. Vanko, R. Verbeni, P. Glatzel, G. Monaco, Phys. Rev. B, 78 (2008) art. n. 041102.
[743] M. van Veenendaal, X.S. Liu, M.H. Carpenter, S.P. Cramer, Phys. Rev. B, 83 (2011) art. n. 045101.
[744] L.J.P. Ament, M. van Veenendaal, T.P. Devereaux, J.P. Hill, J. van den Brink, Rev. Mod. Phys., 83 (2011) 705-767.
[745] V. Stojanoff, K. Hamalainen, D.P. Siddons, J.B. Hastings, L.E. Berman, S. Cramer, G. Smith, Rev. Sci. Instrum., 63 (1992) 1125-1127.
[746] K. Sakurai, H. Eba, Jpn. J. Appl. Phys. Part 1 - Regul. Pap. Short Notes Rev. Pap., 38 (1999) 650-653.
[747] K. Sakurai, H. Eba, K. Inoue, N. Yagi, Nucl. Instrum. Methods Phys. Res. Sect. A-Accel. Spectrom. Dect. Assoc. Equip., 467 (2001) 1549-1552.
[748] K. Sakurai, H. Eba, K. Inoue, N. Yagi, Anal. Chem., 74 (2002) 4532-4535.
[749] Y. Izumi, H. Oyanagi, H. Nagamori, Bull. Chem. Soc. Jpn., 73 (2000) 2017-2023.
[750] E. Welter, P. Machek, G. Drager, U. Bruggmann, M. Froba, J. Synchrot. Radiat., 12 (2005) 448-454.

[751] J.P. Hill, D.S. Coburn, Y.J. Kim, T. Gog, D.M. Casa, C.N. Kodituwakku, H. Sinn, J. Synchrot. Radiat., 14 (2007) 361-365.
[752] E. Kleimenov, A. Bergamaschi, J.A. van Bokhoven, M. Janousch, B. Schmitt, M. Nachtegaal, J. Phys. Conf. Ser., 190 (2009) art. n. 012035.
[753] J.I. Pacold, J.A. Bradley, B.A. Mattern, M.J. Lipp, G.T. Seidler, P. Chow, Y. Xiao, E. Rod, B. Rusthoven, J. Quintana, J. Synchrot. Radiat., 19 (2012) 245-251.
[754] J. Hoszowska, J.C. Dousse, J. Kern, C. Rheme, Nucl. Instrum. Methods Phys. Res. Sect. A-Accel. Spectrom. Dect. Assoc. Equip., 376 (1996) 129-138.
[755] J. Hoszowska, J.C. Dousse, J. Electron Spectrosc. Relat. Phenom., 137 (2004) 687-690.
[756] U. Andiel, K. Eidmann, F. Pisani, K. Witte, I. Uschmann, O. Wehrhan, E. Forster, Rev. Sci. Instrum., 74 (2003) 2369-2374.
[757] H. Hayashi, M. Kawata, R. Takeda, Y. Udagawa, Y. Watanabe, T. Takano, S. Nanao, N. Kawamura, J. Electron Spectrosc. Relat. Phenom., 136 (2004) 191-197.
[758] R. Shepherd, P. Audebert, R. Booth, B. Young, J. Bonlie, D. Nelson, S. Shiromizu, D. Price, D. Norman, J. Dunn, K. Widmann, P. Springer, Rev. Sci. Instrum., 75 (2004) 3765-3767.
[759] J. Szlachetko, M. Nachtegaal, J. Sa, J.-C. Dousse, J. Hoszowska, E. Kleymenov, M. Janousch, O.V. Safonova, C. Konig, J.A. van Bokhoven, Chem. Commun., 48 (2012) 10898-10900.
[760] P. Glatzel, U. Bergmann, J. Yano, H. Visser, J.H. Robblee, W.W. Gu, F.M.F. de Groot, G. Christou, V.L. Pecoraro, S.P. Cramer, V.K. Yachandra, J. Am. Chem. Soc., 126 (2004) 9946-9959.
[761] L.C. Duda, T. Schmitt, M. Magnuson, J. Forsberg, A. Olsson, J. Nordgren, K. Okada, A. Kotani, Phys. Rev. Lett., 96 (2006) art. n. 067402.
[762] W. Schülke, Electron Dynamics by Inelastic X-Ray Scattering, Oxford University Press, Oxford, 2007.
[763] J. Schlappa, T. Schmitt, F. Vernay, V.N. Strocov, V. Ilakovac, B. Thielemann, H.M. Ronnow, S. Vanishri, A. Piazzalunga, X. Wang, L. Braicovich, G. Ghiringhelli, C. Marin, J. Mesot, B. Delley, L. Patthey, Phys. Rev. Lett., 103 (2009) art. n. 047401.
[764] L. Braicovich, J. van den Brink, V. Bisogni, M.M. Sala, L.J.P. Ament, N.B. Brookes, G.M. De Luca, M. Salluzzo, T. Schmitt, V.N. Strocov, G. Ghiringhelli, Phys. Rev. Lett., 104 (2010) art. n. 077002.
[765] P.M. Abdala, O.V. Safonova, G. Wiker, W. van Beek, H. Emerich, J.A. van Bokhoven, J. Sa, J. Szlachetko, M. Nachtegaal, Chimia, 66 (2012) 699-705.
[766] C. Garino, E. Gallo, N. Smolentsev, P. Glatzel, C. Lamberti, R. Gobetto, P.J. Sadler, L. Salassa, Phys. Chem. Chem. Phys., 14 (2012) 15278-15281.
[767] K. Hamalainen, D.P. Siddons, J.B. Hastings, L.E. Berman, Phys. Rev. Lett., 67 (1991) 2850-2853.
[768] F.M.F. de Groot, M.H. Krisch, J. Vogel, Phys. Rev. B, 66 (2002) art. n. 195112.
[769] J.A. van Bokhoven, L. C., J.T. Miller, M. Tromp, O.V. Safonova, P. Glatzel, Angew. Chem.-Int. Edit., 45 (2006) 4651-4654.
[770] F.M.F. de Groot, P. Glatzel, U. Bergmann, P.A. van Aken, R.A. Barrea, S. Klemme, M. Havecker, A. Knop-Gericke, W.M. Heijboer, B.M. Weckhuysen, J. Phys. Chem. B, 109 (2005) 20751-20762.
[771] P. Glatzel, L. Jacquamet, U. Bergmann, F.M.F. de Groot, S.P. Cramer, Inorg. Chem., 41 (2002) 3121-3127.
[772] T. Funk, A. Deb, S.J. George, H.X. Wang, S.P. Cramer, Coord. Chem. Rev., 249 (2005) 3-30.
[773] H.K. Seong, U. Kim, E.K. Jeon, T.E. Park, H. Oh, T.H. Lee, J.J. Kim, H.J. Choi, J.Y. Kim, J. Phys. Chem. C, 113 (2009) 10847-10852.
[774] V.L. Pool, M.T. Klem, C.L. Chorney, E.A. Arenholz, Y.U. Idzerda, J. Appl. Phys., 109 (2011) art. n. 07B529.
[775] S. Staniland, B. Ward, A. Harrison, G. van der Laan, N. Telling, Proc. Natl. Acad. Sci. USA, 104 (2007) 19524-19528.
[776] M.A. Arrio, A. Scuiller, P. Sainctavit, C.C.D. Moulin, T. Mallah, M. Verdaguer, J. Am. Chem. Soc., 121 (1999) 6414-6420.
[777] C. Wackerlin, P. Maldonado, L. Arnold, A. Shchyrba, J. Girovsky, J. Nowakowski, M.E. Ali, T. Hahlen, M. Baljozovic, D. Siewert, A. Kleibert, K. Mullen, P.M. Oppeneer, T.A. Jung, N. Ballav, Chem. Commun., 49 (2013) 10736-10738.
[778] D. Chylarecka, T.K. Kim, K. Tarafder, K. Muller, K. Godel, I. Czekaj, C. Wackerlin, M. Cinchetti, M.E. Ali, C. Piamonteze, F. Schmitt, J.P. Wustenberg, C. Ziegler, F. Nolting, M. Aeschlimann, P.M. Oppeneer, N. Ballav, T.A. Jung, J. Phys. Chem. C, 115 (2011) 1295-1301.
[779] S. Khanra, K. Kuepper, T. Weyhermuller, M. Prinz, M. Raekers, S. Voget, A.V. Postnikov, F.M.F. de Groot, S.J. George, M. Coldea, M. Neumann, P. Chaudhuri, Inorg. Chem., 47 (2008) 4605-4617.
[780] H.C. van der Mei, J. de Vries, H.J. Busscher, Surf. Sci. Rep., 39 (2000) 3-24.
[781] V. Matolin, I. Stara, N. Tsud, V. Johanek, Prog. Surf. Sci., 67 (2001) 167-181.
[782] H. Daimon, F. Matsui, Prog. Surf. Sci., 81 (2006) 367-386.
[783] K. Hirose, H. Nohira, K. Azuma, T. Hattori, Prog. Surf. Sci., 82 (2007) 3-54.

[784] N. Ueno, S. Kera, Prog. Surf. Sci., 83 (2008) 490-557.
[785] M. Faubel, K.R. Siefermann, Y. Liu, B. Abel, Accounts Chem. Res., 45 (2012) 120-130.
[786] P.S. Bagus, E.S. Ilton, C.J. Nelin, Surf. Sci. Rep., 68 (2013) 273-304.
[787] M. Salmeron, R. Schlogl, Surf. Sci. Rep., 63 (2008) 169-199.
[788] A. Knop-Gericke, E. Kleimenov, M. Havecker, R. Blume, D. Teschner, S. Zafeiratos, R. Schlogl, V.I. Bukhtiyarov, V.V. Kaichev, I.P. Prosvirin, A.I. Nizovskii, H. Bluhm, A. Barinov, P. Dudin, M. Kiskinova, Adv. Catal., 52 (2009) 213-272.
[789] F. Tao, S.R. Zhang, L. Nguyen, X.Q. Zhang, Chem. Soc. Rev., 41 (2012) 7980-7993.
[790] D.E. Starr, Z. Liu, M. Havecker, A. Knop-Gericke, H. Bluhm, Chem. Soc. Rev., 42 (2013) 5833-5857.
[791] S.V. Didziulis, S.L. Cohen, A.A. Gewirth, E.I. Solomon, J. Am. Chem. Soc., 110 (1988) 250-268.
[792] E. Stavitski, F.M.F. de Groot, Micron, 41 (2010) 687-694.
[793] B. Hvolbaek, T.V.W. Janssens, B.S. Clausen, H. Falsig, C.H. Christensen, J.K. Norskov, Nano Today, 2 (2007) 14-18.
[794] J. Greeley, M. Mavrikakis, Nat. Mater., 3 (2004) 810-815.
[795] J.B. Wu, Y.F. Lin, J.L. Wang, P.J. Chang, C.P. Tasi, C.C. Lu, H.T. Chiu, Y.W. Yang, Inorg. Chem., 42 (2003) 4516-4518.
[796] K. Kobayashi, M. Yabashi, Y. Takata, T. Tokushima, S. Shin, K. Tamasaku, D. Miwa, T. Ishikawa, H. Nohira, T. Hattori, Y. Sugita, O. Nakatsuka, A. Sakai, S. Zaima, Appl. Phys. Lett., 83 (2003) 1005-1007.
[797] K. Kobayashi, Nucl. Instrum. Methods Phys. Res. Sect. A-Accel. Spectrom. Dect. Assoc. Equip., 601 (2009) 32-47.
[798] J.C. Woicik, E.J. Nelson, D. Heskett, J. Warner, L.E. Berman, B.A. Karlin, I.A. Vartanyants, M.Z. Hasan, T. Kendelewicz, Z.X. Shen, P. Pianetta, Phys. Rev. B, 64 (2001) art. n. 125115.
[799] J.C. Woicik, Nucl. Instrum. Methods Phys. Res. Sect. A-Accel. Spectrom. Dect. Assoc. Equip., 547 (2005) 227-234.
[800] J. Zegenhagen, Surf. Sci. Rep., 18 (1993) 199-271.
[801] D.P. Woodruff, Prog. Surf. Sci., 57 (1998) 1-60.
[802] I.A. Vartanyants, J. Zegenhagen, Solid State Commun., 115 (2000) 161-161.
[803] E.I. Solomon, L. Basumallick, P. Chen, P. Kennepohl, Coord. Chem. Rev., 249 (2005) 229-253.
[804] P. Kennepohl, E.I. Solomon, Inorg. Chem., 42 (2003) 679-688.
[805] A. Boccia, V. Lanzilotto, A.G. Marrani, S. Stranges, R. Zanoni, M. Alagia, G. Fronzoni, P. Decleva, J. Chem. Phys., 136 (2012) art. n. 134308.
[806] N.B. Muddada, U. Olsbye, T. Fuglerud, S. Vidotto, A. Marsella, S. Bordiga, D. Gianolio, G. Leofanti, C. Lamberti, J. Catal., 284 (2012) 236-246.
[807] E. Furimsky, Carbons and Carbon Supported Catalysts in Hydroprocessing, RSC, Cambridge, 2008.
[808] P. Serp, L.J. Figueiredo, Carbon Materials for Catalysis, John Wiley & Sons, Hoboken, 2009.
[809] E.A. Bekturov, S.E. Kudaibergenov, Catalysis by Polymers, Wiley-VCH, Weinheim, 2002.
[810] E. Groppo, W. Liu, O. Zavorotynska, G. Agostini, G. Spoto, S. Bordiga, C. Lamberti, A. Zecchina, Chem. Mat., 22 (2010) 2297-2308.
[811] K. Seenivasan, E. Gallo, A. Piovano, J.G. Vitillo, A. Sommazzi, S. Bordiga, C. Lamberti, P. Glatzel, E. Groppo, Dalton Trans., 42 (2013) 12706-12713.
[812] M.A. Newton, Chem. Soc. Rev., 37 (2008) 2644-2657.
[813] G.A. Ozin, S. Ozkar, Chem. Mat., 4 (1992) 511-521.
[814] G. Perego, Catal. Today, 41 (1998) 251-259.
[815] G.T. Palomino, S. Bordiga, A. Zecchina, G.L. Marra, C. Lamberti, J. Phys. Chem. B, 104 (2000) 8641-8651.
[816] J. Marti-Rujas, M. Kawano, Accounts Chem. Res., 46 (2013) 493-505.
[817] A. Corma, H. Garcia, F. Xamena, Chem. Rev., 110 (2010) 4606-4655.
[818] F. Llabrés i Xamena, J. Gascon, Metal Organic Frameworks as Heterogeneous Catalysts, RSC, Cambridge, 2013.
[819] N. Ren, Y.H. Yang, Y.H. Zhang, Q.R. Wang, Y. Tang, J. Catal., 246 (2007) 215-222.
[820] C.X. Xiao, N. Yan, Y. Kou, Chin. J. Catal., 30 (2009) 753-764.
[821] Y. Yuan, N. Yan, P.J. Dyson, ACS Catal., 2 (2012) 1057-1069.
[822] T. Balcha, J.R. Strobl, C. Fowler, P. Dash, R.W.J. Scott, ACS Catal., 1 (2011) 425-436.
[823] A. Maclennan, A. Banerjee, R.W.J. Scott, Catal. Today, 207 (2013) 170-179.
[824] M.A. Vannice, Kinetics of Catalytic Reactions, Springer, New York, 2005.
[825] L. Salassa, E. Borfecchia, T. Ruiu, C. Garino, D. Gianolio, R. Gobetto, P.J. Sadler, M. Cammarata, M. Wulff, C. Lamberti, Inorg. Chem., 49 (2010) 11240-11248.
[826] E. Borfecchia, C. Garino, L. Salassa, T. Ruiu, D. Gianolio, X.Y. Zhang, K. Attenkofer, L.X. Chen, R. Gobetto, P.J. Sadler, C. Lamberti, Dalton Trans., 42 (2013) 6564-6571.

[827] D. Gianolio, E. Borfecchia, C. Garino, T. Ruiu, C. Lamberti, L. Salassa, J. Phys. Conf. Ser., 430 (2013) art. n. 012125.
[828] E. Borfecchia, C. Garino, D. Gianolio, L. Salassa, R. Gobetto, C. Lamberti, Catal. Today, 229 (2014) 34-45.
[829] P. Hu, J.Q. Wang, F.S. Wang, G.X. Jin, Chem.-Eur. J., 17 (2011) 8576-8583.
[830] J. Rabeah, M. Bauer, W. Baumann, A.E.C. McConnell, W.F. Gabrielli, P.B. Webb, D. Selent, A. Bruckner, ACS Catal., 3 (2013) 95-102.
[831] Y. Miyoshi, T. Akatsuka, S. Okuoka, A. Tsukajima, M. Makino, M. Saito, K. Yonehara, Chem.-Eur. J., 18 (2012) 7941-7949.
[832] R. Jennerjahn, R. Jackstell, I. Piras, R. Franke, H.J. Jiao, M. Bauer, M. Beller, ChemSusChem, 5 (2012) 734-739.
[833] J. March, Advanced Organic Chemistry: Reactions, Mechanisms, and Structure (3rd ed.), Wiley, New York, 1985.
[834] R.T. Morrison, R.N. Boyd, Organic Chemistry, 4th ed., Allyn and Bacon, Boston, 1983.
[835] R. Bates, Organic Synthesis using Transition Metals (2nd ed.), John Wiley & Sons, Chichester, 2012.
[836] S.G. Fiddy, J. Evans, T. Neisius, M.A. Newton, N. Tsoureas, A.A.D. Tulloch, A.A. Danopoulos, Chem.-Eur. J., 13 (2007) 3652-3659.
[837] R.F. Heck, Accounts Chem. Res., 12 (1979) 146-151.
[838] S.J. Gurman, N. Binsted, I. Ross, J. Phys. C: Solid State Phys., 17 (1984) 143-151.
[839] S.J. Gurman, N. Binsted, I. Ross, J. Phys. C: Solid State Phys., 19 (1986) 1845-1861.
[840] N. Binsted, S.S. Hasnain, J. Synchrot. Radiat., 3 (1996) 185-196.
[841] A.A.D. Tulloch, S. Winston, A.A. Danopoulos, G. Eastham, M.B. Hursthouse, Dalton Trans., (2003) 699-708.
[842] J. Evans, L. O'Neill, V.L. Kambhampati, G. Rayner, S. Turin, A. Genge, A.J. Dent, T. Neisius, J. Chem. Soc.-Dalton Trans., (2002) 2207-2212.
[843] J.G. de Vries, Dalton Trans., (2006) 421-429.
[844] E.E. Benson, M.D. Sampson, K.A. Grice, J.M. Smieja, J.D. Froehlich, D. Friebel, J.A. Keith, E.A. Carter, A. Nilsson, C.P. Kubiak, Angew. Chem.-Int. Edit., 52 (2013) 4841-4844.
[845] J. Mizuki, J. Phys. Soc. Jpn., 82 (2013) art. n. 021001.
[846] O.V. Safonova, M. Tromp, J.A. van Bokhoven, F.M.F. de Groot, J. Evans, P. Glatzel, J. Phys. Chem. B, 110 (2006) 16162-16164.
[847] P. Glatzel, J. Singh, K.O. Kvashnina, J.A. van Bokhoven, J. Am. Chem. Soc., 132 (2010) 2555-2557.
[848] W.M. Heijboer, D.C. Koningsberger, B.M. Weckhuysen, F.M.F. de Groot, Catal. Today, 110 (2005) 228-238.
[849] K. Asakura, K. Kitamurabando, Y. Iwasawa, H. Arakawa, K. Isobe, J. Am. Chem. Soc., 112 (1990) 9096-9104.
[850] J. Corker, F. Lefebvre, C. Lecuyer, V. Dufaud, F. Quignard, A. Choplin, J. Evans, J.M. Basset, Science, 271 (1996) 966-969.
[851] F.B.M. Duivenvoorden, D.C. Koningsberger, Y.S. Uh, B.C. Gates, J. Am. Chem. Soc., 108 (1986) 6254-6262.
[852] Y. Iwasawa, K. Asakura, H. Ishii, H. Kuroda, Zeitschrift Fur Physikalische Chemie Neue Folge, 144 (1985) 105-115.
[853] T. Maschmeyer, J.M. Thomas, A.F. Masters, in: C.R.A. Catlow, A.K. Cheetham (Eds.) New Trends in Materials Chemistry, Kluwer Academic Publishers, Dordrecht; Boston, 1997, pp. 461-494.
[854] C. Coperet, New J. Chem., 28 (2004) 1-10.
[855] A.P. Kozlova, A.I. Kozlov, S. Sugiyama, Y. Matsui, K. Asakura, Y. Iwasawa, J. Catal., 181 (1999) 37-48.
[856] B. Rhers, A. Salameh, A. Baudouin, E.A. Quadrelli, M. Taoufik, C. Coperet, F. Lefebvre, J.M. Basset, X. Solans-Monfort, O. Eisenstein, W.W. Lukens, L.P.H. Lopez, A. Sinha, R.R. Schrock, Organometallics, 25 (2006) 3554-3557.
[857] J.M. Thomas, R. Raja, Top. Catal., 40 (2006) 3-17.
[858] S. Chavan, J.G. Vitillo, M.J. Uddin, F. Bonino, C. Lamberti, E. Groppo, K.P. Lillerud, S. Bordiga, Chem. Mat., 22 (2010) 4602-4611.
[859] J. Evans, M. Tromp, Materials and process, in: P. Barbaro, F. Liguori (Eds.) Heterogenized Homogeneous Catalysts for Fine Chemicals Production, Springer Netherlands, 2010, pp. 433-448.
[860] J. Sa, J. Szlachetko, E. Kleymenov, C. Lothschutz, M. Nachtegaal, M. Ranocchiari, O.V. Safonova, M. Servalli, G. Smolentsev, J.A. van Bokhoven, RSC Adv., 3 (2013) 12043-12048.
[861] L.A. Williams, N. Guo, A. Motta, M. Delferro, I.L. Fragala, J.T. Miller, T.J. Marks, Proc. Natl. Acad. Sci. U. S. A., 110 (2013) 413-418.
[862] S. Takakusagi, W.J. Chun, H. Uehara, K. Asakura, Y. Iwasawa, Top. Catal., 56 (2013) 1477-1487.
[863] J.F.W. Mosselmans, J.M. Corker, J. Evans, J.T. Gauntlett, J.M. Rummey, Catal. Today, 9 (1991) 175-182.
[864] K. Weissermel, H.J. Arpe, Industrial Organic Chemistry, in: J. Rose (Ed.) Applied Organometallic Chemistry, John Wiley & Sons, Ltd., Weinheim, 1997, pp. 857-858.
[865] W.A. Weber, B.C. Gates, J. Catal., 180 (1998) 207-217.

[866] J.F. Goellner, B.C. Gates, G.N. Vayssilov, N. Rosch, J. Am. Chem. Soc., 122 (2000) 8056-8066.
[867] G.N. Vayssilov, B.C. Gates, N. Rosch, Angew. Chem.-Int. Edit., 42 (2003) 1391-1394.
[868] J.O. Ehresmann, P.W. Kletnieks, A. Liang, V.A. Bhirud, O.P. Bagatchenko, E.J. Lee, M. Klaric, B.C. Gates, J.F. Haw, Angew. Chem.-Int. Edit., 45 (2006) 574-576.
[869] P.W. Kletnieks, A.J. Liang, R. Craciun, J.O. Ehresmann, D.M. Marcus, V.A. Bhirud, M.M. Klaric, M.J. Haymann, D.R. Guenther, O.P. Bagatchenko, D.A. Dixon, B.C. Gates, J.F. Haw, Chem.-Eur. J., 13 (2007) 7294-7304.
[870] A.J. Liang, R. Craciun, M.Y. Chen, T.G. Kelly, P.W. Kletnieks, J.F. Haw, D.A. Dixon, B.C. Gates, J. Am. Chem. Soc., 131 (2009) 8460-8473.
[871] P. Serna, B.C. Gates, J. Am. Chem. Soc., 133 (2011) 4714-4717.
[872] M. Flytzani-Stephanopoulos, B.C. Gates, Atomically Dispersed Supported Metal Catalysts, in: Annual Review of Chemical and Biomolecular Engineering, Vol 3, Annual Reviews, Palo Alto, 2012, pp. 545-574.
[873] D. Yardimci, P. Serna, B.C. Gates, ACS Catal., 2 (2012) 2100-2113.
[874] J. Lu, C. Martinez-Macias, C. Aydin, N.D. Browning, B.C. Gates, Catal. Sci. Technol., 3 (2013) 2199-2203.
[875] J.D. Kistler, P. Serna, B.C. Gates, Dalton Trans., 42 (2013) 12626-12632.
[876] D. Yardimci, P. Serna, B.C. Gates, Chem.-Eur. J., 19 (2013) 1235-1245.
[877] A.M. Argo, J.F. Odzak, F.S. Lai, B.C. Gates, Nature, 415 (2002) 623-626.
[878] P. Serna, B.C. Gates, Angew. Chem.-Int. Edit., 50 (2011) 5528-5531.
[879] P. Serna, B.C. Gates, J. Catal., 308 (2013) 201-212.
[880] A.S.K. Hashmi, G.J. Hutchings, Angew. Chem.-Int. Edit., 45 (2006) 7896-7936.
[881] Z.G. Li, C. Brouwer, C. He, Chem. Rev., 108 (2008) 3239-3265.
[882] A. Arcadi, Chem. Rev., 108 (2008) 3266-3325.
[883] A. Corma, A. Leyva-Perez, M.J. Sabater, Chem. Rev., 111 (2011) 1657-1712.
[884] J. Vaclavik, M. Servalli, C. Lothschutz, J. Szlachetko, M. Ranocchiari, J.A. van Bokhoven, ChemCatChem, 5 (2013) 692-696.
[885] M. Ranocchiari, J.A. van Bokhoven, Phys. Chem. Chem. Phys., 13 (2011) 6388-6396.
[886] M. Servalli, M. Ranocchiari, J.A. Van Bokhoven, Chem. Commun., 48 (2012) 1904-1906.
[887] M. Ranocchiari, J.A. van Bokhoven, Chimia, 67 (2013) 397-402.
[888] A.S.K. Hashmi, C. Lothschutz, R. Dopp, M. Rudolph, T.D. Ramamurthi, F. Rominger, Angew. Chem.-Int. Edit., 48 (2009) 8243-8246.
[889] J.P. Weyrauch, A.S.K. Hashmi, A. Schuster, T. Hengst, S. Schetter, A. Littmann, M. Rudolph, M. Hamzic, J. Visus, F. Rominger, W. Frey, J.W. Bats, Chem.-Eur. J., 16 (2010) 956-963.
[890] D. Gianolio, E. Groppo, J.G. Vitillo, A. Damin, S. Bordiga, A. Zecchina, C. Lamberti, Chem. Commun., 46 (2010) 976–978.
[891] J. Puga, T.P. Fehlner, B.C. Gates, D. Braga, F. Grepioni, Inorg. Chem., 29 (1990) 2376-2381.
[892] V. Vidal, A. Theolier, J. ThivolleCazat, J.M. Basset, Science, 276 (1997) 99-102.
[893] A.O. Bouh, G.L. Rice, S.L. Scott, J. Am. Chem. Soc., 121 (1999) 7201-7210.
[894] M.K. Richmond, S.L. Scott, H. Alper, J. Am. Chem. Soc., 123 (2001) 10521-10525.
[895] T. Sasaki, C.M. Zhong, M. Tada, Y. Iwasawa, Chem. Commun., (2005) 2506-2508.
[896] S. Nemana, B.C. Gates, J. Phys. Chem. B, 110 (2006) 17546-17553.
[897] J. Amor Nait Ajjou, S.L. Scott, Organometallics, 16 (1997) 86-92.
[898] C.A. Demmelmaier, R.E. White, J.A. van Bokhoven, S.L. Scottt, J. Phys. Chem. C, 112 (2008) 6439-6449.
[899] F. Blanc, J.M. Basset, C. Coperet, A. Sinha, Z.J. Tonzetich, R.R. Schrock, X. Solans-Monfort, E. Clot, O. Eisenstein, A. Lesage, L. Emsley, J. Am. Chem. Soc., 130 (2008) 5886-5900.
[900] K. Motokura, S. Itagaki, Y. Iwasawa, A. Miyaji, T. Baba, Green Chem., 11 (2009) 1876-1880.
[901] K. Motokura, S. Tanaka, M. Tada, Y. Iwasawa, Chem.-Eur. J., 15 (2009) 10871-10879.
[902] M. Tada, S. Muratsugu, M. Kinoshita, T. Sasaki, Y. Iwasawa, J. Am. Chem. Soc., 132 (2010) 713-724.
[903] A. Fihri, M. Bouhrara, B. Nekoueishahraki, J.M. Basset, V. Polshettiwar, Chem. Soc. Rev., 40 (2011) 5181-5203.
[904] F. Rascon, R. Wischert, C. Coperet, Chem. Sci., 2 (2011) 1449-1456.
[905] L.T. Zhuravlev, Langmuir, 3 (1987) 316-318.
[906] J.M. Thomas, R. Raja, D.W. Lewis, Angew. Chem.-Int. Edit., 44 (2005) 6456-6482.
[907] T.J. Pullukat, R.E. Hoff, Catal. Rev.-Sci. Eng., 41 (1999) 389-428.
[908] M.P. McDaniel, Adv. Catal., 33 (1985) 47-98.
[909] M.P. McDaniel, Adv. Catal., 53 (2010) 123-606.
[910] A. Zecchina, E. Groppo, Proc. R. Soc. A-Math. Phys. Eng. Sci., 468 (2012) 2087-2098.
[911] E. Groppo, C. Lamberti, G. Spoto, S. Bordiga, G. Magnacca, A. Zecchina, J. Catal., 236 (2005) 233-244.
[912] B.M. Weckhuysen, R.A. Schoonheydt, J.M. Jehng, I.E. Wachs, S.J. Cho, R. Ryoo, S. Kijlstra, E. Poels, J. Chem. Soc. Faraday Trans., 91 (1995) 3245-3253.

[913] A. Filipponi, A. Dicicco, R. Zanoni, M. Bellatreccia, V. Sessa, C. Dossi, R. Psaro, Chem. Phys. Lett., 184 (1991) 485-490.
[914] A. Damin, F. Bonino, S. Bordiga, E. Groppo, C. Lamberti, A. Zecchina, ChemPhysChem, 7 (2006) 342-344.
[915] G.G. Hlatky, Chem. Rev., 100 (2000) 1347-1376.
[916] M.Y. Lee, S.L. Scott, Chem.-Eur. J., 17 (2011) 4632-4639.
[917] K. Seenivasan, A. Sommazzi, F. Bonino, S. Bordiga, E. Groppo, Chem.-Eur. J., 17 (2011) 8648-8656.
[918] A. Kytokivi, S. Haukka, J. Phys. Chem. B, 101 (1997) 10365-10372.
[919] K. Schrijnemakers, P. Van Der Voort, E.F. Vansant, Phys. Chem. Chem. Phys., (1999) 2569-2572.
[920] C. Lamberti, E. Groppo, G. Spoto, S. Bordiga, A. Zecchina, Adv. Catal., 51 (2007) 1-74.
[921] C. Lamberti, A. Zecchina, E. Groppo, S. Bordiga, Chem. Soc. Rev., 39 (2010) 4951-5001.
[922] E. Groppo, K. Seenivasan, C. Barzan, Catal. Sci. Technol., 3 (2013) 858-878.
[923] E.M.J. Johansson, M. Odelius, S. Plogmaker, M. Gorgoi, S. Svensson, H. Siegbahn, H. Rensmo, J. Phys. Chem. C, 114 (2010) 10314-10322.
[924] S.I. Pascu, P.A. Waghorn, T.D. Conry, H.M. Betts, J.R. Dilworth, G.C. Churchill, T. Pokrovska, M. Christlieb, F.I. Aigbirhio, J.E. Warren, Dalton Trans., (2007) 4988-4997.
[925] R. Takahashi, Y. Kobuke, J. Am. Chem. Soc., 125 (2003) 2372-2373.
[926] R. Takahashi, Y. Kobuke, J. Org. Chem., 70 (2005) 2745-2753.
[927] F.J.M. Casado, L. Canadillas-Delgado, F. Cucinotta, A. Guerrero-Martinez, M.R. Riesco, L. Marchese, J.A.R. Cheda, Crystengcomm, 14 (2012) 2660-2668.
[928] M. Feyand, M. Koppen, G. Friedrichs, N. Stock, Chem.-Eur. J., 19 (2013) 12537-12546.
[929] S. Gago, J.A. Fernandes, J.P. Rainho, R.A.S. Ferreira, M. Pillinger, A.A. Valente, T.M. Santos, L.D. Carlos, P.J.A. Ribeiro-Claro, I.S. Goncalves, Chem. Mat., 17 (2005) 5077-5084.
[930] M. Hasegawa, S. Kunisaki, H. Ohtsu, F. Werner, Mon. Chem., 140 (2009) 751-763.
[931] L. Cunha-Silva, L. Mafra, D. Ananias, L.D. Carlos, J. Rocha, F.A.A. Paz, Chem. Mat., 19 (2007) 3527-3538.
[932] L. Cunha-Silva, S. Lima, D. Ananias, P. Silva, L. Mafra, L.D. Carlos, M. Pillinger, A.A. Valente, F.A.A. Paz, J. Rocha, J. Mater. Chem., 19 (2009) 2618-2632.
[933] L. Cunha-Silva, D. Ananias, L.D. Carlos, F.A.A. Paz, J. Rocha, Z. Kristall., 224 (2009) 261-272.
[934] A. Curioni, W. Andreoni, R. Treusch, F.J. Himpsel, E. Haskal, P. Seidler, C. Heske, S. Kakar, T. van Buuren, L.J. Terminello, Appl. Phys. Lett., 72 (1998) 1575-1577.
[935] R. Treusch, F.J. Himpsel, S. Kakar, L.J. Terminello, C. Heske, T. van Buuren, V.V. Dinh, H.W. Lee, K. Pakbaz, G. Fox, I. Jimenez, J. Appl. Phys., 86 (1999) 88-93.
[936] P.S.G. Kim, S.J. Naftel, T.K. Sham, I. Coulthard, Y.F. Hu, A. Moewes, J.W. Freeland, J. Electron Spectrosc. Relat. Phenom., 144 (2005) 901-904.
[937] T. Yokoyama, H. Ishii, N. Matsuie, K. Kanai, E. Ito, A. Fujimori, T. Araki, Y. Ouchi, K. Seki, Synth. Met., 152 (2005) 277-280.
[938] A. DeMasi, L.F.J. Piper, Y. Zhang, I. Reid, S. Wang, K.E. Smith, J.E. Downes, N. Peltekis, C. McGuinness, A. Matsuura, J. Chem. Phys., 129 (2008) art. n. 224705.
[939] T.W. Pi, T.C. Yu, C.P. Ouyang, J.F. Wen, H.L. Hsu, Phys. Rev. B, 71 (2005) art. n. 205310.
[940] D. Liu, M. Fina, J.H. Guo, X.B. Chen, G. Liu, S.G. Johnson, S.S. Mao, Appl. Phys. Lett., 94 (2009) art. n. 013110.
[941] W.R. Brito, G. Araujo, W.G. Quirino, C. Legnani, Y. Angulo, M. Cremona, M.L.M. Rocco, J. Braz. Chem. Soc., 21 (2010) 2367-2372.
[942] K. Sauer, J. Yano, V.K. Yachandra, Coord. Chem. Rev., 252 (2008) 318-335.
[943] Govindjee, Photosynth. Res., 87 (2006) 331-335.
[944] J.E. Penner-Hahn, Structural characterization of the Mn site in the photosynthetic oxygen-evolving complex, in: H.A.O. Hill, P.J. Sadler, A.J. Thomson (Eds.) Metal Sites in Proteins and Models Redox Centres, Springer Berlin Heidelberg, Berlin, 1998, pp. 1-36.
[945] V.K. Yachandra, K. Sauer, M.P. Klein, Chem. Rev., 96 (1996) 2927-2950.
[946] X. Liu, F.Y. Wang, Coord. Chem. Rev., 256 (2012) 1115-1136.
[947] G.C. Dismukes, R. Brimblecombe, G.A.N. Felton, R.S. Pryadun, J.E. Sheats, L. Spiccia, G.F. Swiegers, Accounts Chem. Res., 42 (2009) 1935-1943.
[948] R. Brimblecombe, G.F. Swiegers, G.C. Dismukes, L. Spiccia, Angew. Chem.-Int. Edit., 47 (2008) 7335-7338.
[949] R. Brimblecombe, D.R.J. Kolling, A.M. Bond, G.C. Dismukes, G.F. Swiegers, L. Spiccia, Inorg. Chem., 48 (2009) 7269-7279.
[950] R. Brimblecombe, A.M. Bond, G.C. Dismukes, G.F. Swiegers, L. Spiccia, Phys. Chem. Chem. Phys., 11 (2009) 6441-6449.
[951] R. Brimblecombe, A. Koo, G.C. Dismukes, G.F. Swiegers, L. Spiccia, J. Am. Chem. Soc., 132 (2010) 2892-2894.

[952] R.K. Hocking, R. Brimblecombe, L.Y. Chang, A. Singh, M.H. Cheah, C. Glover, W.H. Casey, L. Spiccia, Nat. Chem., 3 (2011) 461-466.
[953] R.K. Hocking, S.L.Y. Chang, D.R. MacFarlane, L. Spiccia, Aust. J. Chem., 65 (2012) 608-614.
[954] R. Okazaki, S. Masaoka, K. Sakai, Dalton Trans., (2009) 6127-6133.
[955] M. Martis, K. Mori, K. Kato, G. Sankar, H. Yamashita, ChemPhysChem, 14 (2013) 1122-1125.
[956] K. Mori, K. Watanabe, Y. Terai, Y. Fujiwara, H. Yamashita, Chem.-Eur. J., 18 (2012) 11371-11378.
[957] K. Mori, K. Watanabe, K. Fuku, H. Yamashita, Chem.-Eur. J., 18 (2012) 415-418.
[958] K. Mori, S. Ogawa, M. Martis, H. Yamashita, J. Phys. Chem. C, 116 (2012) 18873-18877.
[959] A. Fateeva, P.A. Chater, C.P. Ireland, A.A. Tahir, Y.Z. Khimyak, P.V. Wiper, J.R. Darwent, M.J. Rosseinsky, Angew. Chem.-Int. Edit., 51 (2012) 7440-7444.
[960] K.E. Lee, M.A. Gomez, T. Regier, Y.F. Hu, G.P. Demopoulos, J. Phys. Chem. C, 115 (2011) 5692-5707.
[961] X. Ju, J. Zhang, K.W. Wu, Y.J. Hou, P.H. Xie, B.W. Zhang, Surf. Interface Anal., 32 (2001) 95-97.
[962] Y.V. Zubavichus, Y.L. Slovokhotov, M.K. Nazeeruddin, S.M. Zakeeruddin, M. Gratzel, V. Shklover, Chem. Mat., 14 (2002) 3556-3563.
[963] H. Rensmo, K. Westermark, S. Sodergren, O. Kohle, P. Persson, S. Lunell, H. Siegbahn, J. Chem. Phys., 111 (1999) 2744-2750.
[964] E.M.J. Johansson, M. Hedlund, H. Siegbahn, H. Rensmo, J. Phys. Chem. B, 109 (2005) 22256-22263.
[965] K. Schwanitz, U. Weiler, R. Hunger, T. Mayer, W. Jaegermann, J. Phys. Chem. C, 111 (2007) 849-854.
[966] L.C. Mayor, J. Ben Taylor, G. Magnano, A. Rienzo, C.J. Satterley, J.N. O'Shea, J. Schnadt, J. Chem. Phys., 129 (2008) art. n. 114701.
[967] K. Westermark, H. Rensmo, J. Schnadt, P. Persson, S. Sodergren, P.A. Bruhwiler, S. Lunell, H. Siegbahn, Chem. Phys., 285 (2002) 167-176.
[968] K. Westermark, H. Rensmo, H. Siegbahn, K. Keis, A. Hagfeldt, L. Ojamae, P. Persson, J. Phys. Chem. B, 106 (2002) 10102-10107.
[969] J.H. Lambert, Photometria sive de mensura et gradibus luminis, colorum et umbrae (On the measure and gradations of light, colors, and shade), pag. 391, Eberhardt Klett, Augsburg 1760.
[970] A. Beer, Ann. Phys., 86 (1852) 78–88.
[971] B.L. Henke, E.M. Gullikson, J.C. Davis, At. Data. Nucl. Data Tables, 54 (1993) 181-342.
[972] E. Borfecchia, D. Gianolio, G. Agostini, S. Bordiga, C. Lamberti, Characterization of MOFs. 2. Long and Local Range Order Structural Determination of MOFs by Combining EXAFS and Diffraction Techniques, in: F.X. Llabrés i Xamena, J. Gascón (Eds.) Metal Organic Frameworks as Heterogeneous Catalysts, The Royal Society of Chemistry, Cambridge, 2013, pp. 143-208.
[973] E.N. Maslen, A.G. Fox, M.A. O'Keefe, X-ray Scattering, in: E. Prince (Ed.) InternationalTables for Crystallography, Kluwer Academic, Dordrecht, 2004, pp. 554.
[974] C. Kittel, Introduction to Solid State Physics, John Wiley & Sons, 2004.
[975] D.E. Sands, Introduction to Crystallography, Dover Publications, New York, 1994.
[976] M.F.C. Ladd, R.A. Palmer, Structure Determination by X-Ray Crystallography, Kluwer Academic/Plenum Publishers, New York, 2003.
[977] G. Taylor, Acta Crystallogr. D, 59 (2003) 1881-1890.
[978] A.L. Patterson, Z. Kristallogr., 90 (1934) 517-542.
[979] A.L. Patterson, Phys. Rev., 46 (1934) 372-376.
[980] M.G. Rossmann, E. Arnold, Patterson and molecular-replacement techniques, in: International Tables for Crystallography, 2006, pp. 235-263.
[981] M.G. Rossmann, D.M. Blow, Acta Cryst., 15 (1962) 24-31.
[982] G. Oszlanyi, A. Suto, Acta Crystallogr. Sect. A, 64 (2008) 123-134.
[983] J.L. Smith, W.A. Hendrickson, T.T. C., J. Berendzen, MAD and MIR, in: International Tables for Crystallography 2006, pp. 299-309.
[984] C. Cohen-Tannoudji, B. Diu, F. Laloë, Quantum Mechanics, Wiley, New York, 1977.
[985] L.L. Foldy, Phys. Rev., 67 (1945) 107-119.
[986] M. Lax, Rev. Mod. Phys., 23 (1951) 287-310.
[987] G. Green, An essay of the application of mathematical analysis to electricity and magnetism, T.Wheelhouse, Nottingham, 1828.
[988] J.J. Kas, A.P. Sorini, M.P. Prange, L.W. Cambell, J.A. Soininen, J.J. Rehr, Phys. Rev. B, 76 (2007) art. n. 195116.
[989] R. Haydock, The Recursive Solution of the Schrodinger Equation, in: F.S. Henry Ehrenreich, T. David (Eds.) Solid State Physics, Academic Press, 1980, pp. 215-294.
[990] P.J. Durham, J.B. Pendry, C.H. Hodges, Comput. Phys. Commun., 25 (1982) 193-205.
[991] F. Gel'mukhanov, H. Agren, Phys. Rep.-Rev. Sec. Phys. Lett., 312 (1999) 87-330.